REFERENCE

FAA-76-22.III

Report No. FAA-RD-75-173, III

AIR TRAFFIC CONTROL EXPERIMENTATION AND EVALUATION WITH THE NASA ATS-6 SATELLITE

Volume III: Summary of U.S. Aeronautical Technology Test Program

E.H. Schroeder
A.D. Thompson
R.W. Sutton
S.G. Wilson
C.J. Kuo

Boeing Commercial Airplane Company
PO Box 3707
Seattle WA 98124

SEPTEMBER 1976
FINAL REPORT

Prepared for

U.S. DEPARTMENT OF TRANSPORTATION
Federal Aviation Administration
Systems Research and Development Service
Washington DC 20591

NOTICE

This document is disseminated under the sponsorship of the Department of Transportation in the interest of information exchange. The United States Government assumes no liability for its contents or use thereof.

NOTICE

The United States Government does not endorse products or manufacturers. Trade or manufacturers' names appear herein solely because they are considered essential to the object of this report.

REPORT NO. FAA-RD-75-173,III

AIR TRAFFIC CONTROL EXPERIMENTATION AND EVALUATION WITH THE NASA ATS-6 SATELLITE

Volume III: Summary of U. S. Aeronautical Technology Test Program

ERRATA

Pages 6-10 and 6-12 of this volume are replaced by the attached figures.

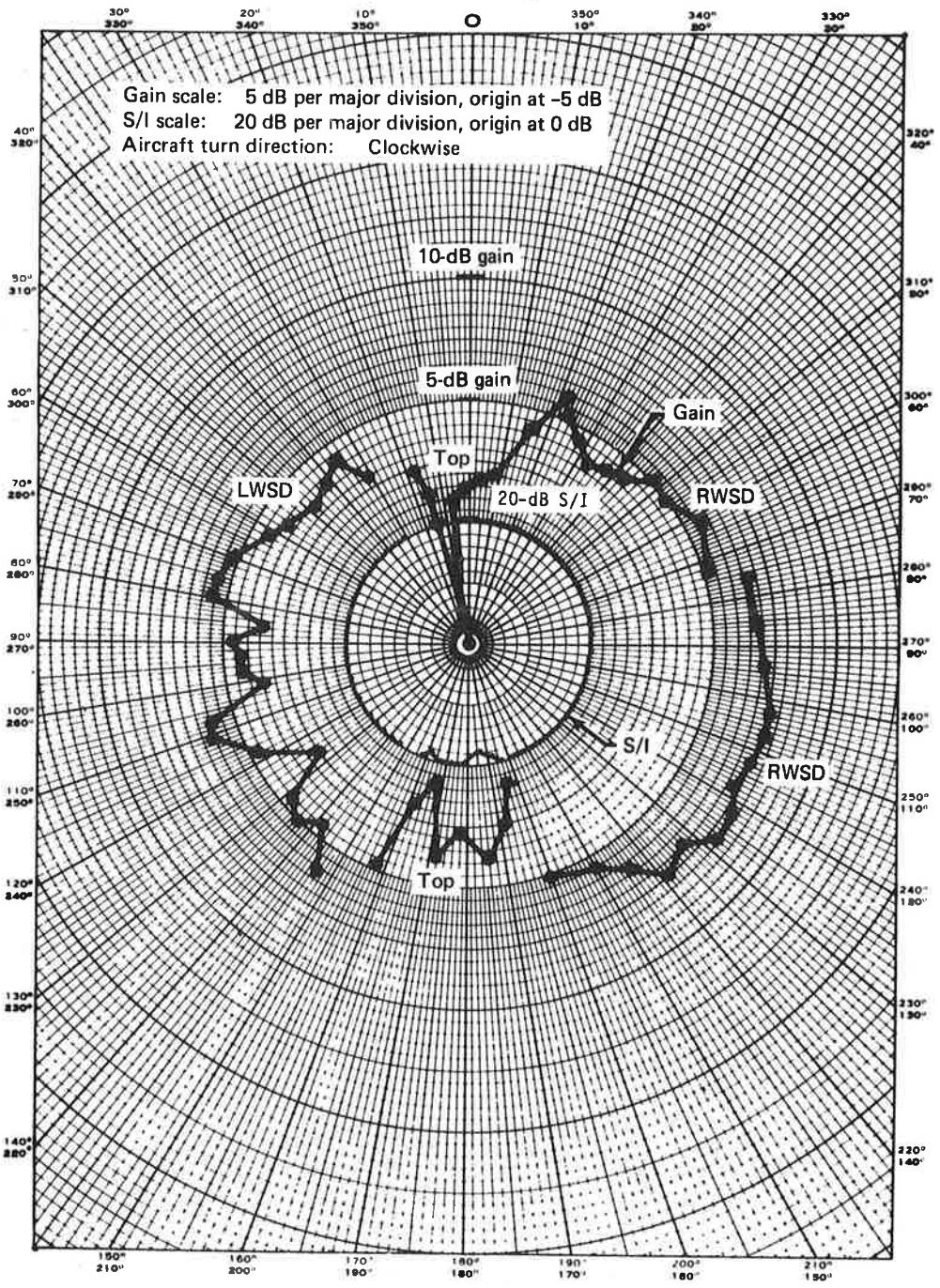

Figure 6-4. Three-Element Slot-Dipole Antenna System Gain and S/I, March 25, 1975, Elevation Angle = 15°

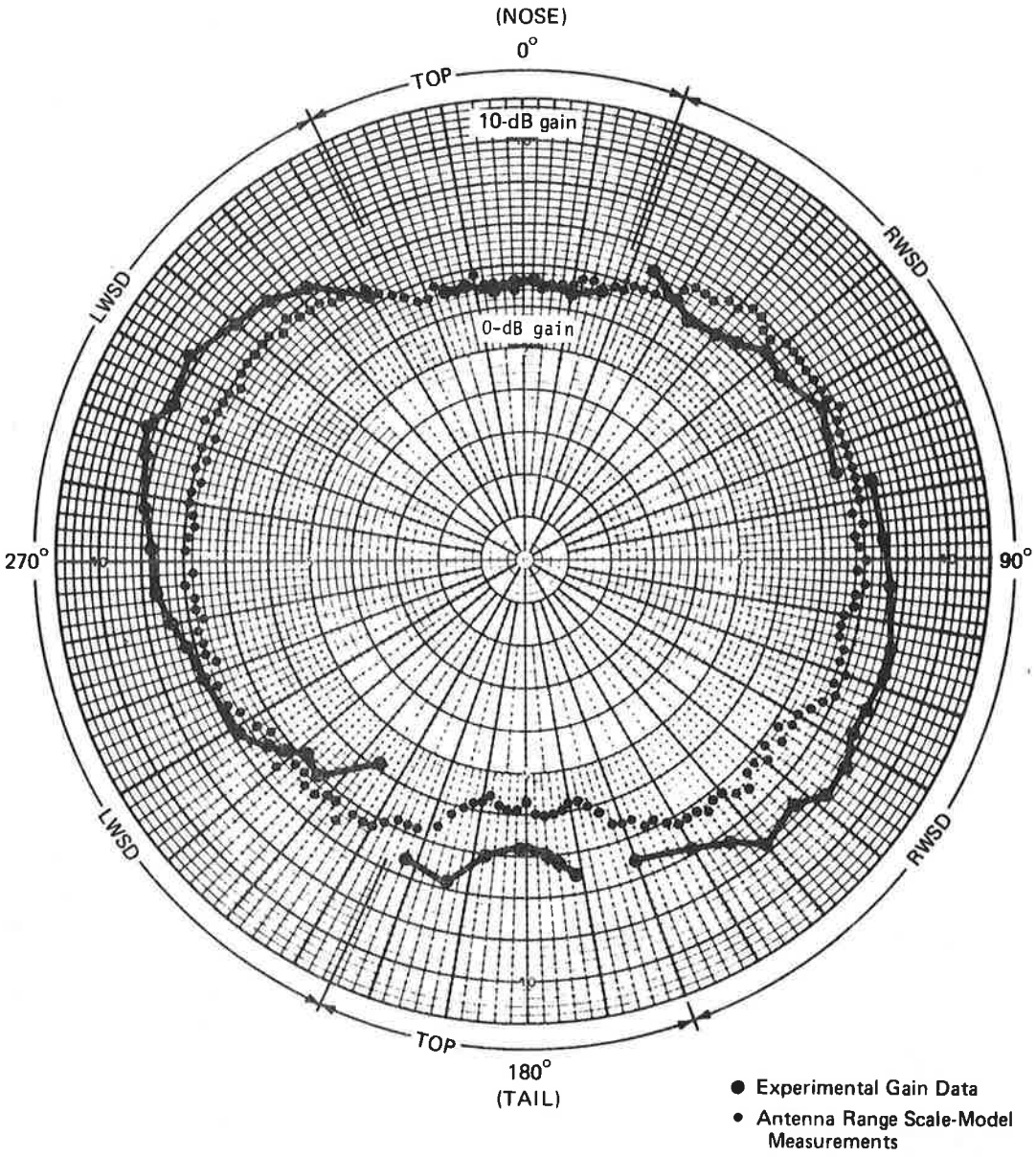

Figure 6-6. Slot-Dipole-System Composite Gain at 20° Elevation

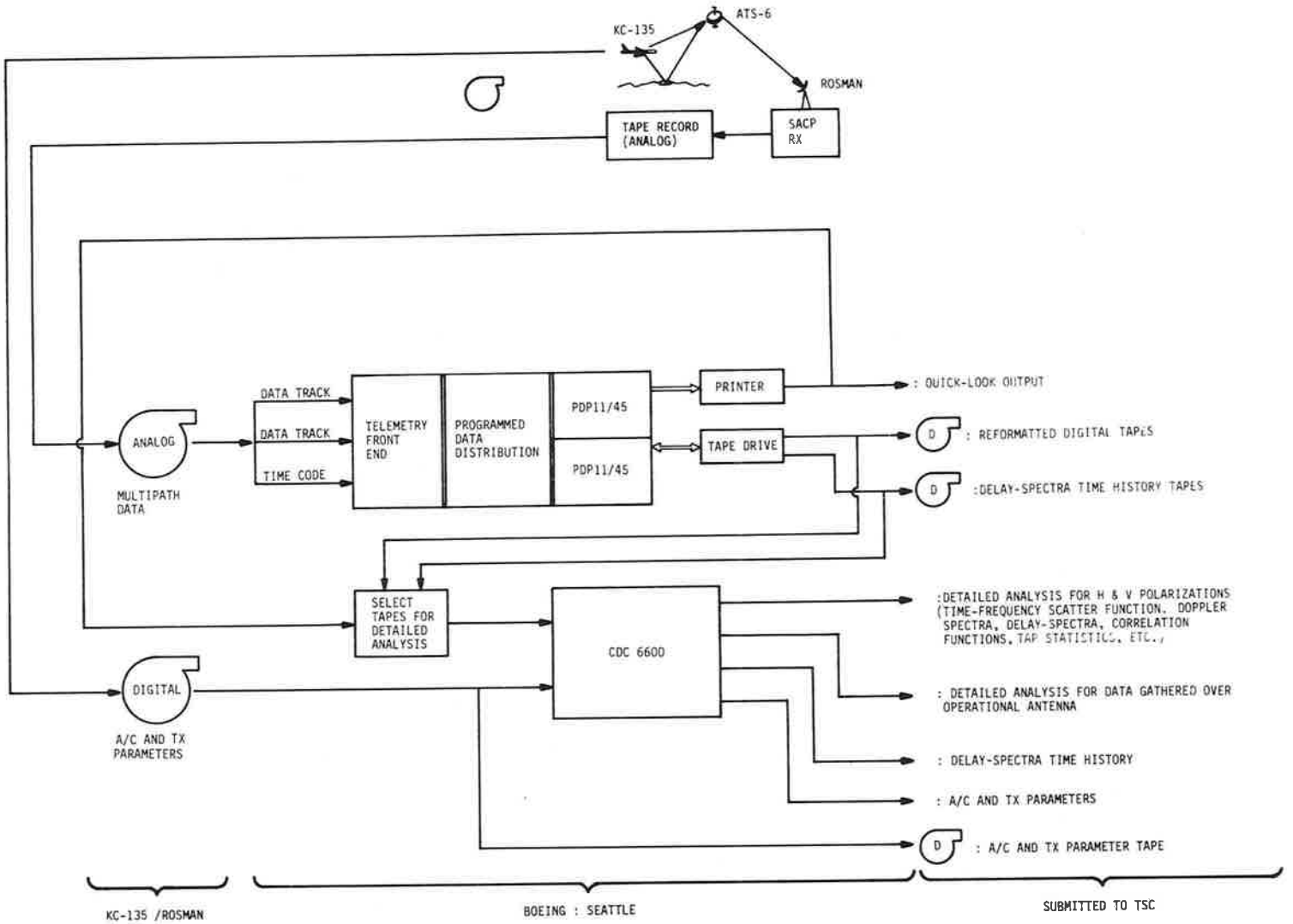

Figure 4-3. Data Reduction and Analysis Functional Flow

TABLE 4-2. MULTIPATH DATA ACQUISITION SUMMARY

Date, mo-day-yr	Elevation angle, deg	Test duration, hr + min	Remarks
A. Oceanic			
9-24-74	30	1+00	Nominal
10-24-74	18 to 23	1+00	Nominal
10-28-74	8 to 12	1+00	Nominal
11-14-74	3 to 8	1+00	SACP receiver data sign bit inoperative causing all Doppler data to be of one polarity. $S(\tau,\omega)$ function could not be calculated. Delay spectra data unaffected.
11-15-74	8 to 13	1+00	
11-16-74	3 to 8	1+00	
11-21-74	19 to 23	1+00	
1-23-75	3 to 8	1+00	Partial data acquisition, faulty 100-W PA (30-W TWT used)
1-27-75	8 to 13	1+00	Nominal
1-28-75	19 to 23	1+20	Aircraft maneuvers due to weather avoidance
1-30-75	3 to 8	1+00	Nominal
2-27-75	30	1+20	Nominal
3-25-75	15	0+20	TOP antenna only
3-27-75	10 to 15	1+00	FMP antenna fault
3-38-75	3 to 8	1+00	FMP antenna fault
3-31-75	10 to 15	1+00	Nominal
4-02-75	7 to 11	1+00	Nominal
4-03-75	16 to 21	1+00	Nominal
		18 hr	Oceanic Test Hours
B. CONUS			
9-19-74	30 to 45	4+00	Eastern U.S., nominal
10-30-74	30 to 45	4+00	Eastern U.S., nominal
11-02-74[a]	30 to 45	4+00	Northwest U.S., 50% of data acquired
2-18-75[a]	16 to 27	4+30	NW Canada to Edmonton, 50% of data acquired, no useful airport landing data
2-19-75[a]	27 to 40	4+30	Central Canada to O'Hare, nominal
2-20-75[a]	28 to 37	4+30	N. Quebec to JFK, nominal
		25.5 hr	CONUS Test Hours

[a]Acquired data with both fan and pencil beams of ATS-6.

modulated (PCM) subsystem to the programmable data distributor (PDD). The PDD merged time words with the data and distributed the information to one or both of the PDP 11/45 computer's input/output (I/O) buses. The dual PDP computer system performed three basic functions: (1) conversion of the analog-recorded data tapes into digital-format computer-compatible tapes, (2) quick-look processing of the multipath data, and (3) calculation of the time-ordered delay-spectra arrays that were used to generate the time history of the multipath channel delay spectra.

Detailed analysis of the prober data was performed in the CDC 6600. This analysis provided a comprehensive characterization of the multipath channel.

Sea-state buoy data was analyzed by CNR, Inc. Analog tapes were stripped and reformatted at a DOT/TSC facility. Detailed processing, as described in appendix B, volume IV, was performed on the DOT/TSC PDP 10 computer.

4.3.2 Algorithm Execution Sequence

The algorithm execution sequence for processing the multipath channel data is given in figures 4-4 and 4-5. Comments relative to selected outputs or processing blocks are given below.

4.3.2.1 Quick-Look Real-Time Playback Data Analysis – This quick-look output, directly available from the PDP 11/45 system, provides both oscilloscope display plots and hard-copy numerical output. From this information, the operator may investigate data quality and system parameters and may identify data intervals of special interest.

4.3.2.2 Reformatted SACP Digital Tapes – Analog source tapes are processed to provide computer-compatible digital tapes.

4.3.2.3 Delay-Spectra Time History – For all periods of valid data collection, the scatter channel's delay power spectral density (psd) is determined in a time running nonoverlapping manner with psd estimates being calculated over a 2-sec interval. The outputs that occur once every 2 sec are given in both numerical and three-dimensional plotted formats. Respectively, these data provide both a quantitative and a comprehensive overview description of the channel's time-variant delay-spectra characteristics.

4.3.2.4 Delay-Doppler Scatter Power Spectral Density: $S(\tau,\omega)$ – This function represents the distribution of diffusely scattered power arriving at the receiver with Doppler frequency ω and time delay τ.

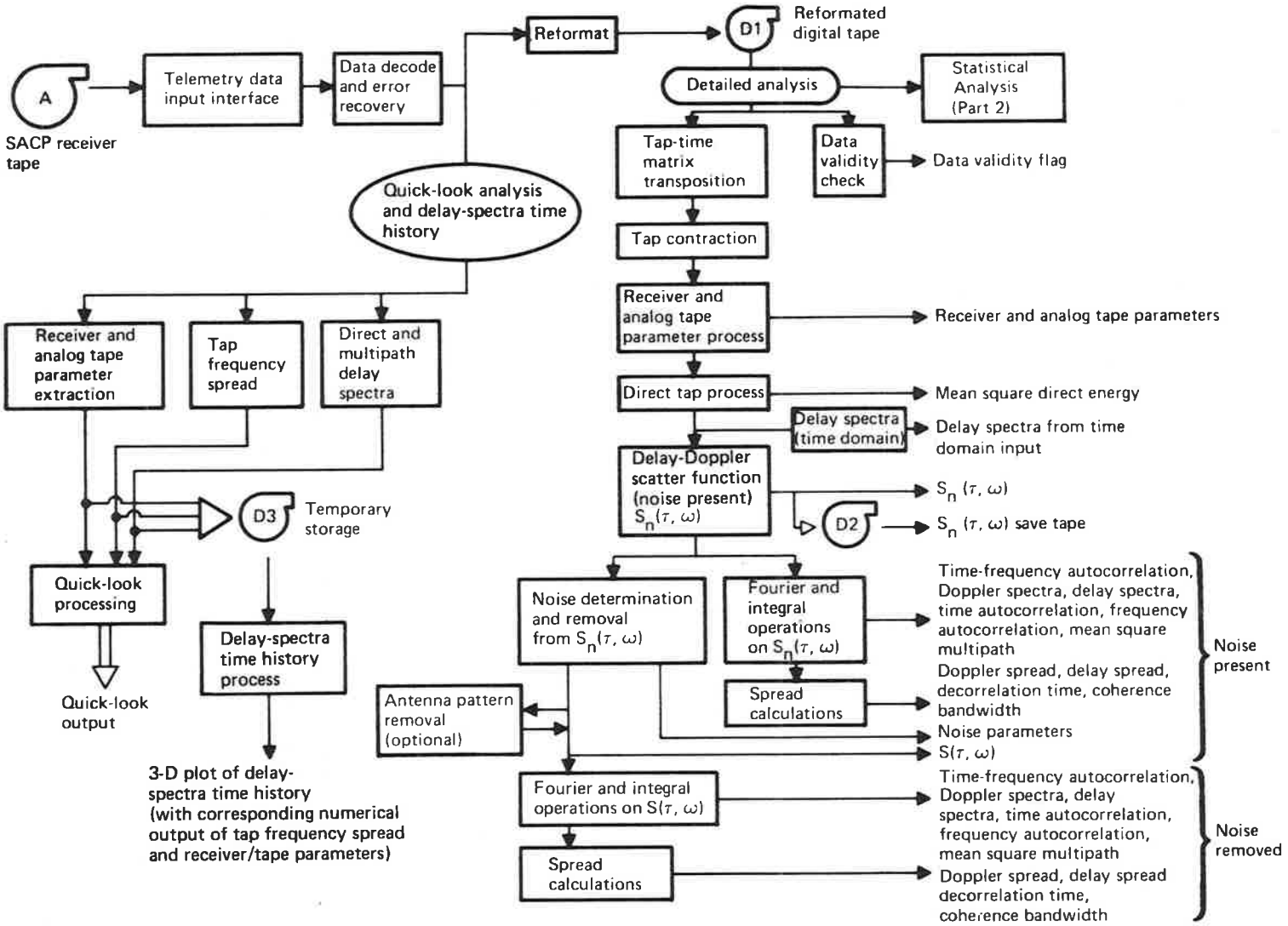

Figure 4-4. Multipath Algorithm Execution Sequence — Part 1

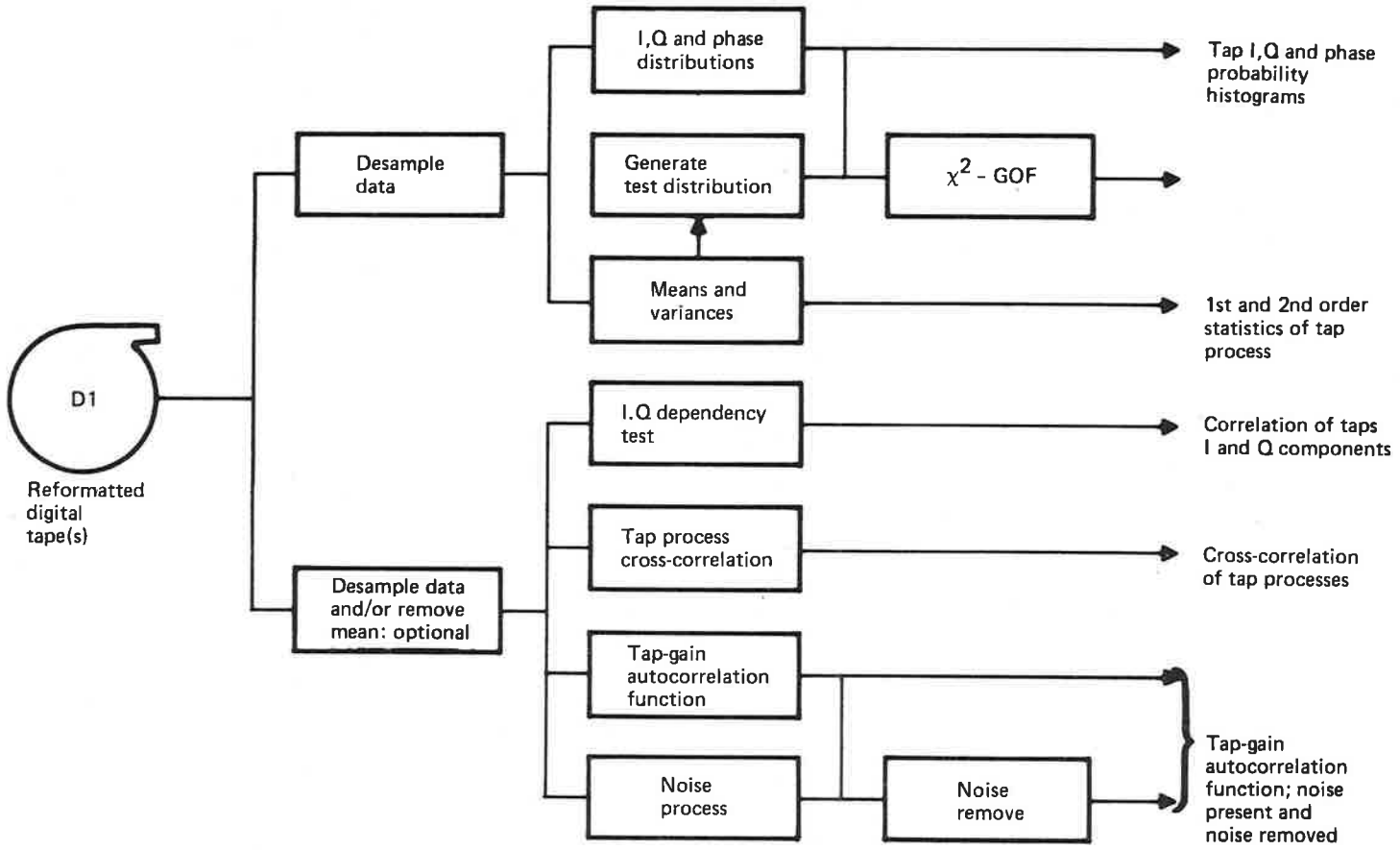

Figure 4-5. Multipath Algorithm Execution Sequence — Part 2

For the zero-mean complex Gaussian random scatter process, $S(\tau,\omega)$ completely characterizes the channel statistics.

4.3.2.5 Integral and Fourier Operations on $S(\tau,\omega)$ – The scatter function $S(\tau,\omega)$ contains all the ingredients needed for the derivation of equivalent and lower order channel parameters. Software modules are contained within the CDC 6600 routines to derive the joint time-frequency autocorrelation function $R(\xi,\Omega)$, time autocorrelation function $R(\xi,0)$, frequency autocorrelation function $R(0,\Omega)$, Doppler spectrum $D(\omega)$, delay spectrum $Q(\tau)$, and total rms scattered energy $<|I|^2>$.

4.3.2.6 Channel Spread Parameters – From the $D(\omega)$, $Q(\tau)$, and $R(\xi,0)$ and $R(0,\Omega)$ distributions, lower echelon first-order channel parameters such as the Doppler spread, delay spread, decorrelation time, and coherence bandwidth of the scatter channel are estimated.

4.3.2.7 Noise Determination and Removal (NDandR) – The outputs of the SACP multipath correlator contain desired signal data, spurious signal terms, low-pass additive thermal noise, and receiver arithmetic noise. Under normal SACP operating conditions, the NDandR algorithm statistically eliminates these noise terms from the data on a tap-by-tap basis.

4.3.2.8 Antenna-Pattern-Effects Removal – Design criteria for the forward multipath antenna were established to provide a radiation pattern with nearly uniform coverage over the effective scatter region. However, for certain flight direction headings, the fidelity of the channel measurement may be enhanced by applying the antenna-effects-removal algorithm. This routine operates on the noise-free $S(\tau,\omega)$ estimate to provide an equivalent scatter function that would be measured with a perfect uniform-gain antenna.

4.3.2.9 Tap Amplitude and Phase Distributions – Determination of the fundamental statistical properties of the scatter process requires that the received signal's time-domain fluctuations be characterized. The probability distribution and its associated mean and variance for these fluctuations are derived for each tap's I component, Q component, and phase angle. The process's composite signal may also be subjected to these operations. Experimental distributions are compared to the results for the complex Gaussian channel via the χ^2 goodness-of-fit test.

4.3.2.10 Tap Process Cross-Correlations – The degree of coherency between any two taps in a particular tap bank or in cross-polarized banks (i.e., one horizontal, the other vertical) is measured through use of the normalized cross-correlation function, $R_{XY}(\xi)$.

4.3.2.11 Tap I and Q Dependency – For random rough-surface scattering where the electromagnetic wave undergoes deep phase modulation at the multipath interface, we expect that the I and Q components of the received signals are statistically independent. This condition is explored by determining the zero-lag normalized correlation coefficient, $R_{IQ}(0)$, between a tap's orthogonal components.

4.3.2.12 Tap-Gain Autocorrelation Function: $U(\tau,\xi)$ – An estimate of the channel's tap-gain autocorrelation function, $U(\tau,\xi)$, is derived. This function measures the autocorrelation function of the multipath process on a tap-by-tap basis and is available (magnitude) as a three-dimensional output plot from the software package.

4.3.2.13 System Calibration Parameter Data – Magnetically recorded data pertaining to receiver system operation (e.g., direct and multipath channel gains), transmitter power amplifier outputs, and aircraft flight parameter descriptors are computer reduced to aid in the normalization of the scatter channel power returns. These data also serve as a data collection integrity measure and are used primarily to augment the logged flight test data.

4.4 OCEANIC MULTIPATH TEST RESULTS

Probes of the oceanic multipath medium were conducted on 18 separate occasions covering a range of elevation angles from 3^{o} to 32^{o} and a variety of North Atlantic sea conditions. Results illustrate the delay-Doppler scatter function; outputs from Fourier and integral operation on the scatter function (e.g., delay spectra, autocorrelation functions, total scattered energy, etc.); the spread values of the delay spectra, Doppler spectra, and autocorrelation functions; and characterization of the complex receiver's time-domain statistics.

Linear polarization results are compared with predictions based on surface integration of the physical optics vector scatter model as applied to a very rough surface possessing an isotropic slope distribution of the Gaussian form. When applicable, the measured channel parameters are also compared with theoretical predictions based on the "steepest descent" solution to the integral formulations that develop under the closed-form approach to the channel characterization. Only a limited amount of sea-state measurement information, acquired during the March 1975 tests, was available. Since the sea-state measurements and the multipath tests were never truly time coincident, a one-to-one comparison of experimental results and theory for a specific measured sea condition was not possible. A range of rms slopes and an assumed "typical" value were therefore used for the bulk of the correlation between experiment and theory. The sea-state measurement data was used for validation of the range of sea slopes and other assumptions relative to sea-slope distributions incorporated in the inputs to the physical optics vector model calculations.

4.4.1 Delay-Doppler Scatter Function: $S(\tau,\omega)$

For oceanic scatter at L-band frequencies, there are scientific reasons (based on the time-series analyses of sec. 5.4, vol. V) to believe that the multipath channel is adequately described as a zero-mean complex Gaussian process. Since the experimental test conditions are processed in time segments on the order of 6 sec, we may also assume in general that the effective scatter region traverses a surface area over which the significant electrical and statistical physical parameters are relatively invariant. Under these conditions, which appear to be representative of the channel statistics, the delay-Doppler scatter function $S(\tau,\omega)$ completely characterizes the statistics of the channel (ref. 4-2). $S(\tau,\omega)$ represents the power spectral density of multipath energy arriving at the receiver with delay τ and Doppler frequency shift ω. It is derived by taking the Fourier transform of the complex delay tap processes.

Several fundamental observations have been made relative to the energy distribution dependencies of $S(\tau,\omega)$ upon grazing angle, flight direction, and polarization. Typically, these functional relationships are most easily discussed when the scatter function is reduced to lower echelon relationships such as the Doppler spectra, spreads, etc. Observations relative to the lower order parameters are found in following sections. In this section we discuss some of the more distinct properties that have been deduced from the $S(\tau,\omega)$ observations.

Three-dimensional plots of the experimentally derived scatter function are presented in volume V for a comprehensive range of test parameter permutations. Drawing from this source, we present sample $S(\tau,\omega)$ distributions for the mid-grazing angle (11^{o} to 16^{o}), horizontal polarization probe. These data, which also include the unidimensional spectra autocorrelation functions, are given in figures 4-6 and 4-7 for flight vectors corresponding to the in-plane and cross-plane directions, respectively.

From these figures and the $S(\tau,\omega)$ data ensemble of volume V, it is readily observed that the scatter function's energy distribution in the Doppler variable coordinate exhibits a pronounced dependence upon the *direction* of the aircraft's velocity vector. For cross-plane flight directions (i.e., KC-135 flying broadside to ATS-6 direction), $S(\tau,\omega)$ possesses a high degree of Doppler coordinate symmetry. On the other hand, for the 45^{o} and in-plane velocity direction the asymmetry of the scatter function becomes increasingly significant. In fact, for the in-plane case we note that as the delay tap number increases, the negative-frequency dispersion of a particular tap's Doppler spectrum increases accordingly; in comparison, the positive-frequency range is rather limited and has a bandwidth that is relatively invariant from tap to tap. We also note that for a particular in-plane delay tap (τ), the resultant Doppler spectrum has two very distinct spectral "humps" that correspond to the upper and lower frequency limits over which physically possible multipath is returned. These aircraft heading dependencies are in agreement with the model-predicted results of section 4.5 and, as outlined there, we may ascribe the spectral "humps" of the in-plane data sets to the following two factors:

a. For in-plane flight directions, the surface elements responsible for returning energy into the upper and lower Doppler limits of a particular delay tap lie along the great circle path

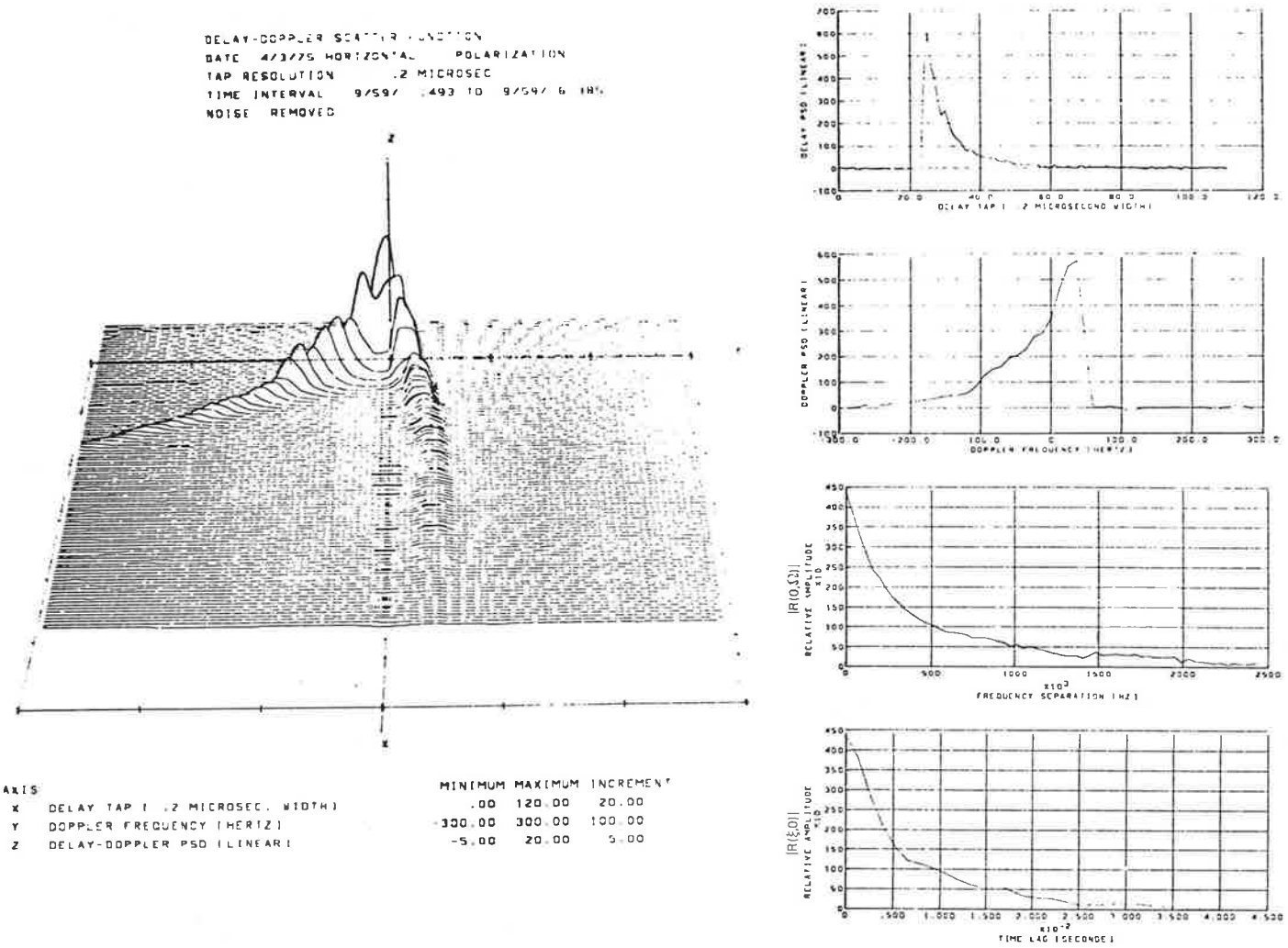

Figure 4-6. Oceanic Multipath Parameters — Horizontal Polarization, 16^{o} Grazing Angle, In-Plane Geometry

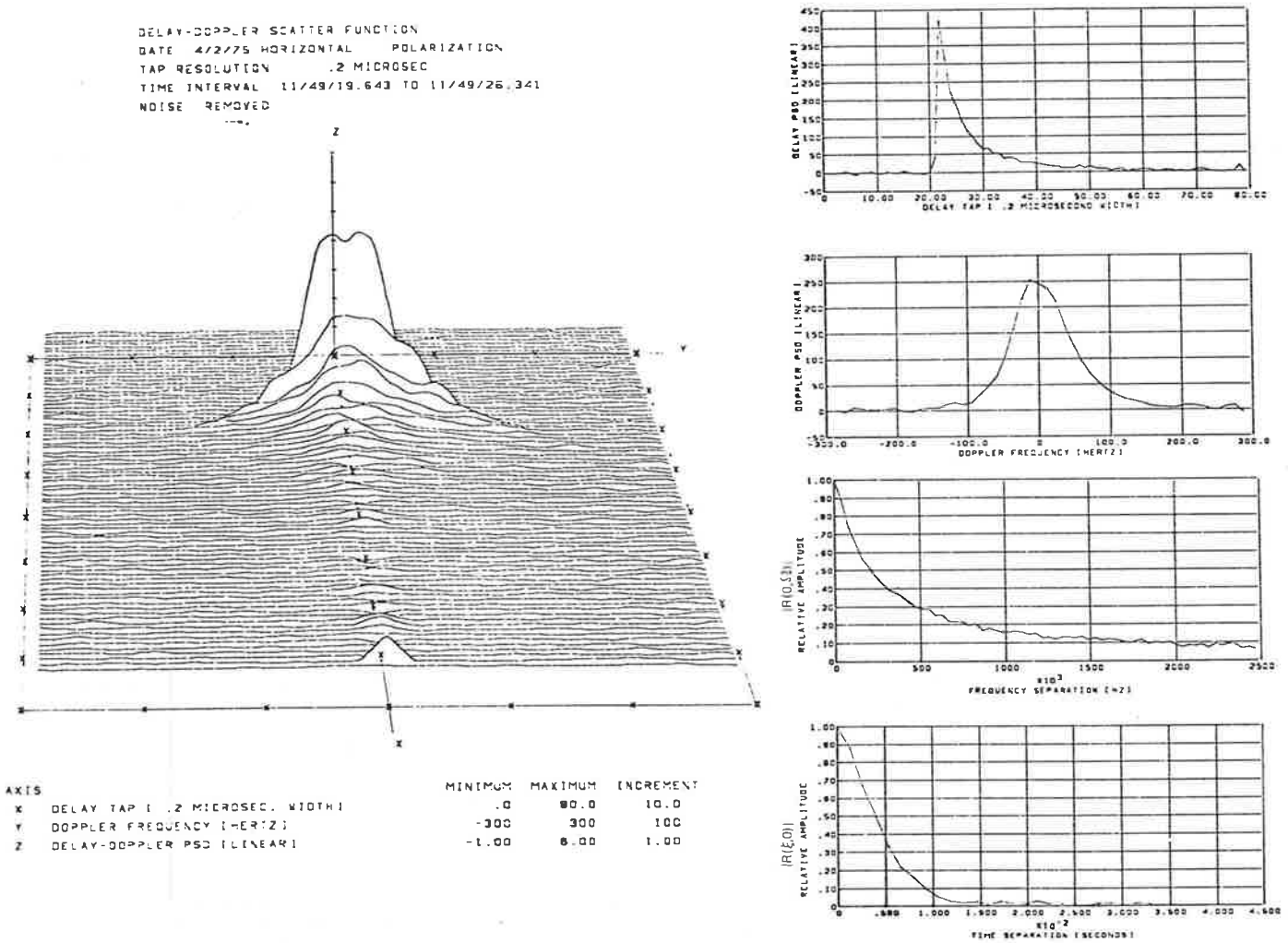

Figure 4-7. Oceanic Multipath Parameters — Horizontal Polarization, 11° Grazing Angle, Cross-Plane Geometry

joining the subaircraft and subsatellite points and thus may be shown to have a significantly larger scatter cross section than any of the other elements that return energy into the delay tap.

b. The second and perhaps more important factor is a consequence of the large area (maximum for each tap) that gets mapped into the extremities of a particular tap's Doppler spectrum. This occurs since the delay contours and the contours of maximum Doppler shift have tangential intersection. Mathematically, this is equivalent to maximizing the Jacobian (ref. 4-2) of the transformation from surface spatial coordinates to the delay-Doppler coordinates of the receiver.

The phenomenon described in item b above holds valid for all flight test directions; however, as the direction moves increasingly away from the in-plane case, the tangential intersections between the delay contours and their extreme Doppler contours move further away from the great circle path and are accordingly associated with reduced scatter cross section (i.e., we have a tradeoff between area intercept and the attendant scatter cross section). For the low delay returns associated with the 45^{o} and cross-plane heading cases, we are able to observe that the area intercept factor outweighs the reduced scatter cross section and produces a distribution tending to be heavy tailed; the opposite appears to be true for the large delay tap values.

With respect to the grazing angle dependence of $S(\tau,\omega)$, it has been observed that a definite decrease in Doppler dispersion corresponds to a decrease in grazing angle. A decrease in grazing angle is also accompanied by an increase in the asymmetry properties of the in-plane scatter function. This factor is responsible for increasing the dissimilarities between the alternate flight direction $S(\tau,\omega)$ functions as the grazing angle decreases. Note that for an upper grazing angle limit of 90^{o}, the scatter function will not be influenced by the direction of the flight velocity vector.

To properly interpret the in-plane mid- to low-angle Doppler spectra characteristics, it is important to note the behavior of $S(\tau,\omega)$'s positive-frequency spectra "humps." Referring to figure 4-6, for example, we observe that the scatter function's positive-frequency shoulder quickly becomes asymptotic to a relatively low-frequency Doppler value. Thus all returns with significant energy from the subsatellite side of the specular point have nearly identical Doppler shifts and produce a resultant composite signal Doppler spectrum with a very pronounced peak density.

The capability to simultaneously conduct horizontal and vertical polarization surface probes allows one to draw comparisons between the two probes under identical surface conditions. Analysis of the appropriate data sets of volume V reveals that the vertical and horizontal $S(\tau,\omega)$ functions have, with the exception of their absolute magnitudes, quite similar distributional shapes. For the lower grazing angle condition, we are able to discern that the relative weighting between a tap's negative and positive Doppler returns is larger for the vertical polarization data than it is for the horizontal polarization counterpart. This phenomenon results from the fact that as the scatter elements move

toward the subaircraft location (i.e., negative Doppler returns), their local elevation angles increase as opposed to a decrease for locations progressively closer to the subsatellite location. Since the vertical reflection coefficient (for grazing angles greater than the Brewster angle) increases with an increase in grazing angle while the horizontal polarization coefficient is relatively constant, the negative Doppler return for a particular tap will have a larger ratio of vertical-to-horizontal scattered energy than the positive Doppler returns. This phenomenon, discussed in more detail in section 5.2.6, volume V, is , referred to as "Brewster angle fill-in."

4.4.2 Delay Spectra, Doppler Spectra, Time and Frequency Autocorrelation Functions

To obtain an alternate representation and, in some cases, an easier interpretation of the multipath scatter characteristics, the delay-Doppler scatter function was subjected to a variety of integral and Fourier operations that yielded the following channel parameter estimates:

Delay spectra
Frequency autocorrelation function
Doppler spectra
Time autocorrelation function
Total rms scattered energy

A summary discussion of the first four parameters is given in the following paragraphs (total rms scattered energy is covered in sec. 4.4.3). A more detailed discussion and a comprehensive set of data are contained in volume V. In addition to the above, the joint time-frequency autocorrelation function is also treated in volume V.

4.4.2.1 *Delay Spectra: $Q(\tau)$* – Estimates of the multipath delay spectra, $Q(\tau)$, are obtained by integrating the "noise-removed" delay-Doppler scatter function over the Doppler variable. Thus $Q(\tau)$ represents the power spectral density of the scattered signal component that arrives at the receiver with delay τ. In this report we select the specular-point return as the zero reference value.

An obvious characteristic of the measured delay spectra is the fact that there is very little observed flight direction or grazing angle influence on the energy distribution. The flight direction independence is, of course, expected. We also note that for a constant surface slope condition, the model predictions (both spectra and spreads) of section 5.3 similarly predict a relatively small grazing angle influence.

Prober polarization influences on the reflection process are observed to produce delay spectra for vertical polarization that are much heavier tailed than their horizontal polarization counterparts. Furthermore, this effect becomes more significant as the grazing angle decreases.

A comparison of the experimental data with the theoretically predicted delay spectra reveals that the above observations are fairly well duplicated by the model. In general, the model results appear to exhibit the greatest degree of similarity to the measured spectra for the assumed sea-slope condition of 6^{o}.

4.4.2.2 Frequency Autocorrelation Function: $R(0,\Omega)$ – The frequency autocorrelation function, $R(0,\Omega)$, represents the degree of correlation between two received signals, separated by Ω hertz, that traverse identical paths through the channel. In this report, the direct line-of-sight signal component is *excluded* and thus $R(0,\Omega)$ is obtained in a straightforward manner by taking the inverse Fourier transform of the multipath delay spectrum.

As for the delay-spectra characteristics, we observe that the magnitude of $R(0,\Omega)$ exhibits almost no dependence on aircraft heading or system grazing angle. Theoretically, aircraft heading should have no influence at all on the delay spectra or the frequency autocorrelation function. These results are in accord with model predictions under the constraint of a constant-sea-surface rms slope.

Prober polarization is observed to have by far the most significant effect on the frequency autocorrelation function, with the horizontal results being heavier tailed than their vertical polarization counterparts. The extent of this effect is seen to increase for a decrease in grazing angle. Again these results are in agreement with the model predictions and are directly related to the observed polarization effects on the delay spectra (vertical polarization spectra heavier tailed than the horizontal results).

4.4.2.3 Doppler Spectra: $D(\omega)$ – A Doppler frequency shift is induced upon the individual components of a scattered signal when a relative motion exists between the rough surface and the transmitter/receiver terminals. In general, this frequency shift is expressed as the sum of two terms, one arising from the surface dynamics and the other being due to terminal motion relative to an instantaneously static surface. In our case the ATS-6 satellite is stationary and the velocity of the KC-135 jet airplane is sufficiently large to consider the oceanic surface to be frozen. Hence, the Doppler shift associated with a particular surface scatter element is a function only of aircraft-oriented system parameters. An estimate of the total scattered signals' Doppler power spectral density, $D(\omega)$, is obtained by integrating the $S(\tau,\omega)$ function over its delay variable. The Doppler coordinate variable, ω, is established relative to the frequency of the direct line-of-sight signal. For cross-plane flight directions, this reference is identical to the specular-point Doppler shift whereas for in-plane directions a differential Doppler on the order of 4 Hz exists between the specular point and direct signal paths.

The experimental data sets show that the channel's Doppler spectrum is very dependent on grazing angle and flight direction system parameters. As would be expected from the corresponding $S(\tau,\omega)$ distribution, the Doppler spectrum is highly symmetrical for the cross-plane flight geometries and resembles a zero-mean Gaussian distribution whose variance decreases with a decrease in grazing

angle. These characteristics also apply fairly well to the 45^{O} flight direction; however, there is a tendency for the negative-spectra realm to be slightly more dispersed and thus heavier tailed than the positive region. On the other hand, for the in-plane flight direction the Doppler spectrum is highly asymmetric, with the distribution being very heavy tailed in the negative-frequency region and possessing a spectral maximum that coincides closely with a frequency upper limit in the positive Doppler realm above which the energy distribution has a precipitous falloff. These in-plane geometry attributes become increasingly pronounced as the grazing angle decreases. In fact, at the lower grazing angle values, the Doppler spectrum has an extreme high-density peak at a very low positive Doppler value above which no energy exists and an exponential-like decay for the energies whose frequencies lie below the Doppler upper limit. This phenomenon results in very low Doppler spread measure for the low-angle, in-plane geometry conditions.

With respect to Doppler spectra polarization dependence, the vertical polarization results have a significantly higher percentage of energy in the negative-frequency portion of their distributions than do the corresponding horizontal results, especially for the low-grazing-angle conditions.

Unlike the results for the delay spectrum, the antenna pattern influence on the Doppler spectrum is shown (in vol. V) to be significant enough to merit consideration. Specifically, for the in-plane flight geometry case we expect that as the grazing angle decreases, the Doppler spectrum is subjected to an *overestimation* bias in the central portion of its negative-frequency realm. This implies that a region on the subaircraft side of the specular point receives more antenna gain than is directed toward the specular point and results from antenna beam pointing factors. As a quantitative measure, the low-angle (7^{O}) in-plane Doppler spectrum for a typical case is predicted to be biased by roughly +10% at its spectra mid-decile level and +30% at its lower decile level.

4.4.2.4 Time Autocorrelation Function: $R(\xi,0)$ – $R(\xi,0)$, the time autocorrelation function of the multipath channel, represents the degree of correlation between two received signals that arrive at the receiver after being transmitted as cw signals with identical frequencies but offset in time by ξ seconds. We restrict our attention entirely to the multipath component of the channel and thus obtain the $R(\xi,0)$ estimate by performing an inverse Fourier transform on the scattered signals' Doppler spectrum.

The $R(\xi,0)$ distribution has characteristic dependencies upon aircraft heading, grazing angle, and probe polarization. While the influence of the aircraft's flight vector direction is noticeable, it is not nearly as distinct as it is for the Fourier transform of $R(\xi,0)$, the Doppler spectrum. In general, we note that the in-plane flight direction produces a time autocorrelation function that appears to be heavier tailed than its cross-plane counterpart.

As expected, the elevation dependence of $R(\xi,0)$ is seen to produce an increase in spread for a decrease in grazing angle. Also, as one would predict from the Doppler spectra measurements, the

horizontal and vertical polarization $R(\xi,0)$ results become increasingly dissimilar as the grazing angle decreases, with the horizontal results exhibiting much slower decay than their vertical polarization counterparts.

The effects of antenna spatial filtering on the in-plane $R(\xi,0)$ estimates are given in volume V. The high-angle data is relatively uninfluenced by the antenna pattern, whereas the low-angle data exhibits effects that are consistent with the observed effects on the Doppler spectrum. In other words, the Doppler spectra overestimation produced by the antenna perturbation is translated into a time autocorrelation function effect that causes the distribution to decay too rapidly (roughly 30% at the origin).

4.4.3 Total RMS Scattered Energy

To relate the intensity of the multipath scatter process to a quantitative measure, the channel mean square scatter coefficient (Γ) has been derived for both horizontally and vertically polarized data. The term Γ is defined as the ratio of total energy scattered into the receiver relative to the energy incident upon the surface and is obtained from the following formulation:

$$\Gamma = \frac{\langle |I|^2 \rangle}{\langle |D|^2 \rangle} \left| + \frac{G_D}{G_I} \right|, \text{ dB},$$

where:

$\langle |I|^2 \rangle =$ mean square multipath power obtained by integrating $S(\tau,\omega)$ over its delay and Doppler variables

$\langle |D|^2 \rangle =$ mean square direct-path signal obtained by coherently summing the direct tap outputs to form a composite signal, which in turn is subjected to a mean square calculation

$G_D/G_I =$ adjustment factor to account for direct and indirect channel gain differences, etc.

Figure 4-8 presents the experimentally derived values of Γ as a function of grazing angle. Also shown are scatter model predictions representing expected results for assumed rms sea slopes of 3^o and 12^o. In general, the experimental and theoretical Γ values predicted by the physical optics vector scatter model are in close accord. We note that for grazing angles greater than roughly 10^o the model predicts rms sea slope to have a very small effect on the total energy content of the scattered signal. Although the scatter coefficient's dependency upon sea slope could not be determined explicitly experimentally because sea-slope measurements with a one-to-one correspondence with the multipath measurements was not available, the experimental data for these elevation angles does appear to be consistent with this observation. At the lower grazing angles, however, the rms scatter coefficients do not appear to be totally immune from the sea-slope influence. For angles in the vicinity of the Brewster

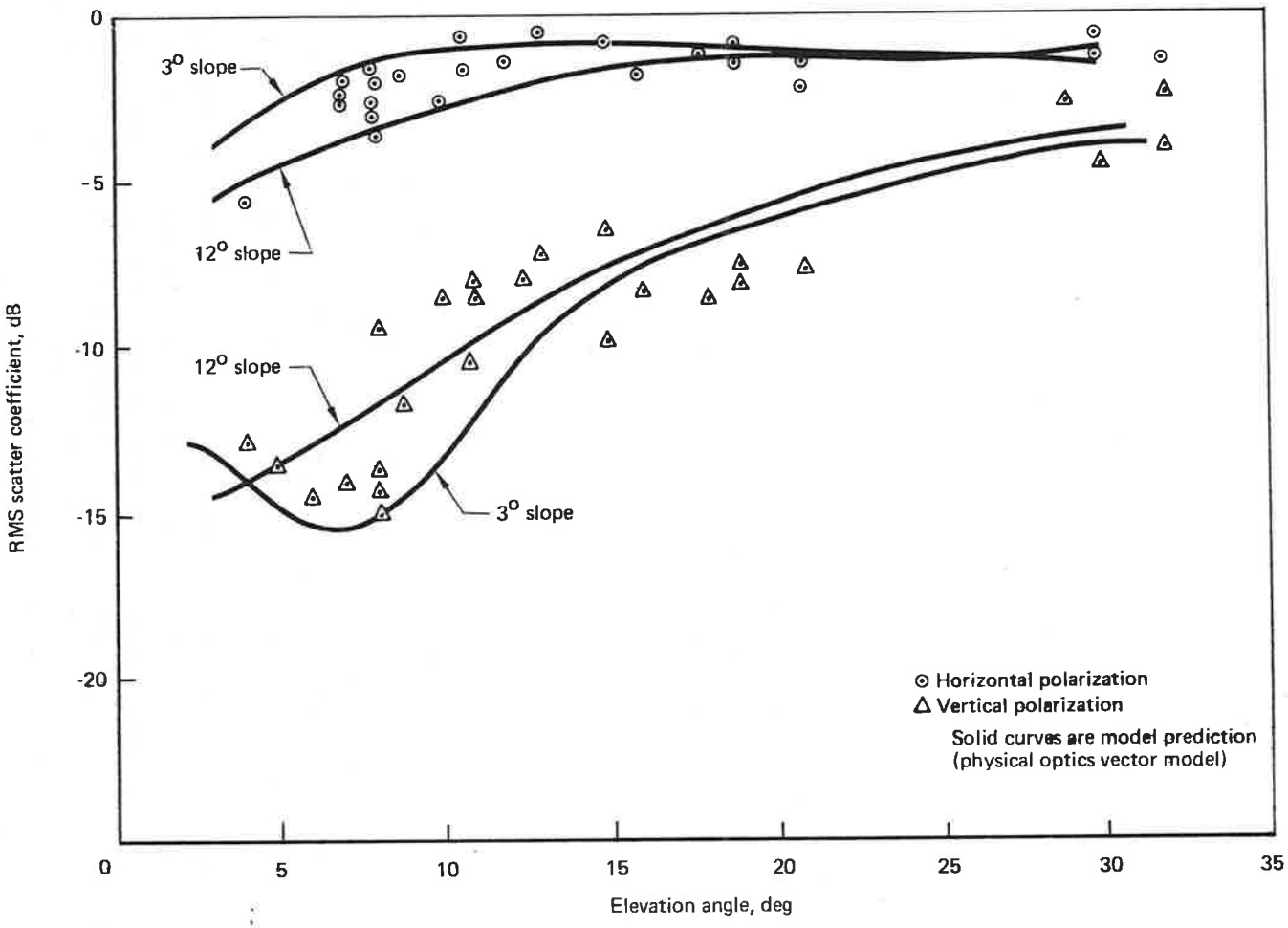

Figure 4-8. Oceanic RMS Total Scatter Coefficients

angle ($\approx 6^{o}$), the vertically polarized Γ values tend to increase with an increase in slope, whereas the opposite occurs for horizontal polarization. In the limit as the surface slope approaches zero, the theoretical curves take on values predicted by the relationship $|DR|^2$, where D is the spherical-earth reflection coefficient and R is the smooth-earth Fresnel reflection coefficient as evaluated at the specular point. This result corresponds to the "steepest descent" closed-form integral solution to the scatter phenomenon (ref. 4-3) and, with the exception of the vertically polarized data in the vicinity of the pseudo-Brewster angle, yields predicted Γ relationships that agree quite well with both the theoretical and experimental results of figure 4-8. At the pseudo-Brewster angle, the expression $|DR|^2$ for vertical polarization is on the order of -20 dB, which is seen to be roughly 5 dB below the experimental data and the scatter model surface integration results. Similar departures have also been observed for numerous VHF experiments (ref. 4-4) as well as for an ATS-5 L-band multipath experiment (ref. 4-5).

4.4.4 Spread Values of Oceanic Scatter Parameters

Some of the most useful and fundamental measures of the multipath phenomena relate to the spread values associated with the scattered signals' delay spectra, Doppler spectra, time autocorrelation function, and frequency autocorrelation function. In this section, these data are given for both horizontal and vertical polarization probes as conducted during the in-plane and cross-plane flight directions. For the delay and Doppler spectra, the total two-sided 3- and 10-dB spreads are presented whereas only the one-sided 3-dB spread is given for the autocorrelation functions.

In comparing the experimental spread results with theoretical expectation, primary emphasis is placed on predictions derived from the surface integration scatter model (see sec. 6 of vol. V). Model results generated for rms total sea slopes of 3^{o}, 6^{o}, and 12^{o} indicate that the majority of flight test conditions were associated with the higher slope values. Hence, in this section we use the average of the model predictions for 6^{o} and 12^{o} sea slopes as our theoretical expectation standard. Although this procedure is not rigorous, one may consider it to be representative of model results corresponding to rms sea slopes of roughly 9^{o}.[1]

4.4.4.1 Delay Spread – Delay spreads for the horizontal and vertical polarization probes are given in figures 4-9 and 4-10, respectively. The solid-line relationships found in these figures correspond to the scatter model surface integration prediction as evaluated for the average of the 9^{o} and 12^{o} rms sea-slope conditions. A very weak increase in spread value for an increase in elevation angle is exhibited by the horizontal polarization data and by the 3-dB spread values of the vertical polarization data. For the 10-dB vertical polarization results, we observe a small increase in the spread for grazing angles in

[1] Alternatively, the experimental results can be compared with model predictions for specific sea-slope values. Such model predictions are given in section 4.5 of this volume (and discussed in more detail in vol. V).

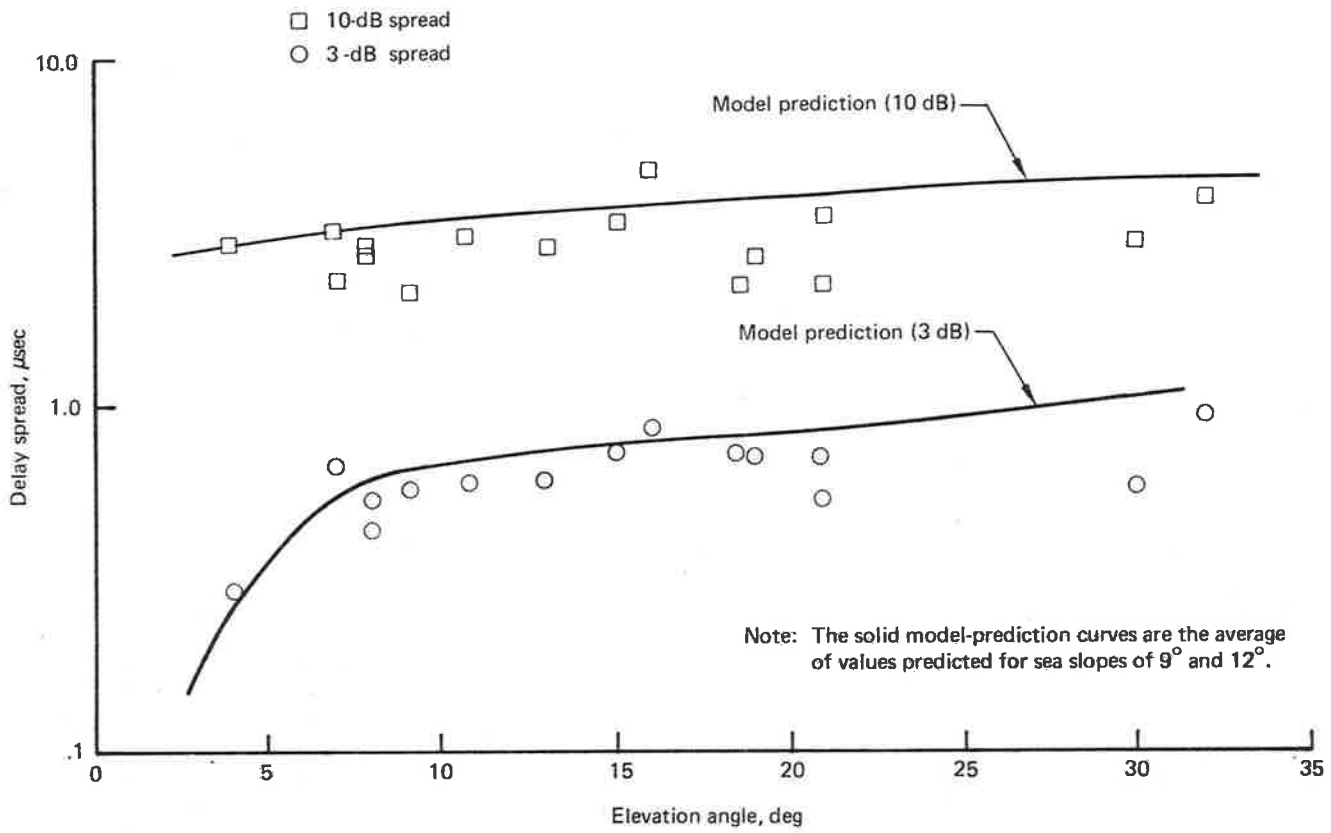

Figure 4-9. Oceanic Delay Spread Results — Horizontal Polarization

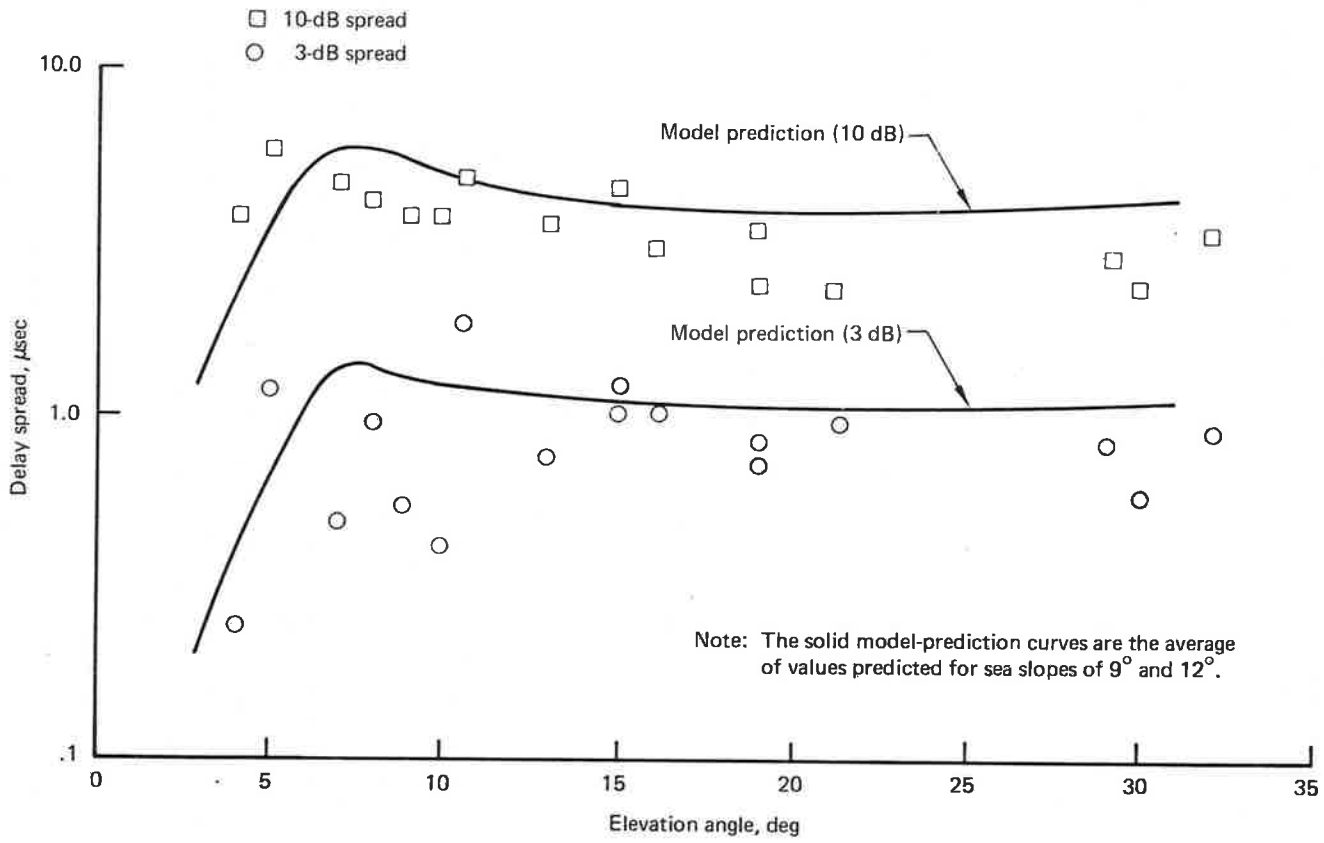

Figure 4-10. Oceanic Delay Spread Results — Vertical Polarization

the vicinity of the pseudo-Brewster angle. Both of these results are predicted by the scatter model, with the Brewster angle effect also being illustrated mildly by the vertical polarization 3-dB spreads. The spread increase for the vertical polarization probe in the vicinity of 6^{o} is related to the same phenomenon referred to previously as "Brewster angle fill-in."

For elevation angles between 10^{o} and 31^{o}, the horizontal polarization 3- and 10-dB spread measures are typically 0.7 and 3.0 μsec, respectively; for the vertical polarization case, these measures are slightly larger and take on typical values of 0.9 and 3.3 μsec. The dispersion associated with the experimental data is ascribed to day-to-day changes in the surfaces rms slope.

4.4.4.2 Frequency Coherence Bandwidth – The term coherence bandwidth is used to describe the spread parameter measure associated with the multipath's frequency autocorrelation function. In essence, it provides us with an upper frequency limit to which two simultaneously transmitted L-band carriers may be separated yet still meet a specified degree of correlation at the receiver. For this presentation we are concerned with the 3-dB coherence bandwidth (i.e., the received signals have a correlation coefficient of 0.5). We deal only with the sea-returned energy and do not include the effects of the excess time delay between the specular-point return and the direct line-of-sight signal. For direct plus multipath signal analyses, this excess differential delay is very significant and hence one cannot use the results presented herein to *directly* predict the coherence bandwidth of the composite channel.

Figure 4-11 contains as a function of elevation angle the experimentally measured 3-dB coherence bandwidth values for both horizontal and vertical polarization probes. Because the frequency autocorrelation function is derived solely from the channel's delay-spectra distribution, it is not dependent on airplane heading. Thus the results from both in- and cross-plane geometries have been combined. It is observed that the experimental results range from a low of 70 kHz to a high of 380 kHz, with a typical value being approximately 200 kHz. The data trend does not exhibit a strong dependence upon grazing angle, although we do note a slight tendency for the results to increase with an increase in grazing angle. This dependency is in accord with the model prediction curves, which also predict a 3-dB coherence bandwidth value that, over the range of elevation angles of interest, is on the same order as the average of the experimental results. We also observe that for the lower grazing angles, the vertical polarization results are generally lower than their horizontal polarization counterparts whereas the opposite trend appears for the larger grazing angles. Again, this observation is in agreement with the model prediction results.

4.4.4.3 Doppler Spread – Results from the spread measurements on the multipath's Doppler spectra are given in figures 4-12, 4-13, and 4-14. The first two figures correspond to in-plane flight directions for horizontal and vertical polarization probes, respectively, whereas the third set presents the cross-plane spreads for both polarizations. The solid curves in each figure represent predictions derived from

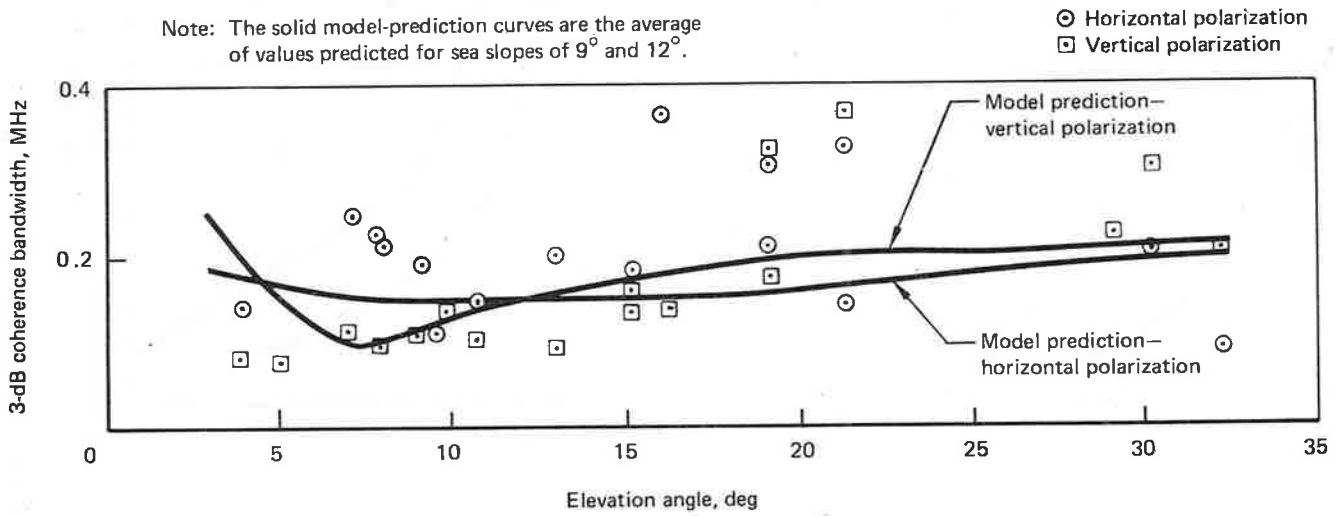

Figure 4-11. Oceanic Coherence Bandwidth Results

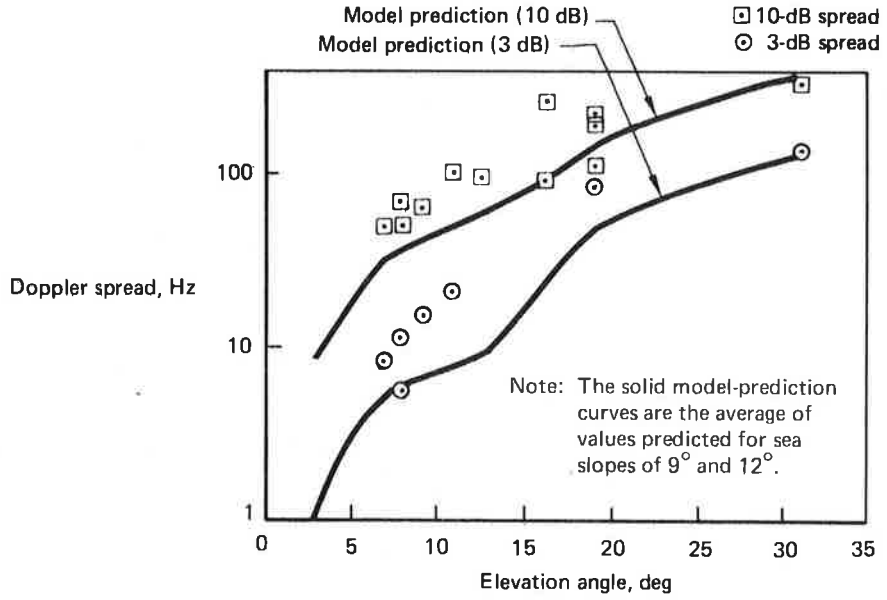

Figure 4-12. Oceanic Doppler Spread Results — Horizontal Polarization, In-Plane Geometry

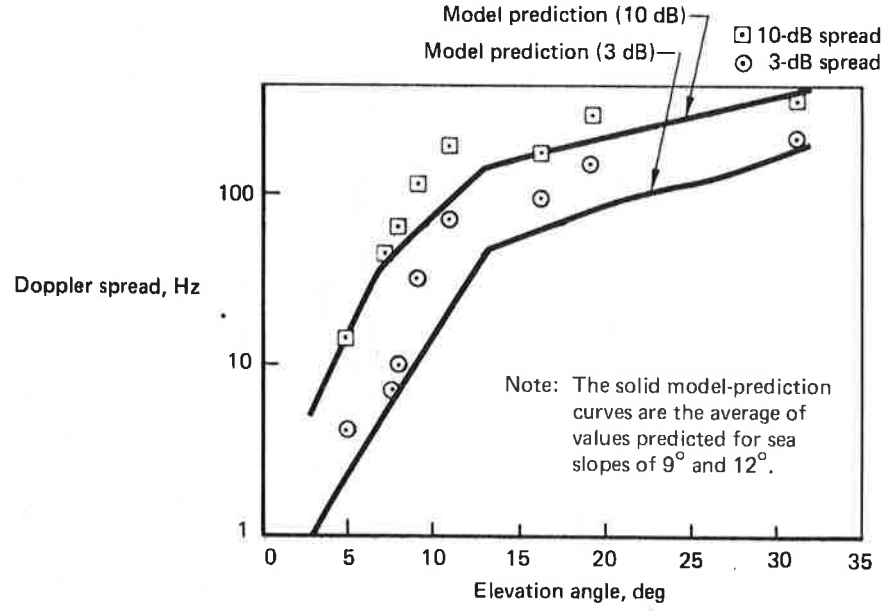

Figure 4-13. Oceanic Doppler Spread Results — Vertical Polarization, In-Plane Geometry

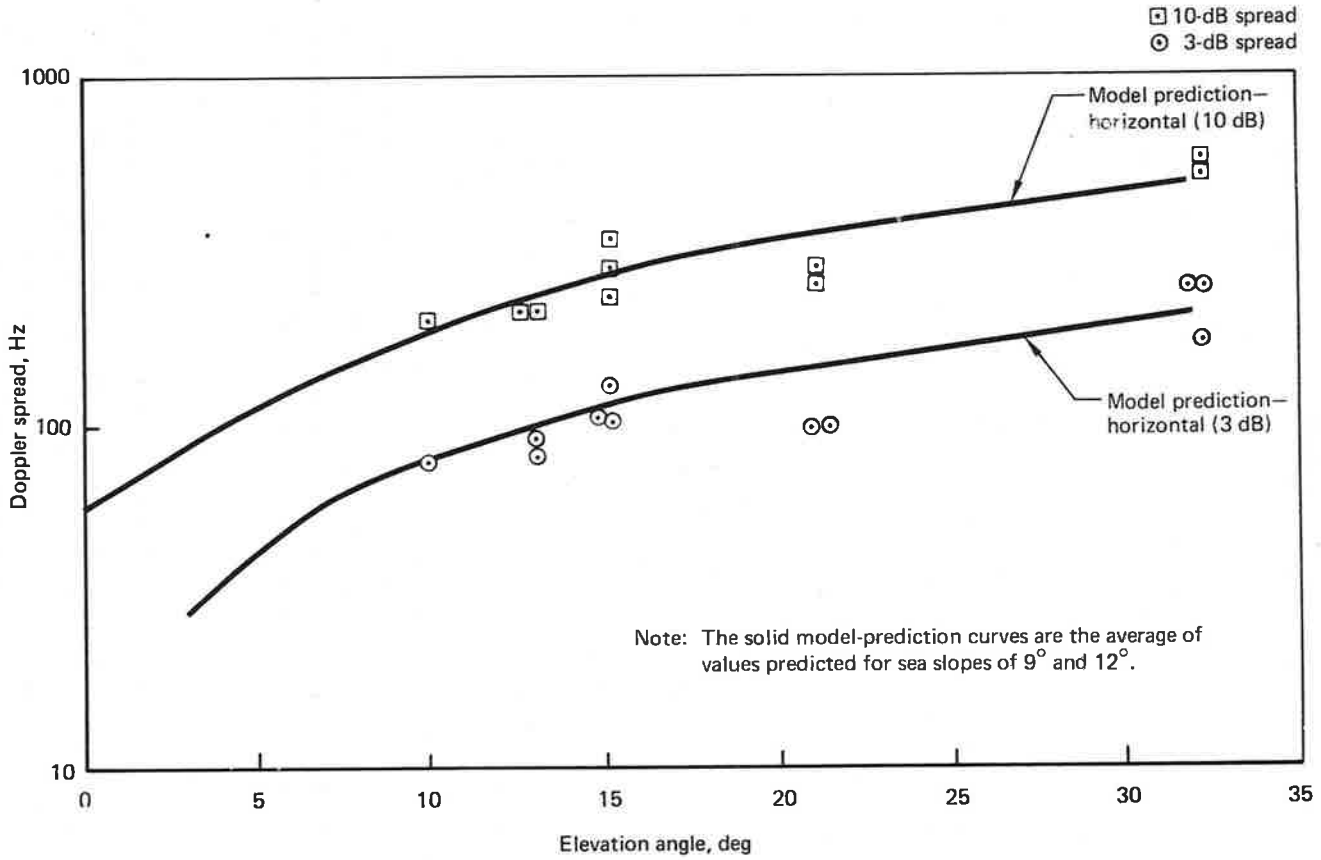

Figure 4-14. Oceanic Doppler Spread Results — Cross-Plane Geometry

the surface integration scatter model. As previously discussed, the model results plotted are the average of predictions for rms sea slopes of 6^{o} and 12^{o} and thus represent a first-order approximation corresponding to an rms slope condition of 9^{o} (see discussion and footnote, p. 4-23).

For all four combinations of prober polarization and aircraft flight direction, the experimental data trends and model predictions are in fairly close agreement. In particular, it is observed that:

a. The data trend shows a definite increase in Doppler spread for an increase in grazing angle.

b. Both the 10- and 3-dB Doppler spread values are appreciably influenced by flight direction, with the in-plane geometry (especially for the lower grazing angle conditions) producing smaller spreads than the cross-plane condition.

c. For the in-plane data ensembles, the spreads corresponding to vertical polarization are typically larger than their horizontal counterparts.

Two fairly significant factors are predicted to provide an *overestimation* bias to the in-plane low-angle Doppler spread experimental measurements. One factor relates to the antenna's spatial filtering effects which, as shown in section 5.6 of volume V, result in overestimation biases on the order of 9% and 29% for the low-grazing-angle Doppler spread 3- and 10-dB measures, respectively. Antenna perturbations for the high-grazing-angle conditions are not nearly so significant, with the 3-dB measure being underestimated by 1% and the 10-dB spread measure being overestimated by 8%. The second overestimation bias factor pertains to aircraft heading meanders that would cause the flight direction vector to deviate somewhat from the true in-plane geometry condition. As discussed previously, the Doppler spectrum for low-grazing-angle in-plane flight direction conditions is very peaked and thus possesses a relatively small spread measure. As the flight vector moves away from the in-plane direction, the spectrum becomes increasingly more Gaussian-like and consequently is associated with a larger spread value. Assuming the aircraft flight vector is offset by 7^{o} from the in-plane direction, the scatter model of section 4.5 predicts that for a 9^{o} rms surface slope the Doppler spreads for the 10^{o} grazing angle geometry are larger than their in-plane 3- and 10-dB counterparts by 89% and 47%, respectively.

4.4.4.4 Decorrelation Time – Decorrelation time provides us with an upper limit on the time separation for which two L-band carriers, transmitted at the same frequency, will still meet a specified degree of coherency at the receiver. It is derived from the time autocorrelation function of the multipath channel, and for this document we have selected the 3-dB spread measure (i.e., that time separation which produces a normalized correlation coefficient between the two received signals of 0.5). As in the coherence bandwidth presentation, we restrict our attention entirely to the multipath signal and do not include any effects that would arise from the presence of a direct line-of-sight received component.

Since the time autocorrelation function is derived exclusively from the multipath Doppler spectrum, one expects the decorrelation time measurements to exhibit a flight direction dependence. For this reason the results are segregated into cross- and in-plane data sets, which are presented for both polarizations in figures 4-15 and 4-16, respectively. Also contained in these figures are the spread relationships as derived from the surface integration physical optics scatter model.

The experimental results are in relatively good agreement with theoretical predictions. For both flight geometry directions, the data trend implies a decrease in decorrelation time for an increase in elevation angle. Typically, the data set averages imply decorrelation values on the order of 7 to 10 msec and 2 to 3 msec for grazing angles in the vicinity of 8^{o} and 30^{o}, respectively. It is also apparent that the vertical polarization probes and the cross-plane flight direction produce modestly smaller decorrelation times than their respective orthogonal parameter counterparts. This tendency appears to be maximized for grazing angles in the vicinity of the Brewster angle.

4.4.5 Cross-Polarization Joint Statistics and Power Spectral Density

This section examines the joint statistical and power spectral density behavior of the horizontal and vertical tap processes. Hence, a portion of this task is reduced to one of estimating the complex H-V correlation coefficient for the tap outputs, i.e.,

$$\rho_{HV} = \frac{\langle HV^{*} \rangle}{[\langle |H|^{2} \rangle \cdot \langle |V|^{2} \rangle]^{1/2}}.$$

The above quantity indicates the physical coupling between horizontally and vertically polarized returns for a single delay contour. In attempting to derive analytical models for the multipath scattering mechanism, this parameter plays an important role. Multipath models currently in use implicitly assume that ρ_{HV} is unity, i.e., that a surface capable of scattering vertically polarized signals will likewise scatter horizontally polarized signals, albeit with a different intensity and phase angle. In general, the experimentally derived ρ_{HV} measurements are in accord with this assumption. After application of a noise-compensation procedure, results were observed to range between 0.88 and 0.97, with an average value of 0.93 being associated with the total analysis data base.

The cross-power spectrum of the H and V polarization tap processes was used to provide an estimate of the relative phase difference induced upon the orthogonally polarized signals by the reflecting medium. Although system bias effects were not compensated, the trend of the data provides substantial agreement with results predicted by the Fresnel reflection coefficient relationships.

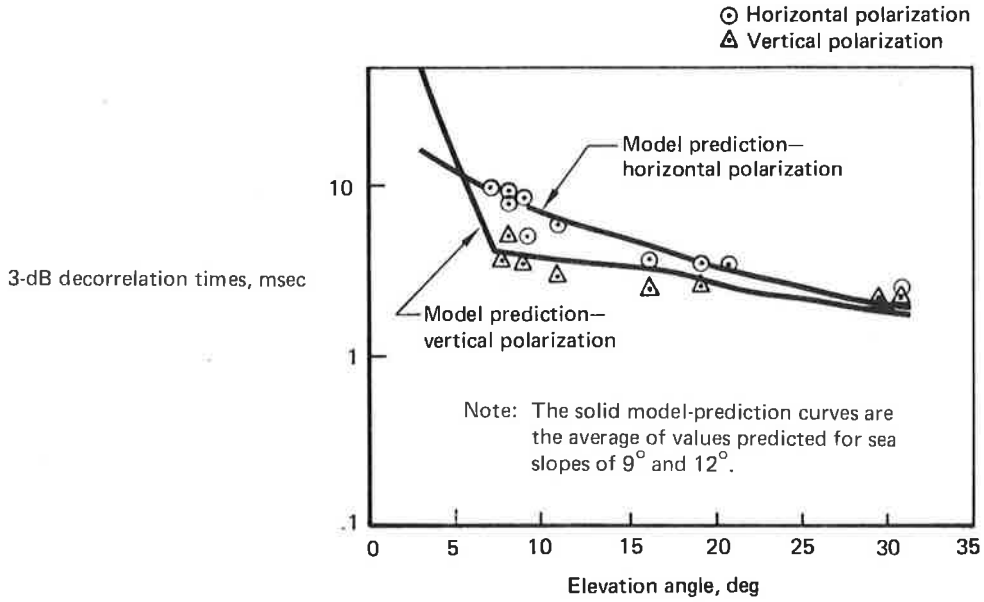

Figure 4-15. Oceanic Decorrelation Time Results — In-Plane Geometry

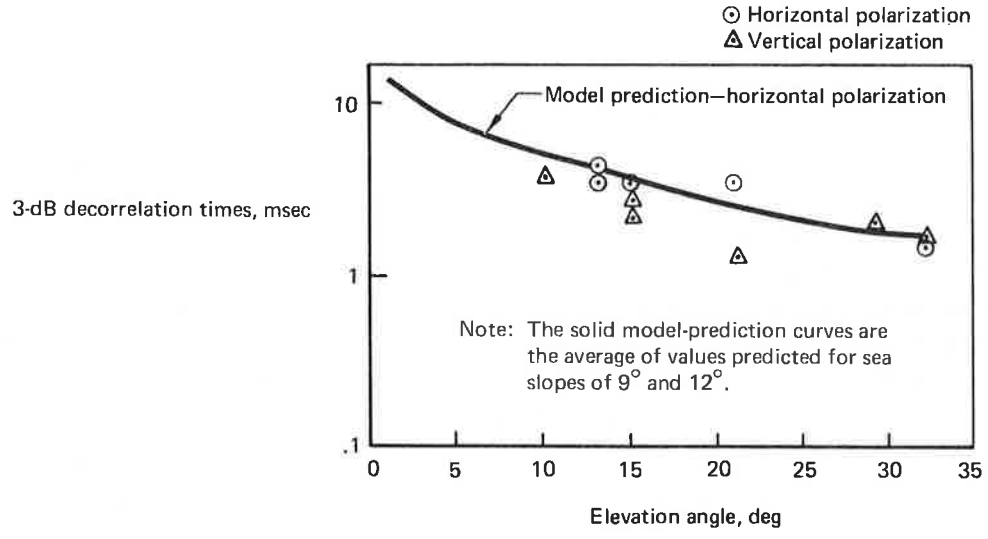

Figure 4-16. Oceanic Decorrelation Time Results — Cross-Plane Geometry

4.4.6 Circular Polarization Results

In the design of operational aeronautical satellite systems, effects of the oceanic multipath interface on circularly polarized waves are of particular importance. Accordingly, several right- and left-hand circular polarization probes of the oceanic surface were conducted during the latter part of the flight test series. From the standpoint of the physical optics vector scatter formulation, it is not necessary to perform model alterations to include the effects of any given receive or transmit polarization vector. In general, model predictions for the LHC and RHC prober configurations yield spectral distributions and autocorrelation functions that are very similar to the corresponding parameters associated with the linear polarization emulations. Similarly, the predicted values of the circular and linear polarization spread parameters are in close accord. As expected, the one area in which the LHC and RHC polarization influence is of significance relates to the total rms scattered energy content of the signal. Because the satellite antenna is RHC, the polarization sense-reversal properties of the surface cause the scattered energy corresponding to probes transmitted with LHC polarization to be received with less loss than for probes transmitted with RHC polarization. This phenomenon is predicted for all grazing angles greater than the pseudo-Brewster angle and should become more significant as the grazing angle increases.

A summary of spread parameter measures and total rms signal energy content obtained for a number of circular polarization probes is given in table 4-3. With the exception of the scatter coefficients, these data are in accord with the linear polarization spread results given previously. The scatter coefficient measurements may be compared with model-predicted results that appear within the parentheses in table 4-3. In general, the experimental and theoretical coefficients are relatively close. However, the RHC coefficients are typically somewhat less than predicted whereas the opposite generally holds valid for the LHC results. This observation could suggest that the ATS-6 antenna's polarization may not be perfectly circular.

4.5 PHYSICAL OPTICS SCATTER MODEL PREDICTIONS

One of the major objectives of this experiment was to substantiate a scatter model that will accurately predict the multipath channel characteristics pertinent to future operational oceanic aeronautical satellite systems. Experimental results have been correlated with theoretical predictions based on a surface integration of the classical physical optics vector formulation scatter model. Sections 4.5.2 through 4.5.4 contain model predictions of selected channel parameters for a variety of system configurations and assumed surface characteristics. Test parameters input to the model (table 4-4) were selected to provide a close emulation to the experimental conditions.

TABLE 4-3. CIRCULAR POLARIZATION SPREAD AND REFLECTION COEFFICIENT MEASURES

Date, mo-day-yr	Polarization	Elev, deg	A/C heading, deg	Delay spread		Coherence BW, 3 dB, kHz	Doppler spread		Decorr time, 3 dB, msec	Scatter coeff,[a] dB
				3 dB, μ sec	10 dB, μ sec		3 dB, Hz	10 dB, Hz		
2-27-75	LHC	32	0	0.93	2.74	234	185	383	2.6	-3.71 (-2.2)
2-27-75	RHC	32	90	0.88	3.26	207	178	440	1.8	-14.6 (-16.8)
4-3-75	LHC	21	90	0.58	2.69	203	143	313	2.5	-3.3 (-3.0)
4-3-75	RHC	21	90	0.72	2.60	203	113	257	2.6	-13.1 (-13.2)
4-3-75	LHC	19	0	0.77	3.02	234	131	222	3.9	-7.7 (-3.2)
4-3-75	RHC	19	0	0.54	2.15	351	119	174	5.2	-11.3 (-12.7)
3-31-75	LHC	15	90	0.76	3.37	168	113	260	3.1	-6.2 (-4.1)
3-31-75	RHC	15	90	0.57	2.57	196	92	211	3.7	-12.4 (-11.6)
3-31-75	LHC	14	0	0.65	2.82	210	43	148	4.4	-6.5 (-4.5)
3-31-75	RHC	14	0	0.59	2.30	237	37	111	6.7	-11.5 (-11.6)

[a]Quantity in parenthesis is value predicted by the physical optics vector model. Model predictions shown are for a sea slope of 9°.

TABLE 4-4. INPUT TEST PARAMETERS FOR PHYSICAL OPTICS SCATTER MODEL

Test parameter	Description
Aircraft altitude	10 km
Aircraft speed	200 m/sec
Aircraft heading	Toward satellite; great circle path (in-plane)
	Broadside to satellite; great circle path (cross-plane)
Aircraft antenna polarization	Horizontal, vertical
ATS-6 antenna polarization	Right-hand circular
Grazing angles	3°, 7°, 13°, 19°, 25°, 31°
Surface type	Sea water
Surface rms slope (total)	3°, 6°, 12°

4.5.1 Model Description

For the case of L-band aeronautical satellite oceanic scatter, the surface will almost always appear to be "very rough." Analysis of scattering from very rough surfaces is usually developed through the physical optics tangent-plane method (commonly called the Kirchhoff approximation). We use the vector formulation of the physical optics model and are thus able to properly account for the electromagnetic polarization dependencies of each particular scattering facet on the surface. Surface integration techniques determine the scatter cross section, Doppler shift, and time delay associated with each area, thus allowing the channel's delay-Doppler scatter function, $S(\tau,\omega)$, to be constructed. From $S(\tau,\omega)$, integral and Fourier transform operations determine the channel's time-frequency autocorrelation function, delay spectrum, Doppler spectrum, time autocorrelation function, frequency autocorrelation function, total energy content, and spread values of the unidimensional distributions. Additional discussion and several references are included in volume V.

4.5.2 Model Prediction of Delay-Doppler Scatter Function

The delay-Doppler scatter function serves as the basic system function from which other model predictions are derived. Consequently, this function has been generated for all parameter combinations delineated in table 4-4; a comprehensive set of $S(\tau,\omega)$ model results is given in volume V. To illustrate a portion of the total ensemble, we present $S(\tau,\omega)$ distributions corresponding to a horizontal polarization probe as configured for a 13^{o} grazing angle, coupled with 12^{o} and 3^{o} rms sea-slope conditions. These data, given for both in-plane and cross-plane flight directions, are illustrated in figures 4-17 through 4-20. In the following section, the integral and Fourier operations on the model-predicted $S(\tau,\omega)$ function are discussed. Examples used for that discussion are derived from the $S(\tau,\omega)$ distributions of this section.

The $S(\tau,\omega)$ model predictions[2] agree closely with experimental results and provide detailed insight on grazing angle, polarization, flight direction, and sea-surface slope dependencies of the oceanic forward-scatter L-band phenomena. One readily observes that the Doppler frequency distribution of the returned energy is strongly influenced by aircraft heading. The dissimilarities between the in- and cross-plane $S(\tau,\omega)$ functions increase as the rms slope increases and as the grazing angle decreases. For the cross-plane case, individual delay taps possess Doppler spectra that are symmetrical with respect to the specular-point return frequency of 0 Hz. On the other hand, the Doppler spectra associated with the individual taps for the in-plane geometry case are highly asymmetrical, with the negative-frequency return being significantly more dispersed than the positive-frequency scatter.

[2]It should be noted that $S(\tau,\omega)$ is theoretically a "smooth function" of τ and ω. The "choppy" appearance of certain model-predicted $S(\tau,\omega)$ plots is caused by the choice of cell-size quantization used in the model computer programs.

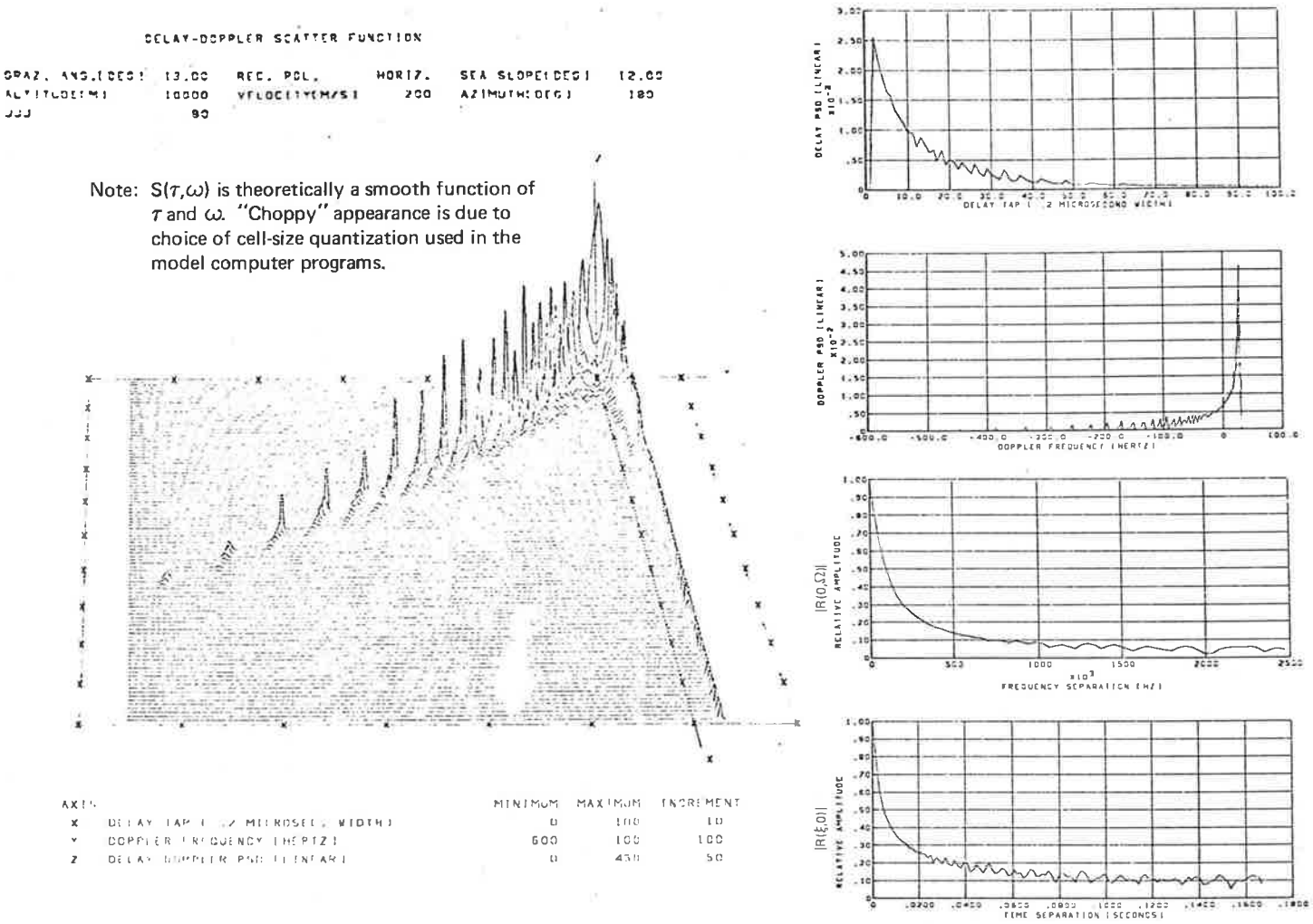

Figure 4-17. Model Predicted Multipath Parameters — Horizontal Polarization, 13° Grazing Angle, 12° Slope, In-Plane Geometry

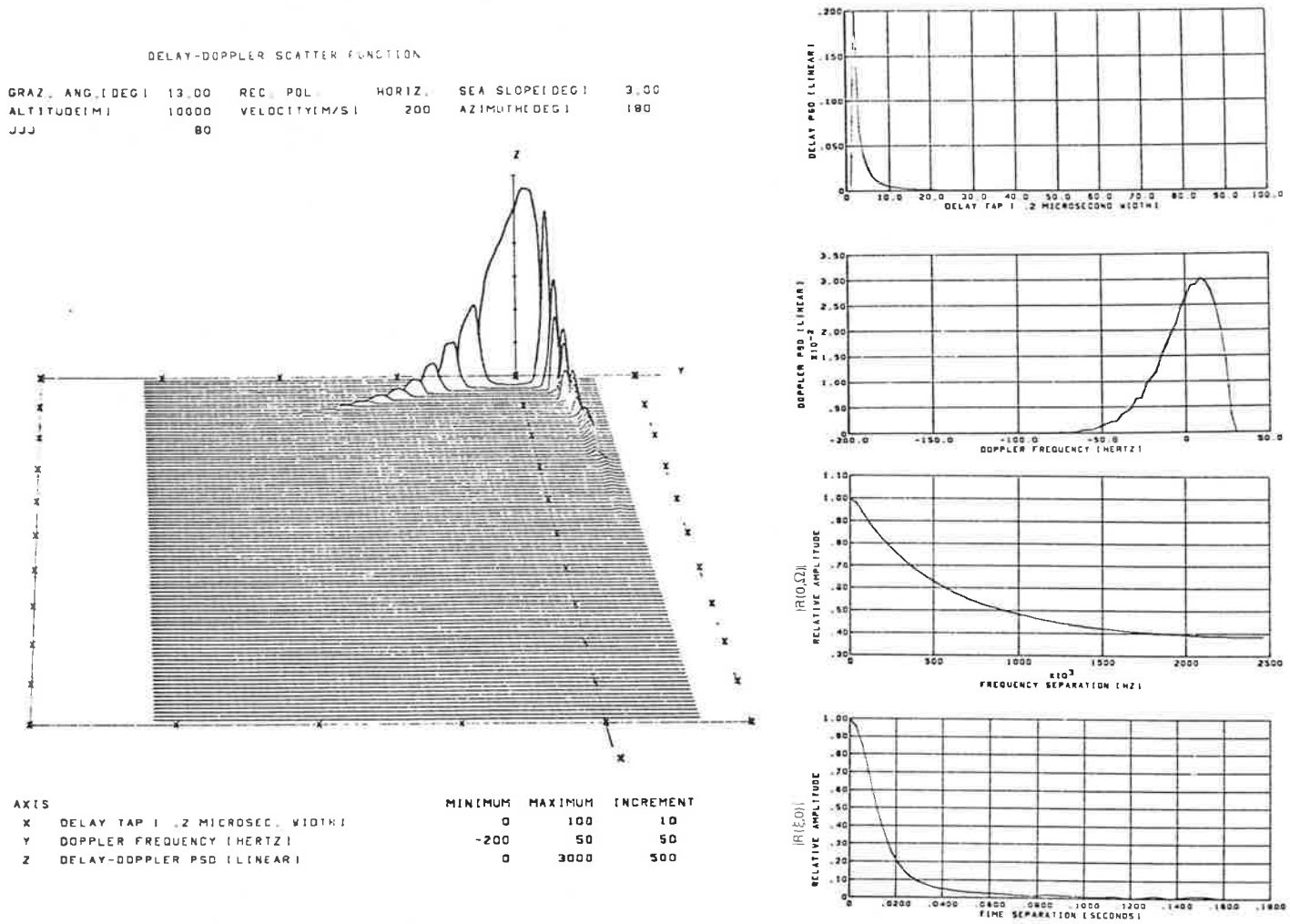

Figure 4-18. Model Predicted Multipath Parameters — Horizontal Polarization, 13° Grazing Angle, 3° Slope, In-Plane Geometry

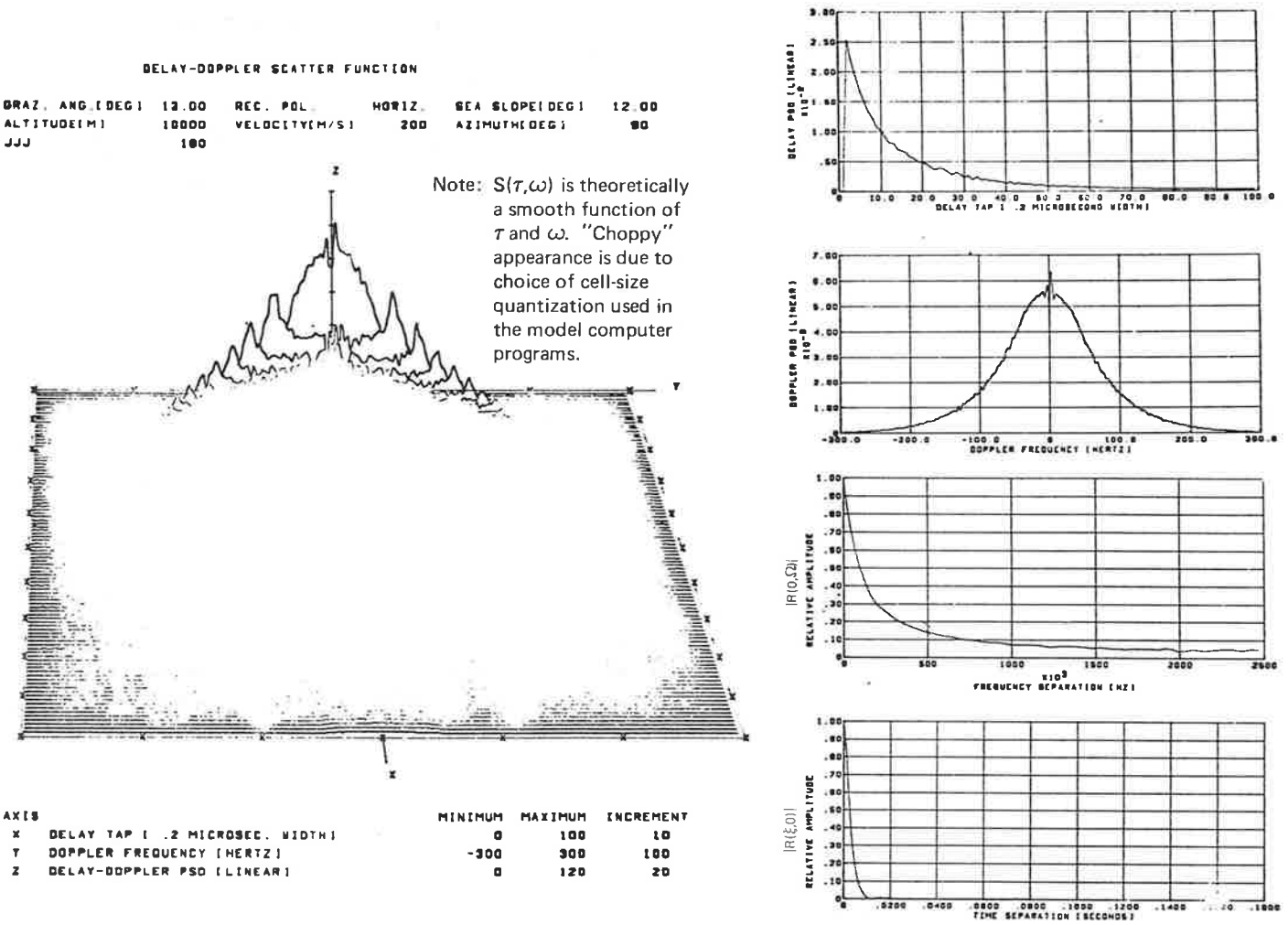

Figure 4-19. Model Predicted Multipath Parameters — Horizontal Polarization, 13° Grazing Angle, 12° Slope, Cross-Plane Geometry

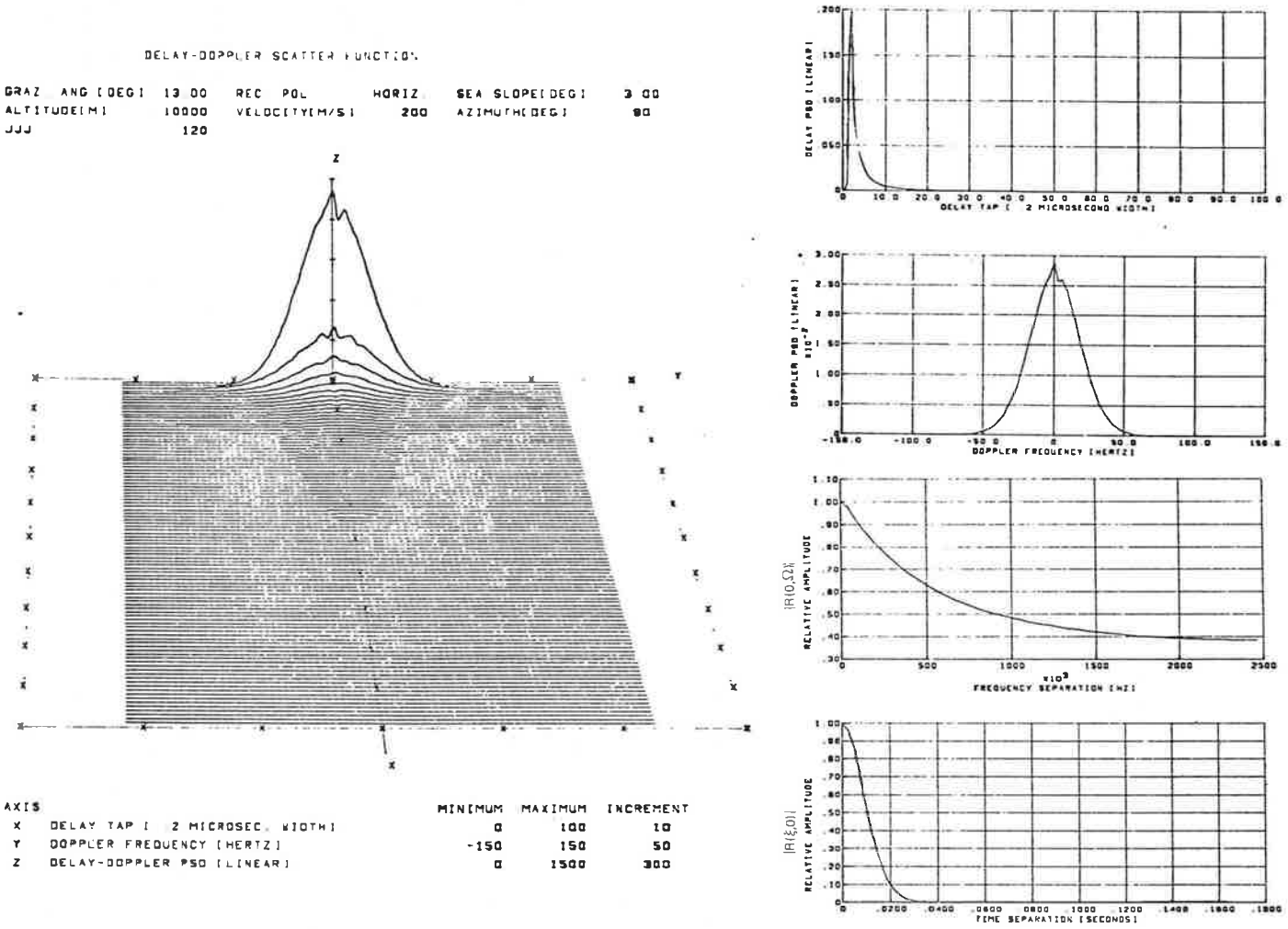

Figure 4-20. Model Predicted Multipath Parameters — Horizontal Polarization, 13° Grazing Angle, 3° Slope, Cross-Plane Geometry

For all elevation angle and sea-slope conditions associated with the in-plane flight geometry, $S(\tau,\omega)$ is characterized by two distinct sets of spectral "humps." For a given delay tap, these humps correspond to the upper and lower Doppler spectra limits over which physically possible multipath will be returned; the negative-frequency portion is due to scatterers located on the subaircraft side of the specular point, whereas the positive-frequency component arises from the subsatellite side of the surface. These observations pertain to in-plane flight directly *toward* the satellite, as in this test program. For in-plane flights *away* from the satellite, the roles of the negative and positive Doppler frequency realms, discussed here and elsewhere, would be reversed. This occurs because scatter from the region on the subaircraft side of the specular point would, in this case, be associated with positive Doppler shifts.

With respect to the Doppler frequency spectral humps, it should be noted that their *position* in the $S(\tau,\omega)$ realm depends only on the system geometry and transmitted frequency of the electromagnetic wave. The sea-surface rms slope controls the relative amount of energy in each spectral bin. An increase in slope is accompanied by a flow of energy from the low delay tap numbers to the higher delays and from the interior region of a tap's Doppler spectrum to the exterior limits for the cross-plane geometry, with the opposite Doppler redistribution occurring for the in-plane case.

4.5.3 Integral and Fourier Operations on $S(\tau,\omega)$

4.5.3.1 Delay Spectra – This parameter is obtained by integrating the model-generated $S(\tau,\omega)$ function over its Doppler variable. Referring to the figures given in the previous section and in volume V allows one to obtain an estimate of the spectra dependence upon the polarization, grazing angle, flight direction, and sea-slope parameters. As expected, the delay spectrum does not depend on the velocity vector of the airplane. Sea-surface slope has a much greater influence on the delay spectrum than does grazing angle; the higher the sea slope, the heavier tailed the distribution becomes. Apart from the relative magnitude differences, the high-angle (31^{o}) vertical and horizontal polarization delay spectra have very similar distributions; on the other hand, the low-angle data (13^{o}) coupled with sea slopes of 6^{o} and 12^{o} produce a vertical polarization spectrum that, when compared with its horizontal polarization counterpart, is visibly more dense in the interior region of its distribution.

4.5.3.2 Frequency Autocorrelation Function: $R(0,\Omega)$ – The frequency autocorrelation function is derived by taking the inverse Fourier transform of the delay spectrum; thus, many of its attributes may be deduced from the preceding discussion. To begin, we note that $R(0,\Omega)$ does not depend on the velocity vector of the airplane. Also, since the delay spectrum is everywhere positive, the frequency autocorrelation function has maximum amplitude for the 0-Hz separation value, as expected. With respect to the sea-surface-slope effects, it is noted that a decrease in slope results in a broadening of

the $R(0,\Omega)$ amplitude distribution. We contrast this to the grazing angle dependence, which produces no appreciable difference in the $R(0,\Omega)$ distributions for the cases illustrated herein. Polarization effects on $R(0,\Omega)$ are also minimal.

4.5.3.3 Doppler Spectrum – Compared with other multipath channel unidimensional measures considered, the Doppler spectrum shows, by far, the greatest dependency upon grazing angle and flight direction system parameters. It is also influenced significantly by the sea-surface rms slope and has a slight dependence upon the polarization of the incident electromagnetic wave.

Referring to the figures of the previous section and volume V shows that for cross-plane flight geometries, the Doppler spectra have distributions closely resembling zero-mean Gaussian, with variance increasing in a linear fashion with an increase in rms sea slope. These characteristics, especially for the larger sea slopes, are distinctly different from those associated with in-plane flight geometries. In general, the Doppler spectra associated with the in-plane flight directions are highly asymmetric, with the distributions being heavy tailed in the negative-frequency realm and possessing spectral maxima that coincide with a frequency upper limit in the positive realm. Above this maximum, the energy density falls off in a precipitous manner. It is observed that these attributes become more pronounced as the sea slope increases and grazing angle decreases. In fact, we note that as the opposite conditions occur (i.e., low slopes coupled with high grazing angle), the in-plane distribution becomes increasingly similar to the cross-plane counterparts. The dependence of the in-plane Doppler spectra on the sea-slope parameter is of particular interest. For an increase in slope, we observe that energy near the 0-Hz center of the function is dispersed toward the extremities of the distribution, with the manner in which the redistribution takes place being markedly different for the negative and positive halves of the spectrum. The positive realm becomes increasingly peaked, with the peak shifting toward the high-frequency cutoff of the spectrum, whereas the spectral density in the negative-frequency region becomes more dispersed, with the falloff resembling an exponential decay.

With respect to the polarization characteristics of the Doppler spectrum, we note that the vertical and horizontal polarization data are in close agreement for high grazing angle and low slopes. For the low-grazing-angle and high-slope conditions, the vertical polarization spectra have a much higher percentage of energy in the negative portion of the distribution than do the corresponding horizontal spectra.

4.5.3.4 Time Autocorrelation Function: $R(\xi,0)$ – Even though the channel's time autocorrelation function is related to the Doppler spectrum by way of the Fourier transform, we observe that its distribution has the same general shape for both choices of aircraft heading. However, for the large sea slopes, the in-plane $R(\xi,0)$ function decays considerably slower than the cross-plane distribution. In general, a systematic increase in the dispersion of $R(\xi,0)$ is associated with a decrease in the sea-surface slope and a decrease in the grazing angle. Also, as would be expected from the Doppler spectra

observations, the horizontal and vertical polarization $R(\xi,0)$ results are fairly similar except for the low-angle, high-slope condition where the horizontal polarization function exhibits a much slower decay than its vertical polarization counterpart.

4.5.3.5 Total RMS Scattered Energy – Model predictions of the sea-surface's total scattered energy as received over the satellite-to-airplane link are presented in figure 4-21. This data has been normalized relative to the energy received over the direct line-of-sight path which, for geostationary satellite altitudes, is closely equivalent to a normalization with respect to the energy incident upon the surface. One observes that sea slope has a very minor effect on the higher grazing angle ($\geq 10^{o}$) data. For the low-grazing-angle results, we note that the vertical polarization coefficients tend to increase with an increase in sea slope, whereas the opposite dependence holds true for the horizontal polarization results. The lower the sea slope, the closer the scatter coefficient approaches the classical Fresnel smooth flat-earth reflection coefficient result as modified by the spherical-earth divergence factor.

4.5.4 Spread Value Predictions

Model-predicted spread values for the multipath channel's delay spectra, frequency autocorrelation function, Doppler spectra, and time autocorrelation function are presented in this section. Definitions pertaining to the spread parameter measures given in section 4.4.4 apply similarly to the model predictions.

Results are presented graphically as a function of grazing angle (3^{o} to 31^{o}) for sea slopes of 3^{o}, 6^{o}, and 12^{o}. Observations pertaining to the spread measure characteristics are summarized below.

4.5.4.1 Delay Spread – Delay spread values are presented in figures 4-22 and 4-23.

a. Aircraft heading has no effect on parameters associated with the delay spectrum.

b. For both polarizations and low-to-modest sea slopes (i.e., up to 6^{o}), the 3- and 10-dB delay spreads are relatively uninfluenced by the grazing angle parameter.

c. For the larger slopes, the delay spreads tend to increase with grazing angle.

d. The *similarity* between the vertical and horizontal spreads increases with an increase in grazing angle or a decrease in sea slope; for the lower grazing angle and higher slopes, the vertical polarization data in general have larger 3- and 10-dB spread values.

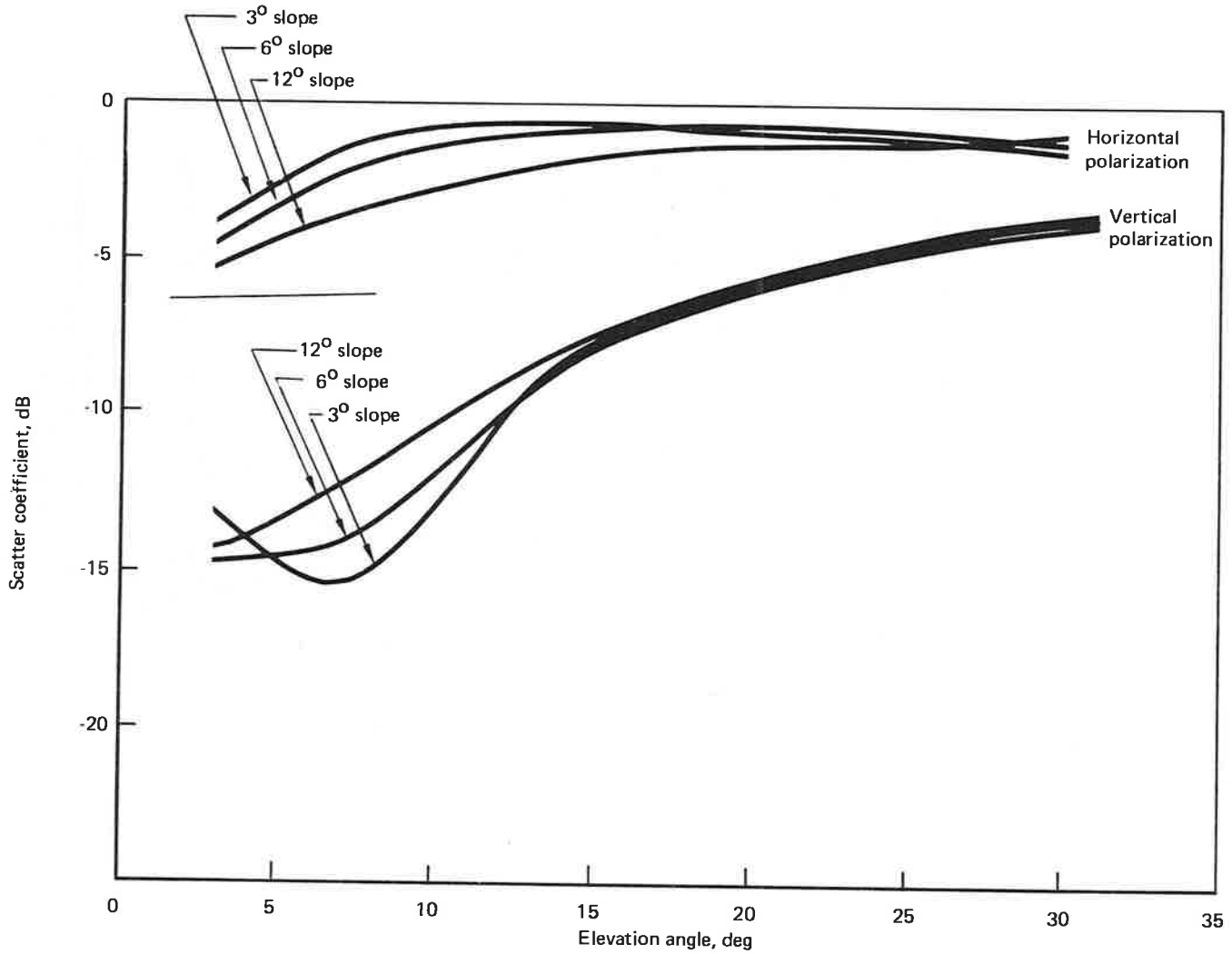

Figure 4-21. Model Predicted Oceanic Scatter Coefficients

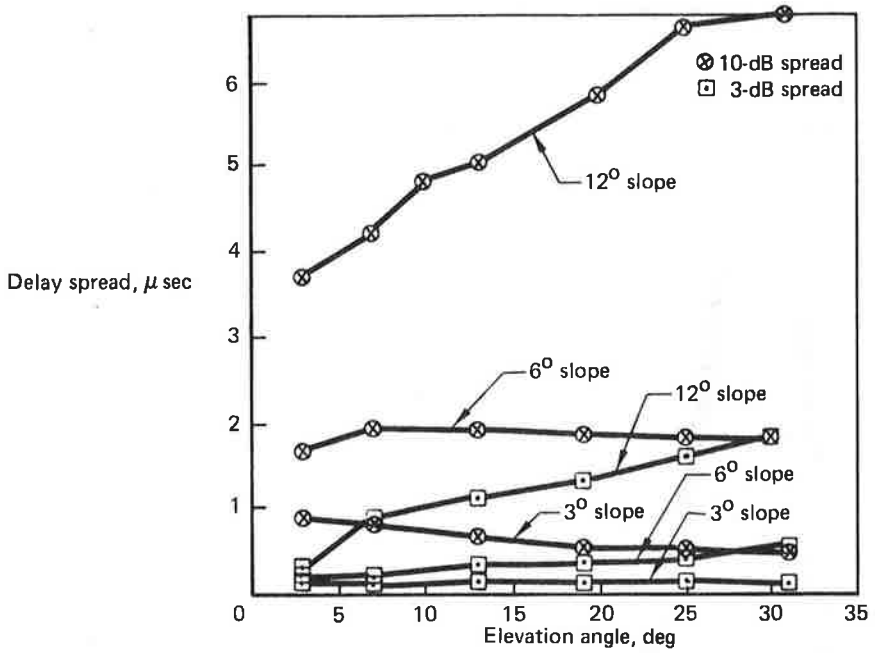

Figure 4-22. Model Predicted Delay Spread — Horizontal Polarization

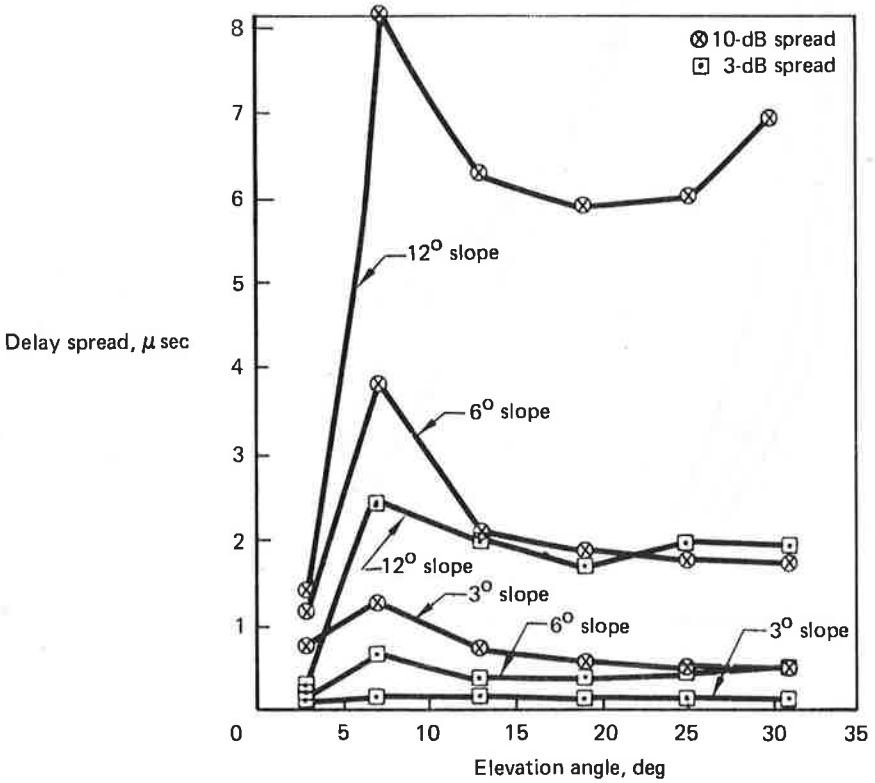

Figure 4-23. Model Predicted Delay Spread — Vertical Polarization

e. All spread measures increase with an increase in rms surface slope; the functional form of the increase, however, does not appear to be systematic.

4.5.4.2 Coherence Bandwidth – Figure 4-24 illustrates model results for the coherence bandwidth.

a. For the higher sea slopes, the 3-dB coherence bandwidth has a very weak dependence upon grazing angle whereas the 3^{o} sea slope yields a 3-dB coherence bandwidth that increases rather sharply for an increase in grazing angle. This result is somewhat in opposition to that obtained for the delay spread parameter.

b. In general, the horizontal and vertical polarization data are quite similar.

c. Coherence bandwidth decreases with an increase in sea slope.

d. For the 12^{o} sea-slope case, a 3-dB coherence bandwidth of roughly 85 kHz appears to be typical for grazing angles lying between 3^{o} and 31^{o}; the 6^{o} slope data yields 3-dB coherence bandwidths ranging from roughly 200 to 275 kHz, with the higher values being associated with the larger grazing angles.

4.5.4.3 Doppler Spread – Doppler spread model predictions are given in figures 4-25, 4-26, and 4-27.

a. Both the 3- and 10-dB spread measures increase monotonically as a function of elevation angle for all three sea slopes.

b. The spreads associated with the cross-plane data increase with an increase in sea slope.

c. For the in-plane geometry case we observe a rather unexpected slope dependency. Namely, the largest slopes do not always correspond to the largest Doppler spreads. This occurs for both the 3- and 10-dB spread measures and for both polarization modes.

d. Comparing the in-plane data with the cross-plane data reveals that dissimilarities between the two sets decrease for an increase in elevation angle and a decrease in sea slope.

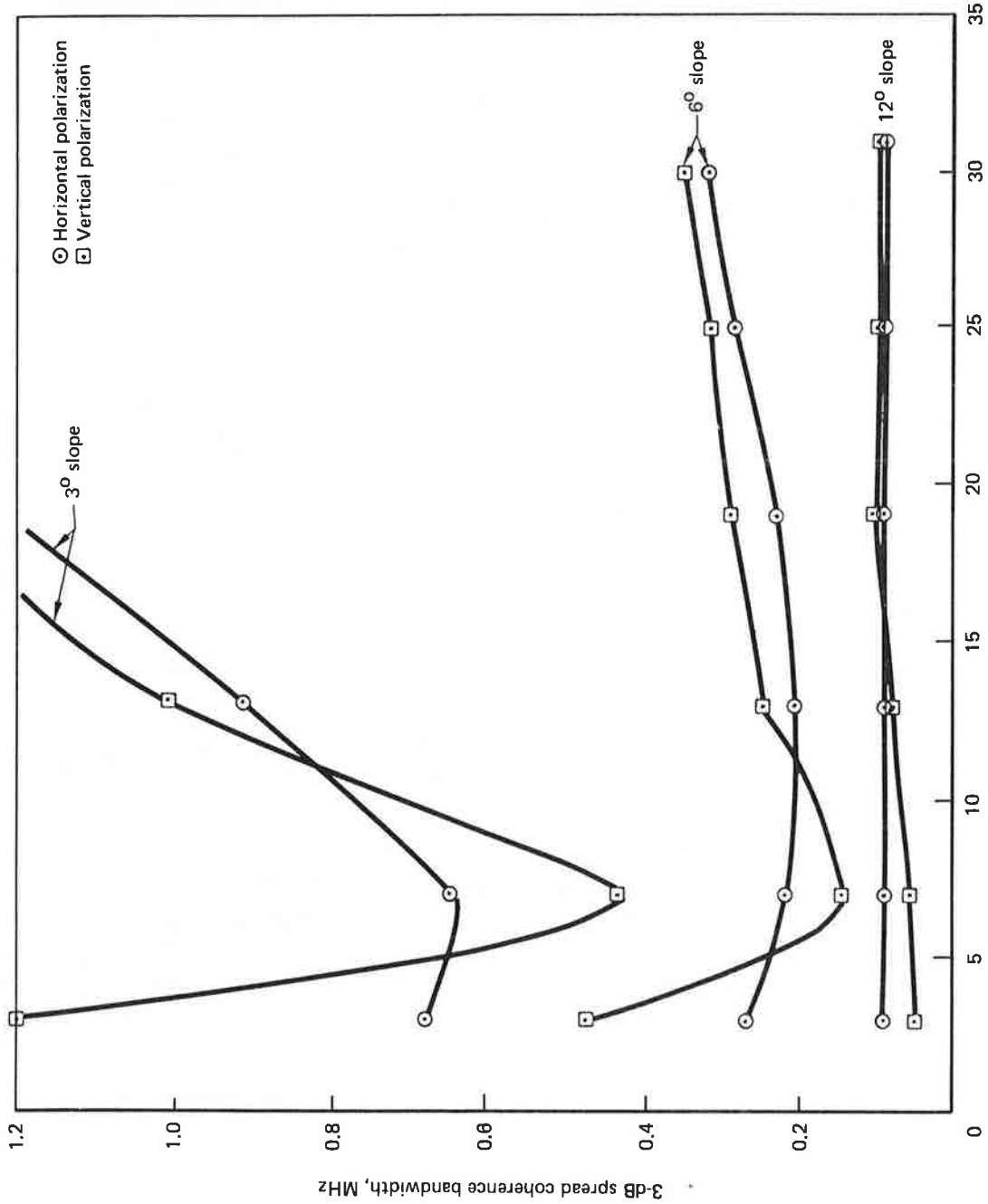

Figure 4-24. Model Predicted Coherence Bandwidth

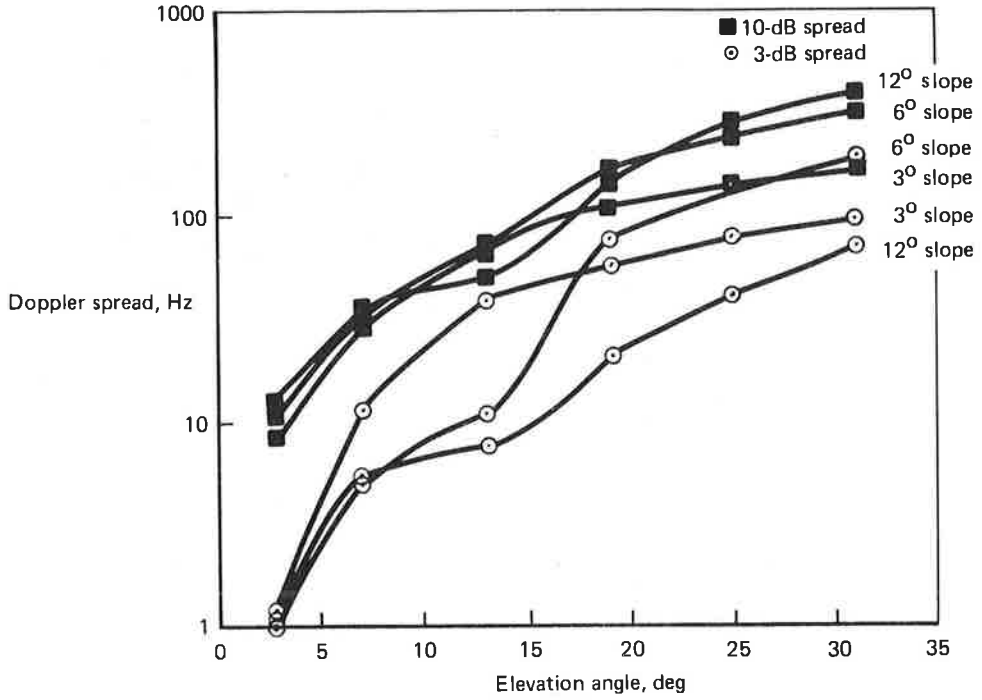

Figure 4-25. Model Predicted Doppler Spread — Horizontal Polarization, In-Plane Geometry

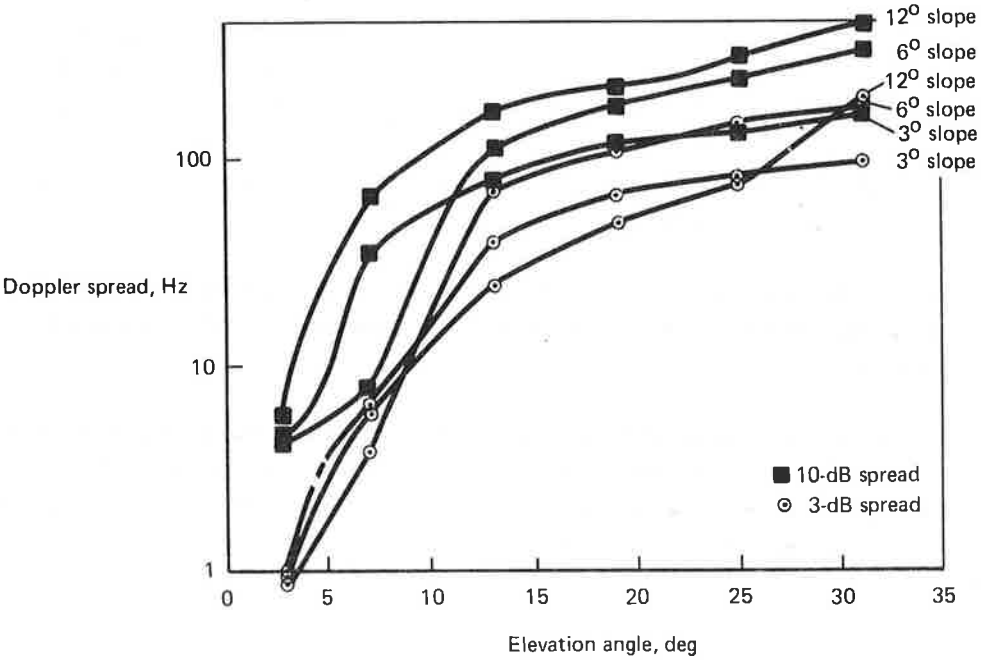

Figure 4-26. Model Predicted Doppler Spread — Vertical Polarization, In-Plane Geometry

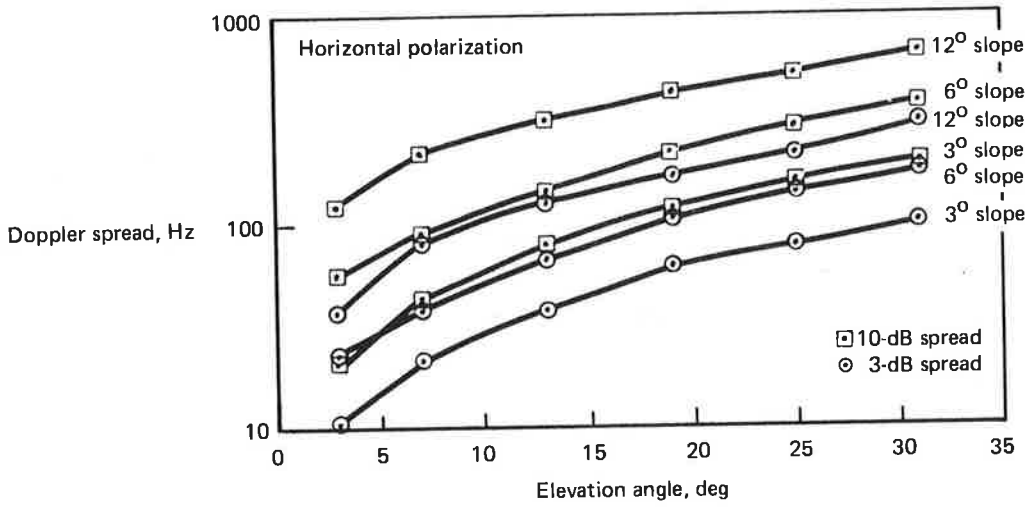

Figure 4-27. Model Predicted Doppler Spread – Cross-Plane Geometry

4.5.4.4 Decorrelation Time – Figures 4-28, 4-29, and 4-30 present model-predicted results for decorrelation time.

a. Like the coherence bandwidth measures, the decorrelation time spread values show systematic dependencies upon grazing angle and rms surface slope, i.e., the decorrelation times monotonically decrease for an increase in either the slope or grazing angle.

b. For most of the grazing angles, the decorrelation time decreases in a manner that is to a close approximation related *linearly* to an increase in sea slope.

c. The aircraft heading is seen to mildly influence decorrelation time, with the in-plane data being slightly higher than the cross-plane results (particularly for the large sea-slope conditions).

d. In general, the vertical and horizontal polarization results are in close agreement; however, we note that for the 6^{o} and 12^{o} slope cases the vertical polarization data tends to have a slightly lower decorrelation time than the horizontal equivalent (with the exception of the 3^{o} grazing angle condition coupled with the 6^{o} surface slope).

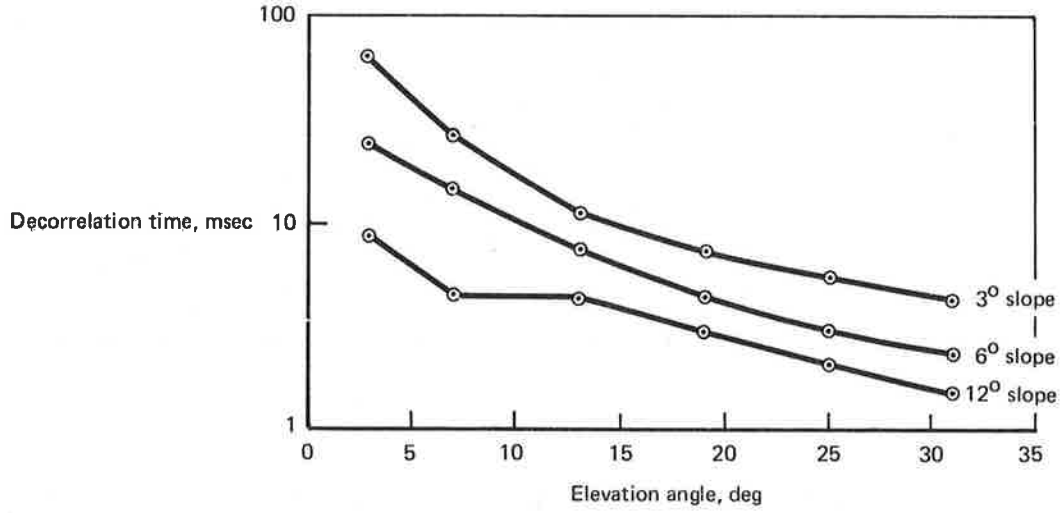

Figure 4-28. Model Predicted Decorrelation Time — Horizontal Polarization, In-Plane Geometry

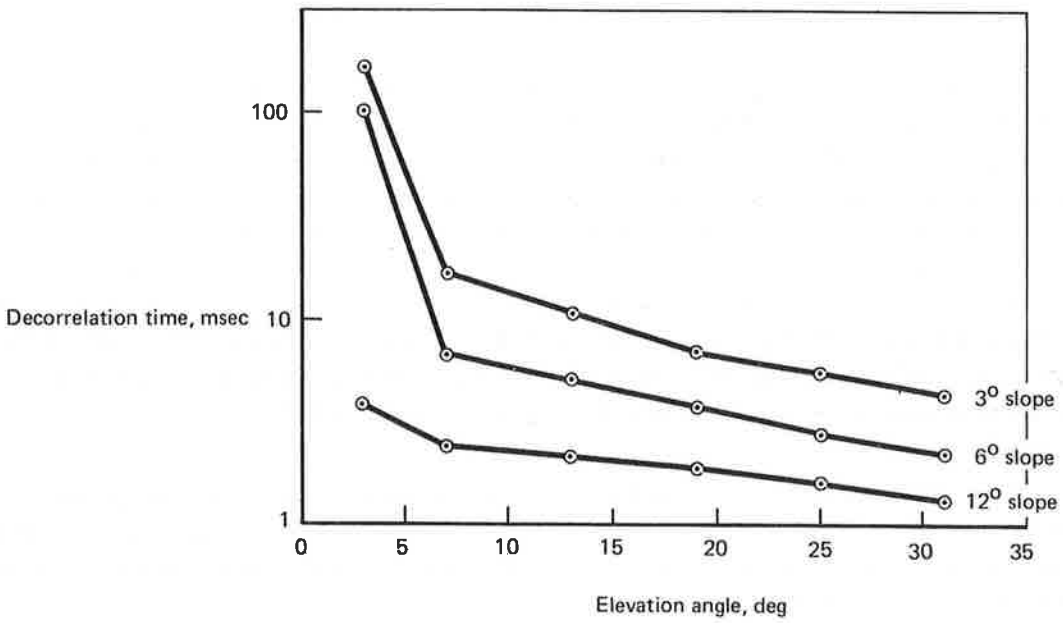

Figure 4-29. Model Predicted Decorrelation Time — Vertical Polarization, In-Plane Geometry

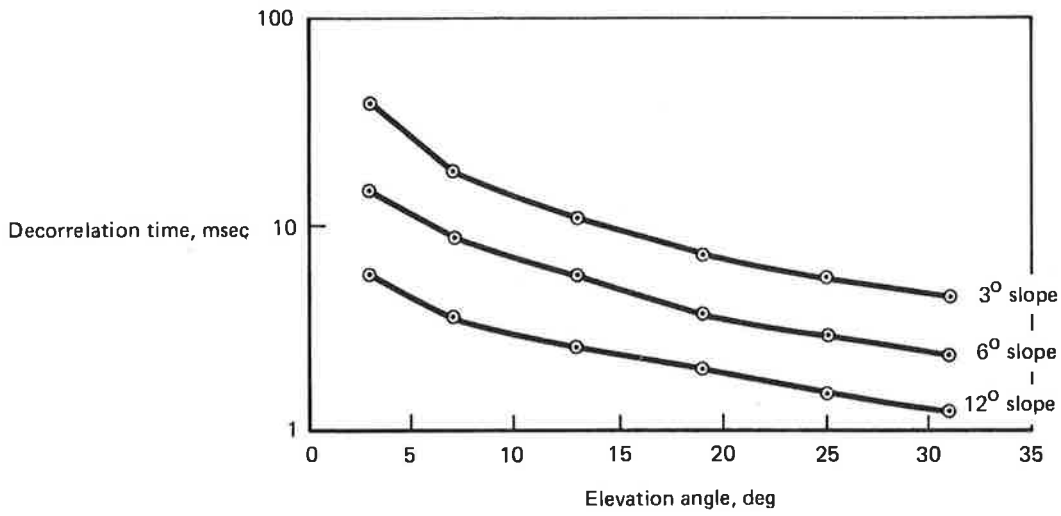

Figure 4-30. Model Predicted Decorrelation Time — Horizontal Polarization Cross-Plane Geometry

4.6 CONUS MULTIPATH TEST RESULTS

An extensive data base of CONUS forward-scatter multipath has been obtained. This collection covers a range of grazing angles from 22° to 48°, and a variety of terrain electrical characteristics (lakes to dry snow), surface roughness (flat plains to mountains), and vegetation coverage (heavily forested to barren). In addition, several hours of data pertaining to multipath reflections during the approach, taxi, and takeoff phases at large airport environments was obtained.

The data base for the CONUS multipath channel characterization is obtained from the September 19 and October 30, 1974, flights over the eastern United States; the February 18 and 19, 1975, flights over central Canada; and the February 20, 1975, flight over eastern Canada and the U.S. Pertinent system parameters for each of the flight tests are listed in table 4-5.

The February flights emphasized data acquisition for various snow-covered terrains (flat and mountainous), lakes (frozen and liquid), and airport environments, whereas the September and October series gathered data from heavily vegetation-covered terrain (both flat and mountainous) and coastal harbor/large city environments (e.g., New York).

TABLE 4-5. SYSTEM PARAMETERS FOR SELECTED CONUS TESTS

Test parameter	Description
Aircraft groundspeed	Approximately 190 m/sec
Aircraft barometric altitude	Approximately 31,000 ft
Elevation angle	30^{o} to 40^{o}: September 19, 1974 40^{o} to 48^{o}: October 30, 1974 22^{o} to 27^{o}: February 18, 1975 27^{o} to 39^{o}: February 19, 1975 28^{o} to 37^{o}: February 20, 1975
Probing rate	10 MHz for September 19 and October 30, 1974, and the airport environment probes 5 MHz for en route portions February 18, 19, 20, 1975

4.6.1 Delay-Spectra Time History

The channel's delay-spectra time history $Q(t,\tau)$ provides a partial illustration of the time-variant nature of the CONUS multipath probes. In addition, $Q(t,\tau)$ may be used to obtain an overview of the magnitude and delay-spectra characteristics associated with generalized terrain characteristics over which the specular point traverses. For this reason, all intervals of valid data acquired have been subjected to delay-spectra time history analysis. In total, this represents approximately 12 hours of experiment time. To discuss the delay-spectra time history data, we have segregated the terrain types into the following categories: vegetation-covered, snow-covered plains, snow-covered mountains, large size lakes, coastal harbors, large industrial cities, and residential areas. The salient $Q(t,\tau)$ features of each of these categories are discussed below:

Vegetation-Covered: Signal amplitude return was very low, most likely due to foliage absorption of the electromagnetic wave. The observable signal structure was relatively time invariant, except for intervals when the specular point traversed a small area of high reflectivity (e.g., lake, river, road, rock outcropping). By comparison, these intervals produced high-energy unitap signals that appear as "spikes" superimposed upon low-level, modestly spread background return.

Snow-Covered Plains: Snow-covered plains produced relatively intense low-spread return, with a modest amount of signal stationarity. The defoliated deciduous trees in the "glistening region" usually effectively attenuated or broadly dispersed, the signal.

Snow-Covered Mountains: Returns were fairly strong, with spreads occasionally somewhat equivalent to the higher grazing angle oceanic data. Possibly due to the large scale size of the scattering elements, the delay spectra exhibited a high degree of granularity and nonstationarity.

Large Lakes (Liquid): In their liquid state, large lakes produced $Q(t,\tau)$ arrays with attributes very similar to the oceanic test probes. Specifically, the signal strength was very large (roughly equivalent to the Fresnel reflection coefficient magnitude) and, for the conditions encountered, the surfaces produced a broadly dispersed return. These characteristics were essentially invariant over the duration of the probes.

Large Lakes (Frozen): The snow-covered large lakes possess signatures similar to those of the flat snow-covered terrain. Lakes that were partially frozen (e.g., along the shoreline) produced larger spreads than those totally frozen and covered by snow.

Coastal Harbors: For the relatively small amount of coastal harbor data gathered, the $Q(t,\tau)$ function revealed characteristics similar to those of the oceanic and large-lake probes. This implies a high-energy, broadly dispersed signal that is fairly stable except for the shoreline areas.

Industrial Areas: Delay-spectra signatures from industrial and business areas typically exhibited very little spreading, with the bulk of the returned energy being contained within 0.1 or 0.2 μsec of the specular-point return.

Residential Areas: The residential areas probed during a test on February 20, 1975, produced multipath signatures distinctly different from those of the industrial areas. Typically, the residential returns did not have an overwhelming amount of energy in the specular-point tap and gave the appearance of being either highly attenuated or broadly dispersed. These characteristics are somewhat similar to those of the vegetation-covered terrain probes.

Figure 4-31, taken from the February 20, 1975, flight over New York State, illustrates the nonstationary behavior of scatter from terrain that is predominantly snow covered. The first 2-min segment (fig. 4-31a) provides intervals of lake (high-amplitude, low-spread) and vegetation (highly attenuated) returns. The second 2-min segment (fig. 4-31b) illustrates low-amplitude, broad spreading associated with rough snow-covered or partially vegetation-covered terrain.

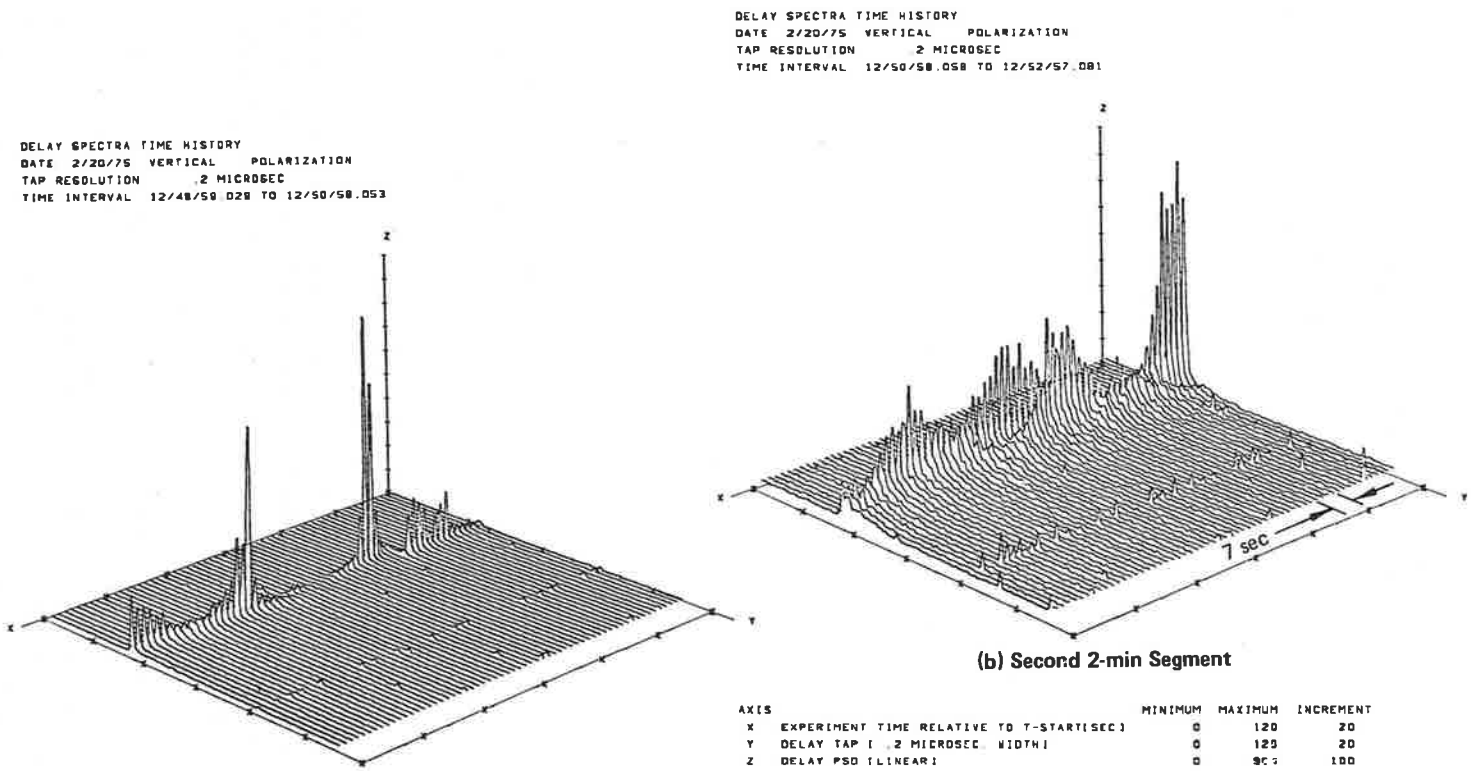

$S(\tau,\omega)_{74}$ (shown in fig. 4-32)

Figure 4-31. CONUS Delay-Spectra Time History Example, February 20, 1975

4.6.2 CONUS Delay-Doppler Scatter Functions and Associated Parameters

As one would expect, when a high degree of nonstationarity in the channel delay spectra is observed, there exists a corresponding degree of delay-Doppler scatter function, $S(\tau,\omega)$, nonstationarity.

Typically, $S(\tau,\omega)$ was derived over a 7-sec time interval. In many cases the surface characteristics being probed will change appreciably over this time interval. Hence, the scatter process cannot be considered to be stationary under these conditions, and thus it should not be assumed that $S(\tau,\omega)$ represents a complete statistical description of the channel.

Figure 4-32 presents an example CONUS $S(\tau,\omega)$ distribution, accompanied by the multipath delay spectra, frequency autocorrelation function, Doppler spectrum, and time autocorrelation function. The $S(\tau,\omega)$ function presented in figure 4-32 corresponds to the 7-sec segment bracketed on the $Q(t,\tau)$ function (fig. 4-31b). This particular example illustrates a high degree of dispersion in both the delay and Doppler domains, which is characteristic of rough snow-covered terrain. The flight direction was in-plane and the grazing angle was roughly 36^{o}. With the exception of the perturbation near the origin of the distribution, which produces a double peak in the delay spectra, we note that the data for this set is to a first order fairly equivalent to a high-angle oceanic scatter function. In fact, the Doppler distributions are seen to be quite similar in shape.

4.6.3 RMS CONUS Scatter Coefficients

The multipath signal's rms scatter coefficient, Γ, is defined as the ratio of total received scattered energy to the energy incident upon the surface. This parameter provides us with a quantitative measure of the total scatter intensity.

Figures 4-33 and 4-34 present the experimentally derived values of Γ for horizontal and vertical polarization, respectively. These data are given as a function of grazing angle and are accompanied by theoretical Fresnel smooth-earth reflection coefficient curves and a series of mid-angle results obtained from the ATS-5 L-band experiment (ref. 4-5). The ATS-5 results have been included in this presentation since they provide information over a range of grazing angles (15^{o} to 20^{o}) for which CONUS data were not acquired with the ATS-6 satellite.

It is well known that the water content of a scatter surface is perhaps the most significant single parameter influencing the magnitude of the Fresnel reflection coefficient. We believe that the CONUS flights traversed surface areas that varied markedly in their water content. Thus the theoretical reflection coefficient relationships have been plotted for a variety of electrical characteristics on each of the figures. Numerical subscripts on the data points allow the data to be cross-referenced to test locations by means of maps showing the calculated path of the specular point during each flight test (presented in vol. V, sec. 7).

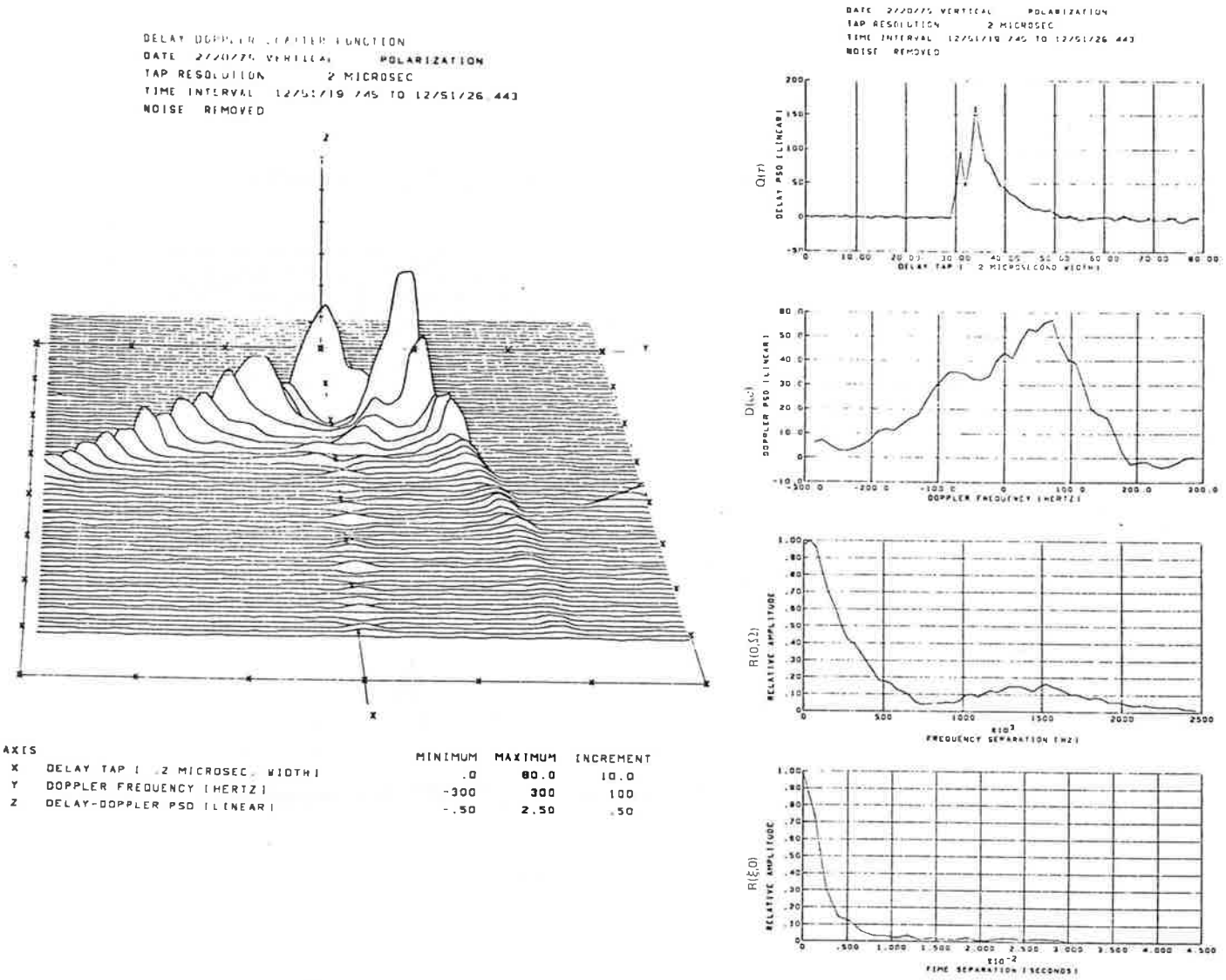

Figure 4-32. CONUS Scatter Channel Parameters – $S(\tau, \omega)_{74}$

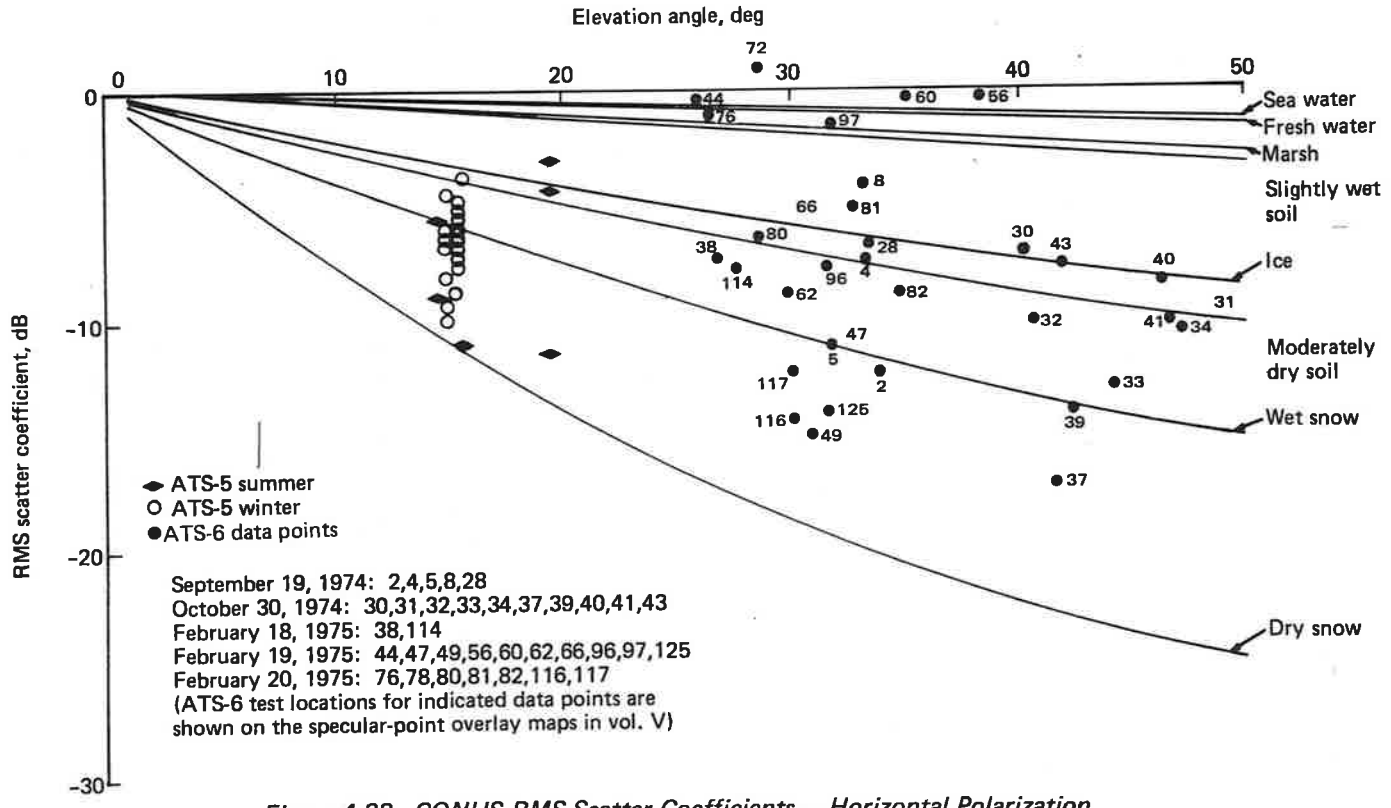

Figure 4-33. CONUS RMS Scatter Coefficients — Horizontal Polarization

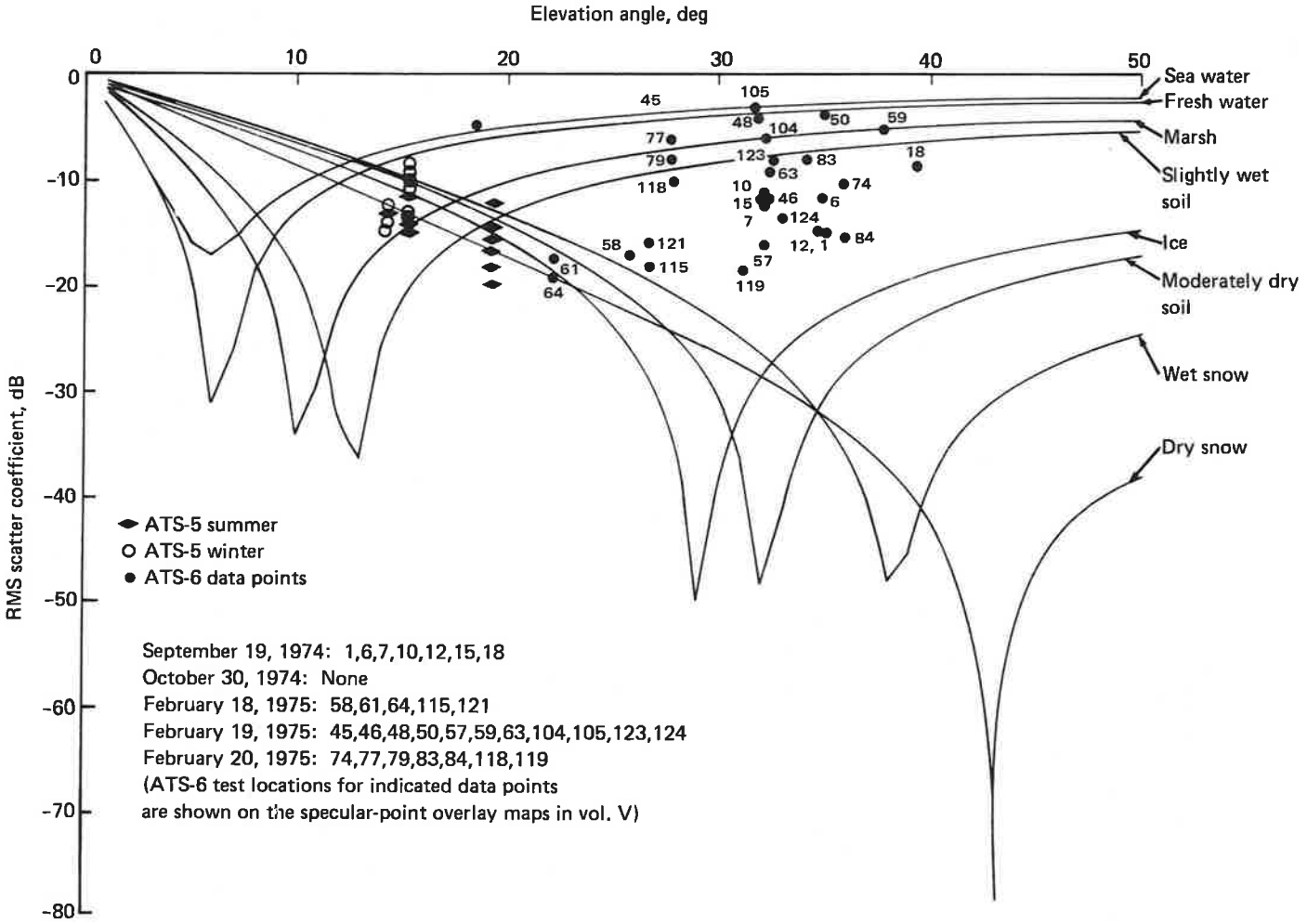

Figure 4-34. CONUS RMS Scatter Coefficients — Vertical Polarization

In general, the data points are fairly well bracketed by the Γ_H and Γ_V relationships corresponding to the above parameters. Horizontal Γ values as low as -18 dB and as high as +2 dB were observed, whereas the vertical coefficients ranged from -24 to -3 dB. On a total point basis, the vertical coefficients are more biased to the high side of the theoretical predictions than are the horizontal coefficients. This is especially true in the vicinity of the Brewster angle and is most likely attributed to the concept of "Brewster angle fill-in" and to the influence of depolarization, which is a natural phenomenon affecting multipath components returned from locations that are not on the great circle path joining the subaircraft and subsatellite points.

Only a small number of values corresponding to scatter from regions completely covered by vegetation have been included since these returns are attenuated to a low level that usually transcends the precision of the system capabilities and are therefore of lesser interest to the designers of an operational CONUS system. Data points with subscript numbers 2 and 1 for the horizontal and vertical reflection coefficient data, respectively, are two examples illustrating the influence of heavy vegetation cover on the intensity of the returned multipath signal. This particular result was obtained for the September flight test probe over the eastern United States. The observed Γ values are roughly 12 dB below the result one might expect for typical underlying soil conditions (slightly moist soil). On many other occasions for the fall flights over vegetation-covered terrain, the delay-spectra time history information indicates Γ values substantially below those associated with the above two examples. In general, the scatter coefficient data included in this section for the non-snow-covered terrain (fall flights) corresponds to selected time segments during which the $Q(t,\tau)$ plots indicate the presence of a significant amount of returned energy. Using detailed map overlays, these data segments can almost always be correlated to time intervals during which the specular point traversed nonforested regions such as small bodies of water, highways, manmade structures, or rock outcroppings.

4.6.4 CONUS Delay Spread, Frequency Coherence Bandwidth, Doppler Spread, and Decorrelation Time

The CONUS 3- and 10-dB delay spread values were determined for a variety of terrain profiles to provide a measure of the time delay dispersion characteristics of the multipath process. The 3-dB delay spread values ranged from a low of approximately 0.1 μsec to a high of 1.2 μsec, whereas the 10-dB measures ranged between 0.1 and 3.0 μsec. In general, all data sets exhibit very little dependence upon grazing angle, a result that is in accord with model predictions for a Gaussian surface. The data ensembles exhibit a rather large variance, most likely due to the gross inhomogeneities of the CONUS surface, which tends to mask any small grazing angle dependence that might be present.

The frequency coherence bandwidth represents the upper frequency limit to which two transmitted carriers may be separated yet still meet a specified degree of correlation (i.e., 0.5) at the receiver. Experimental results for both horizontal and vertical polarization were segregated into fall and winter flight tests categories, and a high degree of dispersion was observed to exist in each data ensemble. This follows directly from a similar delay spread observation, and most certainly relates to the wide variety

of terrain characteristics encountered in the CONUS environment. Comparing the delay spread results to the coherence bandwidth measurements provides a general confirmation of the "inverse proportional" relationship that exists between the two measures. Since the overland scatter process is, on occasion, multimodal, the relationship should not be expected to hold valid for each and every data point of the ensemble.

Considering all CONUS test conditions, the range of coherence bandwidth measures ranged from a low of roughly 150 kHz to a high of several MHz (the resolution capabilities of the prober chip width duration establish an upper limit to which coherence bandwidth may be measured). For the fall test series, a median coherence bandwidth measure of roughly 750 kHz was observed, whereas the winter results produced a somewhat smaller median value of approximately 600 kHz. As discussed in volume V, these findings are thought to be indicative of the terrain regions over which the winter flights were conducted as well as the criteria used to select time intervals for the fall test series data analyses.

The two-sided 3- and 10-dB CONUS Doppler spreads for vertically and horizontally polarized multipath probe signals were determined. The 3-dB spreads are given as a function of grazing angle in figures 4-35 and 4-36. Results are segregated according to flight test series (fall and winter) and aircraft velocity direction (in-plane and cross-plane).

With the exception of data points 50, 56, 59, 60, and 74 (which represent data collected over Lake Michigan, Lake Superior, and the Adieundacy Mountains northeast of Montreal, Canada), the majority of the Doppler spread observations appear to have 3-dB spreads that lie between 20 and 125 Hz, with a typical value of approximately 60 Hz. The 10-dB spread measures were observed to vary over a wide range of values, with the majority of the points falling between a low of 40 Hz and a high of 500 Hz. A slight tendency for the spread values to increase with an increase in grazing angle was observed. This relationship is in accord with theory; however, it is believed to be more indicative of the terrain type differences over which the high- and low-angle flights were conducted.

Spreads associated with CONUS specular-point trajectories subtending large lakes and winter-mountainous regions correlate well with the observed high-angle oceanic results. In particular, the previously delineated points corresponding to flights over Lake Superior (50 and 60), Lake Michigan (56 and 59), and the Adieundacy Mountains (74) provided typical 3- and 10-dB spread values of 200 and 450 Hz, respectively. These may be compared with typical high-angle (31^{O}) oceanic 3- and 10-dB spreads of 170 and 300 Hz.

The CONUS 3-dB decorrelation times were determined as a function of grazing angle for both the horizontal and vertical polarization probes. The data sets were segregated according to test series (fall and winter) and aircraft heading (in-plane and cross-plane). The decorrelation time parameter represents the upper time limit separation to which two identical frequency L-band carriers may be spaced, yet still meet a specified degree of coherency (0.5) at the receiver.

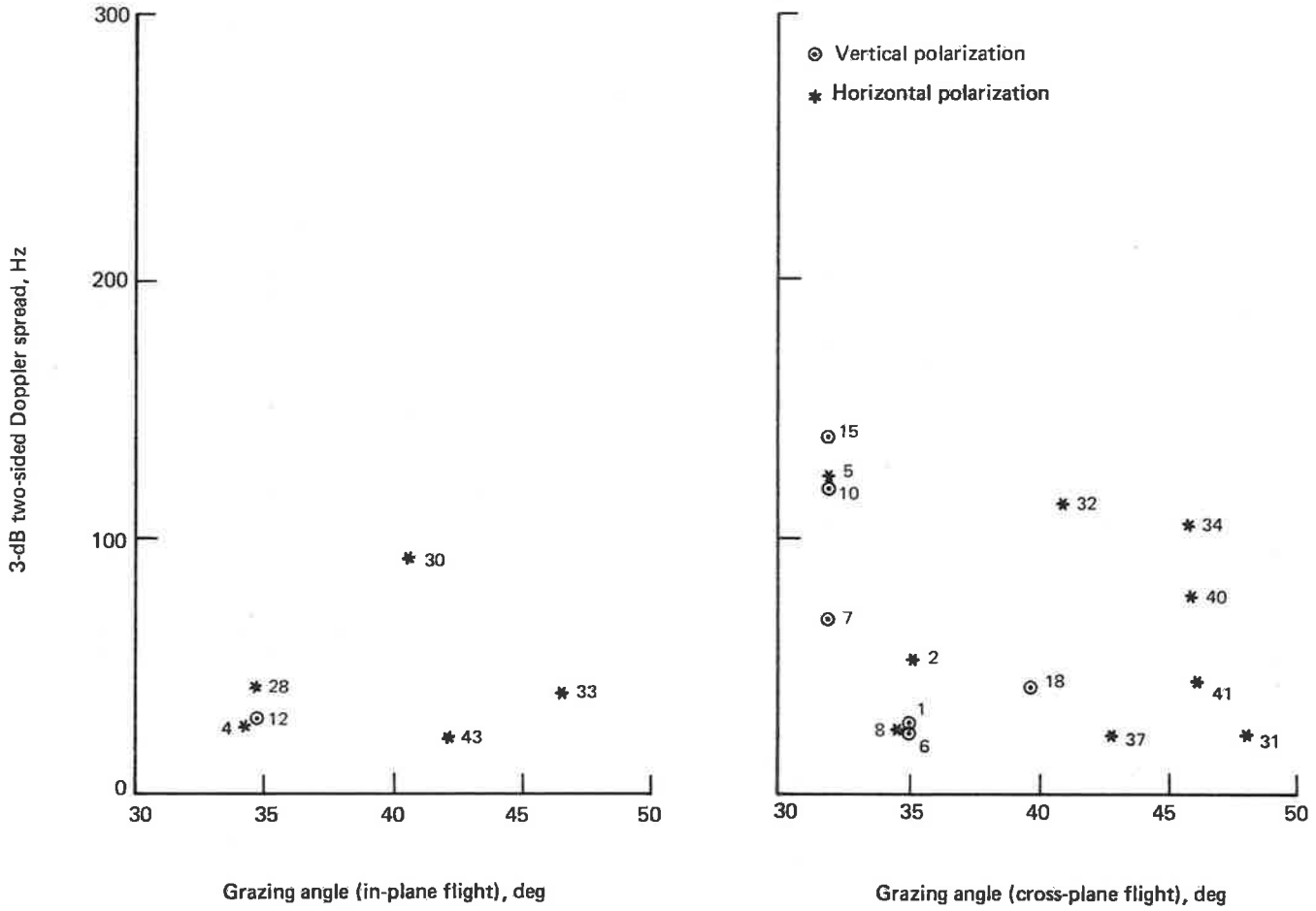

Figure 4-35. CONUS Scatter 3-dB Doppler Spread, Fall Flights

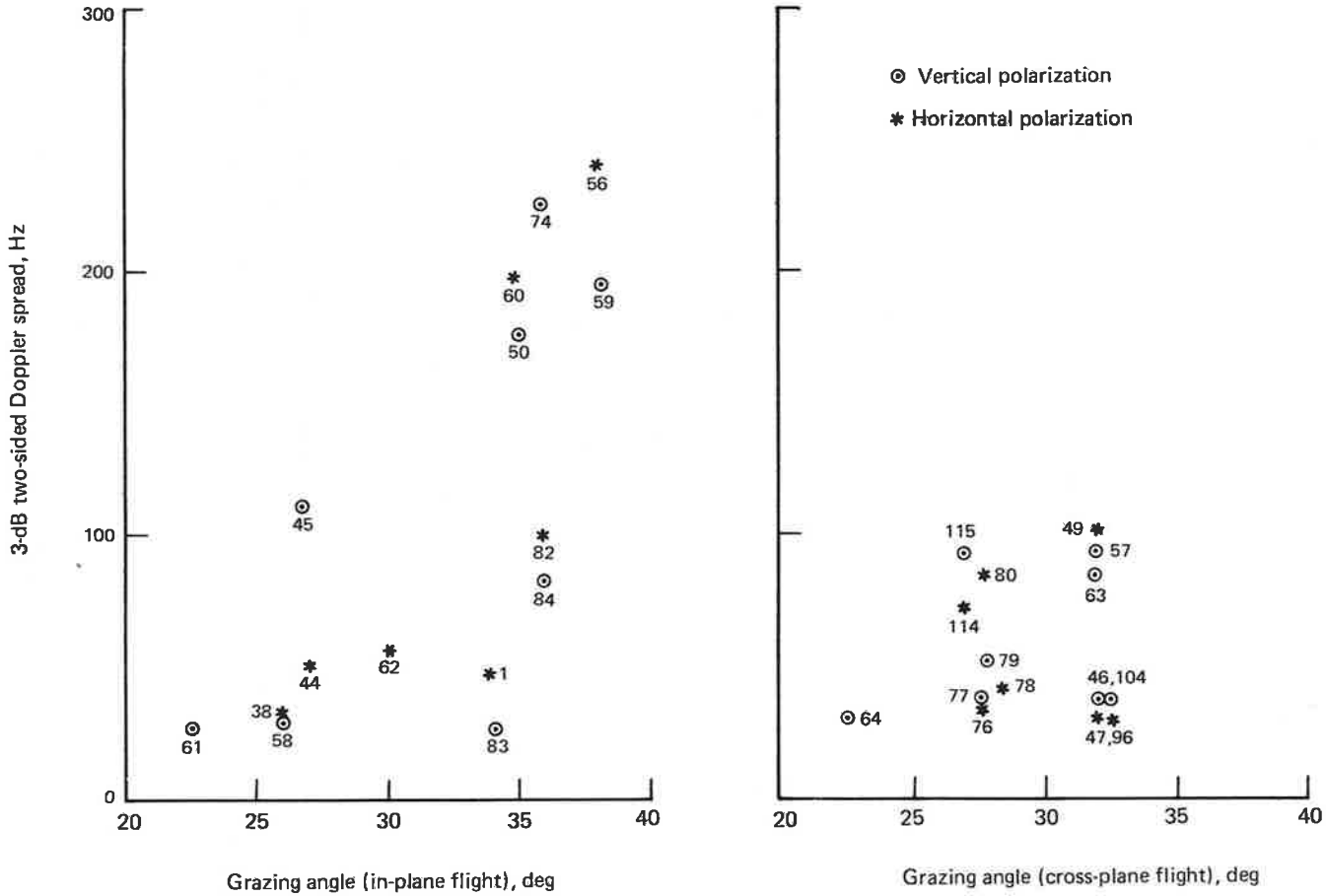

Figure 4-36. CONUS Scatter 3-dB Doppler Spread, Winter Flights

The measured decorrelation times of the CONUS multipath signal spanned a wide range of values. The trend of the data did not indicate a pronounced grazing angle, polarization, flight direction, or flight series dependence. For all but one data point, the decorrelation time measures lie between values of 1 and 10 msec, and we may ascribe an average value of roughly 4 msec to the total ensemble.

4.6.5 Airport Multipath Environments

Multipath airport environment data was gathered on the approach, landing, and taxi phases at three airports: O'Hare International (Chicago), JFK International (New York), and NAFEC, located northwest of Atlantic City, New Jersey. All probes were conducted with a 10-MHz chip rate and used a single low-gain crossed-slot antenna located close to the top centerline of the airplane. This antenna possessed nominal LHC polarization characteristics and thus provided an enhanced multipath return at the expense of a direct signal polarization mismatch relative to the RHC polarized ATS-6 uplink. For all three airports the elevation angle to ATS-6 was approximately 39^{o}.

4.6.5.1 Runway Taxi Conditions – With the airplane on the ground and conducting typical taxi maneuvers, the returned signal structure generally had the following attributes.

a. Significant amplitude fluctuation was observed on the received direct tap[3] signal for the crossed-slot operational antenna. This may be attributed to a number of factors, such as building shielding of the direct line-of-sight signal, antenna pattern variation as a function of aircraft orientation, and interference (both constructive and destructive) due to multipath arrivals falling within the direct tap bank.

b. Very little multipath energy was returned with delays greater than 0.2 μsec from the direct signal arrival. The level of multipath energy with delays greater than 0.2 μsec was at least 20 dB below the direct-path signal.

During the February 19, 1975, airport test sequence at O'Hare (Chicago), signal amplitude fluctuations described in item a above were observed. Results also indicated that the bulk of the delay returns arrived no later than 0.1 or 0.2 μsec after the direct signal, further illustrating item b.

[3]With the aircraft on the ground, the 10-MHz chip rate (the highest available with the SACP equipment) resolution is insufficient to completely discriminate against terrain and building scatter returns on the basis of time separation. Some of these multipath returns therefore fall into the direct-path taps.

4.6.5.2 Approach and Landing Maneuvers – Due to fairly rapid airplane altitude and attitude changes, the multipath characteristics in the landing and approach phases of an airport environment are somewhat different from those associated with en route CONUS conditions. Prior to, or during, its final descent, the airplane may perform one or more rather steep banking maneuvers. Perhaps the most significant impact of these attitude changes relates to the potentially large antenna gain that may be directed toward the effective multipath "glistening region" during banking maneuvers. An example illustrating such an occurrence is given in figure 4-37, where a delay-spectra time history for a 2-min flight segment in the vicinity of the NAFEC FAA airport is illustrated. At 1424:30 the airplane began a banking maneuver (toward the satellite) and we note a very perceptible increase in the multipath return, which is accompanied by a corresponding decrease in the direct signal component. It is of interest to note that the direct signal decreases not because of a decrease in antenna gain but because of an increase in the polarization mismatch between the satellite polarization vector and that of the aircraft antenna (becomes maximum for look angles directly above the airplane). Although the antenna and the mode in which it was used for this probe (with its circular polarization sense reversed on the direct path) are not representative of an operational system antenna, it does provide a vivid example of the banking effects on a receiving system signal-to-multipath-interference (S/I) ratio.

4.7 MULTIPATH TEST CONCLUSIONS

Forward-scatter L-band multipath data was acquired for a comprehensive set of oceanic and CONUS test conditions. The oceanic flight tests subtended elevation angles ranging between 3^{o} and 32^{o}; the CONUS probes were conducted between elevation angles of 22^{o} and 48^{o}. Analysis of these data has concentrated primarily on determining the channel's delay-Doppler scatter function and its associated integral and Fourier parameters. In addition, for the oceanic multipath channel, a scatter model was validated, the spatial filtering effect of the prober antenna was isolated, and selected data sequences were processed to determine time-domain statistics and cross-power spectra.

4.7.1 Oceanic Multipath Test

A major portion of the oceanic multipath analysis effort was directed toward verification of an appropriate scatter model that could extend the experimental results to the prediction of performance for future aeronautical satellite systems. Toward this end, a vector formulation of the widely accepted physical optics very-rough-surface scatter model was used to correlate theory with experiment. In applying the model, the scatter cross section, coupled with complex polarization transmission coefficients, was numerically integrated over the total effective multipath surface. Model predictions were generated for a variety of surface rms slope conditions and were shown to closely emulate the measured multipath channel characteristics. These predictions and the corresponding comparisons were conducted at the level of the delay-Doppler scatter function and its associated lower order integral and Fourier parameters.

DELAY SPECTRA TIME HISTORY
DATE 2/20/75 RHC-KSLT POLARIZATION
TAP RESOLUTION .1 MICROSEC
TIME INTERVAL 14/23/30.000 TO 14/25/30.201

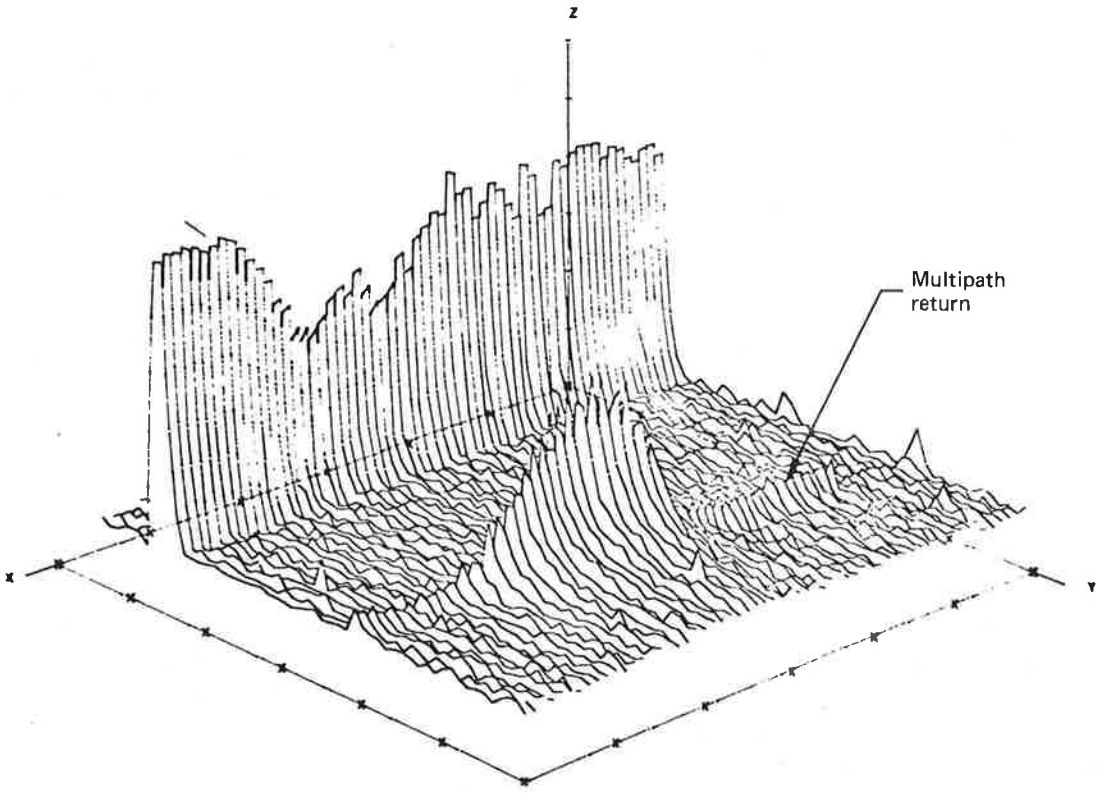

AXIS		MINIMUM	MAXIMUM	INCREMENT
X	EXPERIMENT TIME RELATIVE TO T-START(SEC)	0	120	20
Y	DELAY TAP (.1 MICROSEC. WIDTH)	20.0	80.0	10.0
Z	DELAY PSD (DECIBEL)	15.0	45.0	5.0

Figure 4-37. Airport Environment Multipath Probe — Banking Maneuver

The delay-Doppler scatter function, $S(\tau,\omega)$, was found to be quite dependent on grazing angle, aircraft heading, and rms sea slope. Sea-slope dependencies were investigated mainly through use of the model predictions. These predictions were based on an isotropic slope distribution processing a Gaussian form. Sea-slope distributions used in model predictions were verified by sea-state buoy measurement data.

With the exception of the absolute level of its power spectral density, $S(\tau,\omega)$ is only mildly dependent upon the electromagnetic polarization (horizontal, vertical, or circular) of the incident probe signal. This is particularly the case for the high-angle data, whereas at the lower grazing angles the effect of the vertical polarization reflection coefficient's spatial variation is in evidence. The sea-surface slope strongly influences the dispersion in both the delay and Doppler coordinates. More specifically, an increase in rms shape results in both increased delay dispersion and Doppler dispersion. The distribution of energy in the Doppler coordinate is also a strong function of grazing angle and aircraft heading. As the flight direction departs from the cross-plane direction, the energy distribution in the Doppler realm is no longer symmetrical with respect to the specular-point frequency. This asymmetry increases as the flight direction approaches the in-plane condition and results in the negative-frequency realm of $S(\tau,\omega)$ being significantly more spread than the positive-frequency region.[4] Elevation angle effects are primarily related to the Doppler frequency; for a decrease in elevation angle, the dispersion in the Doppler coordinate also decreases, while the asymmetry of the in-plane $S(\tau,\omega)$ function increases. Hence, $S(\tau,\omega)$ has maximum asymmetry for a combination of low grazing angle, high sea surface slope, and in-plane flight geometry.

When $S(\tau,\omega)$ is reduced to lower order parameters via integral and Fourier transform operation, its properties are generally more self-evident. Using these techniques, the channel's delay spectra, Doppler spectra, frequency autocorrelation function, and time autocorrelation function have been derived. The observed delay spectra exhibit the expected monotonic decay as a function of tap number, with the specular-point tap possessing the maximum density. The delay-spectra data showed no significant dependence upon grazing angle or flight direction. Model emulations show that the dispersion of the delay spectrum increases substantially for an increase in surface slope. The Doppler spectrum measurements exhibited a Gaussian-like distribution associated with the cross-plane flight conditions and a very asymmetrical "ramp-like" relationship for the in-plane direction. For a decrease in grazing angle, the variance of the Gaussian Doppler spectrum decreases whereas the ramp slope of the in-plane distribution increases, with the spectrum possessing an abrupt upper frequency limit. Again, model emulation shows that an increase in sea slope results in an increase in the dispersion of the Doppler spectrum. The frequency autocorrelation function and the delay spectra are a Fourier transform pair:

[4]The frequency realm corresponding to scatter from the region on the "subaircraft" side of the specular point will exhibit the larger spread. For these tests, the in-plane flights were toward the satellite, and hence the negative-frequency realm shows the larger spread. For in-plane flights away from the satellite, the positive-frequency realm would have the larger spread.

similarly, the time autocorrelation function and the Doppler spectra are another Fourier transform pair. Thus the time and frequency autocorrelation function dependencies upon grazing angle, flight direction, and sea slope are extensions from the above discussion (i.e., an increase in spread of a function results in a decrease in spread of its Fourier transform). These inverse relationships between the Fourier transform pair elements are clearly visible from the calculated data. It is of interest to note that, compared with the Doppler spectrum properties, the shape of the time autocorrelation function is not nearly so dependent upon aircraft heading. However, it is apparent that the in-plane result is somewhat heavier tailed than the cross-plane result, as expected.

The total energy content of the scattered signal and the spread measures of the above spectra and autocorrelation functions represent the lowest echelon of channel characterization and were calculated as a function of polarization and grazing angle. Horizontal and vertical polarization total scatter coefficients were found to be within 1 or 2 dB of results predicted by the physical optics vector scatter model. The experimental scatter coefficient dependency upon sea slope was not determined explicitly because sea-slope measurements were not available for the exact times and locations of the multipath tests. The model predictions, however, indicated that the scatter coefficient magnitudes for grazing angles above 10^{o} were only weakly dependent upon sea-surface slope. With the exception of the low-angle vertical polarization data, the scatter coefficients are roughly equivalent to the product of divergence factor and Fresnel smooth-earth reflection coefficient. The low-angle vertical results are some 3 to 5 dB above this relationship; this is not unexpected and may be explained by the concept of "Brewster angle fill-in," which is discussed in more detail in section 5.2.6 of volume V.

Channel spread measures were presented as a function of grazing angle. No appreciable grazing angle dependence was apparent for the delay spread data. Average delay spreads were almost constant (less than 20% change) for grazing angles ranging between 10^{o} and 30^{o}. The 3-dB delay spreads ranged from a low of 0.25 μsec to a high of 1.8 μsec and had a typical value of 0.8 μsec; the 10-dB delay spreads ranged from 2.2 to 5.6 μsec and had an average value of 3.2 μsec. Similarly, the 3-dB coherence bandwidths did not exhibit a strong grazing angle relationship and were observed to vary over a range from 70 to 380 kHz, with the higher values being associated (very weakly) with the higher grazing angles. Doppler spreads exhibited a very strong dependence upon both grazing angle and aircraft heading. For the in-plane geometry condition, very small Doppler spreads are associated with the low grazing angles; for example, at a grazing angle of 7^{o}, typical 3- and 10-dB spread measures of 5 and 44 Hz were measured. These results are significantly lower than those obtained for the cross-plane flight vector and are in accord with prediction. This phenomenon does not imply a low sea surface slope; in fact, as shown by the model predictions, the low-angle in-plane Doppler spreads may actually decrease for an increase in sea slope. At the high end of the grazing angle range ($\approx 30^{o}$), the flight direction vector has very little influence on Doppler spread, with both data sets taking 3- and 10-dB values of 140 and 350 Hz, respectively. Measured values of selected oceanic multipath parameters were summarized in table 2-1.

An additional dimension of the interrelationship between the oceanic surface and the complex vector nature of electromagnetic propagation was investigated by determining the degree of correlation between the simultaneous vertical and horizontal probes and by separately using right- and left-hand circular polarization probes. With the exception of the received signal's absolute amplitude, the circular polarization data was shown to possess attributes similar to those of the linear polarization data. With respect to the total received scattered energy during tests with circularly polarized (CP) probes, the results illustrate the phenomenon of surface-induced polarization sense reversal. This is evident since probes transmitted from the aircraft with LHC polarization are received more favorably at the right-hand circularly polarized satellite than probes transmitted with RHC polarization. The degree of correlation between the probe's horizontal and vertical polarizations was investigated by determining the amplitude of the correlation coefficient between the two signals and by examining the phase of their complex cross-power spectra. In both cases, results are in accord with vector scatter theory and indicate that the orthogonal polarization multipath processes are highly correlated, with the Fresnel reflection coefficients providing the appropriate phase relationship between the scattered vertical and horizontal probes.

With respect to investigations pertaining to the complex Gaussian WSSUS properties of the oceanic multipath process, we have, after rather extensive testing, statistical bases for support of both the complex Gaussian statistics hypothesis and the assumption that the scatterers are uncorrelated. Also, the channel's wide-sense stationary characteristics, which were examined over a relatively short timespan, appeared to exhibit time-invariant statistical properties. While this test was by no means comprehensive, it is thought to be representative of expectations in that the scattering physics are influenced primarily by the surface's slope probability distribution function (pdf), which changes in a manner roughly proportional to the square root of the wind velocity. Thus one may confidently represent the oceanic channel as a complex Gaussian WSSUS scatter process. Under these conditions the $S(\tau,\omega)$ function completely describes all statistical attributes of the channel. Since this function and the lower order measures are well duplicated by the physical optics vector scatter model, the results of this test may be easily extended and applied to the detailed analyses and design of future oceanic L-band systems.

4.7.2 CONUS Multipath Test

One of the most obvious characteristics of the overland CONUS scatter data is its high degree of signal structure nonstationarity. This was readily confirmed through a visual observation of several delay-spectra time history segments. Similarly, the signature of the channel's delay-Doppler scatter function varies markedly with specular-point location and was used to isolate periods of very low spreading, modest spreading, biased positional scatter, large irregular Doppler spectra return, and mixed scatter process return. These data were used to delineate the salient features associated with terrain types falling under the categories of heavy vegetation cover, coastal harbors, large cities, large lakes, and snow-covered plains and mountains.

The above properties of nonstationarity appear to mask out any systematic grazing angle, flight direction, or polarization dependencies that might exist for the channel's rms scatter coefficients and spread parameter measures. A summary of the observed range and typical values associated with the unidimensional channel parameters was presented in table 2-2.

Data gathered during the airport environment multipath probe were analyzed for test sequences entailing runway taxi, landing, and low-altitude-approach airplane maneuvers. These probes were carried out via a single crossed-slot low-gain antenna whose polarization was left circular, thus providing enhancement of the multipath signal at the expense of the direct signal. With the airplane moving on the ground, the received signal structure possessed two rather distinct attributes: (1) fairly large-amplitude fluctuations of the energy received in the direct line-of-sight signal taps were observed (possibly caused by small delay multipath components) and (2) only very low levels (at least 20 dB below the direct-path signal) of multipath power were observed for delays greater than 0.2 μsec relative to the direct signal arrival.

For the approach and landing phases of the airport environment test, the data has been used to identify several fundamental characteristics of the direct and multipath signal components. As expected, airplane banking maneuvers produce substantial changes in the relative direct and multipath signal levels. This was illustrated by an example that showed the antenna's S/I parameter undergoing a change in excess of 20 dB over a timespan of approximately 15 sec. With respect to the influence of the aircraft's altitude decrease during the descent and landing planes, a corresponding decrease in the differential time delay and a relatively large positive differential Doppler frequency shift between the direct and multipath signals were observed. The differential delay is proportional to altitude only, whereas the differential Doppler depends on angle of approach and aircraft velocity. For the JFK approach at an altitude of approximately 0.7 km, a 34-Hz differential Doppler was measured. One further observation relates to the noted tendency for the multipath signal's delay spread to decrease with a decrease in altitude. This is in accord with theory, which predicts a delay spectrum dispersion proportional to the altitude of the airplane.

5. MODEM EVALUATION TEST

A description of the modem evaluation tests and summary results of the voice, digital data, and ranging experiments are provided in this section. More detailed information may be found in volume VI of this report.

5.1 MODEM EVALUATION TEST OBJECTIVES

Various techniques are being considered for the transmission of voice, digital data, and ranging/surveillance signals to and from aircraft via satellites. The general objective of the tests here summarized was to evaluate the performance of several voice, digital data, and ranging modems representing candidate approaches for this application. Specific objectives were:

a. To evaluate modem performance over a range of flight geometries and C/N_0, using the candidate operational left wing-root/right wing-root/top (LWSD/RWSD/TOP) switchable slot-dipole antenna system. Experimental performance data were compared with theoretical and laboratory baseline data to assess the effects of the overocean flight environment on modem performance for a representative set of conditions.

b. To evaluate modem performance parametrically in terms of a wide range of C/N_0 and S/I values for the overocean flight environment. These experimental data provide quantitative measurement of modem performance degradation for various degrees of oceanic multipath interference. Experimental data were compared with theoretical prediction and with performance measurements made using a laboratory multipath simulator.

5.2 MODEM EVALUATION TEST DESCRIPTION

5.2.1 Type I and Type II Test Categories

The modem evaluation tests were divided into two general types:

Type I – Performance With Aircraft Operational Antennas: These tests acquired modem performance with operational antennas at satellite elevation angles ranging from 10^o to 30^o. Bearing angles relative to ATS-6 were approximately 45^o, 135^o, 225^o, and 315^o.

The inherent signal-to-multipath-interference ratio (S/I) for these tests is dependent upon the polarization and gain characteristics of the airborne operational antenna and the magnitude and polarization characteristics of the sea-reflected signals. Type I tests evaluated modem performance over a range of C/N_0 values combined with the S/I values inherent to the antenna system for the geometries tested.

Type II – Performance With Various Levels of Oceanic Multipath Interference. Type II tests used the quad-helix antenna for reception of the direct-path signal and the side multipath antenna for reception of the sea-reflected multipath signals. After preamplification, these signals were combined at RF in the desired power ratio to simulate an antenna with a specified S/I ratio. All flights were approximately broadside to the satellite at an elevation angle of 15^{o}. This constant orientation was used because the SMP antenna pointing was fixed. The test parameters varied were the direct-path C/N_0 and the combining ratio that determines S/I. Tests spanned C/N_0 values between 38 and 52 dB-Hz in combination with S/I values ranging from heavy multipath fading (S/I = 3 dB) to essentially non-fading conditions (S/I > 20 dB).

5.2.2 Airborne Terminal Functional Description

A simplified block diagram of the aircraft terminal is shown in figure 5-1.

5.2.2.1 RF Signal Routing – The RF signal routing normally used for Type I data acquisition is shown in Figure 5-1. The RF switches selected the desired operational antenna (LWSD or RWSD), and the variable attenuator preceding the preamplifier allowed the C/N_0 to be set at the desired value. The PLACE diplexer was normally bypassed as shown.

For Type II tests, the quad-helix antenna received the direct-path signal while the side-mounted multipath antenna, in its horizontal polarization mode, received the sea-reflected signal. The direct-path C/N_0 was again set by the variable attenuator preceding the preamplifier. The outputs of the preamplifiers were routed through two variable attenuators preceding the RF combiner, which allowed the S/I ratio to be adjusted to the desired value.

If needed, a voice link for test coordination could be transmitted using the PLACE transmitter connected to either of the backup slot dipoles (LSD or RSD). The use of separate antennas for transmission and reception functions not only allowed receive channel losses to be minimized but also guarded against the possibility of interference in the receive channel due to diplexer leakage during transmitter operation.

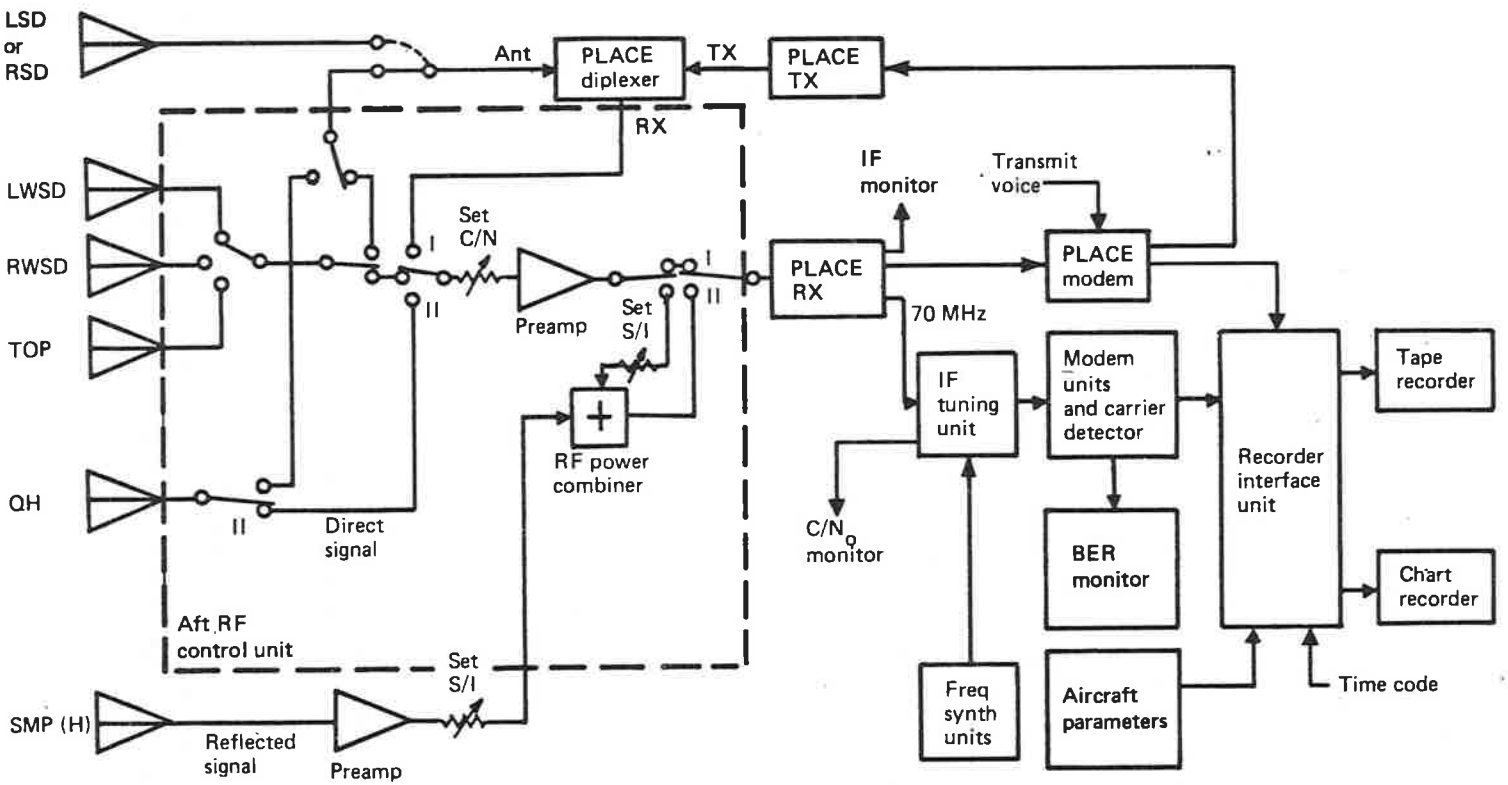

Figure 5-1. Simplified KC-135 Terminal for Modem Evaluation Test

5.2.2.2 Aircraft C/N_0 Measurement – For all modem evaluation tests, the transmission format included a cw carrier at a power level equal to that of other test channels. C/N_0 measurements were therefore made on this channel to infer the C/N_0 on other channels. Frequent independent measurements were made by separate operators at 70- and 10-MHz IF points using an HP 141T spectrum analyzer and HP 312A wave analyzer. These measurements were used to establish and monitor the desired value of the C/N_0 test parameter during flight test conduct.

The cw channel was also processed by an envelope detector in the carrier detector unit. This output was FM recorded for off-line computer analysis to determine C/N_0 and S/I on a more continuous basis in support of the detailed data analysis.

5.2.3 Modem Evaluation Transmission Formats

The principal forward-link transmission formats are given in table 5-1. Uplink signals were transmitted from Rosman at relative power levels such that the L-band downlink channel powers received at the airplane (with modulations applied) would be equal. Special precautions and monitoring techniques ensured this equalization.

Four different voice modems were tested. The test configuration and transmission channel capacity allowed for the simultaneous testing of three voice modems. During the last 2 months of the test program, all four modems were available. Several transmission format options, as indicated in table 5-1, were therefore used for testing the four available modems.

Five digital data demodulators, all utilizing derivatives of phase-shift-keyed signaling, were tested. All digital data demodulators operated on the same PSK downlink test signal, eliminating any uncertainty regarding unequal modulation quality or unequal channel downlink powers. The cw carrier at 1550.6875 MHz was normally the signal used for aircraft operator and carrier detector unit C/N_0 measurements.

The voice/data test mode evaluated performance of the two hybrid modems in their hybrid voice and data (simultaneous) modes. A separate PSK data channel was transmitted for use by the NASA DECPSK demodulator.

During ranging tests, two different ranging modems were evaluated: DOT/TSC digital ranging (in-house DOT/TSC development) and NASA PLACE surveillance and ranging (S&R). The NASA S&R technique was tested on a single-link round-trip basis via the ATS-6 satellite. The DOT/TSC digital ranging modem was tested on a one-way single-link basis, with all measurements made onboard the aircraft and recorded for off-line analysis.

TABLE 5-1. MODEM EVALUATION TRANSMISSION FORMATS

Test mode	Channel frequency, MHz					
	1550.000	1550.075	1550.250	1550.600	1550.675	1550.6875
Voice (1)	–	CW	ANBFM	Hyb 2	Hyb 1	–
Voice (2)	–	CW	ADVM	Hyb 2	ANBFM	–
Voice (3)	–	CW	ANBFM	ADVM	Hyb 1	–
Voice (4)	–	CW	Hyb 2	ADVM	Hyb 1	–
Digital data	–	CW	NBFM	–	PSK	CW
Voice/data	–	CW	Hyb 1 V/D	Hyb 2 V/D	PSK	–
Ranging, NB (1)	CW	S&R	ANBFM	R_N	–	–
Ranging, NB (2)	–	S&R	CW	R_N	PSK	–
Ranging, WB	CW	S&R	ANBFM	R_W	–	–

Legend:

ANBFM:	Adaptive narrowband frequency modulation
ADVM:	Adaptive delta voice modulation
Hyb 1:	Hybrid No. 1, voice-only mode
Hyb 2:	Hybrid No. 2, voice-only mode
Hyb 1 (V/D):	Hybrid No. 1 modem, simultaneous voice and data mode
PSK:	Digital data 1200-bps phase-shift-keyed test signal
NB, WB:	Narrowband, wideband
R_N, R_W:	TSC digital ranging: narrowband, wideband
S&R:	Surveillance and ranging (NASA PLACE).

5.2.4 Modem Evaluation Data Acquisition Summary

Approximately 85 hours of modem evaluation test data (65% Type I, 35% Type II) was acquired over the 7-month period between September 1974 and April 1975.

Modem evaluation test legs were straight-line segments of 23-min duration. The first 3 min of a leg allowed for aircraft turns, antenna selection, and C/N_0 (and S/I, when applicable) setup. Data were acquired during the last 20 min of each leg. Type II tests required an aircraft heading of 110^o relative to the ATS-6 direction at an elevation angle of 15^o. Type I test legs spanned a range of satellite elevation angles between 10^o and 30^o at aircraft headings of 45^o, 135^o, 225^o, and 315^o relative to the satellite direction. Tables 5-2 and 5-3 summarize the Type I and II modem evaluation tests conducted. The tables identify the number of 23-min test legs flown for each type of test.

TABLE 5-2. MODEM EVALUATION DATA ACQUISITION, TYPE I

Date, mo-day-yr	Elevation angle, deg	Number of 20-min runs				
		Voice (no ADVM)	Voice (with ADVM)	Hybrid V/D	Digital data	Ranging[a]
9-24-74	30	1	-	1	1	2
9-26-74	30	5	-	-	5	-
9-30-74	30	4	-	2	2	2
10-24-74	15 - 22	2	-	1	1	-
10-25-74	15	-	-	-	5	1
10-28-74	15 - 17	2	-	-	2	1
11-13-74	12 - 15	-	-	3	1	2
11-14-74	9 - 16	4	-	-	3	-
11-15-74	15 - 17	2	-	-	2	1
11-16-74	9 - 15	4	-	-	1	2
11-19-74	15 - 17	-	-	-	4	-
11-20-74	9	5[b]	-	-	4[b]	2[b]
11-21-74	15 - 17	3	-	1	1	-
1-23-75	8 - 15	4	-	-	1	2
1-24-75	15 - 18	-	-	-	4	-
1-27-75	15	-	-	-	-	1
1-28-75	15 - 22	2	-	1	1	-
1-30-75	8 - 15	4	-	-	1	2
2-24-75	30	-	7	-	3	-
2-26-75	30	-	7	-	1	2
2-27-75	30	-	-	3	-	2
3-25-75	15	-	-	-	1	2
3-27-75	15	-	3[c]	-	-	-
3-28-75	10 - 15	3	-	-	2	-
3-31-75	15	3	-	-	-	-
4-1-75	10 - 17	-	3	1	-	-
4-2-75	10	-	-	-	1	2

[a]Low percentage of success due to erratic modem performance.
[b]Ground test parked at Azores.
[c]No ADVM data.

TABLE 5-3. MODEM EVALUATION DATA ACQUISITION, TYPE II

Date, mo-day-yr	Elevation angle, deg	Number of 20-min runs				
		Voice (no ADVM)	Voice (with ADVM)	Hybrid V/D	Digital data	Ranging[a]
10-24-74	15	3[b]	-	-	-	-
10-25-74	15	-	-	-	3[b]	1[b]
10-28-74	15	3	-	-	-	-
11-13-74	15	-	-	-	4	-
11-14-74	15	-	-	-	3	-
11-15-74	15	3	-	-	-	-
11-16-74	15	-	-	-	3	-
11-19-74	15	-	-	-	4	2
11-21-74	15	2	-	-	-	-
1-23-75	15	-	-	-	2	-
1-24-75	15	-	-	-	4	2
1-27-75	15	3	-	-	-	-
1-28-75	15	3	-	-	-	-
1-30-75	15	-	-	-	3	-
3-25-75	15	-	-	3	3	-
3-27-75	15	-	2[c]	-	1	1
3-28-75	15	1	-	-	2	1
3-31-75	15	2	-	-	2	1
4-1-75	15	-	3	-	-	-
4-2-75	15	1	-	1	1	-

[a]Erratic performance of modem.
[b]Questionable data due to RF power combiner fault.
[c]No ADVM data.

5.3 DATA REDUCTION AND ANALYSIS PROCEDURES FOR MODEM EVALUATION TESTS

Figure 5-2 diagrams the flow of test data for the modem evaluation experiments from the collection phase on the KC-135 through computation. For each of the voice, digital data, and ranging tests, analog instrumentation tapes were returned to Seattle, digitized, and formatted onto seven-track digital tape and processed by a general-purpose computer. Also, strip charts and logs constructed on the airplane were collated to aid in interpreting the processed results.

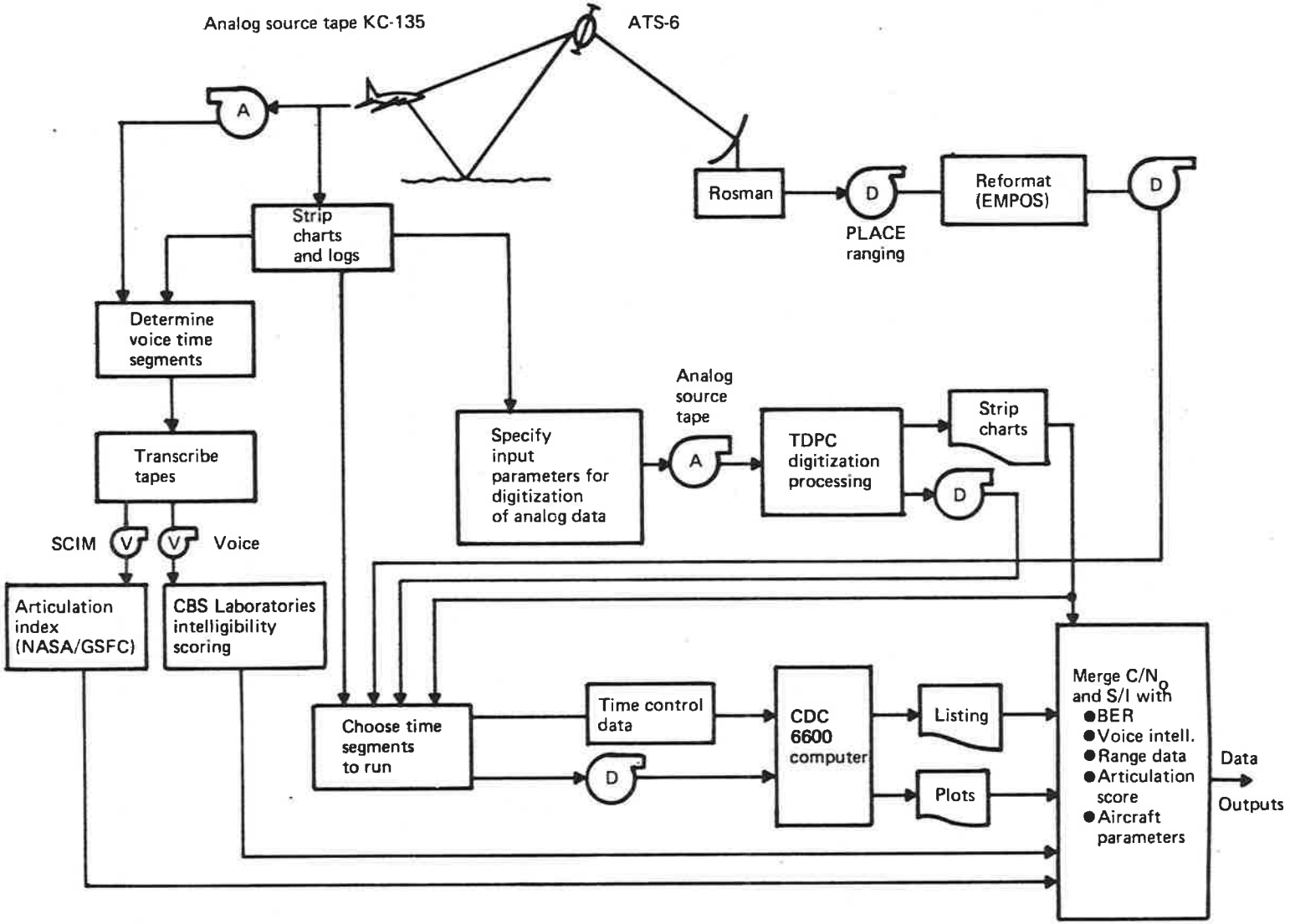

Figure 5-2. Modem Evaluation DR&A System Block Diagram

5.3.1 Determination of C/N_0 and S/I

The carrier-to-noise density ratio, C/N_0, and direct-to-indirect signal ratio, S/I, are the two primary variables in the modem experiments. An automated procedure to determine these channel parameters was devised that was common to the three modem evaluation tests. On the KC-135, linear envelope detection of an unmodulated L-band carrier was performed continually and the detector output was recorded on instrumentation tape. Careful channel setup ensured that the power contained in this probe signal was equal to that of the modulated carriers under test; thus measurements on the probe signal yielded reliable estimates of the channel conditions for nearby channels.

It can be shown (sec. 7., vol. IV) that the low-pass spectrum of the envelope detector output can be expanded in terms of the input RF spectrum, which in turn provides the relative signal, multipath, and noise levels. The contributions of each are thus revealed in the frequency domain, whereas time-domain analysis does not uniquely yield C/N_0 and S/I.

To perform the spectra analysis, the detector output was sampled 1024 times at a 2-kHz rate every 15 sec throughout the test. These samples were then input to a discrete Fourier transform routine, which supplied smoothed spectral estimates every 15 sec. Relating these spectral estimates back to theoretical dependence on C/N_0 and S/I then allowed these parameters to be determined at regular intervals. The accuracy ascribed to these parameter values is ± 0.5 dB for C/N_0 and ± 1 dB for S/I.

In addition, supplemental C/N_0 measurements were performed onboard the KC-135 during the test using a spectrum analyzer.

5.3.2 Voice Data Reduction Procedures

Analog voice tapes were transcribed onto 1/4-in. audio tape with annotative material for use by CBS Laboratories in scoring word intelligibility. Session reports were returned to Boeing for compilation with other test data and documentation. Also, a small number of SCIM signal transmissions were transcribed for computer processing by NASA.

5.3.3 Digital Data Reduction Procedures

For each of five modems, the output bit stream was packed on digital tape and analyzed in the CDC 6600. Error analysis of each track was performed by synchronizing a replica PN sequence to the received sequence. This done, tabulation of the error statistics was performed for each channel. Primary statistics were number of bits processed, number of errors, histograms of the spacing between errors, and histograms of the number of errors per contiguous 24-bit block. Average error probability

was provided by the former two quantities, while information on the channel's memory structure was provided by the two histograms. Channel signal-to-noise density ratio and direct-to-indirect signal ratio were obtained within the same computing run, and the date was compiled manually.

5.3.4 Ranging Data Reduction Procedures

For both TSC ranging and NASA ranging tests, the reformatted tapes were read to construct a range versus time array. An initial fit to the data was performed and obvious "blunder" errors were censored (those having greater than 10-km error). A second least-squares-curve fit with a second-order polynomial was then performed, and the deviations from this reconstructed trajectory were taken as the measurement error. The array of errors was then processed to yield the rms measurement error, and chi-squared goodness-of-fit tests for a normal error distribution were performed.

It is noted that this process determines error statistics relative to a nominal trajectory fit to the data and not relative to any absolute range measurement. No adequate means of providing the range calibrations and signal synchronization necessary for absolute ranging was available.

5.4 VOICE MODEM EVALUATION TEST RESULTS

Four distinct voice modulation techniques were evaluated for a variety of aeronautical channel conditions. Performance was measured primarily by word intelligibility scores achieved using lists of phonetically balanced words. Variables in the tests included C/N_0, the ratio of unmodulated carrier power to noise power density (in dB-Hz), and S/I, the ratio of direct signal power to total scattered multipath power (in dB).

5.4.1 Voice Modems Tested

The four voice modems tested are referred to as adaptive narrowband frequency modulation (ANBFM), Hybrid No. 1 (Q-M/PSK), Hybrid No. 2 (PDM/PSK), and adaptive delta voice modulation (ADVM). The two hybrid modems may operate in either voice-only, data-only, or simultaneous voice/data modes. Characteristics of each are provided in volume VI.

5.4.2 Performance Evaluation Method

The most useful measure of performance for speech transmissions in the ATC environment is the achieved intelligibility. Thus, the voice experiments measured the percent intelligibility associated with unrelated words for different test conditions.

To perform these tests, phonetically balanced word lists were recorded on 1/4 in. tape by CBS Laboratories using alternate male and female speakers. A single intelligibility test involved four separate speakers, each reading two 50-word lists, making a 400-word test. List scrambling was used to minimize learning by the listener panel. The words were spoken at approximately 2.5-sec intervals, and the total test duration, over which conditions were maintained constant, was roughly 22 min. Figure 5-3 illustrates the tape format for all sessions.

The various demodulator outputs were recorded on instrumentation tape on the KC-135. These tapes were returned to Seattle, and the three separate voice tracks were transcribed, along with identification, onto 1/4-in. audio tape that was forwarded to CBS Laboratories for evaluation. The carrier detector signal was digitized for analysis of C/N_0 and S/I channel conditions. This procedure, common to all experiments, is described in section 5.3. For each test condition and each modem under evaluation, CBS provided mean intelligibility and various other statistics. A trained listener panel of 10 persons was employed in the evaluations.

5.4.3 Type I Test Results, Voice-Only Mode

Test results for Type I voice-only modes are summarized for each modem in figure 5-4. The curves shown are actually "best fits" to experimental data obtained over the several months of testing. It is observed that at low C/N_0 values; e.g., 40 to 43 dB-Hz, the Hybrid No. 1 modem performs consistently best, followed by ADVM (analog), the Hybrid No. 2 modem, and ANBFM. The latter three exhibit a rather dramatic decrease in intelligibility with decreasing C/N_0, while the Hybrid No. 1 modem degradation is "softer." This relative ranking is preserved at higher signal-to-noise ratios (up to 49 dB-Hz) except that ADVM seems to out perform Hybrid No. 1 slightly at these higher C/N_0 values. This might be expected, since at high C/N_0, where the channel bit-error rate is small, the delta modulation performance is limited primarily by the quantization distortion. In any case, the relative difference, if any, between the two methods at high C/N_0 is small compared with the sampling uncertainty, and both methods provide high-quality speech performance in this range.

An observation not apparent in the plots of PB word score is the relative intelligibility of male and female speakers. CBS results are segregated to show scores for both sexes, and it is readily apparent that male speakers were more easily understood. Relative scores were a few percent better on the average at high C/N_0 values and typically 6% to 10% better for poorer signal-to-noise ratios. It is shown in volume VI that these differences are statistically significant in relation to the experimental errors and were applicable to all modems tested.

It is suggested that the greater intelligibility for male speakers is due to the audio band-limiting involved in each modem. Since female speech spectra have greater high-frequency energy, band-limiting could be expected to induce a greater loss in speech intelligibility for females than for males.

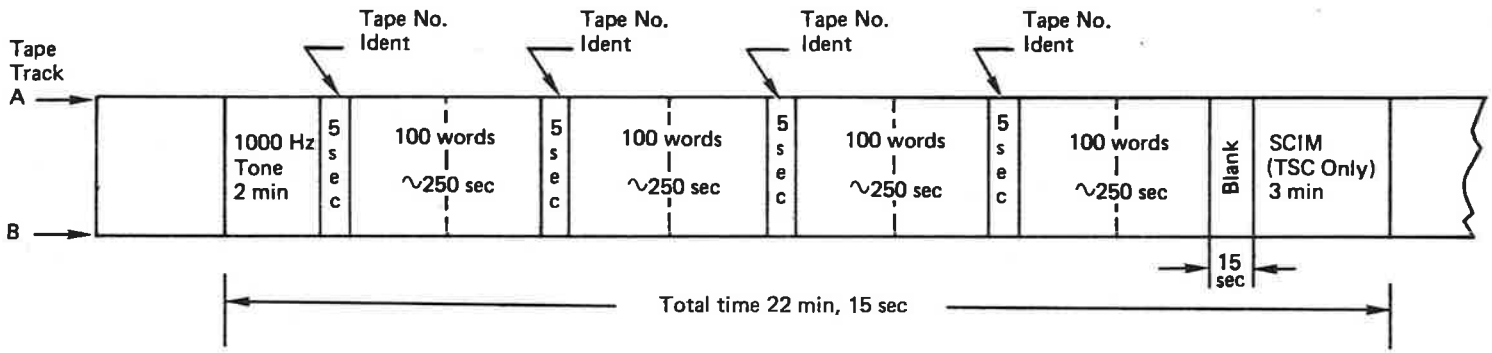

Major Parameters

1) Record Speed: 7 1/2 ips (2 tracks, forward direction)
2) Record Level: 0 VU, average
3) Tape Type: 1/4 - inch, Scotch 260
4) Tape Capacity: 1200 feet, 30 min at 7 1/2 ips, 2 tracks one direction
5) Interpause Period: 2.5 sec (time between start of each word)
6) No. of words per track: 400 uniquely scrambled PB words (8 PB 50-word lists)
7) No. of speakers per track: 4 speakers (100 words each)
8) Total record time: (a) Without SCIM: 19.0 min
   (b) With SCIM (TSC Only): 22 min, 15 sec.

Figure 5-3. DOT/TSC ATS-6 Voice Tape Composition

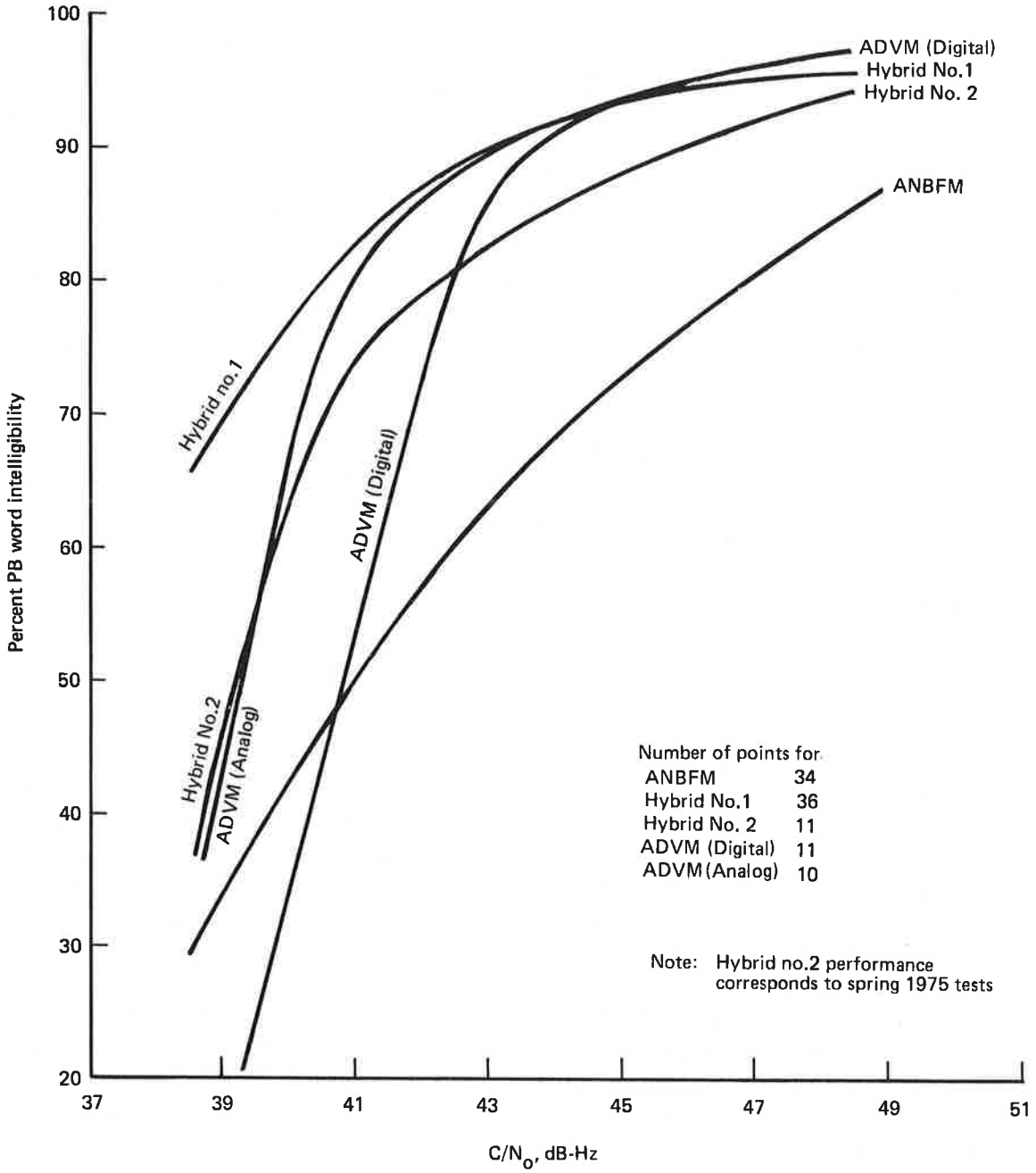

Figure 5-4. Summary Comparison of Voice Modem Performance, Type I Tests

5.4.4 Type II Test Results, Voice-Only Mode

Test setup, conduct, and data reduction procedures were exactly as for Type I tests, except that a higher level of scattered signal was injected into the receiver. The measured S/I (direct-to-indirect power ratio) ranged from 3 dB to about 15 dB, while C/N_o was varied over the 40 to 50 dB-Hz range.

Figure 5-5 compiles the mean PB word scores achieved by the Hybrid No. 1 modem versus C/N_o, with the number associated with each point denoting the measured S/I to the nearest decibel. Type Type II scores agree well, both in absolute and relative performance, with the Type I scores for all values of S/I. To emphasize the relatively large insensitivity to multipath level, the best-fit Type I performance curve has been overlaid on figure 5-5. This same finding has held for the Hybrid No. 2, the ANBFM, and the ADVM modems, although the amount of testing with the latter was less.

Thus, whereas the performance of digital data and ranging systems can be dramatically reduced by relative multipath levels of say -6 dB, the intelligibility of analog voice techniques is not visibly degraded for S/I as low as 3 dB. Intuitive arguments are offered in volume VI for this phenomenon. Basically, we believe the immunity of intelligibility to multipath is due to the demodulated multipath noise being in the subaudio frequency range, as well as to the known fact that fading which is short term relative to phoneme time durations does not inhibit perception radically.

5.4.5 Hybrid Modem Performance in Combined Voice and Data Mode

Figures 5-6 and 5-7 show performance measured for the Hybrid No. 1 and 2 modems when operated in the hybrid mode, i.e., speech simultaneous with 1200-bps data. By comparing performance with figure 5-4, it is observed the presence of data modulation degrades performance at least 3 dB. Since the data and speech carriers are in phase quadrature for each modem, the potential for cochannel crosstalk exists if carrier phase tracking is imperfect. If this factor is ignored, however, a 3-dB degradation can be predicted for Hybrid No. 2 since 50-50 voice/data power sharing is in effect in the hybrid mode.

For Hybrid No. 1, the relative difference to be expected is less clear. An approximation may be gained by noting the rms phase modulation in voice-only cases is 58^o, whereas it is set at about 40^o for the voice/data mode. In terms of demodulated speech power, the relative difference is then about 2.4 dB. Since both modems have additional degradation due to crosstalk, it is not surprising to find the hybrid mode requiring at least 3 dB greater *total* C/N_o for equal speech intelligibility.

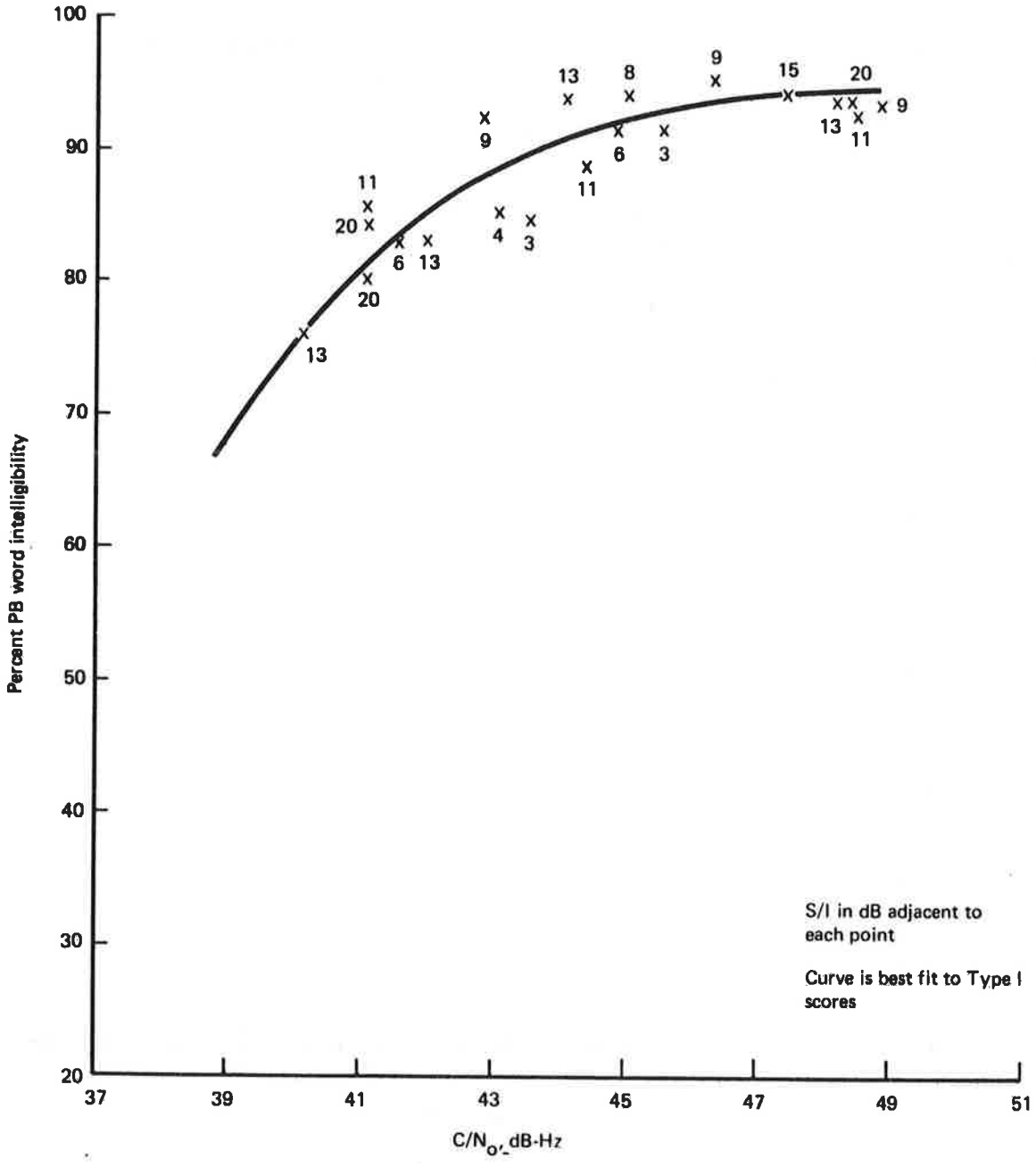

Figure 5-5. H1 Modem Voice Intelligibility, Voice Only Mode, Type II Tests, All Test Series

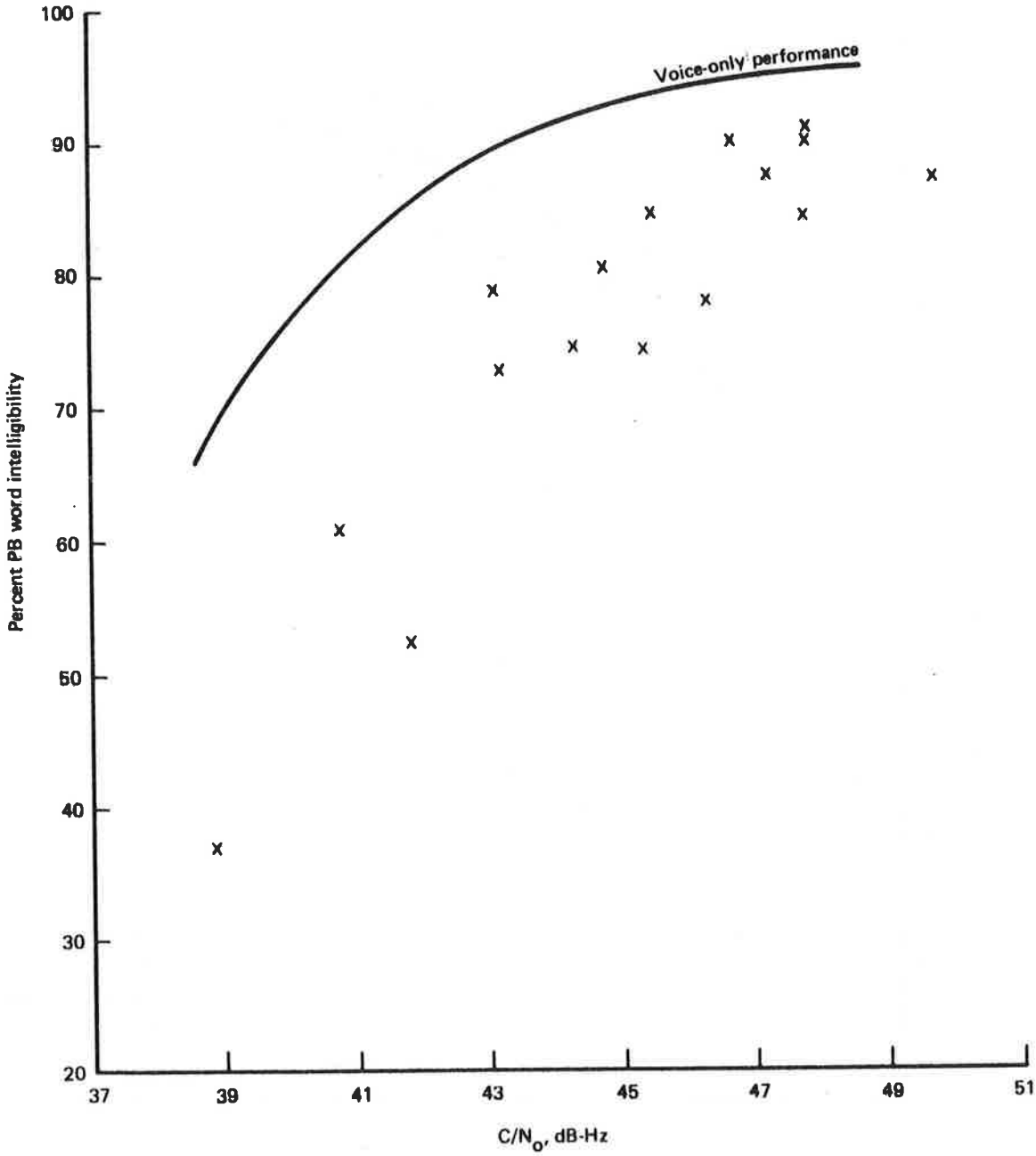

Figure 5-6. H1 Modem Voice Intelligibility, Hybrid Mode, All Test Series

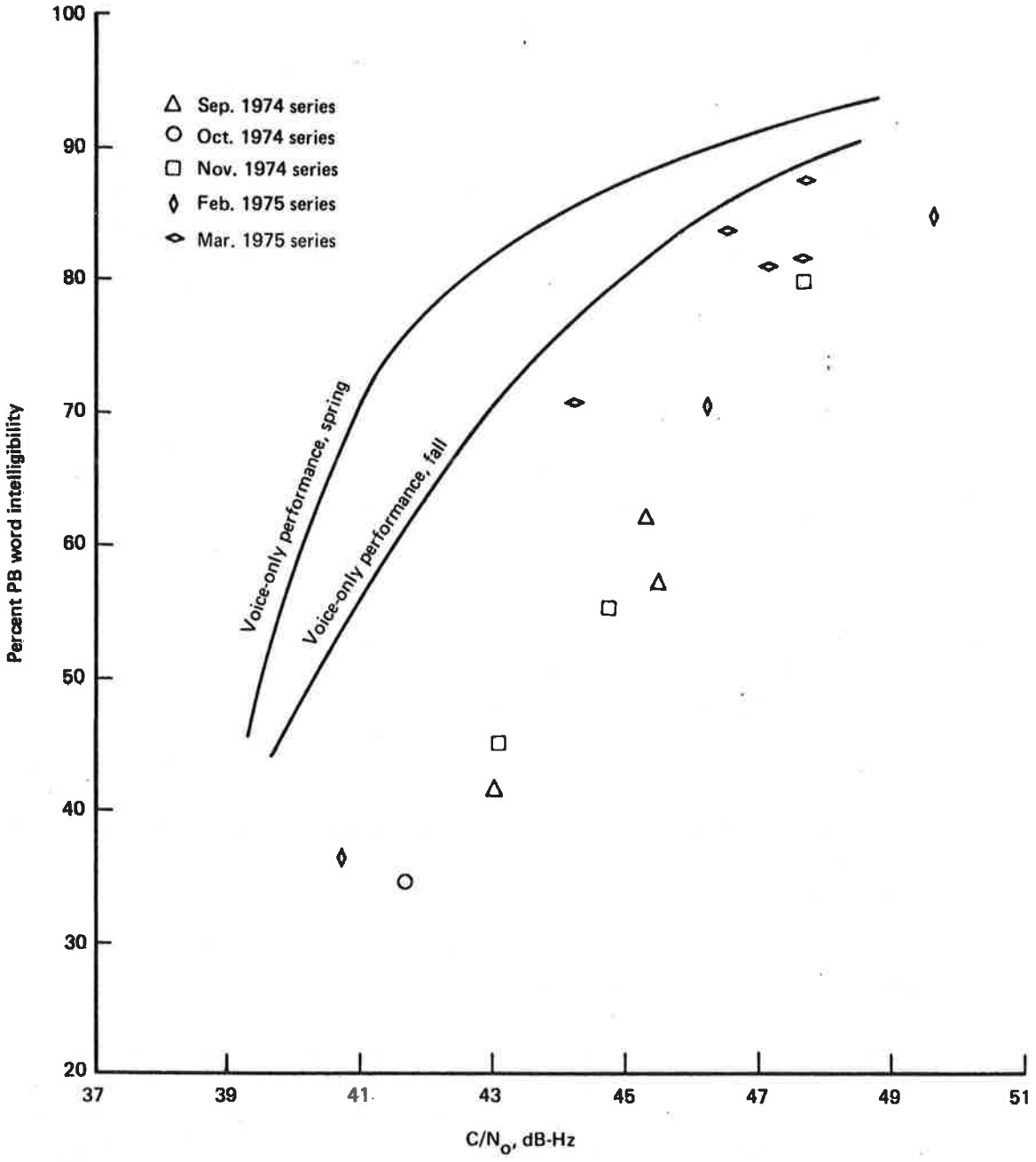

Figure 5-7. H2 Modem Voice Intelligibility, Hybrid Mode, All Test Series

5.4.6 Voice Test Conclusions

After analyzing intelligibility scores for the four speech modems, the following major conclusions can be drawn.

a. Three modems exceeded 70% PB word intelligibility at 43 dB-Hz: Hybrid No. 1 (Q-M/PSK), Hybrid No. 2 (PDM/PSK), and the adaptive delta voice modem (ADVM). The ANBFM technique failed to achieve this performance, though not by far. One modem, the Hybrid No. 1, achieved PB word intelligibility in excess of 70% at 40 dB-Hz. Over the range of 40 to 48 dB-Hz, a relative ranking of modems would place Hybrid No. 1 first, followed by ADVM, Hybrid No. 2, and ANBFM. It should be emphasized that the evaluations pertain to word intelligibility only and do not explicitly include pleasantness of sound, synchronization time, dynamic range, etc. Also, the two male speakers were consistently more intelligible than the two female speakers, probably due to audio band limiting effects.

b. No apparent degradation in word intelligibility was observed in spite of relatively high multipath levels. Results for S/I = 3 dB showed little difference from the no-multipath performances for all modems tested. This is believed due to the natural waveform redundancy of speech and the fact that the distortion due to multipath is largely subaudio.

c. When operated in the hybrid voice/data mode, both the Hybrid No. 1 and 2 modems required roughly 3 dB additional C/N_0 to achieve the same intelligibility registered in the voice-only mode, as expected.

d. Though less costly to conduct, SCIM evaluations do not appear to provide a universal performance evaluation since the relation between SCIM score and word intelligibility is modem dependent. Further discussion and supporting data are found in appendix A of volume VI.

5.5 DIGITAL DATA MODEM TEST RESULTS

This section summarizes results obtained on the performance of five PSK data modems, operating at 1200 bps in various aeronautical satellite channel conditions. The modems represented different implementations of differentially encoded, coherently detected phase-shift keying (DECPSK) and differentially coherent phase-shift keying (DPSK). Tests were conducted in the Rosman/ATS-6/KC-135 link configuration. Reception was with representative operational aircraft antennas (Type I tests) at angles ranging from 12° to 40° and with a multipath-contaminated channel (Type II tests) at an elevation angle of 15°.

5.5.1 Digital Data Modems Tested

Hybrid No. 1: This modem implements DECPSK. In the data-only mode, detection is performed with a Costas-type (B_L = 130 Hz) demodulator and baseband matched filtering. Coherent AGC is employed and IF bandwidths exceed 30 kHz in all cases. The unit can operate in the combined voice/data mode, for which demodulation is accomplished with a narrowband second order phase-lock loop tracking a residual carrier. Bell Aerospace Company manufactured the modem under contract to DOT/TSC.

Hybrid No. 2: This unit was developed by Magnavox Research Laboratories under DOT/TSC contract. DECPSK is again the data modulation and detection strategy. In the data-only mode, the modem uses Costas loop ($B_L \simeq$ 150 Hz) demodulation and baseband matched filtering. Coherent AGC is employed and RF/IF bandwidths exceed 50 kHz. This unit may also operate in a hybrid voice/data mode by placing one-half the signal power in a PDM speech signal in phase quadrature to the data carrier.

NASA DECPSK: This modem also performs DECPSK transmission with a Costas-type demodulator. The predetection filter bandwidth is 15 kHz and $B_L \simeq$ 450 Hz . Operation is data-only at 1200 bps. The unit was developed for NASA by Bell Aerospace Company as part of the PLACE program.

FAA CPSK: The fourth modem performing DECPSK was developed for DOT/FAA by Philco-Ford Corporation. The modem operates at either 1200 or 2400 bps with a Costas demodulator (B_L = 210 Hz) . The signal processing is largely digital, including the carrier and bit timing loops and the integrate-and-dump detector. Coherent AGC is used and RF/IF bandwidths are sufficiently large to avoid band-limiting distortion.

FAA DPSK: This unit represents the only tested version of DPSK. Detection requires carrier phase stability over only two-bit intervals. The center frequency is continually estimated by a quadricorrelator automatic frequency control circuit, and a signal-determined AGC is used. Philco-Ford developed the modem for the FAA ATS-5 experiments. The unit employs largely digital signal processing.

All of the modems are devoid of nonlinear processing effects such as hard-limiting at IF, and intersymbol interference due to band-limiting may be ignored for all 1200-bps data rates tested here.

5.5.2 Test Methodology

For all modems and test conditions, a maximal length 2047-bit sequence was used as the test pattern. This provided a signal having adequate randomness properties, which was easy to replicate and synchronize in a general-purpose computer for error analyses. During hybrid mode tests (voice and data simultaneous), the same test sequence was used, and PB word list tapes were input to the respective modulator audio inputs.

Since all modems operate on versions of PSK signaling, a single data signal was sufficient for transmission from Rosman. This eliminates the uncertainty arising from power balance of several PSK carriers and minimizes intermodulation effects.

L-band signals received on the KC-135 were detected by the five modems. Binary outputs were recorded on instrumentation tape and analyzed as described in section 5.3.

5.5.3 Type I Test BER Performance, Data-Only Mode

Test results for all Type I test series are presented in figures 5-8 through 5-12 for the Hybrid No. 1, Hybrid No. 2, NASA, FAA CPSK, and FAA DPSK modems, respectively. The reference theoretical curve's appropriate additive Gaussian noise environments are given by

$$P_e = \text{erfc}\left[(CT/N_o)^{1/2}\right]\left(1 - \tfrac{1}{2}\,\text{erfc}\left[(CT/N_o)^{1/2}\right]\right) \quad \text{DECPSK}$$

$$= \tfrac{1}{2}\exp\left[-(CT/N_o)\right] \quad \text{DPSK}.$$

In these expressions, T is the bit duration and C/N_o is the total signal-to-single-sided-noise-power density ratio. Also

$$\text{erfc}\,(x) = \left[2/(\pi)^{1/2}\right]\int_x^\infty e^{-Z^2}\,dZ\,.$$

All data points represent the recording of at least 10 error events, except as noted for some points with very low error probability. Also, some intervals were recorded in which no errors were observed. This data is plotted at $P_e = 10^{-6}$, with the number of bits processed noted.

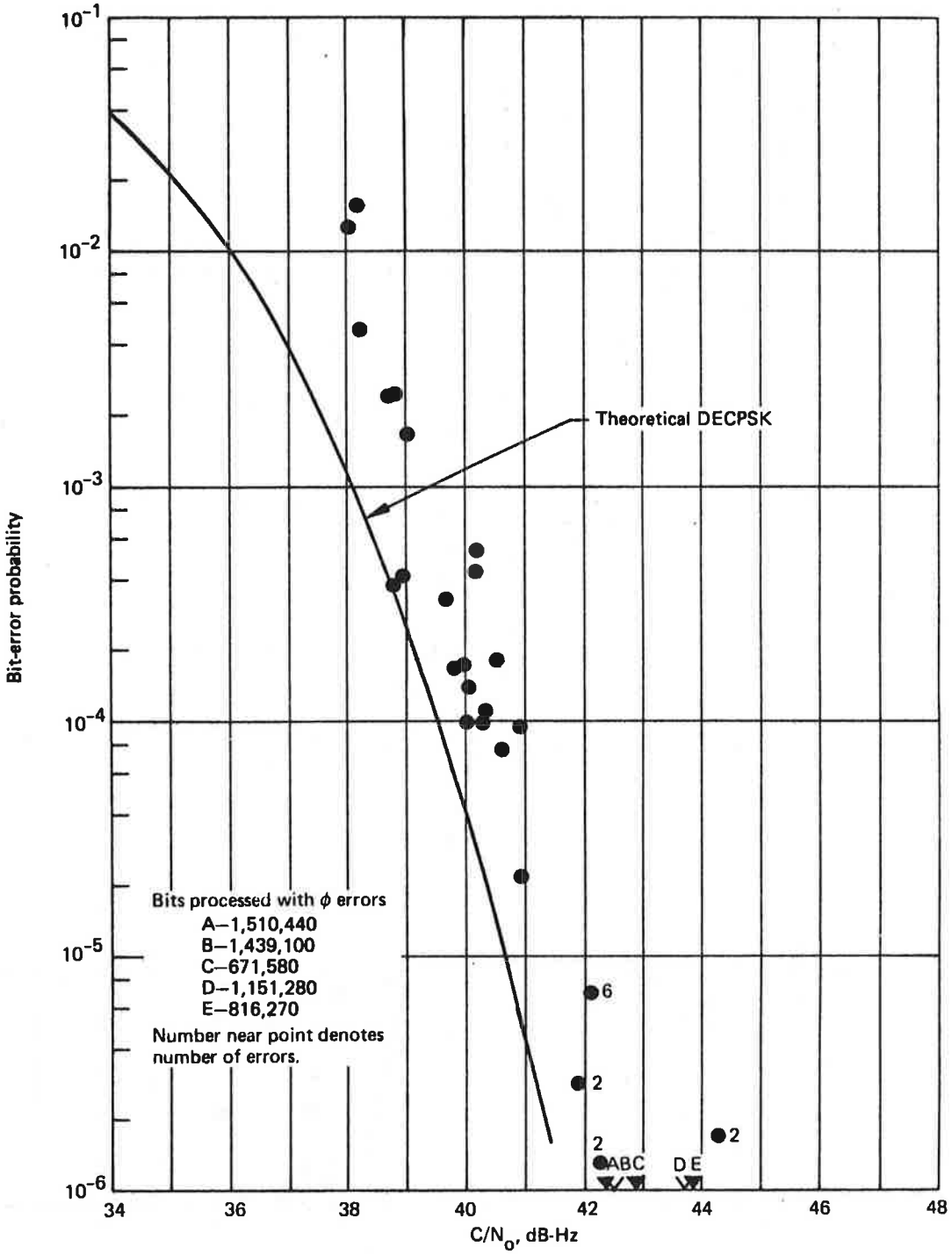

Figure 5-8. Bit Error Rate Performance of Hybrid No. 1 DECPSK Demodulator, 1200 bit/s, Type I Tests

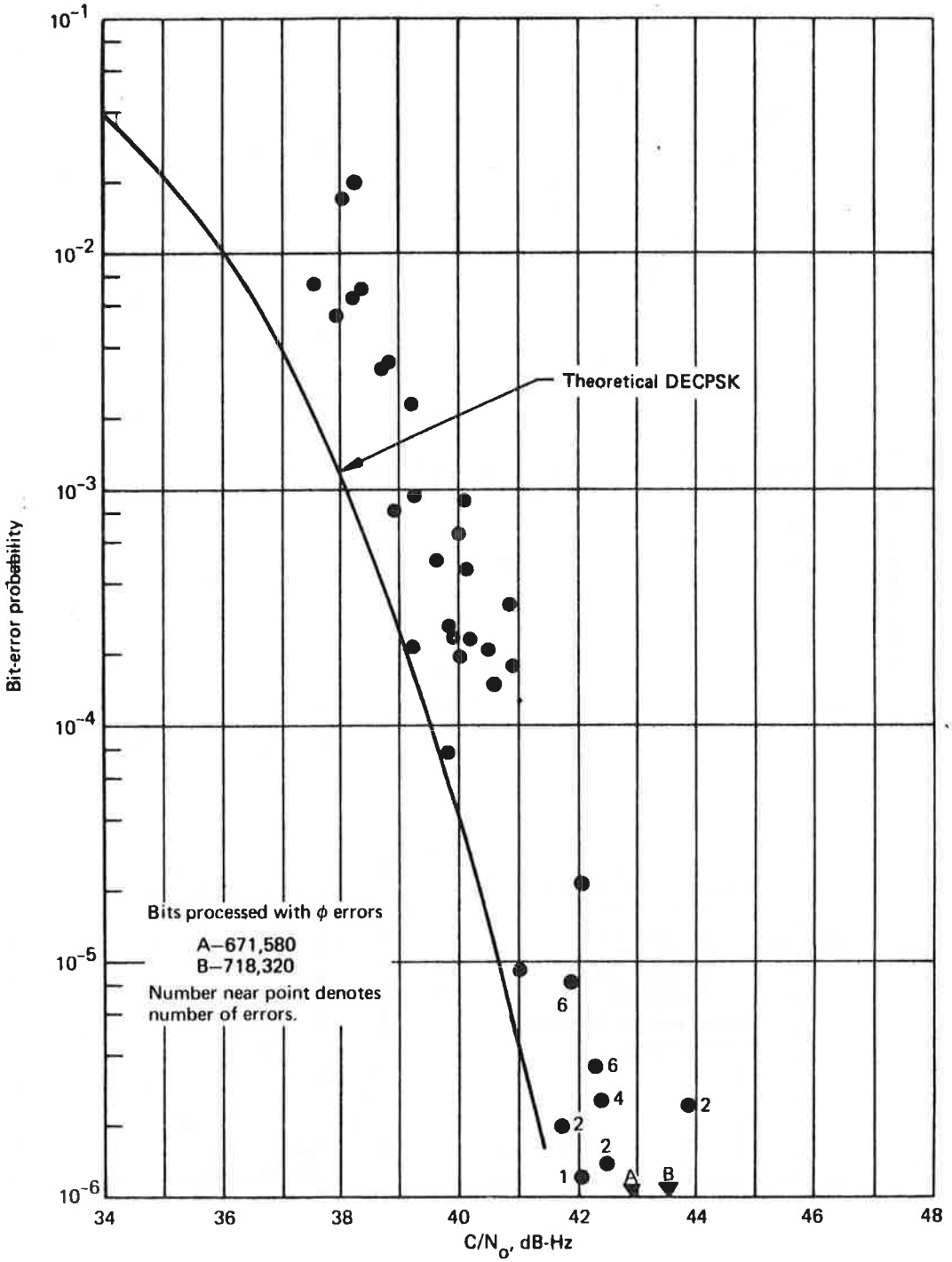

Figure 5-9. Bit Error Rate Performance of Hybrid No. 2 DECPSK Demodulator, 1200 bit/s, Type I Tests

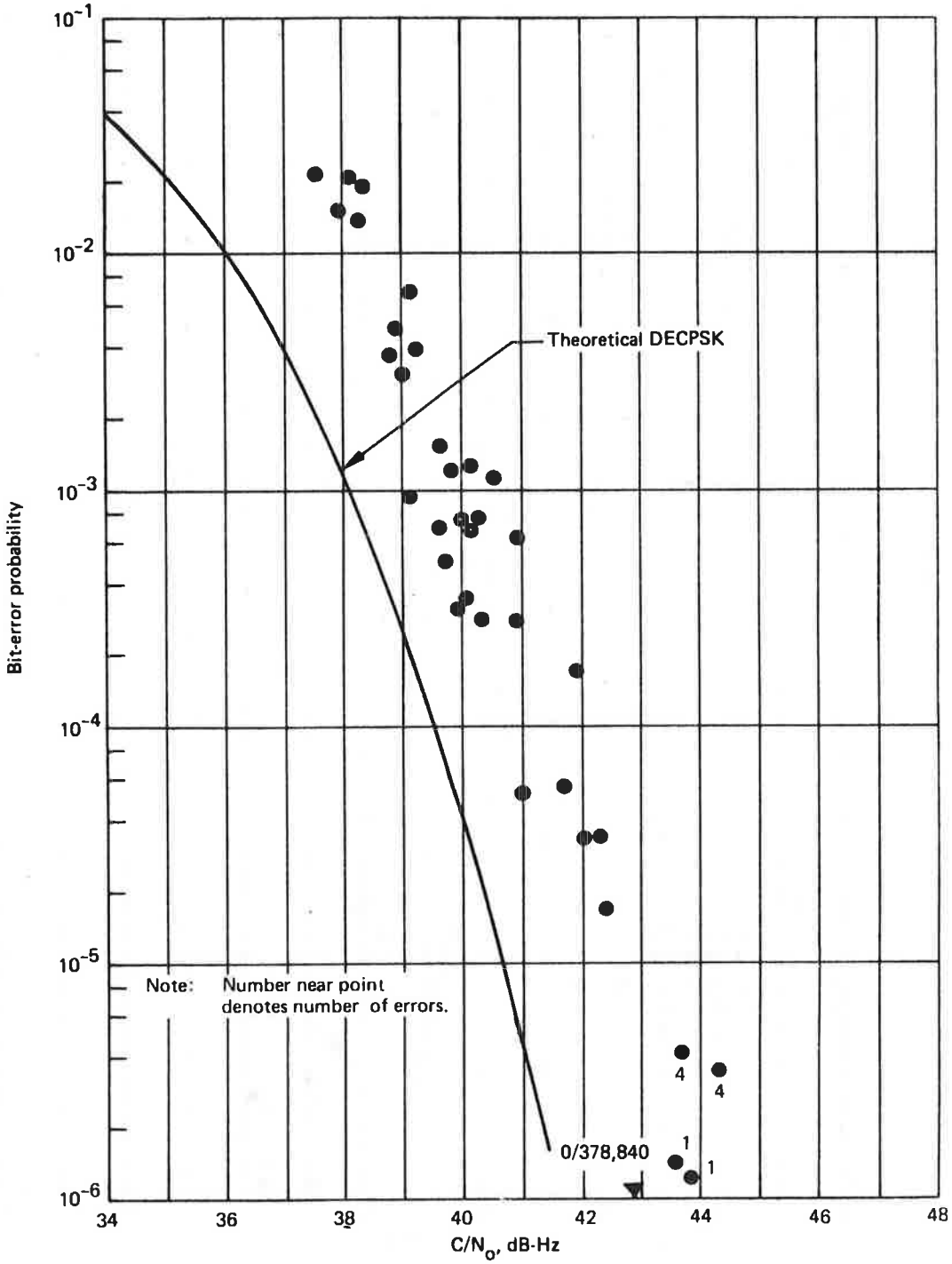

Figure 5-10. Bit Error Rate Performance of NASA DECPSK Demodulator, 1200 bit/s, Type I Tests

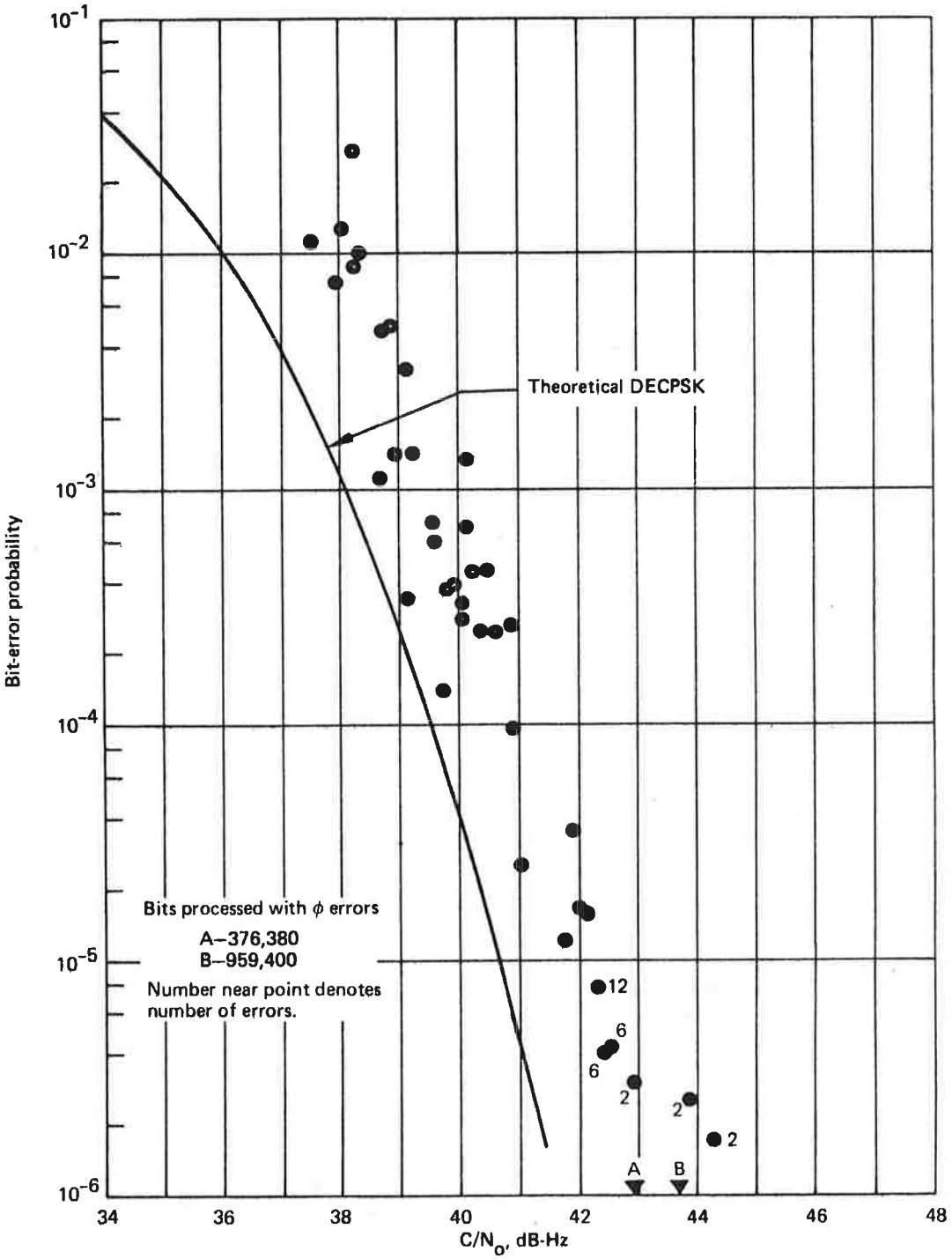

Figure 5-11. Bit Error Rate Performance of FAA CPSK Demodulator, (DECPSK Mode), 1200 bit/s, Type I Tests

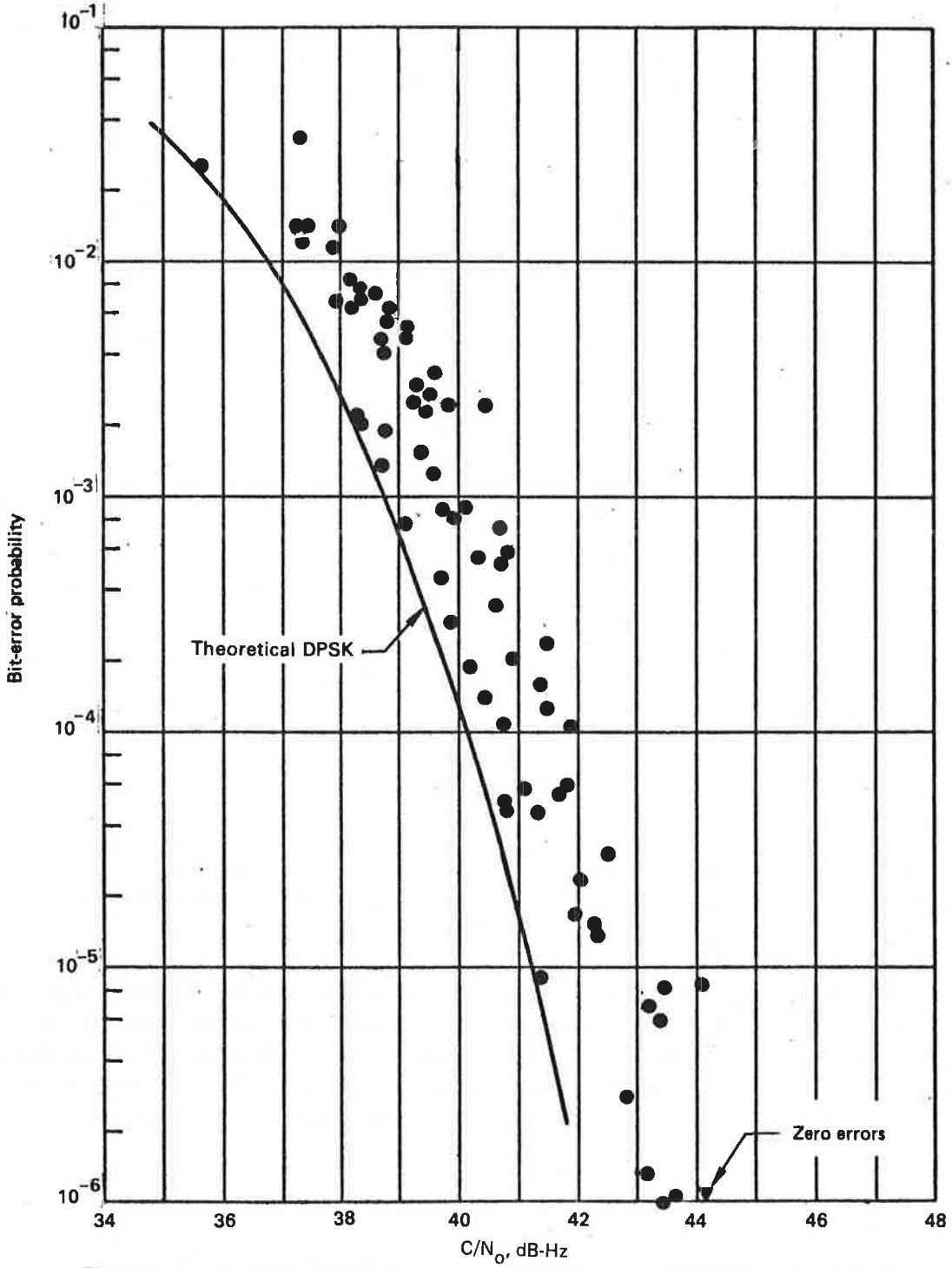

Figure 5-12. Bit Error Rate Performance of DPSK Modem, 1200 bit/s, FAA DPSK Demodulator, Type I Tests

All modems exhibited the exponential dependence on signal-to-noise ratio expected for non-fading channels. Relative to the respective theoretical performance, the modems exhibited the following inefficiencies at an error probability of 10^{-4}:

Hybrid No. 1	0.9 dB
Hybrid No. 2	1.2 dB
NASA DECPSK	1.9 dB
FAA CPSK (DECPSK mode)	1.4 dB
FAA DPSK	1.2 dB[1].

These inefficiencies can be attributed to implementation losses, such as nonideal matched filtering, and carrier and bit synchronization jitter.

Note also that at 43 dB-Hz, each modem meets the current AEROSAT system error rate specification of 1×10^{-5} or less. The NASA DECPSK and the FAA DPSK modems barely meet the specification, while the others exceed the specification with a margin of at least 1 dB.

Since the error probability performance exhibits no divergence from the theoretical non-fading performance as C/N_0 increases, we may conclude there is no appreciable multipath fading phenomenon for the Type I tests. By inference from results of the next section, we may conclude the S/I achieved by the antenna system exceeds about 15 dB. This conclusion is confirmed by results of the antenna tests, which were designed to explicitly measure S/I. The top-left-right slot-dipole system consistently showed $S/I > 15$ dB .

5.5.4 Type II Test BER Performance, Data-Only Mode

Results of Type II test intervals are now presented. In contrast to the Type I tests, a controllable level of multipath was injected into the received signal composite. Thus, modem performance was determined as a function of S/I as well as C/N_0.

To minimize experiment variables, all tests were conducted at a common elevation angle: 15°. With the aircraft altitude kept in the vicinity of 31,000 ft, the delay between direct and specular returns is 16.3 μsec. This represents only a small fraction of the total bit interval (833 μsec). At this elevation angle, multipath delay spread (minus 10-dB value) is approximately 4 μsec. Thus, for all practical purposes, the intersymbol interference due to multipath is of negligible impact.

---

[1] Relative to DPSK theoretical, which is about 0.6 dB less efficient than DECPSK at 10^{-4} error probability.

Commensurate with the scattering theory described and verified in volume V, the channel may then be modeled as having an undistorted direct-path signal, plus a signal passed through a linear, time-varying channel with complex Gaussian statistics, plus additive receiver noise. Presentation of the DPSK results utilizes an analysis of this channel model that accounts for phase decorrelation due to nonzero Doppler bandwidth (ref. 5-1). This model was well verified in ATS-5 test results for DPSK (ref. 5-2) and is used again here.

The bit-error probability formulation for DECPSK is less concise, since performance now critically depends on the behavior of the coherent reference loop. The simplest treatment is to assume that the carrier phase tracking loop estimates the composite signal phase perfectly. By again assuming that fading is slow over a bit interval, numerical integration can easily provide error probability versus C/N_o and S/I.

Perfect tracking of the composite channel phase implies a loop bandwidth much greater than the multipath Doppler bandwidth. Increasing B_L subjects the loop to additional noise jitter and eventual threshold phenomena. An intuitive approach presented in reference 5-3 models the detection performance for B_L on the order of the fading process bandwidth. A parameter γ is defined as

$$\gamma = \frac{B_L}{B_F + B_L} ,$$

so that $\gamma \simeq 0$ indicates that only the direct signal phase is estimated, whereas $\gamma \simeq 1$ indicates perfect composite phase is in effect, again ignoring noise effects. If we assume $B_F = 50$ Hz , typical of the 15^o elevation conditions,

$$\gamma \geq \frac{130}{180} = 0.72 ,$$

since all modems have tracking loop bandwidths exceeding 130 Hz. Thus, to present Type II test results, we use curves for $\gamma = 0.75$ in reference 5-3 as a common standard. The performance is not dramatically different from the perfect estimate case except at very large C/N_o. To account for the error-rate magnification due to differential decoding, the error probability has been scaled by 2 as an approximation.

Figures 5-13 through 5-17 present the measured bit-error rate for each modem for all Type II tests. As for Type I tests, those intervals having less than 10 errors are noted, and intervals having no observed errors are also tagged.

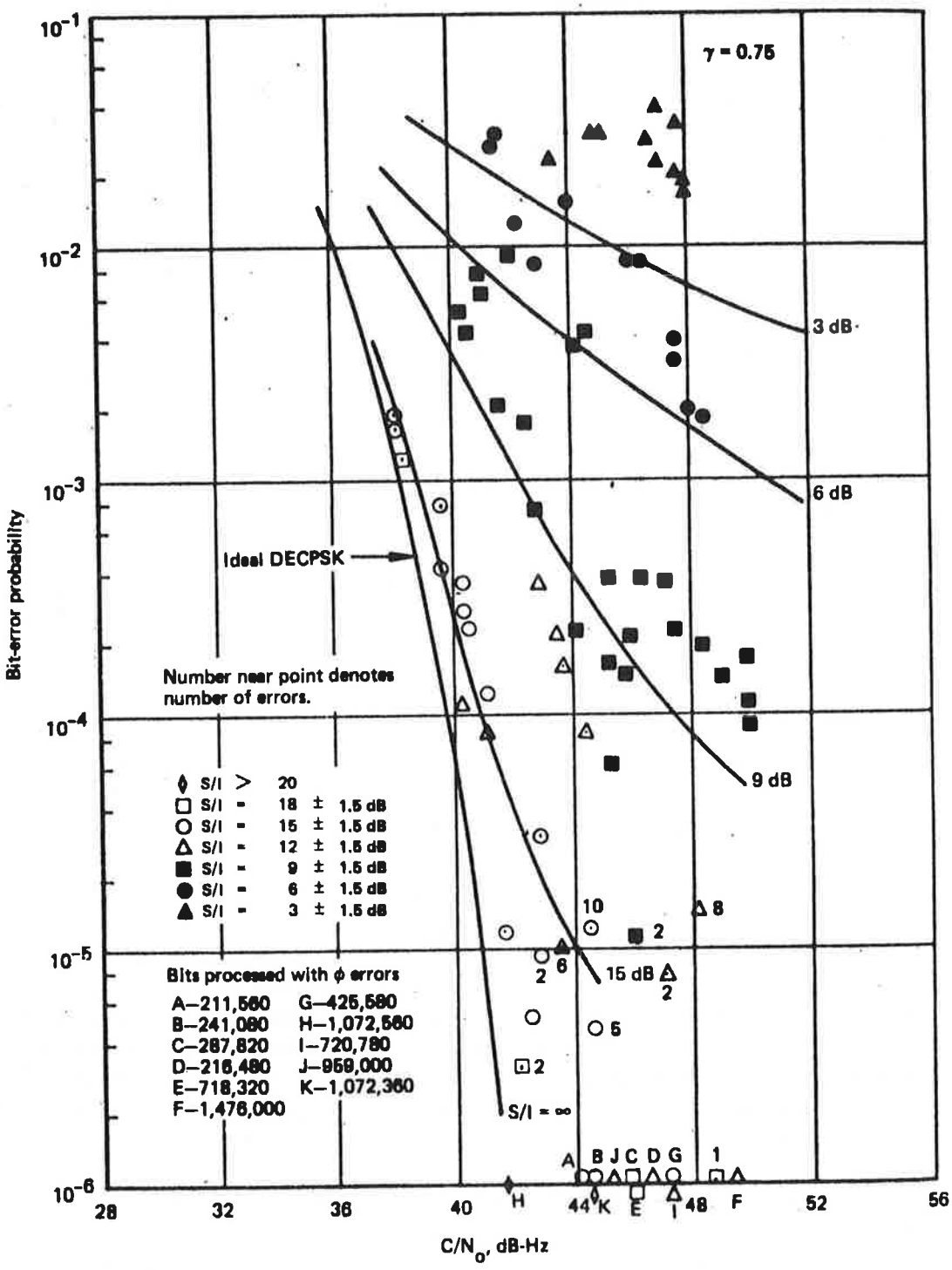

Figure 5-13. Bit Error Rate Performance of Hybrid No. 1 DECPSK Demodulator, 1200 bit/s, Type II Tests

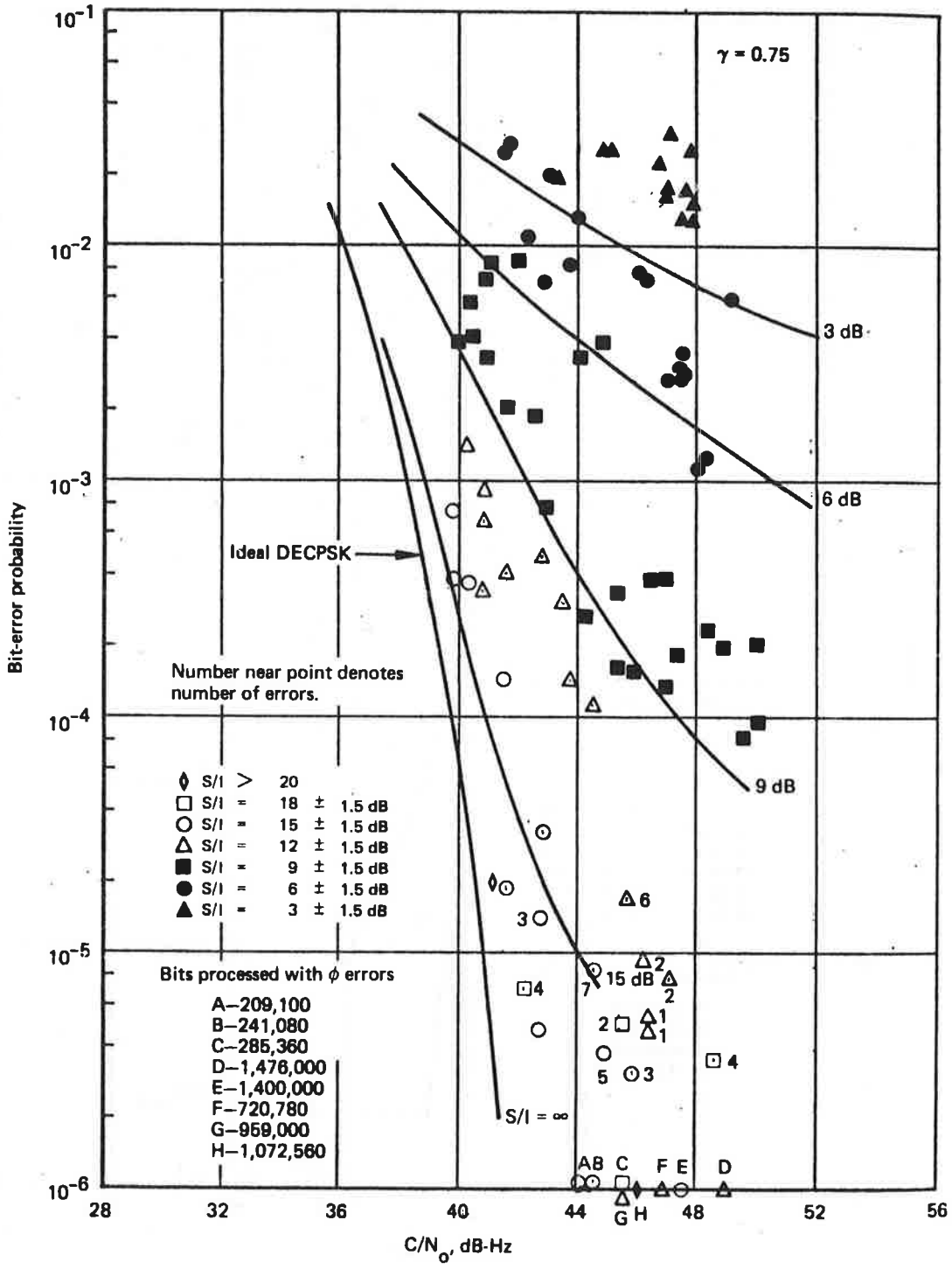

Figure 5-14. Bit Error Rate Performance of Hybrid No. 2 DECPSK Demodulator, 1200 bit/s, Type II Tests

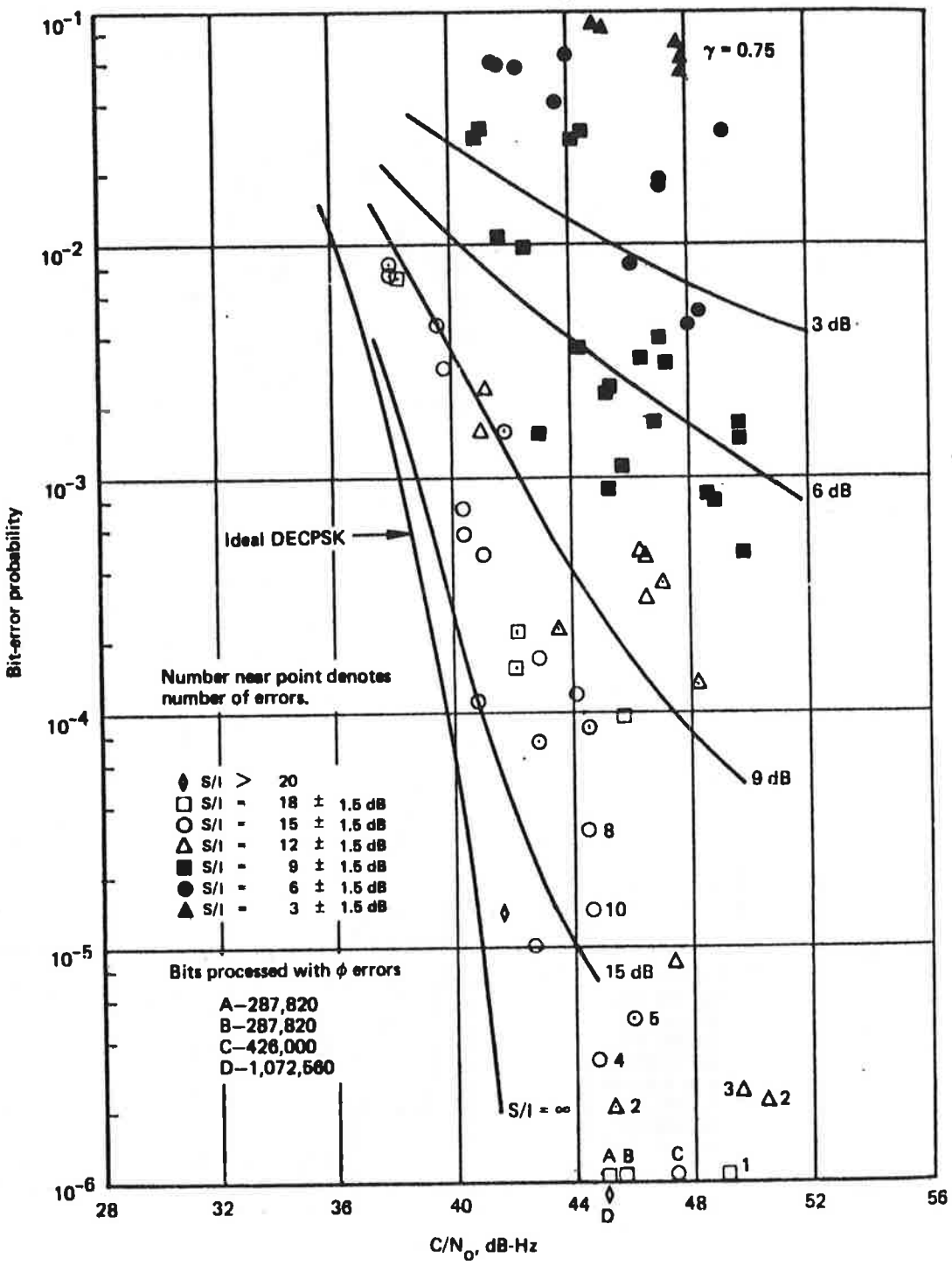

Figure 5-15. Bit Error Rate Performance of NASA DECPSK, Demodulator, 1200 bit/s, Type II Tests

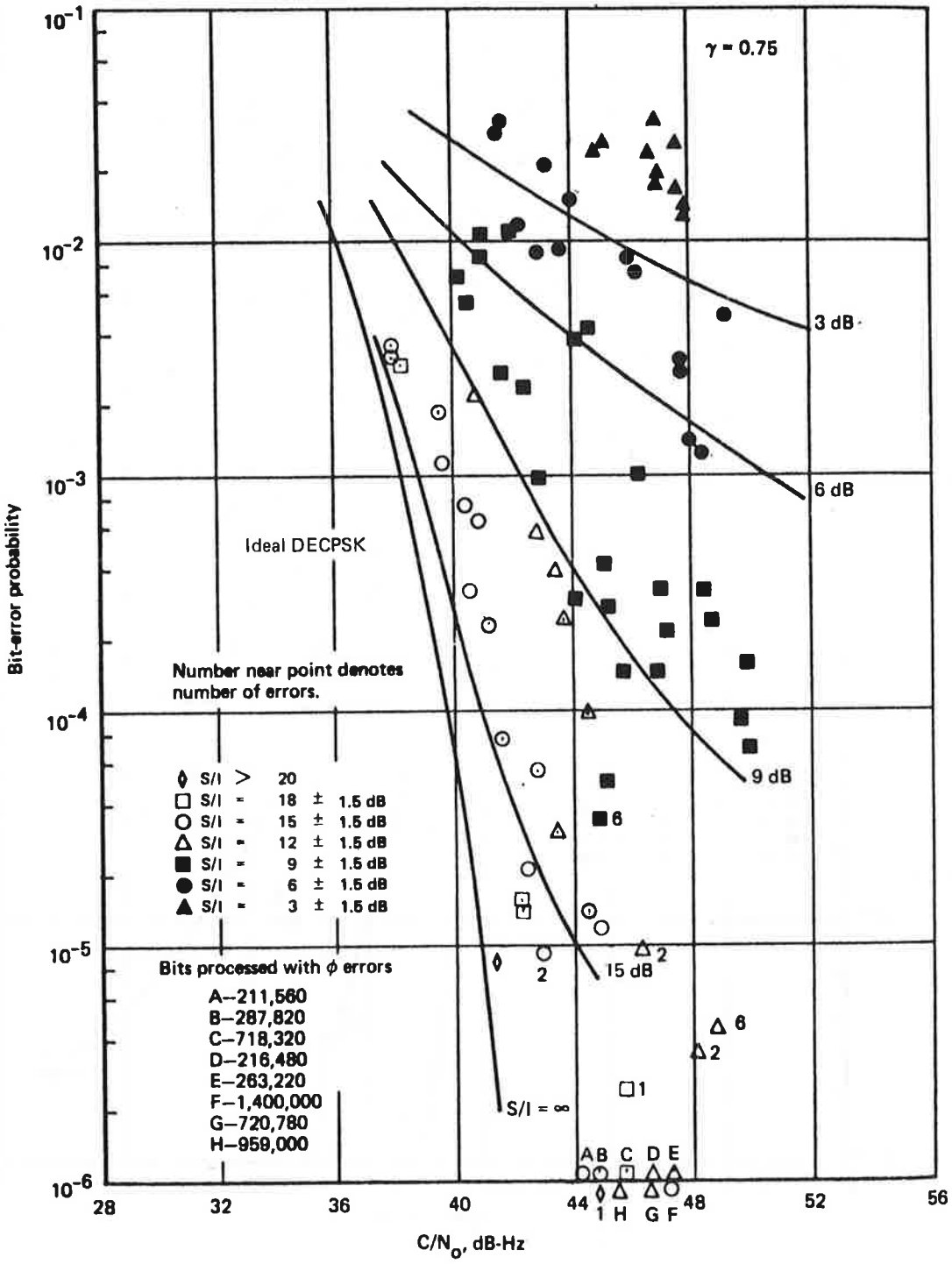

Figure 5-16. Bit Error Rate Performance of FAA CPSK Demodulator (DECPSK Mode), 1200 bit/s, Type II Tests

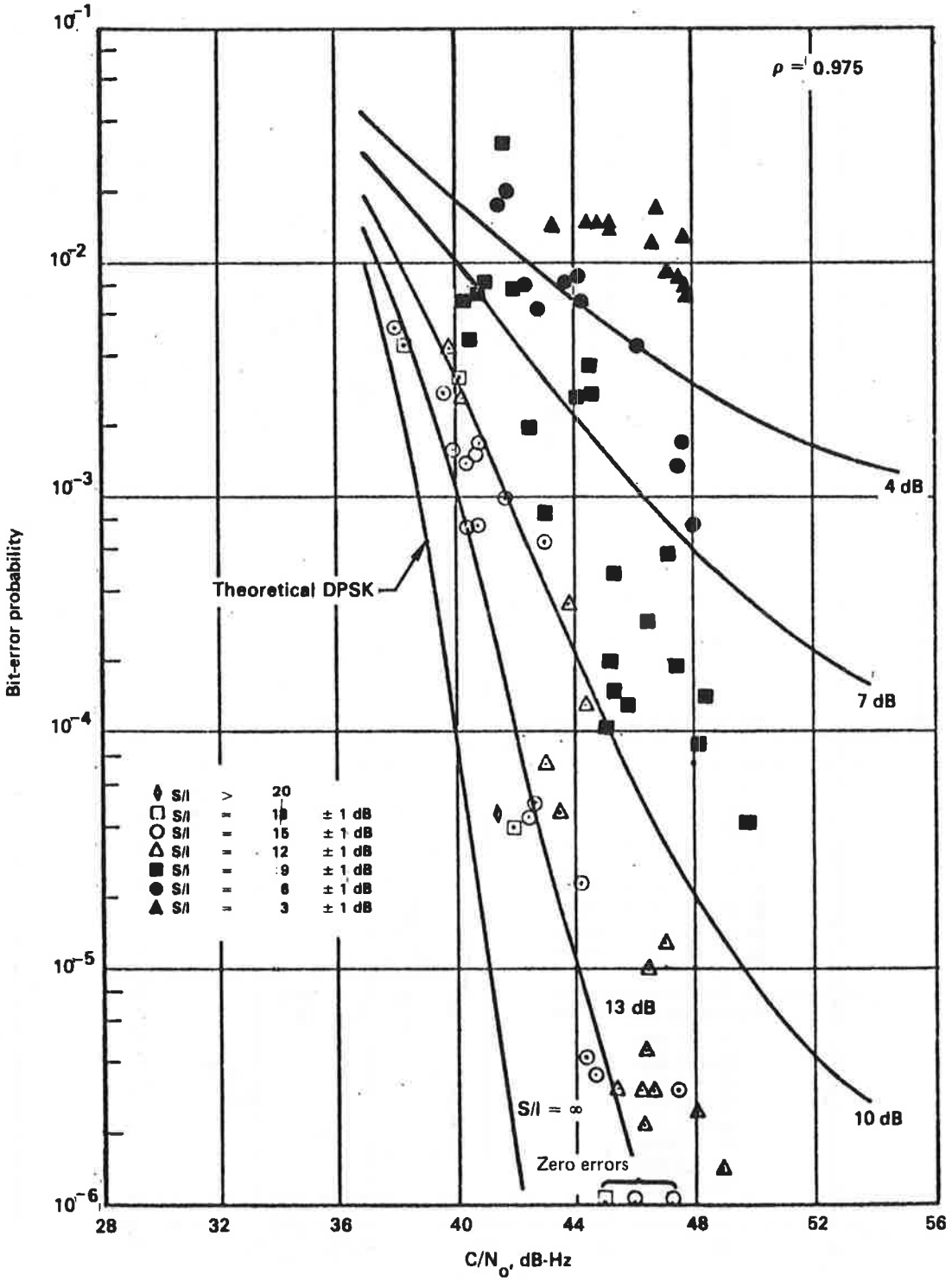

Figure 5-17. Bit Error Rate Performance of FAA DPSK Demodulator, 1200 bit/s, Type II Tests

Since S/I was a variable that could only be approximately set during flight conditions and estimated off-line later, the observed S/I values span a continuum from about 2 dB to an excess of 15 dB. To concisely present the data, the results have been grouped into cells of a particular S/I ± 1.5 dB. Thus the cell boundaries are 3 dB apart in the S/I variable. The ± 1.5 dB is not intended to be the measurement uncertainty associated with each point, but merely the grouping uncertainty. As stated earlier, the estimated measurement uncertainty for S/I is 1 dB.

The performance of the Hybrid No. 1, Hybrid No. 2 and FAA CPSK demodulators is not appreciably different for larger C/N_0 values and for all S/I. For those cases where S/I is large and C/N_0 relatively small, the Hybrid No. 1 modem is slightly superior, followed by the Hybrid No. 2 modem and the FAA CPSK. This is consistent with the findings of Type I tests, with their essentially large S/I conditions. The NASA DECPSK modem performed poorly relative to the other three DECPSK modems. This was especially noticeable at low S/I's and appeared in the simulator data as well as flight test data. A plausible explanation might relate to the NASA modem's B_L of 430 Hz, implying poorer threshold performance in noise, and this is accentuated by heavy fading.

It is also observed that BER performance is slightly poorer than that predicted by the $\gamma = 0.75$ theory. Though the disagreement in terms of effective S/I is roughly 2 to 3 dB at lower S/I for the three best DECPSK modems (figs. 5-13, 5-14, and 5-16), this corresponds to a factor of only 2 to 3 in error probability for these cases. Agreement with theoretical at higher S/I is within the experimental uncertainty. We note that factors acting to make performance poorer than that predicted are the implementation losses for each modem in the nonfading environment, as well as the cycle-slipping phenomenon that is unmodeled by the reference curves. Empirical observations showed this was indeed significant for heavy-fading cases.

DPSK results (fig. 5-17) are in excellent agreement with the slow-fading model predictions[2] (ref. 5-1).

The relative performance of DPSK and DECPSK is also of interest. By comparing the actual error probabilities of the three better DECPSK modems with the DPSK modem, it is found that:

a. For large S/I (greater than about 10 dB), DECPSK outperforms DPSK slightly in error probability, but less than an order of magnitude over the range tested.

b. For poor S/I, say less than 10 dB, DPSK begins to exhibit a superiority, but again not by a large factor in bit-error probability.

---

[2]The parameter ρ in figure 5-17 is a measure of channel gain correlation over a bit period and is given by $(1-\rho) \simeq \pi^2 B_F^2 T^2$. Additional details are available in the reference.

These results can be explained intuitively. For large S/I, the channel is essentially nonfading and it is well known that DECPSK is slightly superior to DPSK for such channels. Section 5.5.3 provides data in this regard. As S/I decreases, however, the ability to maintain the stable coherent reference for DECPSK is diminished. DPSK is relatively unaffected, however, as only relatively crude frequency accuracy is necessary. Thus a crossover in relative performance is not surprising. An identical observation has also been made in reference 5-4.

In terms of the system design for the 1200/2400-bps data channels, no clearcut winner emerges unless the channel character is decidedly either nonfading or very heavy fading (Rayleigh-like). Even then the performance difference is not dramatic, and it is believed by the authors that the differences are perhaps small relative to those that can be effected by careful design techniques.

5.5.5 Error Burst Statistics

Whereas the previous results have displayed the average bit-error probability over a period of minutes, the distribution of the error events in time is also important. The tendency toward error bursting, if present, affects the relation between bit-error rate and character-error rate, for example. Also, such information may be used to design error control schemes for the specific channel conditions involved.

In the presence of additive white Gaussian noise and without fading effects, the correlation structure of the error patterns associated with the various modems is well understood. For the DECPSK-type strategy, errors occur with high probability in pairs. This arises from the fact that decisions are the result of differentially decoding matched filter decisions, which are approximately independent. Single isolated errors are rather infrequent and can be explained only by a carrier-loop phase-slip event. For true DPSK detectors, this strong propensity for paired errors is not observed, although the decision is based on the phasor difference over two successive signal intervals. Single errors still predominate the DPSK on nonfading channels, except perhaps at very poor signal-to-noise ratios (ref. 5-5).

Figure 5-18 provides block-error histogram data for a Type II test interval for various S/I conditions. C/N_O was held approximately constant over the test. We observe that for S/I = 9 dB, the histograms for both DECPSK and DPSK are roughly the same; i.e., have predominantly paired errors for DECPSK and predominantly single errors for DPSK. For both detection strategies, the average error probability increases as S/I decreases. Also, for DECPSK, the predominant error mechanism changes from isolated paired errors to single errors per block, indicating that carrier-loop cycle slipping is becoming significant. An example showing similar behavior, with C/N_O about 43 dB-Hz, is given in volume VI.

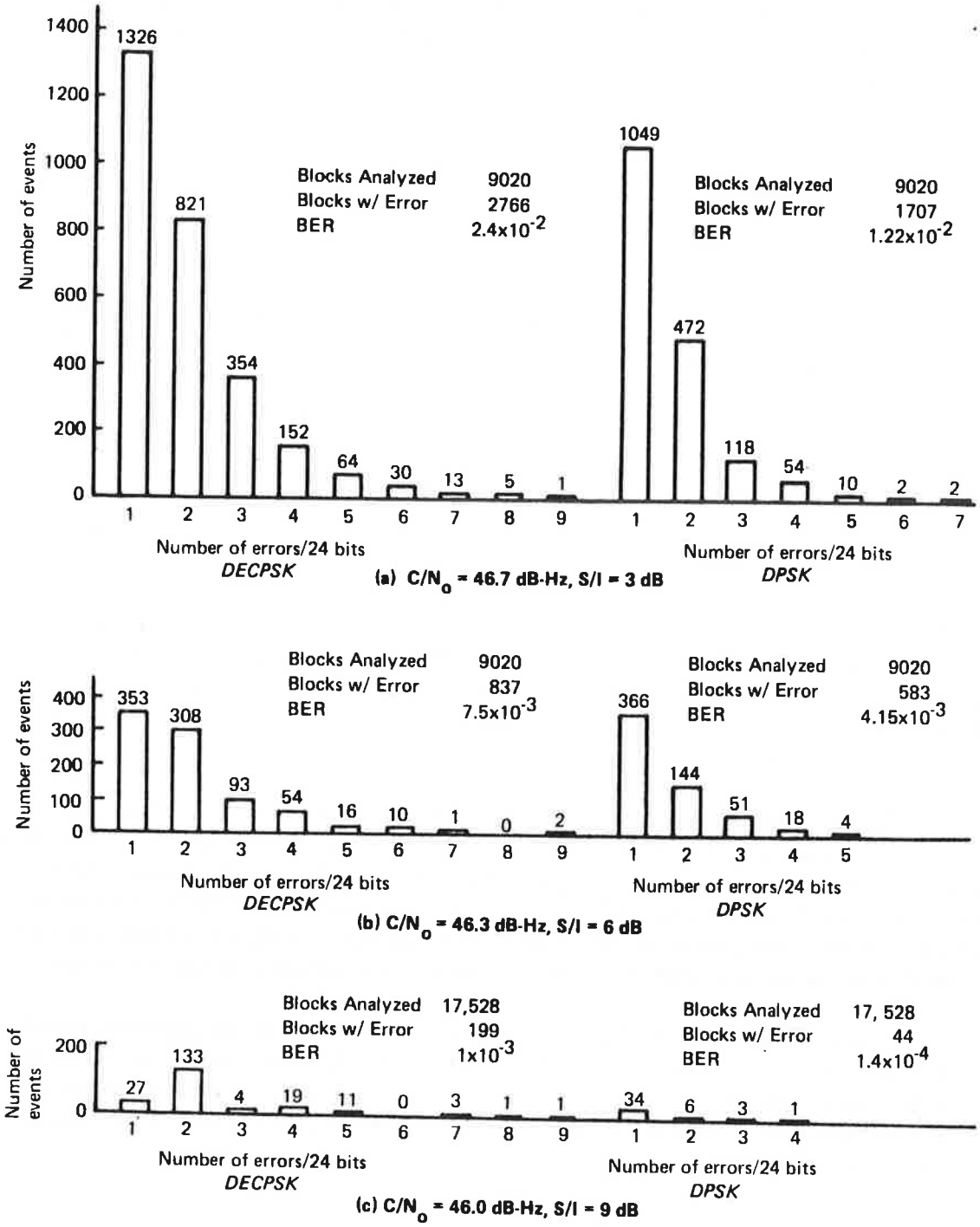

Figure 5-18. Type II Block Error Histograms

An alternate viewpoint for studying the memory, or interdependence, of channel error patterns is that of the spacings between errors. If the error process is truly memoryless, the spacing, or waiting time between errors, is geometrically distributed. That is

$$\text{Prob}\left[\text{spacing} = k\right] = P_e (1 - P_e)^{k-1}, \; k = 1, 2, \ldots$$

where P_e is the average error probability. As the channel or modem induces memory, the frequency of lesser waiting times increases relative to that of a geometric distribution.

Figures 5-19 and 5-20 show error spacing distributions for the Hybrid No. 1 and DPSK modems for two distinct channel conditions. These have been calculated by counting the number of times the spacing between errors was k, k = 1, 2, . . ., 40, and dividing each total by the total number of errors. This provides an estimate of the waiting-time density function. On the same figures, the distribution of spacings assuming a memoryless process with the *same* probability has been plotted for contrast.

Figure 5-19 is for a Type I test with C/N_0 = 38.2 dB-Hz and S/I > 20 dB. We observe that the error process has significant memory over two bits in each case; then the probability of spacing k > 2 falls off with slope characteristic of a memoryless process. Of course, this is the expected result for additive-noise environments due to the detection involving two adjacent bits. Also note that for DECPSK, given an error event, the probability is one-half that another error follows, which is in agreement with theory (ref. 5-2). On the other hand, the corresponding probability for DPSK is 0.186, meaning back-to-back errors are less likely. This value is in very good agreement with the calculations of reference 5-5 (0.19 at C/N_0 = 38.2 dB-Hz).

Figure 5-20 depicts a case with greater C/N_0 and moderately heavy fading. This case was chosen since the average error probabilities were roughly the same as those of figure 5-19. Here, both modems exhibit a two-mode characteristic in the density function. Namely, the density exhibits relatively large weighting for spacings 1, 2, . . ., 7, then decays slowly in accord with a memoryless process with small error probability. Thus, we may conclude that for C/N_0 = 41.6 dB-Hz and S/I = 6 dB, the effective memory length of the error process is on the order of seven bits at 1200 bps.

This information can be used in the design of error-correcting codes for improving channel performance. For the above example, the code should have the capability for correcting bursts of time duration equivalent to at least seven bits long as well as having modest random error-correcting power. If the code rate is one-half, for example, the burst-correcting power should be 14 channel symbols.

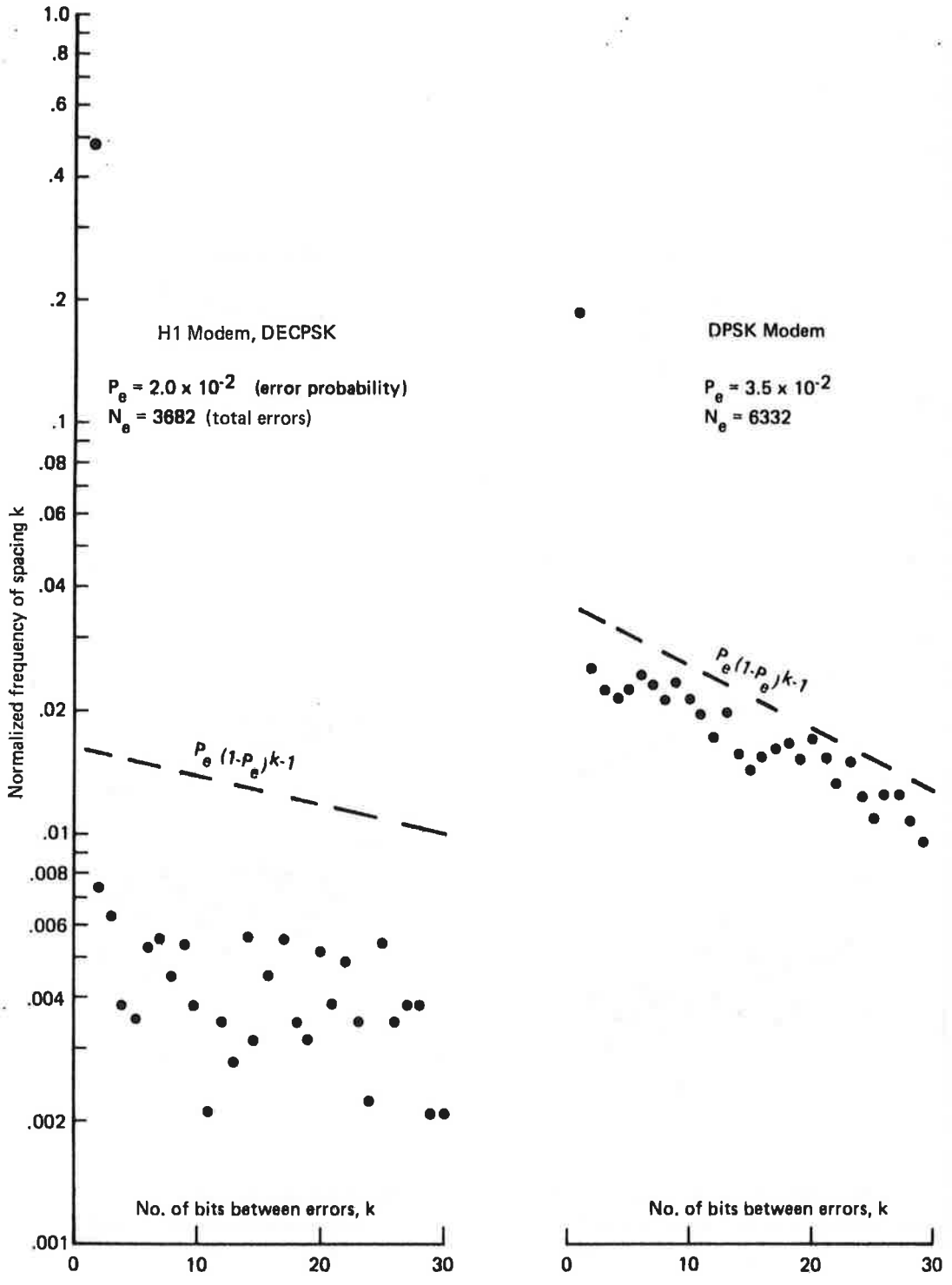

Figure 5-19. Error Spacing Distributions, DECPSK and DPSK, C/N_O = 38.2 dB-Hz, S/I = 20 dB

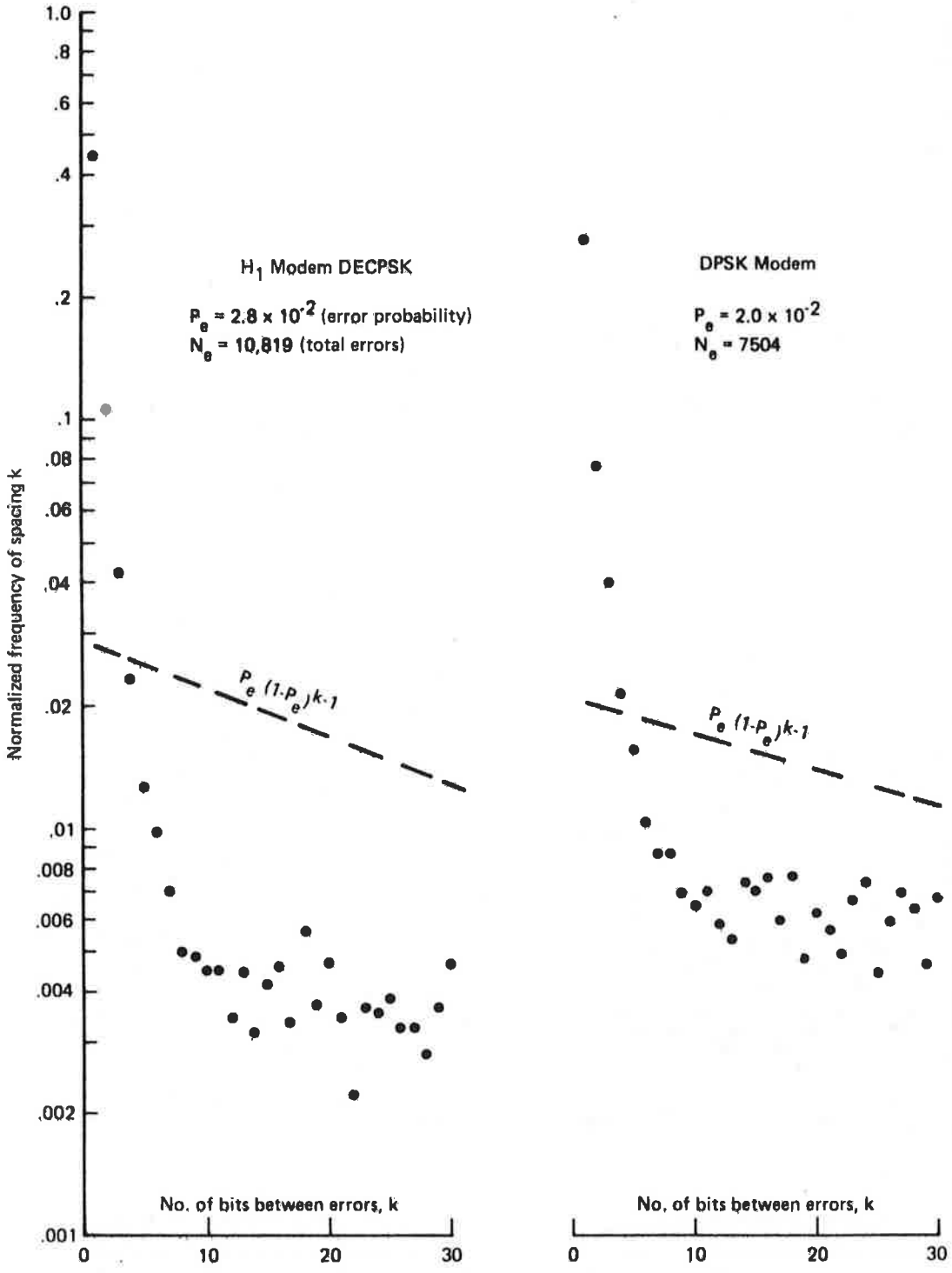

Figure 5-20. Error Spacing Distributions, DECPSK and DPSK, C/N_0 = 41.6 dB-Hz, S/I = 6 dB

For even heavier multipath conditions (example in vol. VI with S/I = 2.5 dB, C/N_o = 47 dB-Hz), the effective memory time of the channel is roughly 14 bits. Memory times as great as 14 bits at 1200 bps are certainly plausible for the AEROSAT channels. If one assumes a two-sided Doppler bandwidth of the multipath process to be 100 Hz, then the process decorrelation time ~ 10 msec, or 12 bits at 1200 bps.

5.5.6 BER Performance of Hybrid Modem in Combined Voice and Data Mode

The Hybrid No. 1 and 2 modems have the capability of transmitting speech and data simultaneously on a single constant-envelope carrier. Tests were performed to measure bit-error rate (and speech intelligibility) when the modems were operating in the hybrid mode.

Figure 5-21 and 5-22 present the measured BER for the Hybrid No. 1 and 2 modems, respectively. All these tests were conducted in the Type I condition, i.e., no appreciable multipath interference is present, except for the points tagged with circled S/I values.

It is noted that the experimental data for the Hybrid No. 1 modem shows a rather dramatic divergence from the theoretical data-only mode performance at low-bit-error rates. Data channel performance will, in fact, be somewhat dependent upon the voice channel due to the speech/data adaptive power-sharing techniques employed within the modem. However, neither the acceptance test data furnished by the modem manufacturer nor laboratory measurements made by DOT/TSC after completion of the test program show the large divergence observed in the experimental data. Laboratory measurements made by DOT/TSC are included in figure 5-21. Several factors have been investigated, including (1) data performance sensitivity to voice channel audio input level and (2) possible presence of multipath degradation during Type I tests. To date, none of these factors appears to be causally related to the observed experimental performance, and hence the disparity between laboratory measurements and field-test data remains largely unresolved. It appears likely that the laboratory performance measurements more closely approximate the achievable performance than does the field test data.

It should be stated that the results exhibited herein pertain to the regular utterance of PB words at 2.5-sec intervals. In operational use, where verbal messages are conveyed, the data BER during voice channel activity may differ somewhat from the results obtained using PB word lists because of the different dynamics associated with the voice channel modulation for the two cases. During periods of voice channel inactivity, the BER would be essentially that achieved in the data-only mode.

The Hybrid No. 2 modem performance (fig. 5-24) seems consistent with the expected 3-dB shift discussed above. Relative to the data-only mode performance at $P_e = 10^{-5}$, the actual difference is approximately 3.5 dB. According to the field test data it is noted that very low error probability, say 1×10^{-5}, was achieved with less C/N_o for the Hybrid No. 2 than for the Hybrid No. 1 modem. On the other hand, the Hybrid No. 1 modem was more efficient at higher error rates. Again, these judgments pertain to the particular speech duty cycle used for these tests.

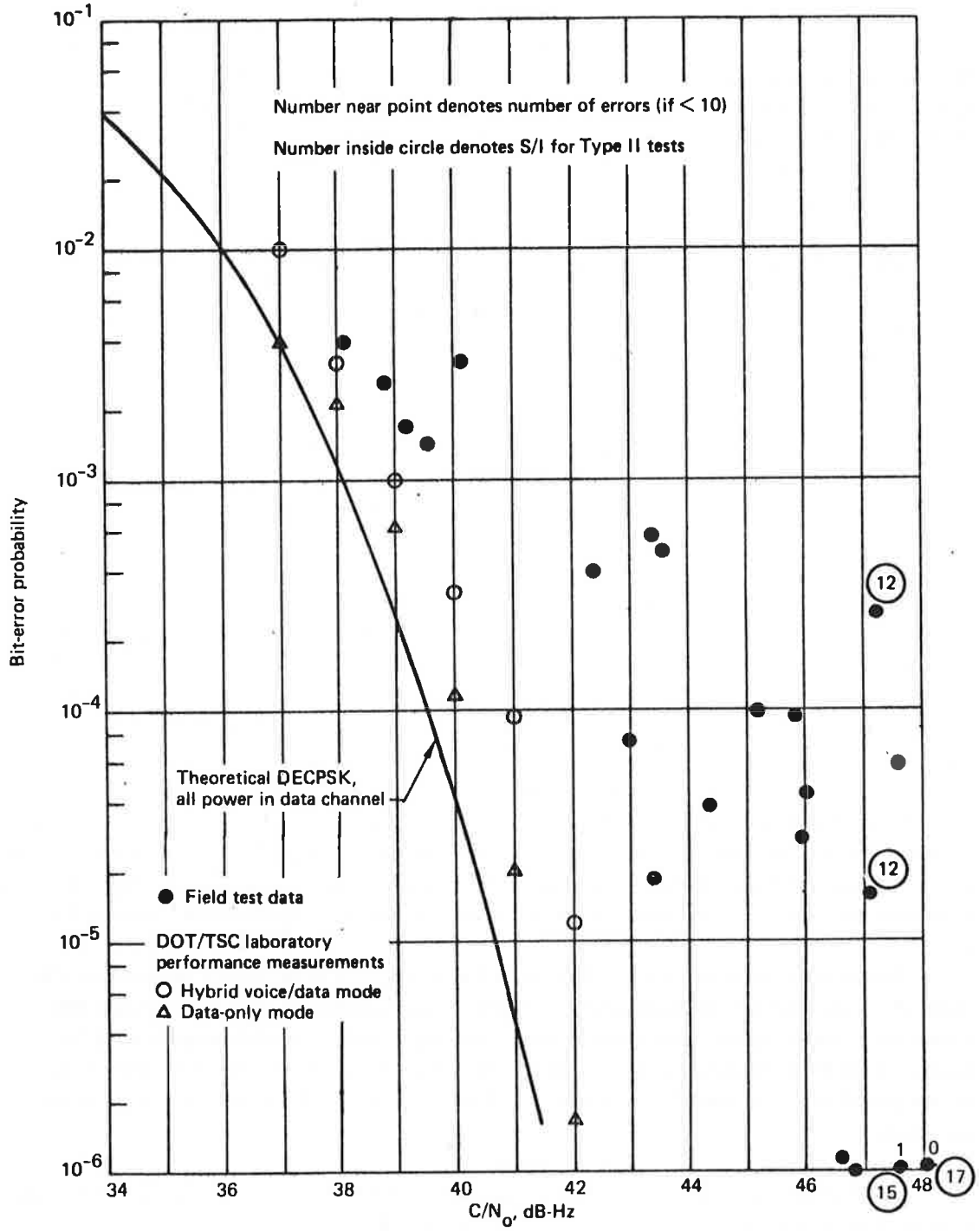

Figure 5-21. BER Performance of Hybrid No. 1 Modem, 1200 bit/s, Hybrid Voice and Data Mode

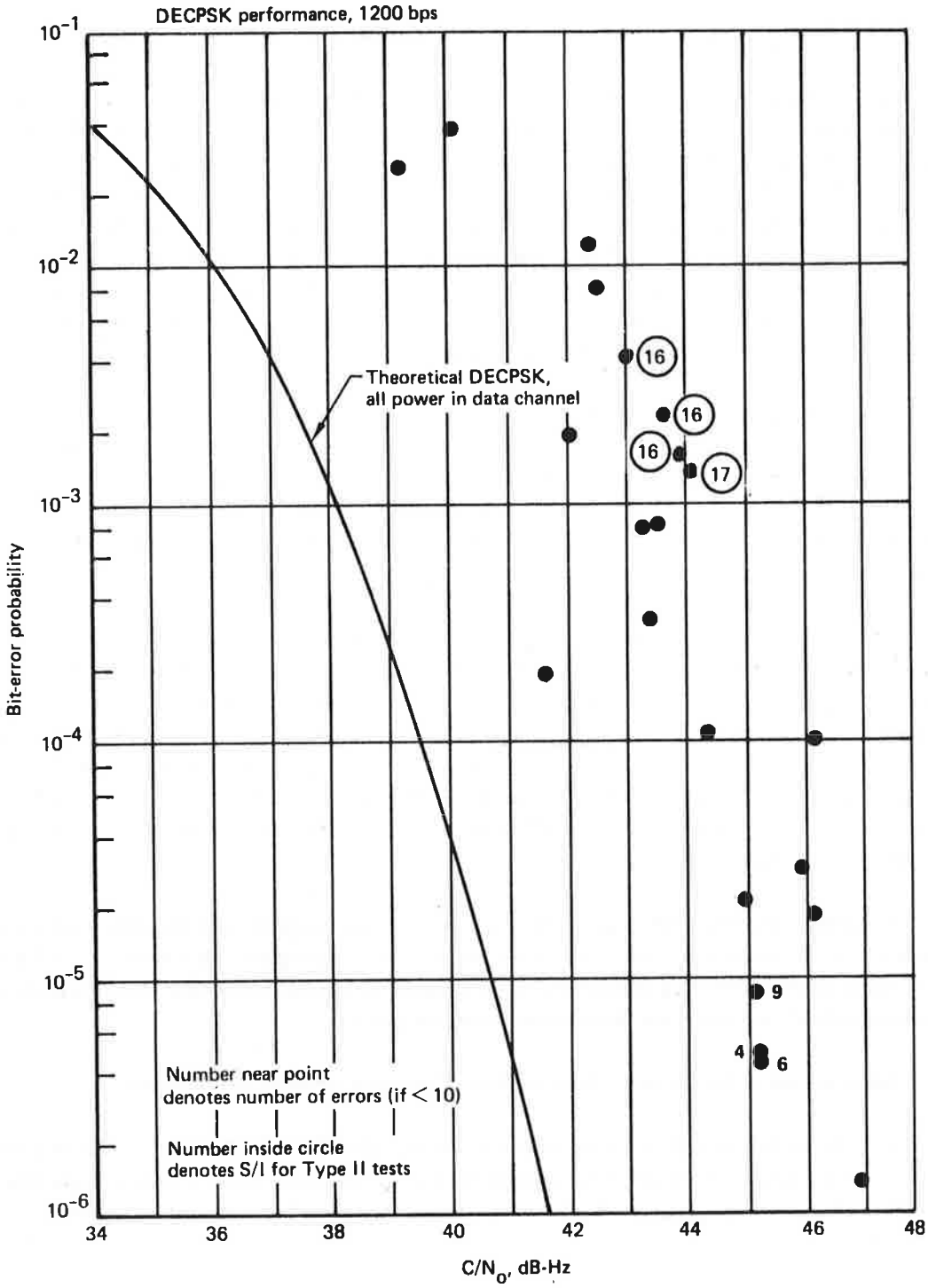

Figure 5-22. BER Performance of Hybrid No. 2 Modem, 1200 bit/s, Hybrid Voice and Data Mode

5.5.7 Digital Data Test Conclusions

The digital data tests have revealed or verified several significant conclusions applicable to the configuration of aeronautical satellite data link channels. First, the bit-error rates achieved with reception via a representative switched antenna system (the top-left-right slot-dipole configuration) are less than 1×10^{-5} at $C/N_0 = 43$ dB-Hz. The latter corresponds to the current AEROSAT system specification, and the conclusion holds for four distinct DECPSK modems and one DPSK modem. Relative to theoretical limits for additive Gaussian noise environments, the modems exhibited inefficiencies of 0.9 to 1.9 dB. By implication, the net S/I achieved by the antenna system for the various Type I geometries exceeded 15 dB since none of the characteristic divergence from theoretical nonfading performance was observed as C/N_0 was increased.

When operated on a Rician fading channel (Type II tests), the DPSK modem performed in general accord with existing theoretical results and with previous experimental flight test results. For example, if the S/I achieved by the antenna system is only 10 dB, an additional 8 dB of channel power is necessary to reduce the error probability to 1×10^{-5}. As concluded in other investigations, error-control coding or multipath-tolerant waveform design appears to be a necessary adjunct to the existing modem designs if S/I values of only 10 dB are anticipated.

The performance of the coherent-detection technique (DECPSK) was rather different for the various modems, possibly due to the different loop bandwidths involved and the impact of cycle slipping. The bit-error rate versus C/N_0 observed for these modems was slightly lower than for the DPSK modem when S/I was large, say greater than 10 dB; as S/I decreased below 10 dB, the DPSK technique exhibited better performance. In ranking the DECPSK modems qualitatively, we conclude that the Hybrid No. 1 modem performed best, followed by the Hybrid No. 2 modem, the FAA CPSK modem, and the NASA modem. The latter seemed to exhibit particularly bad degradation in a multipath environment.

Relative to the DPSK versus DECPSK question, it is our judgment that the difference in performance is not significant in either's favor over a typical operating region of S/I and C/N_0. Other factors not evaluated here, such as acquisition performance, complexity of design, and reliability of operation probably outweigh any observed bit-error-rate factors.

Investigation of the memory characteristics of the error patterns revealed that:

a. In nonfading additive-noise environments, the DECPSK errors generally occur in pairs whereas the DPSK errors are predominantly isolated single errors and, less frequently, paired error events. Both of these results have been earlier theorized and verified.

b. As the level of multipath interference increases, the likelihood of error bursts increases; i.e., the short-term error probability varies over orders of magnitude due to constructive and destructive interference. Also, for DECPSK, cycle slip events become more obvious as evidenced by the increase in frequency of isolated errors. If burst-correction coding is used for either DECPSK or DPSK, the burst-correcting span should be on the order of seven bits at 1200 bps (14 code symbols in a rate one-half code).

Finally, the performance of the two hybrid voice/data modems was evaluated in the hybrid mode. For the Hybrid No. 2 modem, the C/N_0 increase required to maintain equivalent error performance was about 3.5 dB due to the equal power sharing. The Hybrid No. 1 modem exhibited a more complex relationship; for high error rates ($\sim 10^{-2}$), speech and data could be conveyed with only 1 dB additional power while at the 10^{-5} error rate, the necessary increase in C/N_0 for the hybrid mode was on the order of 4 dB. This is somewhat dependent on the duty cycle and statistics of the speech modulation that result when speech is added to data transmission (discussed in sec. 5.4.5). The impact of adding data to speech is roughly 3 dB.

5.6 RANGING MODEM TEST RESULTS

The flight test program evaluated the performance of two distinct satellite-aircraft ranging techniques. Measurements were performed using only a single satellite, whereas an operational surveillance system would require additional measurements for a 3-D position solution. Also, the accuracy was evaluated relative to a best-fit estimate, rather than absolutely.

5.6.1 Ranging Modems Tested

The two ranging techniques tested are referred to as TSC ranging and NASA ranging, the names deriving from the agencies sponsoring the respective modem developments.

5.6.1.1 TSC Ranging Modem – This modem was an in-house development at DOT/Transportation Systems Center. The TSC modem utilizes a binary ranging code, which may be rapidly acquired relative to the acquisition time of a brute-force search. The clock rate of the code is selectable as 156.25 or 19.53 kHz. The clock and 12 (or 9) binary submultiples are used to synthesize the code, with the highest frequency determining ranging precision and the lowest frequency determining unambiguous range. Acquisition of the code requires phase locking to the clock component, then successively generating submultiples that are "in phase" with the incoming code. This involves 12 (or 9) decisions rather than 2^{12} (or 2^9).

At regular intervals a range measurement is performed by measuring the number of 40-MHz counts between epochs of a reference code and the regenerated code. The range measurement is formatted along with modem status bits for tape recording and postflight analyses in Seattle.

5.6.1.2 NASA Ranging Modem – The NASA ranging modem implements a cw sidetone ranging technique developed for NASA as part of the PLACE system. Modems were located on the aircraft and at Rosman, North Carolina, and two-way round-trip range was computed at Rosman. Rosman continuously emitted the surveillance and ranging (S&R) signal, which was acquired and tracked by the aircraft modem as well as by other users. Aircraft emissions were in response to an interrogation signal inserted into the forward-link waveform. In the high-rate mode used for these tests, an interrogation occurs each 6.4 sec.

The S&R signal has four ranging tones (8575, 8550, 8400 and 7350 Hz) double-sideband modulated on a carrier plus a 600-bps Manchester PSK channel in phase quadrature. The composite of these is limited to remove envelope variation. The signal is coherently demodulated with a carrier-tracking loop that tracks the residual carrier. Tone phase for each tone is computed by baseband correlation with reference tones. A digital computer resolves the phase ambiguities implied by the modulo-2π measurements and computes round-trip range. The 600-bps data channel is used for polling of various terminals, transmission of onboard altitude, etc.

The responses received at Rosman were processed and written on digital tape, which in turn was supplied to Boeing for analysis.

5.6.2 Reduction and Analysis of Ranging Data

For both types of tests, range versus time arrays were constructed for a test interval of several minutes' duration. Obvious outliers, or blunder errors, were purged from the data set as described in volume IV to yield a more meaningful calculation of error standard deviation. Using the remaining points, a second-order polynomial fit was performed, and an error array was defined by the deviations between each sample point and the best-fit estimate at the corresponding time. Thus, the experiment measures error deviations relative to a nominal trajectory. The rms value of this deviation is the primary test statistic.

Goodness-of-fit tests were performed for both modem experiments to test the assumption of normally distributed range error. The chi-squared test was used, with mean and variance of the hypothetical distribution computed from the error data.

For the TSC tests, the signal envelope samples were processed as described in section 5.3.1 to provide C/N_0 and S/I estimates for the channel. The forward-link C/N_0 for the NASA signal is assumed identical to that of the TSC signal. No corresponding C/N_0 and S/I data was available at the Rosman ground station relative to the return-link channel quality during tests of the NASA ranging modem.

5.6.3 TSC Digital Ranging Modem Performance

Results presented for the TSC ranging modem are confined to November 1974 through April 1975 test periods. Although data was collected during September and October 1974, this data could not be reduced because of a waveform anomaly in the modem output consisting of a phase discontinuity that appeared in the Manchester bit stream shortly prior to each range reading. This occurred only when the modem was forced to make entire code acquisition for each measurement; subsequently the modem was operated in a four-readings-per-second mode where reacquisition was performed only if the lock was broken.

Type I test results for a standard deviation of range error in meters are found in figure 5-23 for both narrowband and wideband modes. Test data encompasses the November 1974 through April 1975 test series. Superimposed are best-fit curves from baseline laboratory data provided by TSC. For the narrowband data, the points straddle the laboratory curve but in general lie above it. Also, data scatter is greater than that attributable to finite-sampling error.

One potential reason for the higher rms error in the flight test environment is the presence of small amounts of multipath interference. Although the slot-dipole antenna system used in Type I tests provides rather large discrimination as determined from spectral analysis of the envelope detector output, even low multipath levels can increase the rms deviation significantly beyond that predicted for additive noise only. For example, with $C/N_0 = 43$ dB-Hz, the clock loop signal-to-noise ratio is 38.9 dB (effective tone-power-to-noise ratio in B_L). The signal-to-multipath ratio may be calculated by assuming for the present that the S/I achieved by the antenna system is 20 dB. Also, assuming the multipath one-sided bandwidth is 50 Hz and noting that $B_L \simeq 1$ Hz, an additional 17-dB rejection accrues via narrowband tracking. The loop output S/I then is 37 dB. This is approximately equal to the signal-to-noise ratio. Thus the net rms error will be larger than that calculated for noise alone. This points out the potential dominance of multipath effects in the ranging system error budget, particularly for high-precision systems.

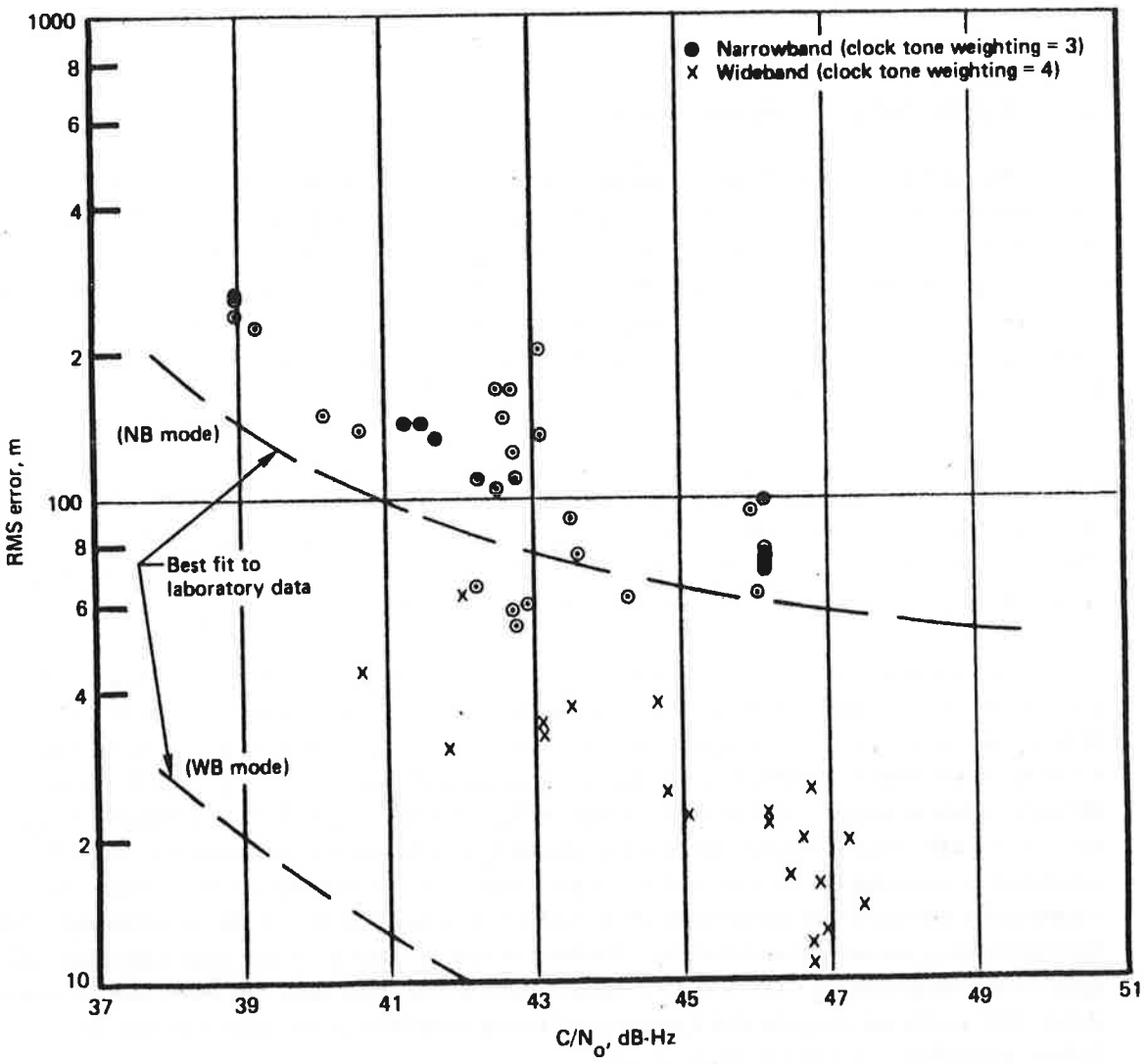

Figure 5-23. RMS Error Performance, TSC Ranging Modem, Type I Tests

For the *wideband* case, the flight test results have considerably larger rms deviation than the laboratory measurements. Aside from multipath factors described above, two factors may contribute to this. First, experience with the modem indicated that the carrier loop needs continual monitoring of loop stress to maintain optimum modem performance in the wideband mode. Since the operator's workload prevented such monitoring, the performance observed here could be expected to be poorer than laboratory measurements. Second, the assumed second-order aircraft trajectory may not be adequate to model the short-term motion of the aircraft due to gusting and flight control actions. These perturbations are insignificant when error deviations on the order of 100 m are under study. In the wideband mode, however, the ranging precision is on the order of a few tens of meters, and these unmodeled variations could be important. If so, the apparent rms deviation is inflated relative to that obtained with exact knowledge of aircraft motion.

Type II test results for the TSC modem are found in figure 5-24. The number adjacent to each point is the computed S/I. The data is limited to those conditions for which the S/I is relatively high since the cases with stronger multipath yielded erratic modem performance, presumably due to loss of lock. It is noted that in both the narrowband and wideband cases, data points lie roughly in the same location versus C/N_0 as do the Type I data points. This is a reasonable result since the effective S/I of the slot-dipole system generally exceeded 20 dB for the test geometries flown.

In Type I and II tests, frequent range jumps were observed, either due to loss of lock or incorrect ambiguity resolution. These points are censored from the data set unless the frequency of occurrence was too large to permit reasonable processing of the set.

It was also determined that range quantizing effects associated with the digital clock tracking PLL was a significant factor in the total error budget. In some cases with reasonably large C/N_0 and S/I, quantizing is clearly the dominant effect.

5.6.4 NASA Ranging Modem Performance

Seven digital tapes were supplied to Boeing, spanning 7 days of ranging experiments: November 13 and 19, 1974, and January 23, January 29, March 27, March 28, and March 31, 1975. Upon careful examination, it was decided that the January 23 tape contained no usable data.

Pertinent information for the remaining six test intervals is found in table 5-4. Contained in the table are the number of points accepted and total number of points, the standard deviation of error, the chi-squared goodness-of-fit result, and the measured link C/N_0.

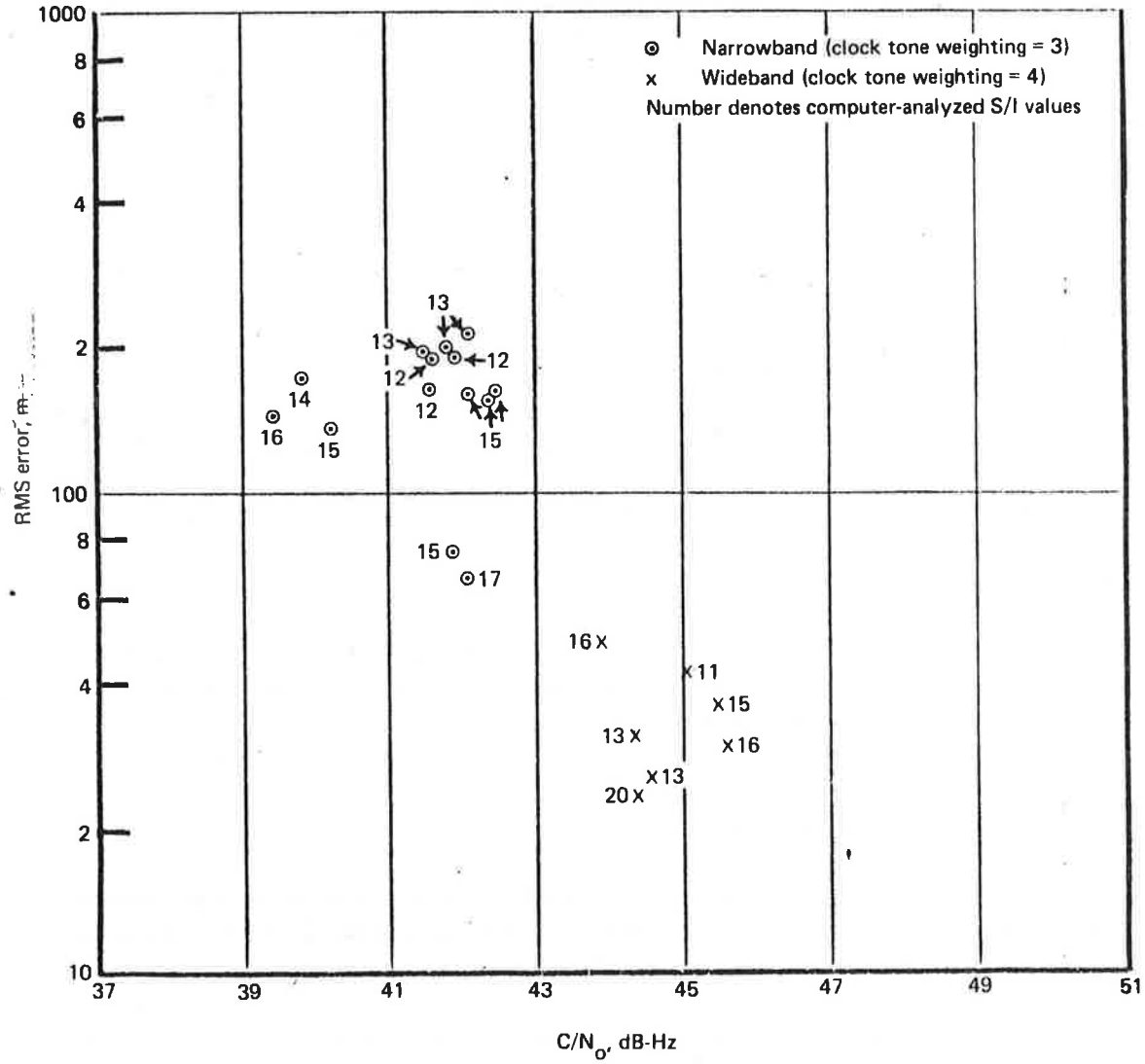

Figure 5-24. RMS Error Performance, TSC Ranging Modem Type II Tests

TABLE 5-4. NASA RANGING SUMMARY

Date, mo-day-yr	Test type	Start time	Stop time	Total points	Points accepted	σ_R, meters	P (X^2>t)	C/N_o, dB-Hz
11-13-74	II	0941	0946	42	32	298	0.70	42.0
11-13-74	I	0958	1007	79	69	248	0.27	—
11-13-74	II	1011	1016	32	23	332	0.62	44.5
11-19-74	II	1203	1208	43	23	225	0.79	—
1-29-75[a]	I	1020	1028	76	76	56	0.35	60
1-29-75[a]	I	1030	1038	67	67	125	0.92	46
3-27-75	II	1220	1233	127	120	334	0.03	44.6
3-28-75	I	1353	1359	48	45	236	0.75	42.7
3-31-75	II	1217	1221	33	27	263	0.27	42.0

[a]Ground test.

Several conclusions can be drawn from table 5-4. First, roughly 25% of the range readings written on tape had huge errors (greater than 10,000 m) and were therfore purged. These large errors perhaps correspond to incorrect resolution of the ambiguous phases of the four tones. Whatever the cause, the frequency of blunder errors would have to be reduced to be usable in any operational sense. Second, there is no strong basis for rejecting a normal distribution of error from chi-squared tests, since only one batch produced a test statistic exceeding the 0.05 significance level. However, due to the small sample sizes involved, the power of the test, i.e., the probability of rejecting the hypothesis when in fact the samples were not normally distributed, is probably not large. In other words, many near-Gaussian distributions, appropriately scaled, might be approved by the test. Since there is a physical basis for a Gaussian model and it is not rejectable from the data, it is plausible to invoke its assumption except perhaps for describing events lying in the far tail of the distribution.

Calculations found in volume VI show the observed performance is reasonably consistent with expectations. For total C/N_o = 42 dB-Hz, the theoretical rms range error is 285 m; for forward-link C/N_o = 42 to 44 dB-Hz, the average of observed standard deviations is 276 m. Although only the forward-link C/N_o was measured directly, link calculations indicate the return link should contribute little additional noise. Thus, 42 to 44 dB-Hz round-trip C/N_o may be expected for most of the cases in table 5-4, and we see that the observed standard deviation is roughly what should be expected.

It is noted that the rms range error achieved falls short of the current AEROSAT system specification of σ_R = 50 m at 43 dB-Hz. (The modem obviously was not designed to achieve this performance.)[3] Satisfaction of the specification with a tone-ranging format will thus require considerably wider signal bandwidths. Tone integration time cannot be significantly lengthened due to the necessity to acquire and process each user response in 0.5 sec.

5.6.5 Ranging Test Conclusions

The flight test performance of two distinct ranging techniques has been determined over a 6-month test program. Type I tests were performed with operational-class aircraft antennas. Type II tests measured performance on the multipath channel by inducing various multipath levels with a second antenna.

Results of the TSC ranging test showed that rms range error was typically 100 m at 43 dB-Hz carrier-to-noise density ratio in the narrowband mode (19.53-kHz clock). In the wideband mode (156.25-kHz clock), the rms error was reduced to roughly 30 m at the same condition. These results are generally larger than corresponding laboratory measurements, particularly so for the wideband mode.

NASA ranging tests exhibited a typical rms error of 276 m in the 42 to 44 dB-Hz region, a performance measure in reasonable agreement with theoretical expectations.

The NASA modem exhibited a rather high frequency of blunder error, perhaps due to incorrect ambiguity resolution. This was also observed to a lesser degree with the TSC modem when the modem was operated in a mode forcing reacquisition of the code on each measurement.

---

[3]The current AEROSAT system ranging performance specification was not applicable during the design phase of this modem.

6. ANTENNA EVALUATION TEST

The antenna evaluation test quantitatively evaluated the in-flight performance of candidate aircraft antennas for aeronautical L-band satellite applications.

6.1 ANTENNA EVALUATION TEST OBJECTIVES

The antenna performance figures of merit of major interest are the gain (which directly determines achievable C/N_o) and the ratio of received signal to multipath interference (S/I). The specific test objective was to acquire and analyze data to determine gain and S/I over a range of satellite elevation and relative bearing angles for the selectable three-element slot-dipole system, phased-array, and patch antennas.

6.2 ANTENNA EVALUATION TEST DESCRIPTION

6.2.1 KC-135 Terminal Configuration

A simplified block diagram of the KC-135 terminal is shown in figure 6-1. Two independent receiving channels were available for simultaneous reception of the same cw downlink ATS-6 test signal via two separate antennas. Either the quad helix or the selected slot dipole could be connected to the PLACE receiver, and either the phased array or patch could be connected to the other receiving system.

After amplification and down-conversion to 10 MHz, the two signals were time multiplexed, at a 3-sec switching rate, to an envelope detector. The detected output was recorded for off-line computer analysis to determine C/N_o and S/I for each receiving system. Two spectrum analyzers and several other instruments were used for system monitoring, calibration, and real-time performance measurements. An eight-channel chart recorder provided a hard-copy log of selected inflight reference data.

6.2.2 Test Geometries and Scenarios

Both circular and linear flightpaths were used to acquire antenna performance data at elevation angles ranging between 10^o and 40^o. Except for a few tests conducted with the aircraft parked on the ground, all tests were overocean in order to assess performance in the overocean multipath environment.

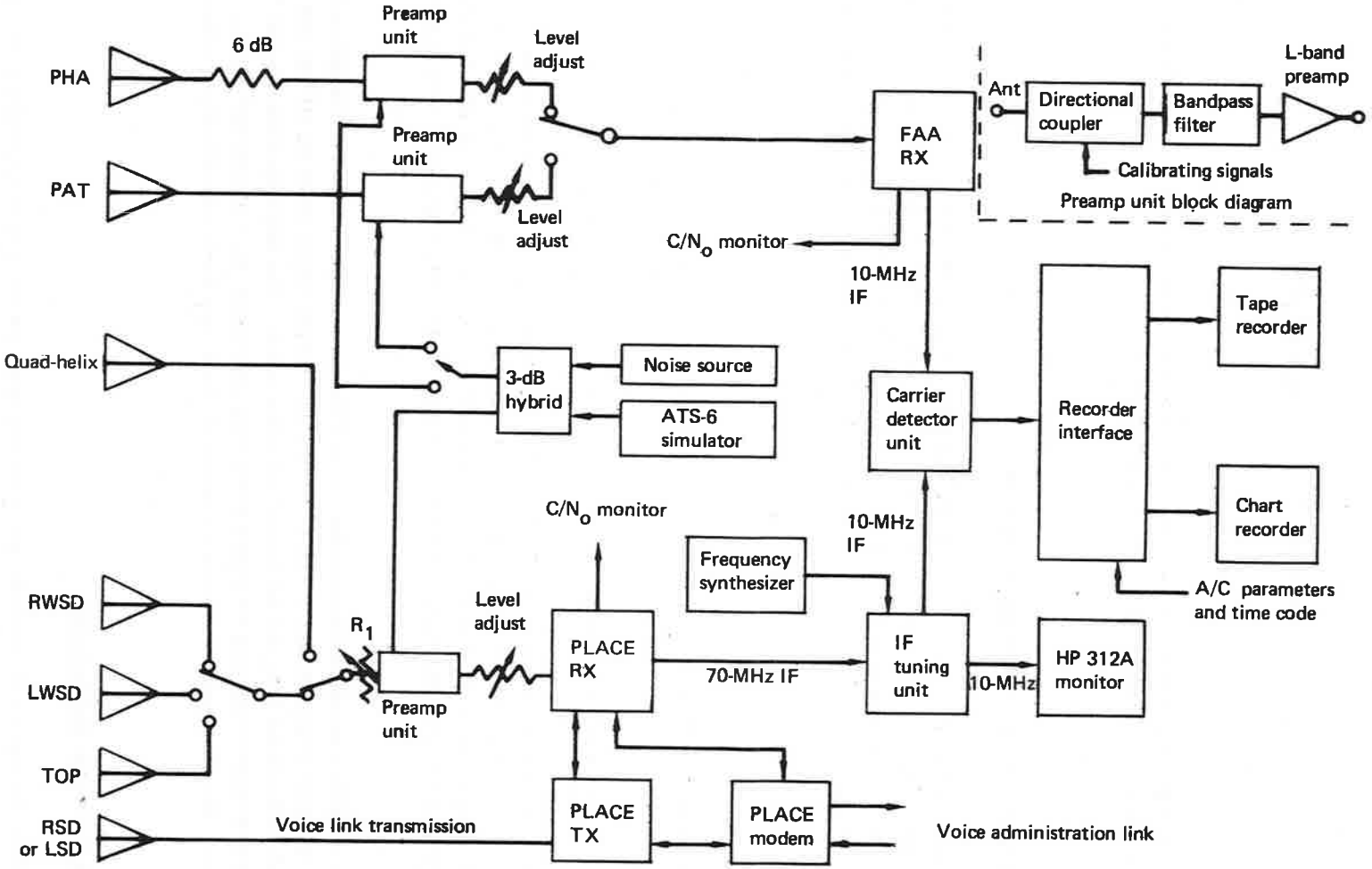

Figure 6-1. Simplified KC-135 Terminal for Antenna Evaluation Test

For circular flightpaths, the airplane was flown in a large circle (20-nmi radius) with near-zero bank angle, thus acquiring antenna data on a quasi-continuous basis. Figure 6-2 gives the basic test geometry and scenario. A test began with a 6-min linear-flight segment broadside to the satellite direction. During the first 4 min of this segment, the quad helix was connected to one receiving system while the phased array was connected to the other. After the QH pointing was optimized and PHA elevation beam position was selected, final signal level adjustments were made; calibration data was then acquired with the carrier detector unit multiplexing between the PHA and QH channels. During the final 2 min of the initial calibration portion, the QH was replaced by the RWSD. At t_o+06, the aircraft began a turn at a planned turn rate of 18^o per minute. During the turn the aircraft heading was continuously monitored and antenna changeovers (as indicated in fig. 6-2) were made when the aircraft heading relative to the satellite reached the value specified in the test operations plan. Throughout the circular portion of the flight, one receiving system acquired data for the three-element slot-dipole antenna while the other acquired data for the phased-array/patch combination. After the circle was completed, a 4-min straight-line segment was flown to allow verification and backup for the initial calibration period at the start of the test. The instrumentation recorder was operated continuously throughout the test.

During the 1974 fall series, seven such tests were planned at elevation angles ranging between 10^o and 40^o. These circular paths were difficult to fly successfully, and the continually changing heading made manual C/N_o measurements (used as a backup check during the subsequent analysis) less accurate. During the data analysis it was also found that the "conical" cuts through the phased-array beam did not acquire all the data desired because of the characteristic beam shape of the antenna. The beam shape causes the elevation beam position that yields maximum gain to change as the relative bearing angle to the satellite is changed. Typically, two or three different elevation beam positions were needed to maintain optimum reception during a 90^o heading change from the broadside direction.

In the spring 1975 test series, some additional antenna tests based on linear flightpaths were designed specifically to acquire data for the phased array. For these tests, the planned flightpath consisted of seven straight-line segments, each of 13-min duration. The segments were offset 0^o, 30^o, 60^o, 90^o, 120^o, 150^o, and 180^o relative to ATS-6 on the right side of the aircraft. These segments were easy to fly and were long enough to allow phased-array-antenna beam selection optimization as well as manual measurement of C/N_o and gain calibration for each antenna under test. Data were also acquired for the three-element slot-dipole and patch antenna systems during these tests.

The linear flightpaths, however, had several disadvantages compared with circular paths: (1) less efficient use was made of satellite and flight time, (2) data was available at 30^o azimuthal increments only, rather than quasi-continuously, (3) the total flightpath spanned a much larger geographic region over which the ATS-6 antenna gain coverage may not be entirely constant, and (4) the duration of the test was much longer, increasing the possibility of ATS-6 RF power output variation. The circular flightpath was therefore used for all antenna evaluation tests for which the primary objective

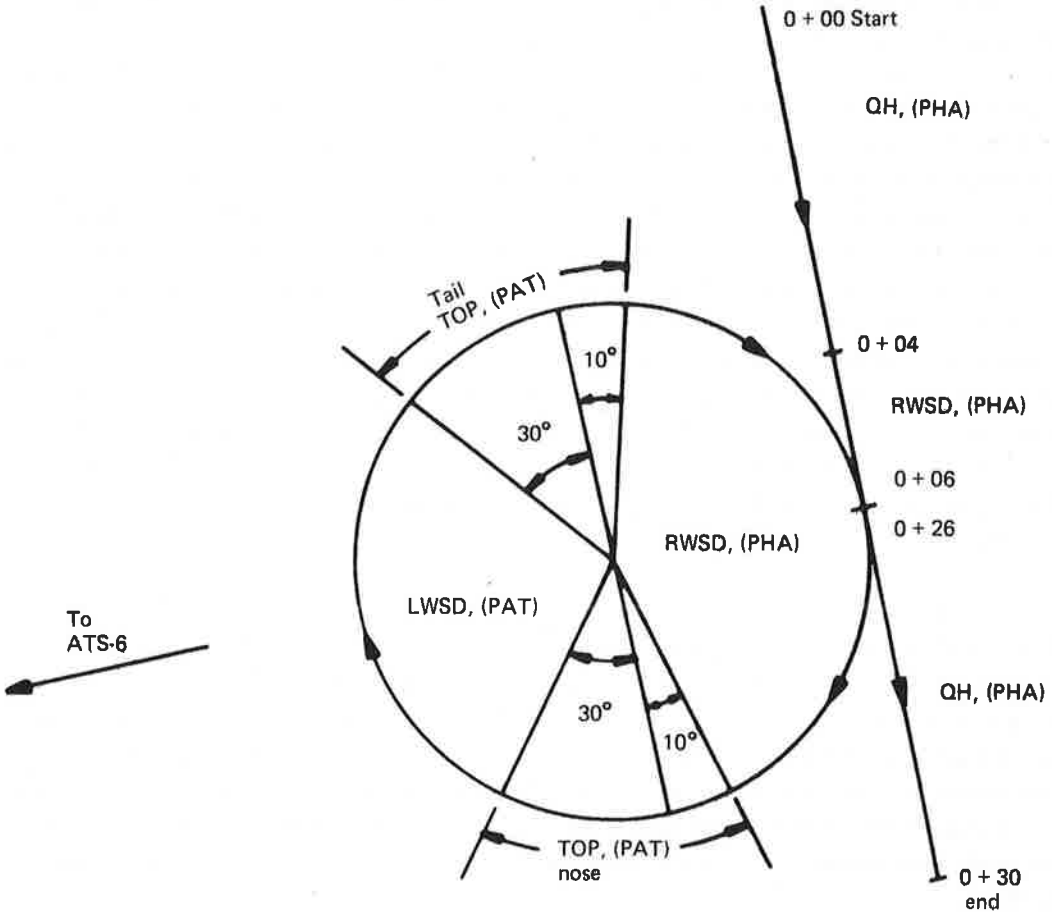

Test segment	Hdg. relative to ATS-6	PLACE RX	FAA RX
Initial calibration	270°	QH, RWSD	PHA
Circle	270° to 350°	RWSD	PHA
	350° to 30°	TOP	PAT
	30° to 150°	LWSD	PAT
	150° to 190°	TOP	PAT
Circle	190° to 270°	RWSD	PHA
Final calibration	270°	QH, RWSD	PHA

Figure 6-2. Antenna Evaluation Test Geometry

was the acquisition of data for operational-type antennas such as the slot dipoles. Several additional circular-path tests were conducted during the spring test series.

6.2.3 Antenna Evaluation Data Acquisition Summary

A summary of the antenna evaluation tests is given in table 6-1.

6.3 DATA ANALYSIS PROCEDURES

The parameters required for presentation of antenna evaluation test results are antenna gain, signal-to-multipath interference ratio (S/I), elevation angle, and relative bearing angle to ATS-6.

6.3.1 Bearing and Elevation Angles Computation

The satellite elevation angle was computed from fundamental trigonometry using the known satellite and aircraft locations. The relative bearing angle to the satellite was computed from stripouts of aircraft magnetic heading used in conjunction with the known satellite direction and magnetic variation at the test location.

Aircraft roll angle stripouts were examined whenever such information was available, and data points were discarded if roll exceeded $\pm 5^{o}$. During normally executed flights, the aircraft roll angle exceeded $\pm 5^{o}$ only on infrequent occasions; hence, data purges due to aircraft roll constituted only a small percentage of the data base. Aircraft pitch angle was normally between 4^{o} and 6^{o} (nose up) during data acquisition. This flight attitude is normal at the altitude and velocity conditions (30,000 ft, 375 kn) employed for antenna tests. No adjustments (or data censoring) were made due to pitch angle considerations.

6.3.2 C/N_o and S/I Determination

The calculation of C/N_o and S/I is basic to all antenna evaluation tests. The cw carrier transmitted from Rosman to the aircraft via ATS-6 was processed by the envelope detector in the carrier detector unit. The detected envelope output was FM recorded and computer analyzed off-line to determine C/N_o and S/I. Values of S/I up to 20 dB, which represents the multipath resolution capability of the analysis technique, can be estimated. A detailed description of the mathematical basis for this analysis and the algorithms used are given in volume IV of this report. The data acquisition procedures and algorithm made it possible to obtain C/N_o and S/I estimates as often as every 3 sec for the antenna tests.

TABLE 6-1. ANTENNA EVALUATION DATA ACQUISITION SUMMARY

Date, mo/day/yr	Elev angle, deg	Flight geometry	Test duration, hr + min	Antenna tested	Remarks
9-24-74	30	Circular	0+30	SDP, PHA	As per figure 3-5
10-01-74	40	Circular	0+30	SDP, PHA	Flightpath deviations due to ATC conflicts
10-23-74	25	Circular	0+30	SDP, PHA, PAT	As per figure 3-5
10-24-74	19	Circular	0+30	SDP, PHA, PAT	As per figure 3-5
10-29-74	15	Circular	0+30	SDP, PHA, PAT	As per figure 3-5
11-21-74	19	Circular	0+30	SDP, PHA, PAT	As per figure 3-5
1-21-75	40	Linear	1+50	SDP, PHA, PAT	Ground test at NAFEC, various headings by taxiing aircraft
1-22-75	9	Linear	0+30	SDP, PHA	Three segments
1-27-75	17	Linear	1+30	SDP, PHA, PAT	Seven segments
3-25-75	15	Circular	0+20	SDP	Bad weather
3-27-75	14	Linear	1+30	SDP, PHA, PAT	Seven segments
4-01-75	15	Circular	0+20	SDP	Bad weather

6.3.3 Antenna Gain Calculation

The relative gain of the antennas was deduced by comparing the received power levels at the antenna terminals. Absolute gain was estimated by using the quad helix as a standard, since it is known to provide 15.5-dB gain to RHC polarized signals when optimally pointed. As a first step in calculating antenna gain, the value of the receiving system's equivalent noise power density, N_o (in dBW/Hz), referred to the antenna terminals is determined. The applicable equation is

$$N_o = -204.0 + L_t + NF_{op} , \qquad (6\text{-}1)$$

where:

L_t = total RF losses (in dB) between the antenna terminals and the preamplifier input terminal, as determined from RF subsystem calibration measurements

NF_{op} = measured receiving system operating noise figure (in dB) referred to the preamplifier input terminals

The received signal strength, S_A (in dBW), at the antenna terminals is then calculated from the measured C/N_o and the N_o value determined above; i.e.,

$$S_A = C/N_o + N_o \quad . \tag{6-2}$$

The unknown gain, G_A (in dB), of an antenna under test can then be determined from

$$G_A = G_{QH} - (S_{QH} - S_A) \ , \tag{6-3}$$

where:

G_{QH} = known gain of reference QH antenna (dB)
S_{QH} = received signal strength at QH output terminals (dBW)
S_A = received signal strength at output terminals of antenna under test (dBW).

Quad-helix gain calibration data, i.e., S_{QH}, was not available for all segments since (1) quad-helix azimuthal steering was restricted to $\pm 110^o$ from the nose and (2) operational procedures and RF subsystem hardware constraints sometimes precluded acquisition of quad-helix reference gain data. However, additional information was available from signal strength measurements made during other tests in adjacent time periods. These measurements allowed the expected ATS-6 signal strength to be determined for certain test areas, especially along the modem evaluation Type II test path at an elevation angle of 15^o. These data have been used on occasion to augment the normal quad-helix antenna gain calibration data, especially during those portions of the linear-path tests for which the quad helix could not be pointed toward the Satellite. Test results that incorporate the use of such data are so identified.

6.3.4 Reference Gain Antenna

Inherent in all experimentally derived values of antenna gain is the assumption that the reference quad-helix antenna gain actually achieved during the calibration measurement portion of the flightpath is, in fact, 15.5 dB. The peak gain of the quad-helix antenna was verified by full-scale measurements on the antenna range on three separate occasions: once prior to initial installation and twice during subsequent removals for antenna servicing and recalibration. The most recent recalibration was in mid-1974 just prior to installation for the ATS-6 test program. During the initial development of the antenna, measurements were made using a 1/20-scale-model horn antenna, installed on a model KC-135 aircraft. These measurements confirmed that the pattern was not significantly affected by the airframe for broadside pointing. It is therefore concluded that the gain characteristics broadside to the aircraft at elevation angles above 15^o are closely represented by the full-scale gain measurements referred to above.

6.4 THREE-ELEMENT SLOT-DIPOLE ANTENNA SYSTEM RESULTS

This section presents plotted and tabulated gain and S/I data for the slot-dipole antenna system. Gain and S/I data derived from antenna range measurements are presented for comparison.

6.4.1 Experimental Gain and S/I Data for Slot Dipoles

Seven circular-path flight tests were conducted for the slot-dipole antenna system. The test conditions are summarized in table 6-2 and selected results are plotted in figures 6-3 through 6-6.

6.4.1.1 Experimentally Measured Gain – Results obtained for the April 1 and March 25, 1975, flight tests will be discussed first. These two tests were conducted in the same area at a nominal ATS-6 elevation angle of 15°. Although high-quality received signal strength data for the antennas was obtained on each occasion, aircraft roll and pitch data was not acquired for either of these tests due to a hardware fault associated with operation of the instrumentation gyro sensor. Aircraft heading data was recorded and confirms that both tests were well flown.

Comparison of results reveals gain asymmetry that is opposite for the two tests: on March 25 the measured gain was higher for the right-side antenna, while on April 1 the gain was higher for the left-side antenna. This suggests that the aircraft bank angle may have been nonzero and of opposite polarity for the two tests. Closer investigation tends to confirm the plausibility of this argument.

TABLE 6-2. SLOT-DIPOLE-ANTENNA CIRCULAR FLIGHT SUMMARY

Date	Elev angle, deg	Figure
April 1, 1975	15	6-3
March 25, 1975	15	6-4
November 21, 1974	19	6-5
Composite[a]	20	6-6
October 24, 1974	19	5-5 of volume VII
October 29, 1974	16	5-6 of volume VII
October 23, 1974	25	5-8 of volume VII
September 24, 1974	28	5-7 of volume VII

[a]Composite plot derived from figures 6-3, 6-4, and 6-5.

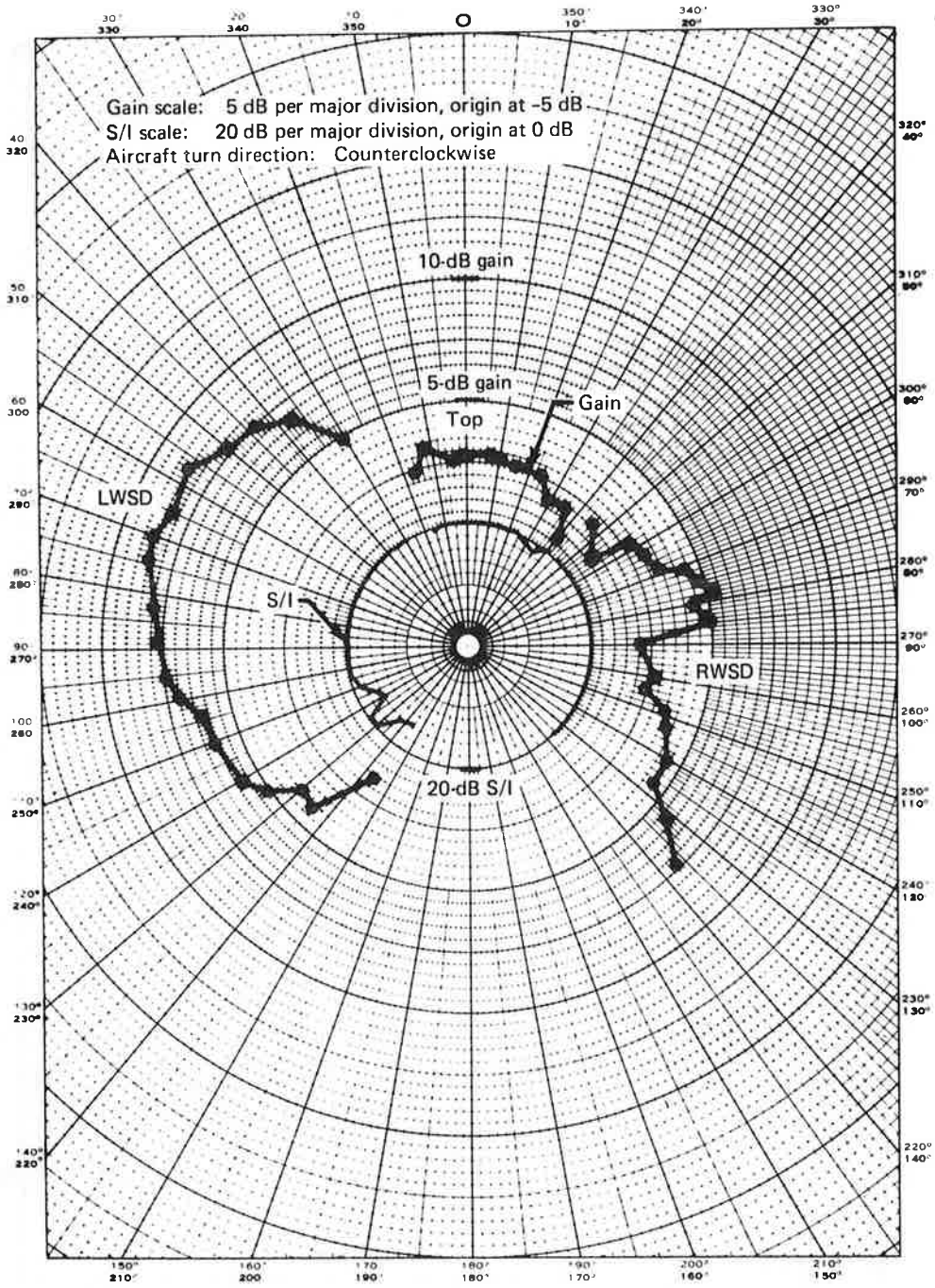

Figure 6-3. Three-Element Slot-Dipole Antenna System Gain and S/I, April 1, 1975, Elevation Angle = 15°

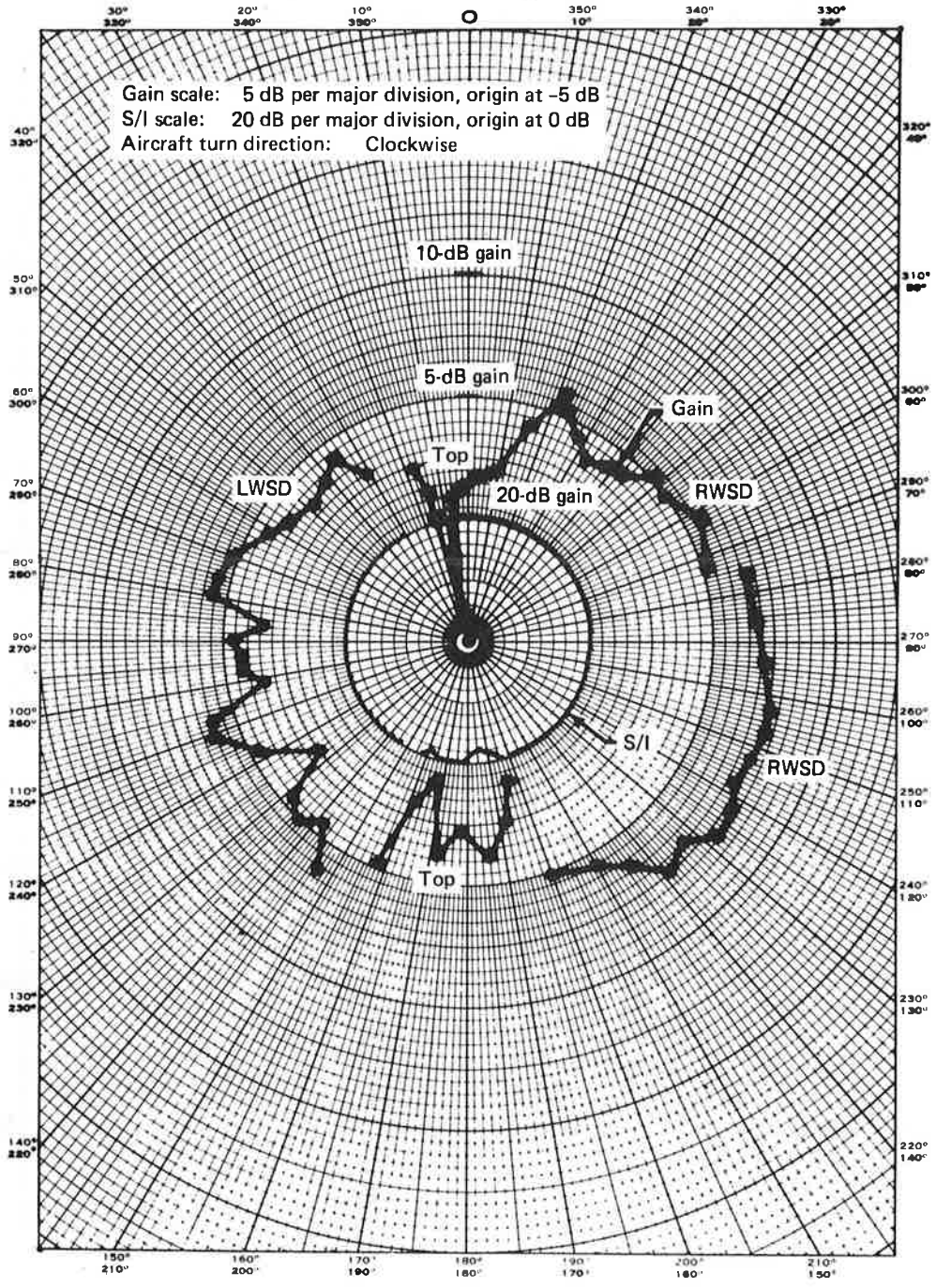

Figure 6-4. Three-Element Slot-Dipole Antenna System Gain and S/I, March 25, 1975, Elevation Angle = 15°

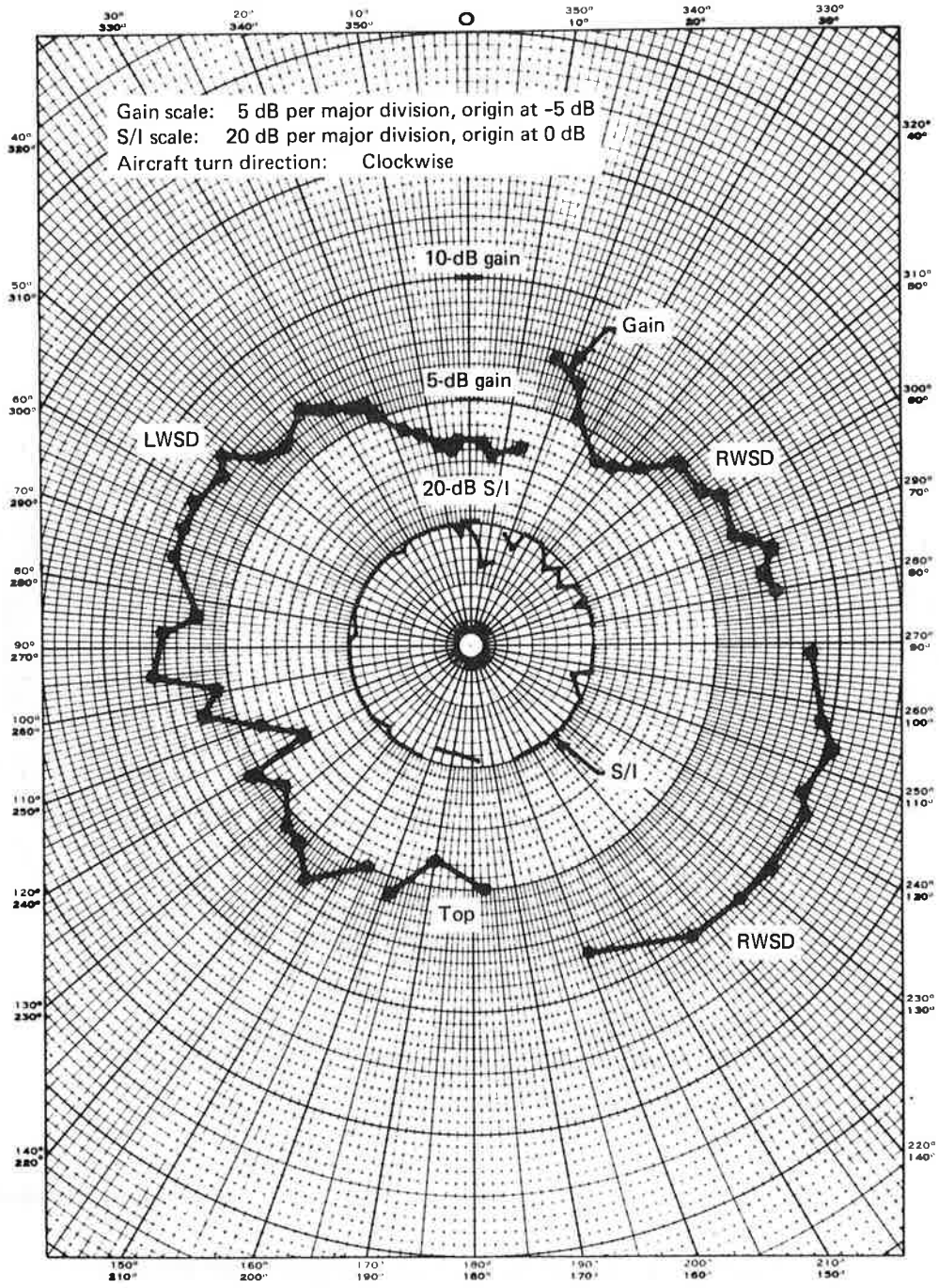

Figure 6-5. Three-Element Slot-Dipole Antenna System Gain and S/I, November 21, 1974, Elevation Angle = 19°

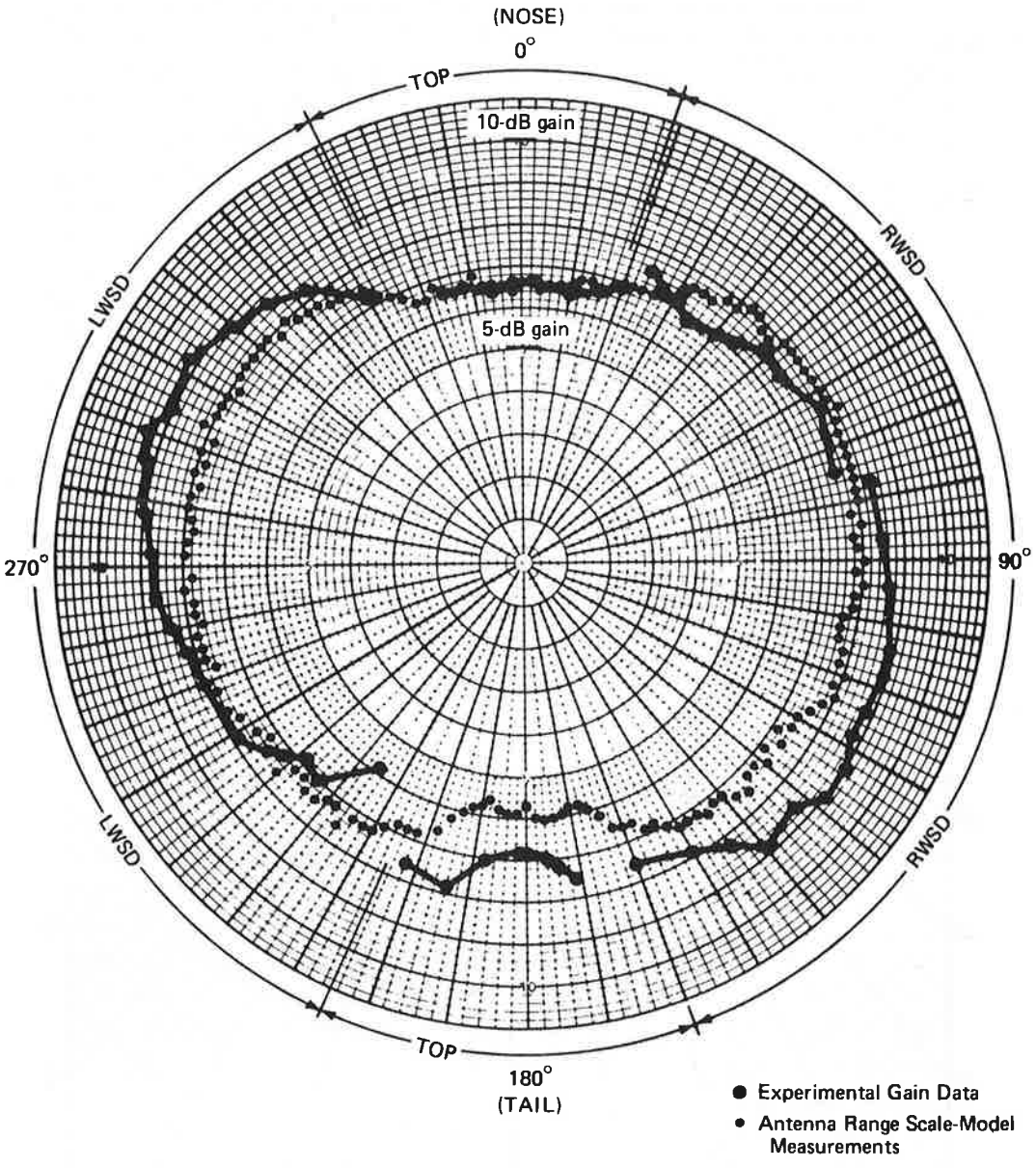

Figure 6-6. Slot-Dipole-System Composite Gain at 20° Elevation

On April 1, the circular flightpath was counterclockwise as viewed from the top, i.e., the airplane heading was decreasing and the relative bearing to the satellite was gradually increasing during the test. The small bank angle for this circular path would be expected to effectively increase the elevation angle for the LWSD and decrease it for the RWSD. On this particular flight, westerly winds of approximately 150 kn were experienced at altitude. A discussion with flight personnel confirmed that a compensating banking maneuver would be expected, which would increase the effective elevation angle for the LWSD but would reduce the elevation angle during the RWSD illumination portion. As a result, it is estimated that the broadside effective elevation angle for the LWSD was approximately 20^{o} while that for the RWSD was roughly 10^{o}. At the lower elevation angles, the antenna gain is very sensitive to small changes in elevation angle. The foregoing effects appear to explain the gain asymmetry in figure 6-3.

On March 25, the circular path was clockwise. The resultant bank angle would therefore be expected to have the opposite effect on effective elevation angle for the two side-mounted antennas (increase for RWSD, decrease for LWSD). Because wind velocity was less than on April 1, any compensating bank angle due to crosswind should be less for this test. Again, the effects of bank angle seem to be present in the data of figure 6-4. Comparison with figure 6-3 also reveals the complementary nature of the measured antenna gains, which is attributed to the opposite direction of circular flight for the two tests. The reason for the March 25 signal dropout at 10^{o} left of the nose is not known. This type of dropout was not observed on any other data runs at similar geometries, and hence it can be concluded that it is due to causes other than the antenna itself.

A third test result corresponding to an elevation angle of 19^{o} is presented in figure 6-5. This test was conducted on November 21, 1974, with the circular portion being in a clockwise direction. The aircraft parameter data shows that the average bank angle was near 0^{o} for the major portion of the test, with only a few excursions in excess of 5^{o}. The pitch angle was in the range of 3^{o} to 7^{o}, nose-up attitude. The results agree reasonably well with the higher elevation angle portions of the March 25 and April 1 tests, but a higher than expected gain was observed for the RWSD between 90^{o} and 160^{o} from the nose. For the clockwise flightpath used, data for these angles was acquired on the northeast quadrant of the circle. The test area was near the 3-dB contour of the ATS-6 antenna pattern. Pattern overlays on the test area show that nonuniform illumination by the ATS-6 antenna of 1 to 3 dB is likely, with the maximum signal strength expected in the northeast quadrant. This may explain the unexpectedly large apparent gain for this portion of the test.

A composite-gain pattern derived from the foregoing three tests is shown in figure 6-6. The LWSD data is primarily taken from the April 1 test, the RWSD is essentially that of the March 25 test, and the TOP data is a weighted combination of all three. This represents an experimental composite-gain conic for the slot-dipole system for an elevation angle of about 20^{o}. For reference, the antenna range scale-model gain conic obtained from radiation distribution plots is given and is seen to agree reasonably well with the experimental data.

Tests performed on September 24 and October 23, 1974, and a ground test conducted January 21, 1975, provide slot-dipole antenna performance data at higher elevation angles. Results for the ground test are given in table 6-3. Data was acquired while the aircraft was parked at the NAFEC airport (elevation angle 40^{o}). Various bearing angles relative to the satellite were obtained by taxiing the aircraft to a new orientation between measurements. Results agree closely with those of the October 23 test.

TABLE 6-3. RWSD ANTENNA GAIN DATA,[a] JANUARY 21, 1975, ELEVATION ANGLE = 40^{o}

Bearing angle to ATS-6, deg	Real-time measured C/N_o, dB-Hz	Antenna gain, dB
16	45.3	6.9
30	46.6	7.6
60	46.5	7.5
89	48.7	10.8
124	48.7	10.8[b]
150	45.9	7.8[b]
164	44.5	6.4[b]

[a]Data acquired during KC-135 taxi test at NAFEC, Atlantic City, New Jersey.

[b]Direct gain calibrator using quad helix was not available. ATS-6 forward-link calibration measurements made at other times and locations during the same test have been used.

6.4.1.2 Experimentally Measured S/I – Also shown in figures 6-3 through 6-5 are the measured values of S/I derived from computer analysis of the recorded envelope detector output. As previously mentioned, the procedure has limited multipath resolution at S/I values in excess of 20 dB: therefore, points with an estimated S/I larger than 20 dB are plotted at the 20-dB level. For all cases, it is observed that S/I is usually greater than 20 dB, with occasional dips into the 15- to 20-dB range, and a few more severe drops in the vicinity of the nose for the top-mounted antenna. This S/I performance is in general agreement with predicions of S/I based on antenna range measurements used in conjunction with the specular-point and surface integration models discussed in section 6.4.2.

6.4.2 Slot-Dipole Gain and S/I Determined From Antenna Range Measurements

Principal-polarization and cross-polarization radiation patterns of the three-element slot-dipole system were obtained on an antenna range using scale-model antennas installed on a 1/20-scale-model KC-135. For these scale-model measurements, the side-mounted antenna was installed at station 696 in the wing/body fairing area, a location somewhat forward of the actual installed location (station 766). These range measurements provided a full set of radiation distribution plots and analog gain patterns. The side-mounted antennas were sufficiently characterized to allow calculation of the

theoretical S/I presented below. Representative gain patterns (conics) from the scale-model measurements for one of the side-mounted antennas for angles of 10^{o} and 20^{o} above the horizon are shown in figure 6-7.

A computer program was used in conjunction with the antenna range measurements to calculate the theoretical S/I as a function of aircraft/satellite geometry for the side-mounted antennas. The top-mounted antenna was not included in these calculations because the range data acquired for the TOP antenna (RHC and LHC patterns) did not provide the complete antenna characterization required for the theoretical S/I calculations. The calculated theoretical S/I for the side-mounted wing-root slot dipoles is shown in figure 6-8. Although the S/I computations in the fore and aft directions are included, the TOP antenna would normally be used fore and aft. The S/I for the side antennas in these directions is therefore somewhat academic but provides a comparison reference for the experimental S/I data.

A rigorous determination of the multipath interference requires integration of the complex antenna pattern over the total ocean surface and thus a large amount of computer time. In the S/I derivation of figure 6-8, we have assumed the "steepest descent" solution and have characterized the multipath signal by its specular-point values in order to reduce the computational effort. The results presented are thus not exact but are a good approximation, especially for modest sea-slope cases. In fact, the above approach may be argued to provide worst-case estimates of S/I since the earth's divergence effect is neglected and the scattered energy is assumed to arrive only from the specular-point region. For grazing angles on the order of 10^{o}, the divergence factor will attenuate the I component of the S/I by approximately 2 dB and if the aircraft antenna pattern is integrated over the diffuse sea scatter process, its well-known rolloff characteristics (θ-plane) provide further multipath rejection.

Some sample calculations of predicted S/I were made using an integration over the sea surface rather than the specular-point model. For the cases tested, a larger value of S/I was predicted by the surface integration model, as expected, providing good agreement with experimental data. Comparative results obtained for the specular-point and surface integration model are given in table 6-4. Details of the derivation of S/I from antenna range data are given in appendix A of volume VII.

6.4.3 Discussion of Slot-Dipole Results and Conclusions

Performance data for the three-element slot-dipole antenna system was acquired experimentally over a range of satellite elevation angles between 10^{o} and 40^{o}. At elevation angles above 20^{o}, the experimentally measured antenna gain was in excess of 4 dB at essentially all azimuthal angles except in the forward direction with the TOP antenna. In the forward direction ($\pm 20^{o}$ from the nose), the TOP antenna gain was 3.5 dB at an elevation angle of 40^{o}. The peak gain measured for the side-mounted antennas was approximately 10 dB. At the higher elevation angles, the experimentally measured gain frequently exceeded the gain values determined from antenna range data by about 2 dB.

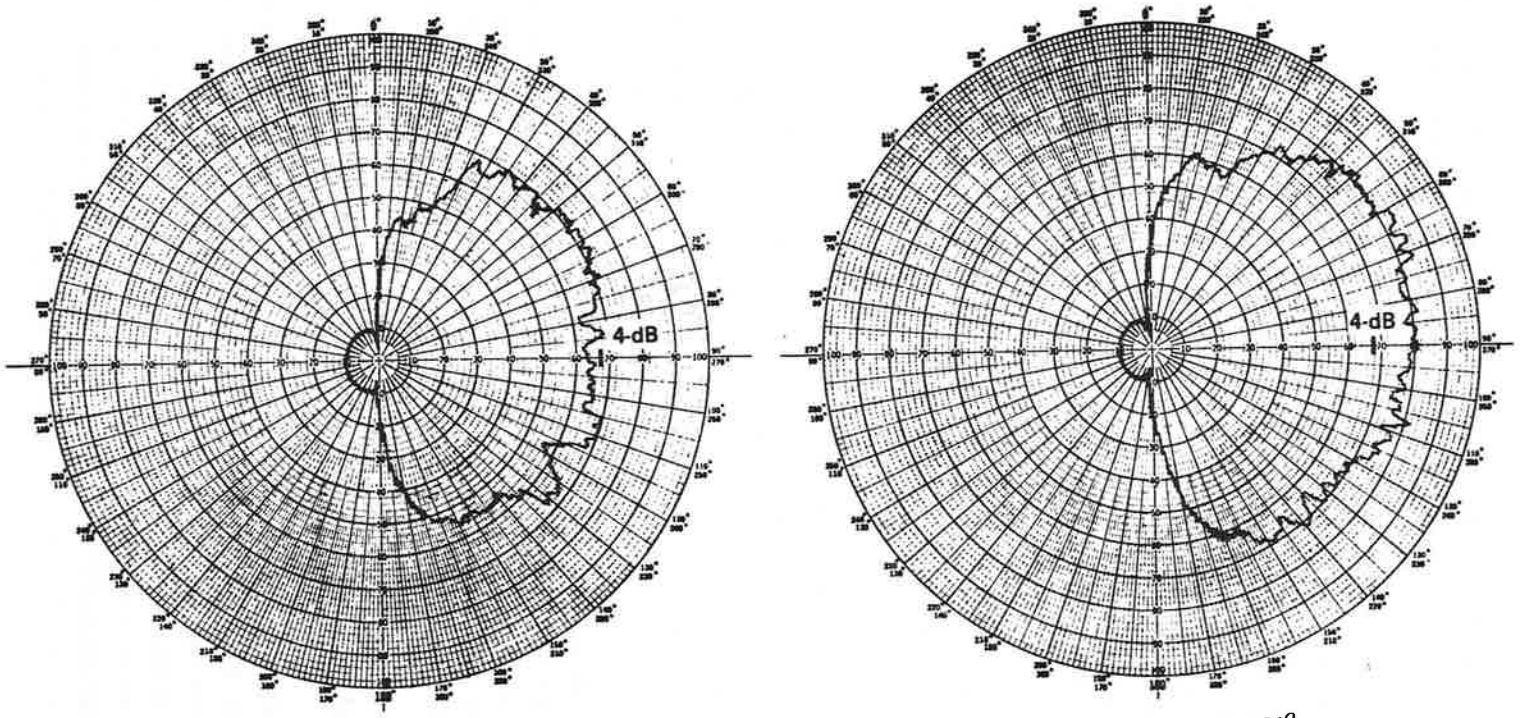

(a) Elevation Angle = 10°

(b) Elevation Angle = 20°

Note:

1) Plots are in voltage units, 67V equivalent to 4.0-dB gain.
2) Patterns are conical cuts; polarization is RHC.
3) Range data acquired using 1/20th-scale model

Figure 6-7. Wing-Root Slot-Dipole Antenna Range Gain at Elevation Angles of 10° and 20°

TABLE 6-4. COMPARISON OF SPECULAR-POINT AND SURFACE INTEGRATION MODEL PREDICTION OF S/I FOR SLOT-DIPOLE ANTENNA

Elevation angle, deg	Azimuthal angle, ϕ (from aircraft nose), deg	S/I predicted by specular-point model, dB	Surface integration model	
			RMS sea slope, deg	Predicted S/I, dB
15	90	17	9	22.0
19	45	20	1	23.6
19	45	20	6	25.0
19	45	20	15	26.8

At elevation angles below 20^{o}, the experimental gain measurements were quite sensitive to aircraft motions affecting the aircraft/satellite geometry but were in general agreement with range data gain values. Although experimental scatter was observed in the measured gain data, there was no evidence of significant pattern holes or coverage deficiencies at any of the geometries tested. The several sets of data at a nominal elevation angle of about 15^{o} illustrate that gain measurement repeatability at low elevation angles is difficult because of the sensitivity to aircraft maneuvers caused by the characteristic rapid change in gain patterns at the lower elevation angles.

The experimental data suggests that the slot dipoles may be somewhat more directional in the roll plane than indicated by the antenna range scale-model measurements. The experimental data scatter and the relatively small amount of data available, however, preclude drawing firm conclusions on this point.

Specific items with potential for causing the experimentally measured gains to exceed those determined from antenna range measurements have been investigated but have not been positively isolated as contributors. Several possibilities are discussed below.

a. The overall RF insertion loss, L_t, between an antenna and the preamplifier has an uncertainty (in all cases less than 1.0 dB). Review of available calibration data suggests that the value of L_t tabulated for the RWSD andLWSD RF paths may be too large by 0.5 to 1.0 dB. As shown by equations (6-1) to (6-3), an error in L_t translates directly into a corresponding error in the calculated antenna gain. It is therefore possible that calculated gains for the RWSD and LWSD are too large by 0.5 to 1.0 dB because of this contribution. (Error contribution due to NF_{op} measurements is believed to be small due to the high degree of consistency indicated by the cross-checks available and the large number of measurement repetitions.)

Note:

1) S/I values computed in accordance with specular point model. Values are in dB.
2) Conic angle (θ) = 80° corresponds to elevation angle of 10°.
3) Slot-dipole antennas located at station 696 in wing-body fairing.
4) Range pattern data acquired using 1/20th-scale model.

Conic angle, θ

50	9	10	11	11	13	13	14	14	15	17	17	18	18	18	18	18	19	19	20	20	19	20	19
	8	9	10	12	12	13	15	14	15	16	17	17	17	18	18	18	18	19	19	19	19	19	20
	8	10	10	10	12	14	14	15	16	17	16	17	17	18	18	18	19	20	19	19	20	19	19
	9	8	11	12	12	15	14	15	16	16	16	18	18	19	18	18	19	18	19	18	19	19	20
	8	9	11	11	12	13	14	14	15	16	17	17	17	18	19	18	18	19	19	19	19	19	19
60	8	10	11	13	13	14	14	15	16	16	18	17	19	18	18	19	19	18	18	18	19	19	20
	9	10	12	13	13	13	15	16	16	16	17	17	18	18	18	18	18	19	18	18	19	19	19
	6	9	11	12	13	15	15	17	16	19	19	17	18	18	19	20	19	19	19	18	18	19	19
	7	7	11	11	11	13	15	15	16	17	17	18	17	17	17	18	18	18	18	19	19	19	18
	5	8	12	11	12	13	15	15	15	16	16	17	18	16	18	18	17	18	17	21	19	18	18
70	6	7	9	10	12	12	14	15	16	19	16	17	17	17	17	17	17	18	18	17	18	18	18
	7	7	11	11	13	14	14	15	16	16	16	17	20	20	18	17	17	19	20	17	19	17	17
	6	8	8	12	13	13	18	15	15	19	17	17	16	17	19	16	17	18	20	20	18	17	20
	1	6	8	12	13	13	16	19	16	16	17	17	17	16	17	18	18	17	18	20	17	16	17
	4	8	8	12	14	14	15	17	17	17	18	16	17	17	17	16	17	20	16	18	16	16	16
80	0	5	10	12	14	16	15	18	18	19	17	18	17	17	17	19	16	18	17	17	16	19	15
	180					190					200					210					220		

Azimuth angle, ϕ

Conic angle, θ

50	21	22	21	21	21	21	21	21	21	21	21	21	21	20	22	20	21	20	20	20	20	21	19
	21	20	20	21	21	22	21	21	21	21	21	21	21	21	21	20	20	21	20	20	20	20	20
	21	22	22	22	22	20	20	21	20	21	21	21	20	21	21	21	20	21	20	21	20	19	19
	20	20	21	21	21	21	20	20	22	21	21	21	21	21	21	20	20	20	19	20	21	19	19
	22	20	22	21	20	21	21	22	20	20	22	21	22	21	21	21	21	21	20	21	21	19	19
60	20	21	20	21	22	22	21	21	21	20	21	20	22	22	23	22	22	20	20	20	19	19	20
	21	20	20	20	21	21	20	20	20	20	21	20	20	20	22	21	21	21	21	20	21	19	19
	20	19	22	20	20	19	20	20	20	19	20	20	20	21	20	20	21	20	22	20	19	19	19
	19	20	19	19	19	19	19	19	20	21	21	20	20	20	20	23	21	21	21	20	20	21	21
	19	19	18	18	20	19	21	19	20	20	20	20	21	21	20	20	20	20	20	20	20	20	19
70	18	18	20	19	19	19	18	19	19	19	20	20	21	20	19	20	20	20	21	20	20	22	20
	18	19	19	21	19	19	18	21	19	20	19	19	20	20	19	20	20	19	19	20	19	20	20
	19	18	17	18	18	21	19	19	18	19	20	20	20	21	21	19	20	20	21	20	22	20	21
	17	18	18	18	17	19	18	18	21	19	20	22	21	20	20	20	20	20	22	20	20	21	24
	16	16	17	18	17	16	17	17	18	19	21	18	18	18	19	23	20	21	20	18	18	19	18
80	17	16	17	16	17	17	16	17	17	19	18	16	16	16	20	17	17	17	17	17	16	17	16
	270					280					290					300					310		

Azimuth angle, ϕ

Figure 6-8. Computed S/I for Wing-Root Slot-Dipole Antenna

21	20	20	20	20	21	20	21	21	20	21	21	20	21	21	21	21	22	21	21	21	21	21
20	19	20	20	21	20	20	20	20	21	21	21	21	21	21	21	22	21	21	21	22	21	21
20	20	20	20	20	20	20	22	20	21	20	20	21	20	22	21	21	21	21	20	21	21	21
20	20	19	19	19	20	20	20	20	20	21	21	21	21	21	21	20	22	21	20	20	21	20
19	20	19	19	19	20	19	20	21	19	19	20	20	20	20	20	20	20	21	20	20	21	22
19	20	20	20	20	21	20	19	19	20	21	19	20	20	20	20	20	20	20	20	20	20	20
18	19	19	20	19	19	20	19	20	20	21	21	21	22	21	21	21	21	20	20	20	20	21
18	20	19	18	19	20	21	19	19	20	19	19	19	19	20	21	20	20	20	20	21	18	20
18	18	19	19	18	18	18	19	19	20	20	18	20	19	19	19	19	20	20	20	20	19	19
18	18	18	18	18	18	18	20	20	19	19	19	19	19	19	19	20	19	19	19	19	20	19
17	17	17	18	18	18	18	19	18	18	18	19	20	19	18	19	18	19	19	18	19	20	19
18	18	21	18	18	18	18	18	18	20	19	18	18	19	18	20	21	18	18	19	20	19	18
17	17	17	17	17	18	17	17	18	18	18	18	19	18	17	17	19	18	19	17	17	18	19
16	17	18	15	18	16	16	16	16	16	16	17	16	16	18	18	18	18	20	18	17	17	17
16	15	16	16	18	16	15	17	17	18	18	17	19	17	15	17	16	17	17	16	17	16	16
16	17	17	16	17	19	16	18	15	14	15	19	18	17	17	17	17	17	17	17	16	16	17

50 60 70 80

Conic angle, θ

230 240 250 260 270

Azimuth angle, ϕ

20	20	20	19	19	19	18	19	18	18	19	18	18	18	18	18	17	17	17	15	16	15	50
19	19	19	19	19	19	18	18	19	18	19	19	18	18	19	17	17	17	17	16	15	15	
19	19	18	19	19	20	18	19	18	18	18	18	19	18	19	18	17	17	17	16	15	14	
19	19	19	19	19	19	19	18	18	19	18	18	18	19	18	18	18	17	16	15	15	15	
19	18	20	19	19	19	20	18	19	19	19	18	18	18	18	19	17	17	16	15	16	14	
19	19	19	20	19	19	18	18	20	18	18	18	19	18	18	17	18	17	17	16	15	14	60
20	21	19	19	19	20	19	19	19	19	18	17	17	17	18	18	17	17	18	16	16	15	
21	19	20	19	21	20	19	21	20	20	18	18	17	18	18	18	17	17	16	16	16	16	
19	19	19	19	21	20	20	21	21	19	19	18	18	18	20	18	17	17	17	17	16	14	
20	20	21	21	20	22	20	21	21	19	21	19	19	19	20	20	19	17	16	16	15	15	
21	20	21	21	22	21	21	20	21	21	20	21	20	20	19	20	19	19	19	16	15	15	
20	22	21	22	22	20	20	20	21	20	19	18	17	20	18	19	19	20	19	18	18	15	70
21	22	21	20	20	20	21	20	21	22	21	19	18	17	17	19	17	20	19	17	17	15	
22	22	21	20	18	17	17	17	16	18	18	18	22	20	17	20	20	17	18	19	17	15	
18	19	20	17	16	16	16	15	15	16	16	17	17	16	16	17	18	18	18	15	17	14	
16	16	15	14	14	15	14	13	14	14	14	14	14	13	14	16	15	16	17	16	14	12	80

Conic angle, θ

320 330 340 350 360

Azimuth angle, ϕ

b. The antenna gain values calculated from the experimental data would contain a systematic error, making their values too high if the actual gain achieved with the quad-helix reference antenna was less than the 15.5-dB value determined from full-scale measurements on the antenna range. It is believed that systematic error caused by overestimating the gain of the reference antenna is less than 0.5 dB since (1) experimentally measured peak gains of the phased-array and patch antennas agree well with expected values and (2) the quad-helix antenna was removed and recalibrated on the antenna range on two separate occasions, each time confirming the 15.5-dB value employed. It should also be noted that any systematic error in the gain value assumed for the quad-helix reference gain antenna will affect the calculated gains for all antennas (slot-dipoles, phased array, patch) identically. Gain data for these antennas relative to each other would therefore be unaffected by an error of this type.

c. The scale-model patterns of the slot-dipole antenna were taken at station 696, but the antennas were actually installed at station 766 of the KC-135 due to insufficient space at the original design location. This relocation of antennas is believed to have small effect on the patterns at elevation angles above 10^{o} and, in particular, should not influence the peak gain. This factor is therefore believed to be only a minor contributor, if at all, to the higher than expected gains observed.

The experimentally measured gain of the TOP antenna was usually observed to be less in the forward than in the aft direction, indicating that the normal aircraft pitch angle (4^{o} to 6^{o} nose up) may be influencing performance. This suggests that a more forward location of the TOP antenna might result in improved over-the-nose performance at low elevation angles.

The experimental data showed conclusively that very good multipath rejection was achieved by the three-element slot-dipole antenna system at all geometries tested. The S/I was usually greater than 20 dB, with occasional dips into the 15- to 20-dB range, and a few more severe drops in the vicinity of the nose for the top-mounted antenna. The high multipath rejection achieved is due in part to the fact that the wing-root location provides natural multipath shielding. This performance is in general agreement with the predicted S/I values based on antenna range measurements. The rather large S/I values observed are consistent with results for Type I digital data modem tests, where the bit-error-rate performance curves closely resemble the performance predicted for a purely additive-noise environment without multipath interferance. The Type I BER curves thus confirm that S/I exceeded 15 dB.

6.5 PHASED-ARRAY ANTENNA TEST RESULTS

This section presents gain and S/I data for the phased-array antenna.

6.5.1 Experimental Gain and S/I Data for the Phased Array

One portion of the phased-array antenna data was acquired from "straight-line" flight segments as described in section 6.2.2. Table 6-5 and figure 6-9 present results for three groups of data acquired on the dates and at the locations specified below.

a. Ground test at NAFEC on January 21, 1975, at an elevation angle of 40^{o}
b. Flight test on March 27, 1975, over the North Atlantic at elevation angles between 10^{o} and 15^{o}
c. Flight test on January 27, 1975, over the North Atlantic at elevation angles between 15^{o} and 18^{o}.

During each straight-line segment, the optimum beam position for maximum signal reception was selected. The beam positions are identified according to the manufacturer's nomenclature. Since quad-helix gain calibration data was not available for all straight-line segments, the phased-array gain values sometimes use signal strength calibration measurements of the ATS-6 downlink that were made at other times or locations during the same test. These cases have been so identified in table 6-5.

Five tests were also conducted on circular-track antenna flights. A summary of the test conditions for these flights is tabulated in table 6-6. Due to the antenna's location, data were acquired only in the right-hand hemisphere.

Results for tests conducted on September 24 and October 29, 1975, are presented in figures 6-10 and 6-11. For the test of September 24, at 28^{o} elevation, the elevation beam position selected resulted in near-optimum reception throughout the flights. The data values plotted in figure 6-10. however, appear to be about 1 dB below their expected values, possibly due to a calibration error for this test. The corresponding RWSD data acquired concurrently (plotted in fig. 5-7, vol. VII) also indicate this possibility.

From the results achieved on September 24, October 29, and the straight-line segment tests, it is observed that when the elevation beam position is optimized, the array provides gain of about 10 to 12 dB over a broadside sector. As the azimuth changes toward 0^{o} or 180^{o}, the gain decreases as expected. The measured S/I for this antenna was always in excess of 20 dB whenever the beam position was optimized. This appears to be the expected result due to the narrow roll-plane beamwidth and the side-lobe taper control.

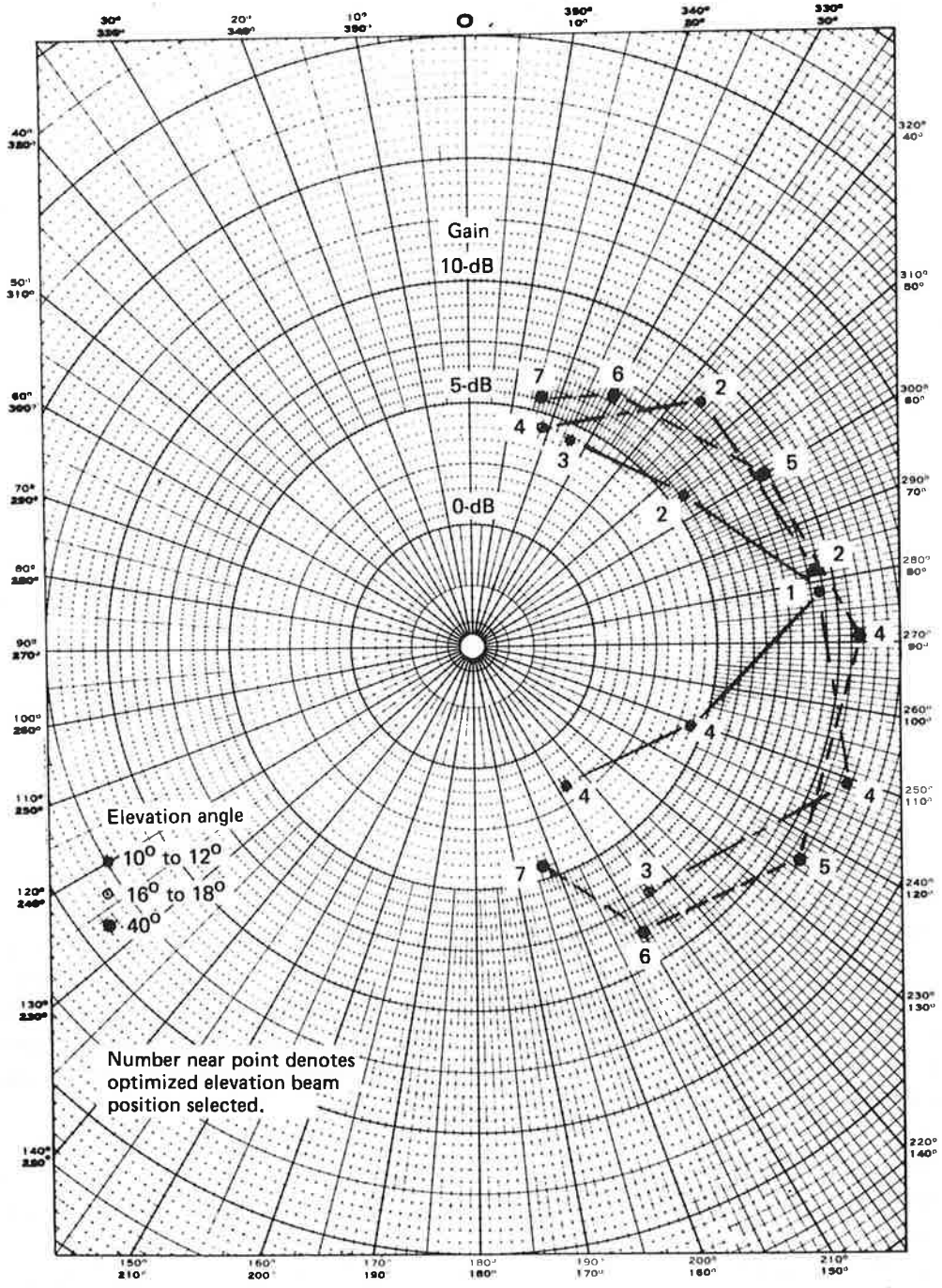

Figure 6-9. Phased-Array Gain Data for "Straight-Line" Tests

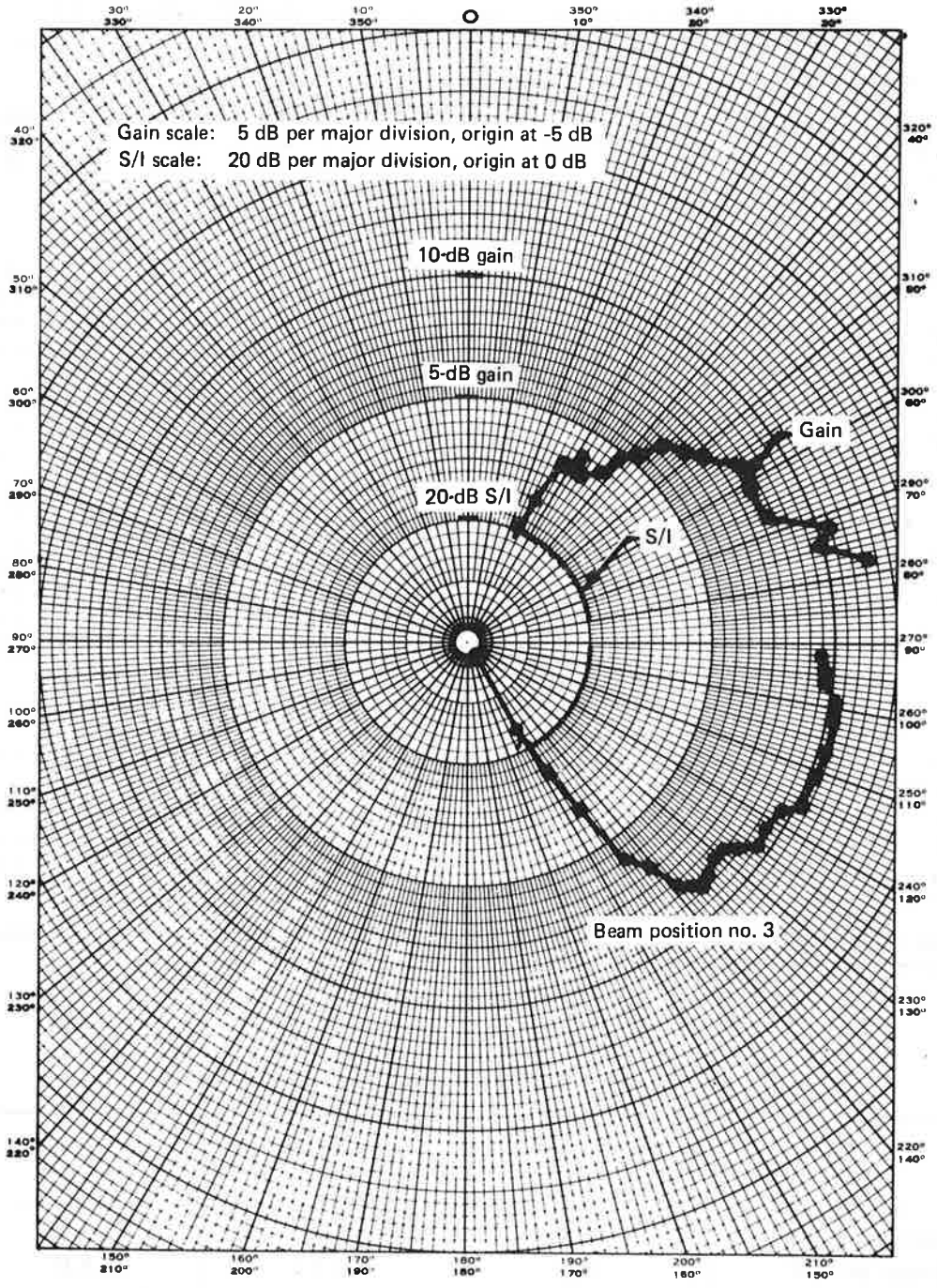

Figure 6-10. Phased-Array Antenna Gain and S/I, September 24, 1974, Elevation Angle = 28°

TABLE 6-5. PHASED-ARRAY GAIN DATA FOR LINEAR SEGMENT TEST

ATS-6 direction, deg		Optimum antenna beam position	C/N_o, dB-Hz		Received signal level, -dBW	Antenna gain, dB
Relative bearing	Elev		Real-time measured	Computer analyzed		
NAFEC Ground Test, January 21, 1975						
16	40	7	42.9	N/A	149.8	5.5
30	40	6	45.1	N/A	147.6	6.8
60	40	5	47.2	N/A	145.5	8.9
89	40	4	48.0	N/A	144.7	10.8
124	40	5	48.1	N/A	144.6	10.9
150	40	6	45.7	N/A	147.0	8.5[a]
164	40	7	42.1	N/A	150.6	4.5[a]
Flight Test, March 27, 1975						
26	12	3	46.6	45.0	147.7	4.3
55	11	2	48.5	46.4	146.3	5.5
82	10	1	50.0	49.9	142.8	9.4
111	11	2	46.0	45.4	147.3	4.5[a]
147	12	4	43.2	42.5	150.2	1.8[a]
Flight Test, January 27, 1975						
18	16	4	41.4	41.6	151.1	4.4[a]
44	17	2	42.9	42.7	150.0	8.7
78	18	2	49.2	49.0	143.7	9.3
111	17	2	51.8	51.5	141.2	11.3[a]
145	16	3	47.9	47.6	145.1	7.4[a]

[a]Indicates that direct gain calibration using the quad helix was not available. ATS-6 downlink calibration measurements made at other times and locations during the same test have been used.

TABLE 6-6. PHASED-ARRAY CIRCULAR FLIGHT SUMMARY

Date	Elevation angle, deg	Elevation beam position	Figure
September 24, 1974	28	3	6-10
October 29, 1974	16	2, 3	6-11
October 24, 1974	19	Not recorded	6-4 of volume VII
November 21, 1974	19	5	6-5 of volume VII
October 23, 1974	25	4	6-6 of volume VII

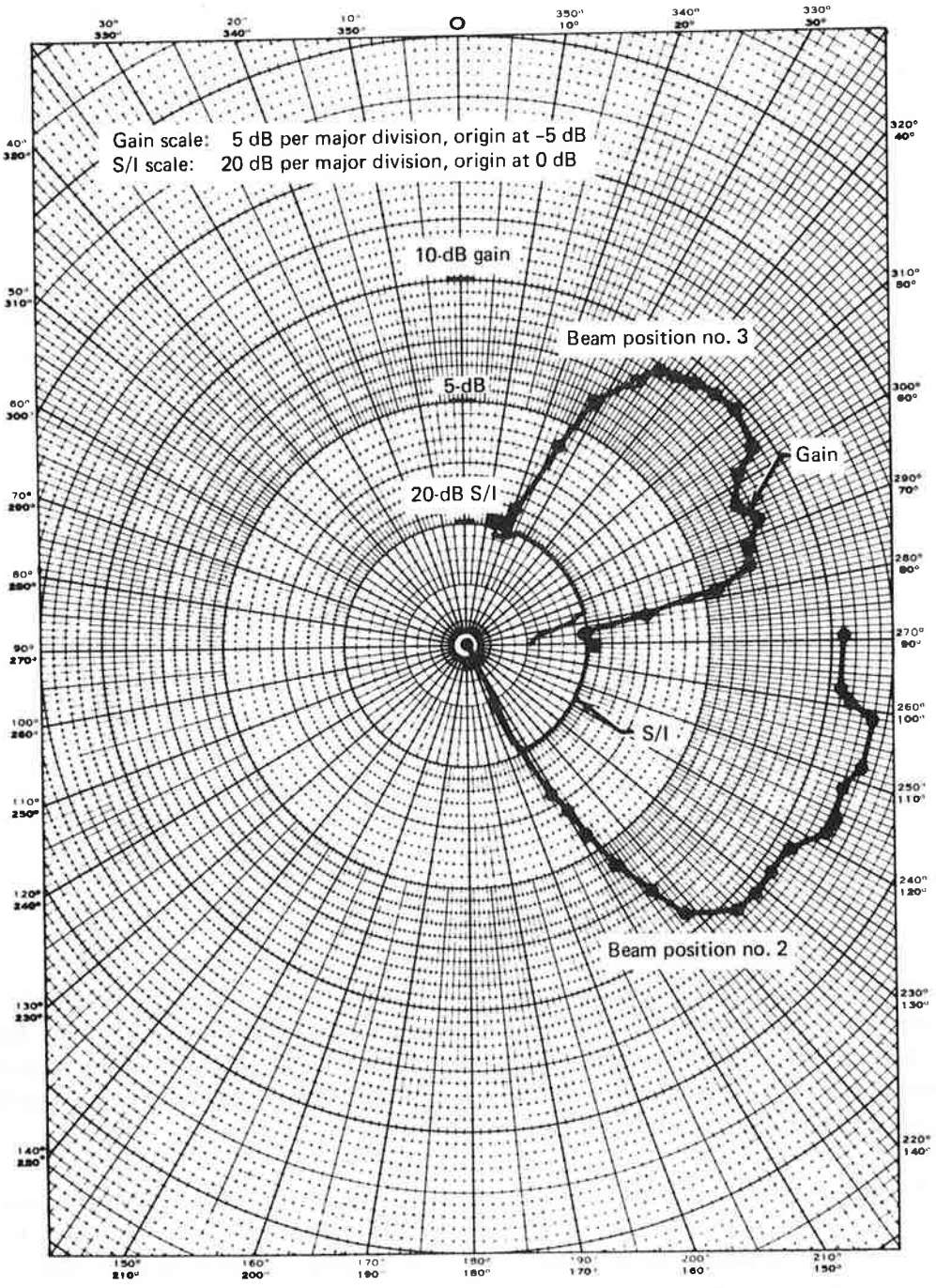

Figure 6-11. Phased-Array Antenna Gain and S/I, October 29, 1974, Elevation Angle = 16°

Test results for other circular flights are provided in figures 6-4, 6-5, and 6-6 of volume VII. For these flights, the elevation beam position experimentally selected during the initial calibration period did not provide optimum reception throughout the tests. These experimental data therefore do not represent the achievable performance under optimized conditions and thus are of limited value. However, the results do serve to illustrate to some degree the interdependency of optimum elevation beam position and relative bearing angle discussed in section 6.2.2. This effect is somewhat typical of phased-array antennas and is caused by their characteristically shaped beam.

From the circular and straight-line flight test data, it can be concluded that the phased array as mounted on the KC-135 provides a peak gain of 11 to 12 dB approximately broadside at an elevation angle of 40^{o}. This measured value agrees well with the full-scale antenna range peak gain value. At an elevation angle of 40^{o}, the 3-dB azimuthal beamwidth is approximately 100^{o}, with the minus 3-dB points of the pattern occurring at 50^{o} and 150^{o} from the nose. For the small amount of data available at elevation angles of 10^{o}, the experimentally measured maximum achievable gain was between 9.0 to 9.5 dB and the 3-dB azimuthal beamwidth was approximately 50^{o}. At azimuthal angles beyond the above useful coverage region, the gain dropped rapidly to low or negative values. No attempt was made to measure side-lobe levels experimentally.

The antenna exhibited consistently good multipath rejection, with the measured S/I being in excess of 20 dB within the useful coverage region.

6.5.2 Antenna Range Pattern Measurements for the Phased Array

Radiation pattern measurements were made by the antenna manufacturer, Ball Brothers Research Corp. Range patterns taken with the full-scale antenna mounted on a 4-ft ground plane show that expected peak gain is approximately 12 dB, and roll-plane beamwidth is between 12^{o} and 15^{o} for each of the nine selectable elevation beam positions.

A limited number of scale-model pattern measurements were also made by the manufacturer. One-tenth-scale antenna units were designed for beam positions 1, 2, and 4. Beam positions 1 and 2 were selected since they are most likely to be affected by the presence of the aircraft wings. Beam position 4 was selected since it represents the higher steering angles and would allow comparison of the patterns from the full-scale model with those from the 1/10-scale model for a position not likely to be seriously affected by the presence of the aircraft structure.

Antennas for the 1/10-scale model were made using etched microstrip circuit-board techniques. The radiating elements were scaled directly from the full-sized elements. The feed lines were too narrow to scale, and therefore a modified feed circuit was designed and tested for use on the 1/10-scale model. The elements were combined in a 1-by-8 array with appropriate phasing for the beam position being modeled.

The scale-model antennas were mounted on a 1/10-scale ground plane using the same coordinates as the full-scale ground plane. Elevation and conical patterns were taken for comparison with full-scale patterns. A 1/10-scale Convair 880 was used to model the aircraft. After installation of the antennas on the 1/10-scale aircraft model, the previously recorded patterns were repeated.

Antenna range patterns for the flight antenna and for the 1/10-scale-model antenna installed on the model Convair 880 are given in figure 6-12 for beam position 2. Since antenna efficiency cannot be scaled, no particular gain is implied in these patterns. Pattern shape is the only comparison that can be made.

6.6 PATCH ANTENNA TEST RESULTS

Four circular-path tests were conducted for the patch antenna. A summary of the test conditions is presented table 6-7.

TABLE 6-7. PATCH ANTENNA CIRCULAR FLIGHT SUMMARY

Date	Satellite elevation angle, deg	Figure
October 23, 1974	25	6-13
November 21, 1974	19	6-14
October 29, 1974	16	6-15
October 24, 1974	19	7-4 of volume VII

Selected test results are presented in figures 6-13, 6-14, and 6-15. From these figures it is apparent that the patch antenna had a gain of approximately 4 dB forward over the nose at elevation angles above 15^{o}. The gain gradually decreased as the satellite bearing angle changed toward the broadside and aft directions or as the satellite elevation angle reduced toward the horizon. Gain in the broadside and more aft directions is about 0 dB at an elevation angle of 16^{o}, increasing to about 2.5 dB at a 25^{o} elevation angle.

Gain data acquired during a ground test at NAFEC is given in table 6-8. This data shows that gain in the forward over-the-nose direction at a higher elevation angle is on the order of 4 dB (3.7 dB measured), decreasing to about 2.5 dB aft of broadside. These results are consistent with the data of figures 6-13, 6-14, and 6-15. Antenna range data for this antenna was not available for inclusion in this report.

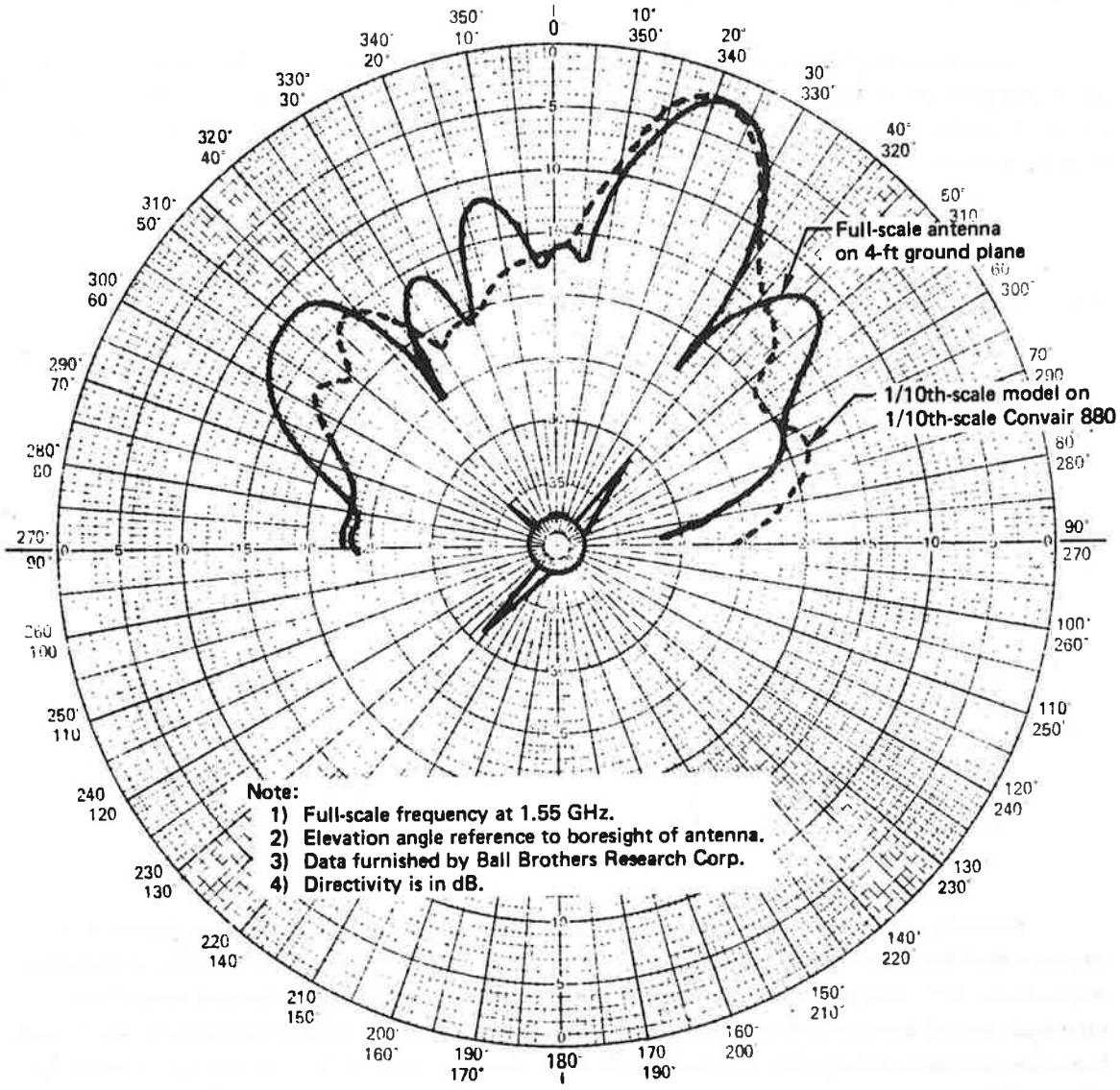

Figure 6-12. Phased-Array Roll-Plane Directivity Determined from Antenna Range Measurements, Beam Position 2

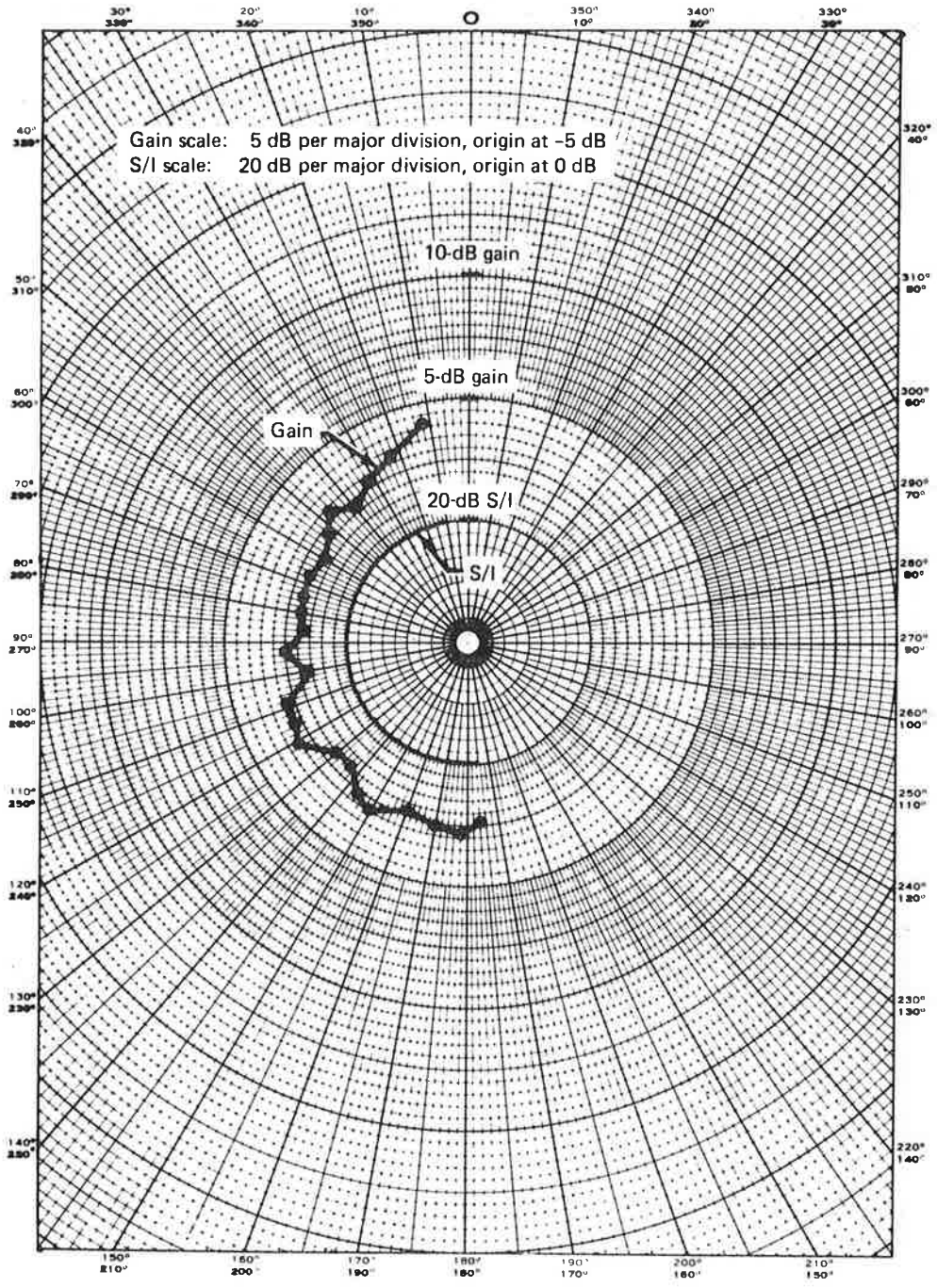

Figure 6-13. Patch Antenna Gain and S/I, October 23, 1974, Elevation Angle = 25^0

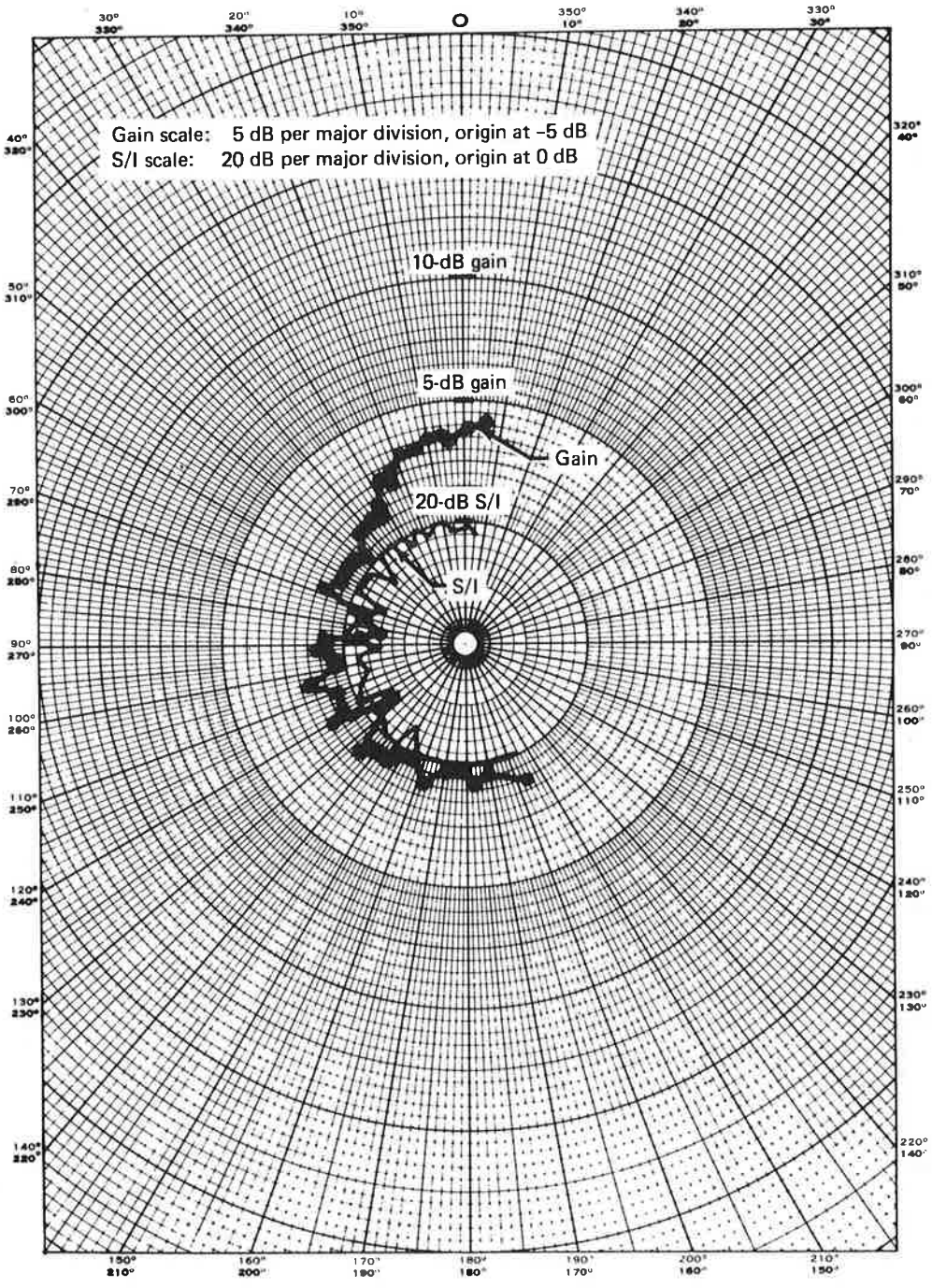

Figure 6-14. Patch Antenna Gain and S/I, November 21, 1974, Elevation Angle = 19^{0}

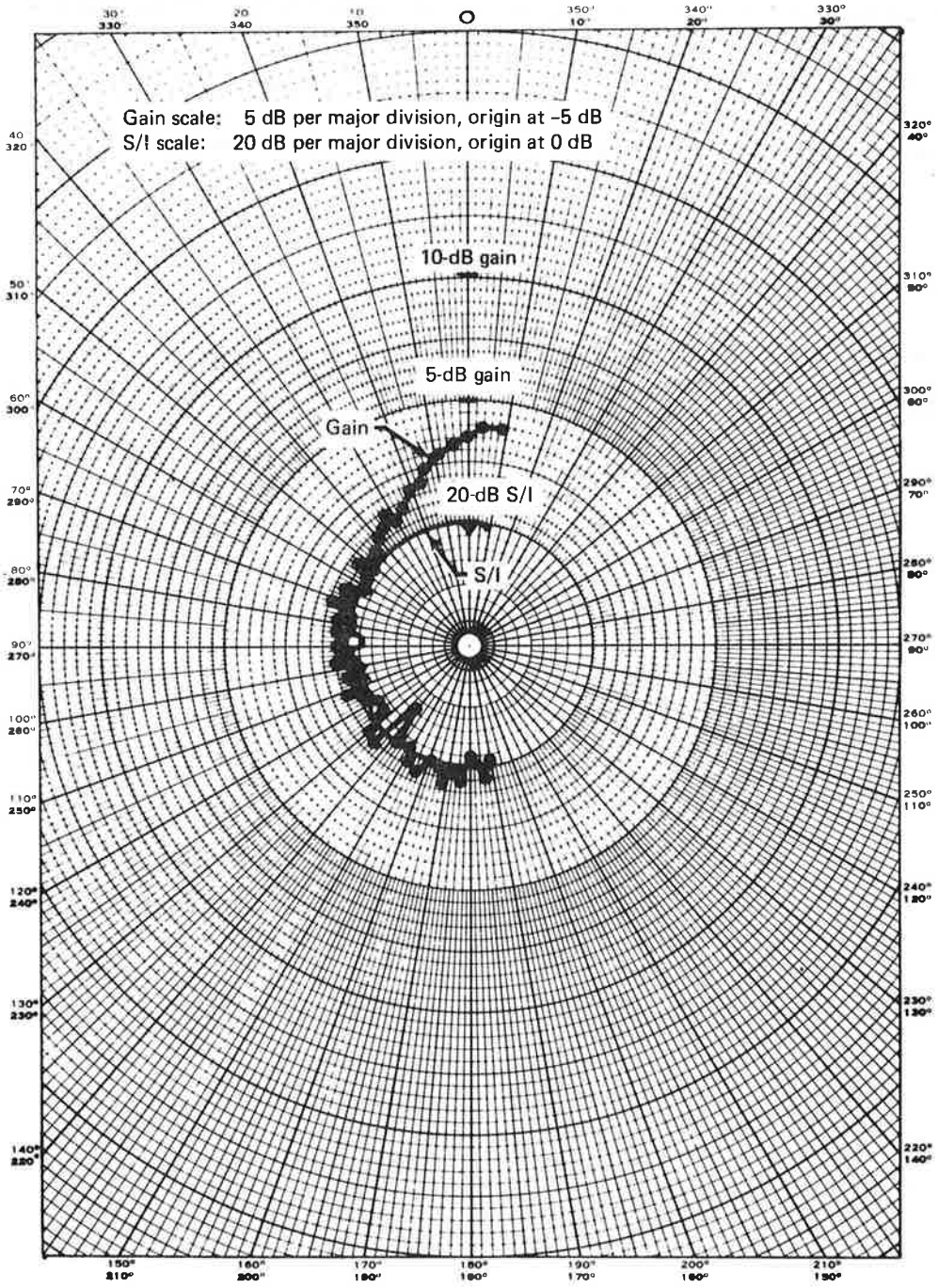

Figure 6-15. Patch Antenna Gain and S/I, October 29, 1974, Elevation Angle = 16°

TABLE 6-8. PATCH ANTENNA GAIN DATA[a] FOR GROUND TEST AT 40° ELEV. ANGLE

ATS-6 direction, deg		C/N_o, dB-Hz		Received signal level, -dBW	Antenna gain, dB
Relative bearing	Elevation	Real time measured	Computer analyzed		
0	40	47.5	N/A	151.6	3.7
16	40	47.5	N/A	151.6	3.4
164	40	45.9	N/A	153.2	2.3[b]

[a]Data acquired during NAFEC ground test.

[b]Direct gain calibration using quad helix was not available. ATS-6 downlink calibration measurements made at other times and locations during the same test have been used.

REFERENCES

1-1 "Integrated Test Plan for ATS-F L-Band Experiment," NASA/GSFC report TP-750-73-1, September 1973.

3-1 R. E. Munson, "Conformal Microstrip Antennas and Microstrip Phased Arrays," IEEE Trans. on Antennas and Propagation, January 1974, p. 74-78.

3-2 G. G. Sanford, "Conformal Microstrip Phased Array for Aircraft Tests With ATS-6," National Electronics Conference, Chicago, 1974, p. 252-257.

3-3 G. G. Sanford and L. Klein, "Development and Test of Conformal Microstrip Airborne Phased Array for Use With the ATS-6 Satellite," paper presented at the IEE Conference on Antennas for Aircraft and Spacecraft, London, England, June 1975.

3-4 "ATS-5 Multipath/Ranging/Digital Data L-Band Experimental Program, Phase I – Experimental Program: Aircraft Communications/Surveillance Via Satellite at L-Band," report FAA-RD-73-57-I, Boeing Commercial Airplane Company, April 1973.

3-5 T. Olsson and B. P. Stapleton, "L-Band Orthogonal-Mode Crossed-Slot Antenna and VHF Crossed-Loop Antenna," contract DOT-TSC-130, August 1972

4-1 P. A. Bello et al., "Impact of Satellite Aeronautical Channel on Modem Specifications, Phase I," report FAA-RD-74-54, March 1974.

4-2 P. A Bello, "Aeronautical Channel Characterization," IEEE Trans. on Comm., vol. COM-21, no. 5, May 1973, p. 548-563.

4-3 H. Staras, "Rough Surface Scattering on a Communication Link," Radio Science, vol. 3 (new series), no. 6, 1968, p. 623-631.

4-4 P. Beckman and A. Spizzichino, THE SCATTERING OF ELECTROMAGNETIC WAVES FROM ROUGH SURFACES, Macmillan Co., New York, 1963, p. 320.

4-5 "ATS-5 Multipath/Ranging/Digital Data L-Band Experimental Program, Phase V – Multipath/Ranging Analysis and Results," report FAA-RD-73-57-V, Boeing Commercial Airplane Company, April 1973.

REFERENCES (Concluded)

5-1 L. A. Frasco and H. D. Goldfein, "Signal Design for Aeronautical Channels," IEEE Trans. on Communications, May 1973, p. 534-547.

5-2 "ATS-5 Multipath/Ranging/Digital Data L-Band Experimental Program, Phase IVD, Volume I – Satellite/Aircraft L-Band Data Communication Tests," report FAA-RD-73-57-IVD, Boeing Commercial Airplane Company, April 1973.

5-3 J. C. Blair and J. F. Balcewicz, "Results of an Experimental Study of Coherent PSK in a Multipath Environment," EASCON '68 Record, p. 607-614.

5-4 H. C. Salwen and C. B. Duncombe, "Performance Evaluation of Data Modems for the Aeronautical Satellite Channel," IEEE Trans. on Communications, July 1975, p. 695-705.

5-5 J. Salz and B. R. Saltzberg, "Double Error Rates in Differentially Coherent Phase Systems," IEEE Trans. on Communication Systems, June 1964, p. 202-295.

A-1 K. D. Kryter and J. H. Ball, "SCIM–A Meter for Measuring the Performance of Speech Communication Systems," interim report, ESD-TDR-64-674, contract AF 19 (628)-2453, Bolt Beranek and Newman, Inc., October 1964.

A-2 N. R. French and J. C. Steinberg, "Factors Governing the Intelligibility of Speech Sounds," JASA, vol. 19, no. 1, January 1947, p. 90-118.

APPENDIX A

RESULTS OF SCIM MEASUREMENTS FOR VOICE MODEMS

One method developed for evaluating voice channel performance has been the speech communication index meter (SCIM) (ref. A-1). The technique is based on the articulation index (AI) concept, as described in reference A-2, and uses synthetic speechlike signals to measure the signal-to-noise ratio at the end of the channel at various audio frequencies. This ensemble of signal-to-noise ratio measurements is then used to calculate the articulation index, a value ranging between 0 and 1. Somewhat implicit in the AI concept is the notion that the AI can be related to other psychometric measures of speech performance, e.g., PB word intelligibility, and thus that an automated SCIM scoring approach could eliminate the need for listener panel evaluations.

SCIM signal transmissions were recorded for each modem following transmission of the word lists. The November test data was transcribed and evaluated at NASA/GSFC using a computerized version of earlier hardware analyzers. AI scores provided by NASA were then collated with the PB word intelligibility scores derived at CBS Laboratories during the same test interval; the resultant plot is shown in figure A-1.

The curves of figure A-1 are from reference A-1 and indicate a universal relationship between AI and various intelligibility measures. For the 400-word lists used here, a curve somewhere between the 256- and 1000-word relationships should presumably be used.

It is observed from the data that the results, in total, straddle such an interpolated curve. However, a definite modem dependency seems to exist. For example, a given articulation index for ANBFM corresponds in general to a much lower word intelligibility than that for the Hybrid No. 1 and 2 modems. Thus, this data refutes a universal relationship between AI (as estimated by SCIM) and word intelligibility.

If in the future it is desired to use the SCIM technique for meaningful evaluations of speech modem performance, a minimum requirement appears to be that the AI (as estimated by SCIM) versus intelligibility curve be calibrated accurately for each modem under test.

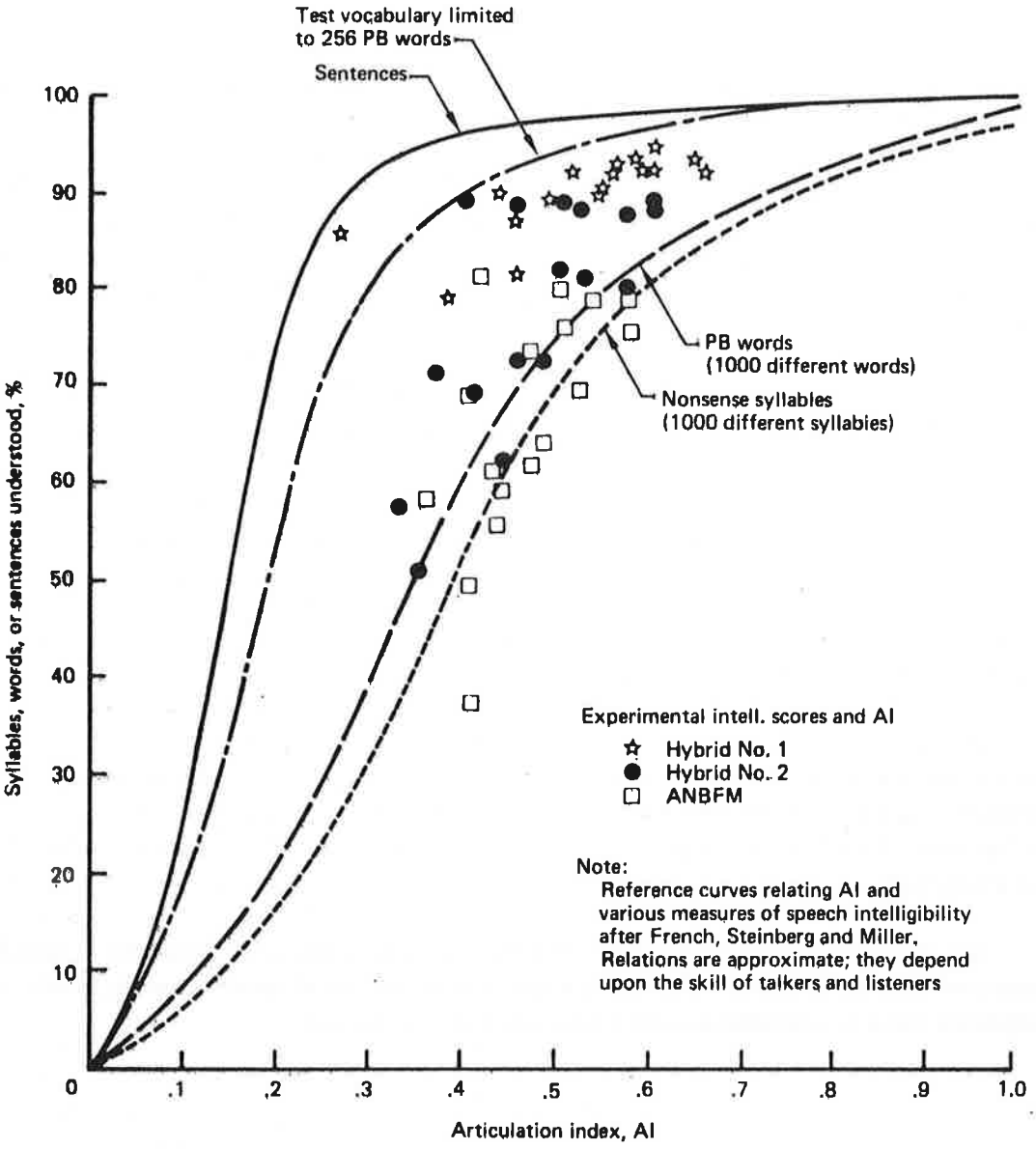

Figure A-1. Voice Modem Intelligibility Scores (400 PB Words) Versus Articulation Index Determined From SCIM Measurements

APPENDIX B

EQUIPMENT LIST AND MAJOR CHARACTERISTICS OF SELECTED SPECIAL TEST EQUIPMENT

This appendix provides (1) an abbreviated list of special test equipment used for the aeronautical technology tests and (2) summaries of major characteristics for selected subsystems. A comprehensive list of test instrumentation items (including calibration and test equipment) plus additional design information are given in "U.S. Aeronautical Technology Test Program – Terminal Design," document and design data package submitted under contract DOT-TSC-707, August 1975.

B.1 ABBREVIATED LIST OF SPECIAL TEST EQUIPMENT

A list of selected special test equipment used at the aircraft terminal is given in table B-1. A comparable list of selected special test equipment used at the Rosman ground terminal is given in table B-2.

B.2 MAJOR CHARACTERISTICS OF SELECTED SPECIAL TEST EQUIPMENT SUBSYSTEMS

B.2.1 Multipath Test

B.2.1.1 Satellite Aeronautical Channel Prober (SACP) – Major characteristics of this subsystem are given in table B-3. Information in table B-3 is extracted from "Instruction Manual for the Satellite Aeronautical Channel Prober: Volume I, System Description and Operation," contract DOT-TSC-634, Stein Associates, Inc., June 1974.

B.2.1.2 Three-Channel Up-Converter – Major characteristics are summarized in table B-4. Information in table B-4 is based partly on measurements and partly on information provided by the manufacturer (Aertech Industries).

TABLE B-1. AIRCRAFT TERMINAL SPECIAL TEST EQUIPMENT SUMMARY

Item	Manufacturer/model
Antennas (L-Band)	
Forward multipath	Boeing
Quad helix	Boeing
Three-element slot-dipole system	Boeing
Phased array	Ball Brothers Research Corp.
Patch	Ball Brothers Research Corp.
Right/left slot dipoles (RSD/LSD)	Boeing
Crossed-slot	Boeing
Side-mounted multipath	Boeing
RF Subsystem	
Aft RF control unit	Boeing
Forward RF control	Boeing
RF preamplifiers	Avantek AM 1600N
Place R/T units	Bell Aerospace Co.
FAA L-band receiver	Bell Aerospace Co.
IF, Baseband and Recording	
IF tuning unit	Boeing
Carrier detector	Boeing
Aircraft data system	DOT/FAA
Frequency standards	Tracor 304D
Aft patch panels	Boeing
Recorder interface	Boeing
Instrumentation recorders	Honeywell 5600C
Digital recorder	Kennedy 8707
Strip-chart recorder	HP 7418A
Multipath Test	
SACP modulator	Stein Associates, Inc.
Three-channel up-converter	Aertech Ind., C1402
RF amplifiers, 20-W, L-band	Acronetics/Wavecom, Inc.
RF amplifier, 100-W, L-band	Microwave Power Deivces
RF amplifier, 40-W, L-band	Microwave Power Devices
RF amplifier, 20-W, L-band	Singer, Model 5110

TABLE B-1 (CONCLUDED)

Item	Manufacturer/model
Modems	
[a] Adaptive narrowband frequency modulation (ANBFM)	Bell Aerospace Co.
FAA CPSK	Philco-Ford Corp. (WDL)
FAA DPSK	Philco-Ford Corp. (WDL)
[a] NASA DECPSK	Bell Aerospace Co.
Digital ranging modem	DOT/TSC
[a] PLACE S&R ranging	Bell Aerospace Co.
Hybrid No. 1 (Q-M/PSK)	Bell Aerospace Co.
Hybrid No. 2 (PDM/PSK)	Magnavox Research Lab.
Adaptive delta voice modem (ADVM)	Bell Aerospace Co.

[a]Part of PLACE modem unit.

TABLE B-2. ROSMAN TERMINAL SPECIAL TEST EQUIPMENT SUMMARY

Item	Manufacturer/model
Antennas	
Antennas and RF system	NASA station equipment
IF, Baseband and Recording	
Subcarrier multiplex unit	Boeing
Interface units 1 and 2	Boeing
Audio panels 1 and 2	Boeing
Instrumentation recorder	Ampex FR1900
Voice tape recorders	Ampex AG500
Data test set	HP 1645A
Multipath Test	
SACP receiver system	Stein Associates, Inc.
Modems	
Hybrid No. 1 modulator	Bell Aerospace Co.
Hybrid No. 2 modulator	Magnavox Research Lab.
PLACE ground equipment	Bell Aerospace Co. (NASA station equipment)
Adaptive delta voice modulator	Bell Aerospace Co. Adaptive delta voice modulator

TABLE B-3. SATELLITE AERONAUTICAL CHANNEL PROBER (SACP) SYSTEM FEATURES

SACP Transmission Subsystem Modulator	
Probing rate (selectable)	0.5, 1.0, 1.25, 2.5, 5.0, 10 Mbps
Modulation	$\pm 90^{o}$ pseudo-random PSK
PN sequence length (selectable)	1023, 511, 255
IF frequency	70 MHz
Power output (into 75Ω)	0 dBm
SACP Receive Subsystem Demodulator	
IF interface frequency	70 MHz
Video PN rates (selectable)	0.5, 1.0, 1.25, 2.5, 5.0, 10.0 Mbps
Number of multipath complex demodulator taps	112
Output multipath tap low-pass filter bandwidths (1-dB) (selectable)	37.5, 75, 150, 300, and 600 Hz
Output tap dynamic range	40 dB
Number of direct-path complex demodulator taps and filter characteristics	6 at 20 Hz (3-dB)
Real-Time Display	
Display method	Standard oscilloscope
Parameter displayed	Average power at each complex demodulator output
Number of outputs displayed across oscilloscope face	All complex demodulator taps (10-tap selectable zoom)
Averaging time	1/16, 1/4, 1, 4 sec
Input dynamic range	40 dB
Input bandwidth (3-dB)	600 Hz

TABLE B-4. THREE-CHANNEL UP-CONVERTER CHARACTERISTICS

Channel Characteristics	
Number of channels	Three, isolated
Input frequency	70 MHz
Input level	0 dBm, nominal
Output frequency	1650 MHz
Output level	+15 dBm (+3, -0 dB)
Bandwidth (1-dB)	±10 MHz
Up-Converter	
Type	Dual conversion; local oscillators are phase locked to reference frequency
Reference frequency	5 MHz, 0 dBm nominal (external input)
First local oscillator	315 MHz
Second local oscillator	1265 MHz
Frequency coherence	Local oscillators are common to all three channels

Note: The unit was modified to allow a 55-MHz (+7 dBm) external input to be used as the reference frequency as an alternate. The overall frequency conversion (Δf = 1580 MHz) was unchanged when using this alternate.

B.2.2 Modem Test

B.2.2.1 Hybrid No. 1 (Q-M/PSK) Modem – Table B-5 lists the major characteristics of the modem. The information given is extracted from "Handbook of Operating and Maintenance Instructions for Advanced Modem," report 6381-954001, contract DOT-TSC-631, Bell Aerospace Company.

B.2.2.2 Hybrid No. 2 (PDM/PSK) Modem – Table B-6 lists the major characteristics of this modem. The information given is extracted from "Final Report/Technical Manual for Advanced Modem MX480/481 and MX482 C/N_0 Test Set," contract DOT-TSC-623, Magnavox Research Laboratory, March 1974.

TABLE B-5. HYBRID NO. 1 MODEM (Q-M/PSK) CHARACTERISTICS

Modulator	
Audio inputs/outputs:	
Tape	600-ohm, balanced (0 VU)
Microphone	150 ohm, single-ended (-50 VU)
Headphone	600-ohm, single-ended (0 VU)
Data inputs:	
External clock and data	1200 or 2400 bps, Q to +5 V
Internal clock and data	1200 or 2400 bps, choice of PN sequences with 2^{11}-1, 2^{7}-1, or 2^{6}-1 bits
Modulation:	
Voice only	Quadrature modulation
Data only	DCPSK
Voice plus data	Voice and DCPSK on quadrature phase components of carrier
RF output:	
Frequency	70 MHz
Level	0 dBm (50 ohms)
Demodulator	
RF input:	
Frequency	70 MHz, +4 kHz
Level	-20 to +10 dBm (50 ohms)
C/N_0 range	35 to 55 dB-Hz, nominal
Demodulator:	
Voice only	Second-order PLL
Data only	Costas loop
Voice plus data	Costas loop
Acquisition and tracking:	
Mode	Automatic
Range	$\pm$4 kHz, minimum
Audio outputs:	
Recorder	600-ohm, single-ended, 0 VU
Headphone	600-ohm, single-ended, 0 VU
Data outputs:	
Detector type	Matched filter (I&D)
Data rates	1200 or 2400 bps
Data signal	Differentially decoded data
Clock signal	Available
Internal error detector:	
Data rates	1200, 2400 bps
Codes	PN sequences of 2^{6}-1, 2^{7}-1, 2^{11}-1 bits
Adaptive Delta Voice Mode	
Clock rate	19.2 kbps
Step size	Adaptive, dependent on input waveform slope
Modulation	PSK with residual carrier at 7.0 dB0
Carrier demodulation:	
Type	Coherent, second-order PLL
Loop bandwidth	B_L = 100 Hz
Processing options:	
Digital	I&D (matched filter) detection, bit sync derived from data
Analog	Linear filtering, bit sync not required

TABLE B-6. HYBRID NO. 2 MODEM (PDM/PSK) CHARACTERISTICS

Modulator	
Data inputs:	
Rates	1200 or 2400 bps
Levels	Bipolar, +1 to +10 V for logical one, -1 to -10 for logical zero
Voice inputs	Low-level microphone at 150 ohms High-level recorder input into 10 kΩ
Internal test data	2^{11}-1, ($x^{11} + x^2 + 1$) maximal linear sequence 2^7-1 maximal linear sequence 2^4 -1 maximal linear sequence All ones All zeros
Data clock output	1200 or 2400 bps at T^2L level
Demodulator	
70-MHz signal input	0 dBm nominal (+10 to -20 dBm, range acquirable over ±4 kHz doppler offset)
Data outputs:	
Bit rates	1200 or 2400 bps
Levels	0 V for logical zero +1 V for logical one
Bit-error detector	+1 pulse whenever an error occurs
Internal test data	2^{11}-1 ($x^{11} + x^2 + 1$) maximal linear sequence 2^7-1 maximal linear sequence 2^4-1 maximal linear sequence
Voice outputs:	
Recorder	1 V rms nominal into high-impedance recorder
Headphone	600-ohm balanced line with volume control

B.2.2.3 FAA CPSK and DPSK Demodulators – These two demodulators were originally designed and optimized for the DOT/FAA ATS-5 test program (ref. 5-2). The primary design constraint was the need to operate with the discontinuous ATS-5 L-band forward-link signal. (Due to the spin of ATS-5, the L-band forward link was "pulsed"; i.e., the signal was available to the demodulators in bursts of 50-msec duration, separated by channel "dead times" of 733 msec). For the DOT/TSC ATS-6 aeronautical technology tests, the demodulators were used in their original design configuration (so that results could be compared with previous performance and simulator tests) rather than being reoptimized for the ATS-6 test program. Certain demodulator design features, such as DECPSK Costas loop B_L, tracking range, etc. are therefore somewhat different than they would be for a design specific to the ATS-6 test program.

A more detailed description of the design and block diagrams of the demodulator implementations are given in reference B-1. Major characteristics are summarized in table B-7.

B.2.2.4 PLACE Modem Unit – This unit includes the adaptive NBFM voice, DECPSK data, and S&R ranging modems. The unit is described in "Handbook of Operating and Maintenance Instructions for PLACE Airborne Equipment," report 6203-954002, Bell Aerospace Company, March 1973.

TABLE B-7. FAA DECPSK AND DPSK DEMODULATOR CHARACTERISTICS

IF Amplifier and Down-Converters	
Input frequency	10 MHz (±300 Hz)
Input signal level	-20 dBm, nominal
IF gain control:	
Type	Selectable, AGC or manual
AGC type	Derived from signal
AGC/MGC range	20 dB, minimum
Image Suppressions	40 dB, minimum
IF Bandwidth (3-dB)	8 kHz
DECPSK/CPSK Data Demodulator	
Carrier demodulation	Costas loop (digital), $B_L \simeq 200$ Hz
Acquisition and tracking range	±500 Hz, minimum
Bit rates	1200, 2400 bps
Data outputs	Both decoded data and differentially decoded data
Data clock output	Available
DPSK Data Demodulator	
Automatic frequency control:	
Type	Quadricorrelator
Frequency tracking range	±600 Hz
Output frequency error	Less than ±50 Hz
Data detection	Baseband implementation of phase-comparison detection
Bit rates	1200, 2400 bps
Data output	Differentially decoded data
Data clock	Available

APPENDIX C

REPORT OF INVENTIONS

Work performed under this contract consisted of test support related to the U.S. aeronautical ATS-6 L-band technology test program. Major tasks included test instrumentation, conduct of the field test program, and analysis of the data acquired. Although the program has yielded a substantial body of valuable data which provide a significant extension to existing scientific knowledge, a diligent review of the work performed under this contract has revealed no innovation, discovery, improvement, or invention.

☆U.S. GOVERNMENT PRINTING OFFICE: 1976—700-696/124

350 Copies